Imperial College London
Department of Physics

LIGHT MATTER INTERACTION IN MESOSCOPIC SYSTEMS

Federico Armata
August, 2017

Supervised by Prof. Myungshik S. Kim
Report submitted in partial fulfilment of the requirements of the degree of PhD
of Imperial College London

“Pick a flower on Earth and you move the farthest star.”

Paul A.M. Dirac

Declaration of originality

I hereby declare that the following thesis is composed of my own original work, developed during my PhD at Imperial College in the Controlled Quantum Dynamics group. All published and unpublished work of others has been appropriately referenced and acknowledged.

Declaration of copyright

Acknowledgements

I would like to first thank my supervisor, Myungshik Kim, for having taken me on as a student, for his support and help during these years, for all the teachings and for having allowed me to freely explore the physical world. ‘Kamsahamnida’!

I am also deeply indebted to Peter Rabl for having given me the opportunity to work in his group, for the quality of his help and for having shared with me his physical insight. I would like to then extend my gratitude to the Quantum Optics Theory research Group of the Atominstitut (TU Wien) for the warm hospitality during my numerous visits to Vienna. In particular, an extraordinary thank to Giuseppe for his true friendship and to Tuomas for his great patience and his help.

A special thank also to Doug Plato and Carlo Di Franco for their help and mentorship during these three years, and to Tommaso Tufarelli and Marco Genoni for having taught me so much physics. Thanks also to the other members of my group: Luca, Chuanqi and Alejandro, for the many stimulating discussions and the good time.

I also express my gratitude to Roberto Passante and Lucia Rizzuto for their continuous support during all my studies and for being always there when I need; and to my friends Giulio and Pablo: you are always a true source of inspiring and original points of view. I really hope to continue to work with you in the future.

Thanks also to Michael Vanner for his precious collaboration and his warm hospitality during my several visits to Oxford.

Many thanks also to Farhang for the fun and the always kind words towards my land. It is always a pleasure to chat with you. I wish you all the best.

And then, Ludovico. Thank you very much for your friendship, your support and for having shared with me so much of your time. Ad maiora!

Last but not least, Valentina: every success I have collected during these years has been possible thanks to you.

LIST OF PUBLICATIONS

This thesis is based upon the following publications and pre-prints.

- *Probing anharmonicity of a quantum oscillator in an optomechanical cavity*, L. Latmiral, **F. Armata**, M. G. Genoni, I. Pikovski, and M. S. Kim, Physical Review A **93**, 052306, 2016.
- *Quantum and classical phases in optomechanics*, **F. Armata**, L. Latmiral, I. Pikovski, M. Vanner, C. Brukner and M. S. Kim, Physical Review A **93**, 063862, 2016.
- *Dynamical Casimir-Polder force between an excited atom and a conducting wall*, **F. Armata**, R. Vasile, P. Barcellona, S. Buhmann, L. Rizzuto, R. Passante, Physical Review A **94**, 042511, 2016.
- *Dynamical dressing process of a mobile mirror interacting with a field*, **F. Armata**, M. S. Kim, S. Butera, L. Rizzuto, R. Passante, Physical Review D, **96**, 045007, 2017.
- *Harvesting multiqubit entanglement from ultrastrong interactions in circuit quantum electrodynamics*, **F. Armata**, G. Calajo, T. Jaako, M. S. Kim, and P. Rabl, Physical Review Letters, **119**, 183602, 2017.

Other works carried out during the PhD (not directly included in the thesis):

- *Vacuum energy densities of a field in a cavity with a mobile boundary*, **F. Armata**, R. Passante, Physical Review D **91**, 025012, 2015.
- *Effect of boundaries on vacuum field fluctuations and radiation-mediated interactions between atoms*, **F. Armata**, S. Butera, G. Fiscelli, R. Incardone, V. Notararigo, R. Palacino, R. Passante, L. Rizzuto, S. Spagnolo, J. Phys. Conf. Series - Proceedings of the Eighth International Workshop DICE 2016 Spacetime-Matter-Quantum Mechanics, 880, 012064, 2017.
- *Quantum Limits to Gravity Estimation with Optomechanics*, **F. Armata**, L. Latmiral, A. D. K Plato and M. S. Kim, Physical Review A, **96**, 043824, 2017.

Abstract

The study of light-matter interaction has led to many fundamental discoveries as well as to the development of new technology. In this thesis, we investigate the interaction between light and matter in different mesoscopic systems such us Fabry-Perot cavities with fixed and/or moving mirrors (optomechanical cavities) and superconducting circuits. In the context of optomechanical cavities, we isolate genuine quantum contributions of the interaction between an optical field and a mechanical mirror and study how to probe nonlinearities of the mechanical motion. We also investigate dynamical corrections, arising from an initial non-equilibrium configuration of the system, to the Casimir energy induced by the interaction between a quantum multimode field and the quantum fluctuations of the movable mirror. In a cavity scenario, we further consider such kind of dynamical corrections for the Casimir-Polder force between an excited atom and a perfectly conducting mirror, finding new features that can allow for an easier way to single-out the dynamical Casimir-Polder effect. In the context of superconducting circuits, we explore the light-matter interaction between microwave fields and artificial atoms in the ultrastrong coupling regime, where the system displays a high degree of entanglement. We show how to extract these (otherwise inaccessible) quantum correlations, and how such correlations can potentially be exploited as a resource for entanglement-based applications. In all these investigations we provide feasible experimental scenarios where such new effects can be probed.

Contents

List of Figures

Introduction

Quantum mechanics is usually associated with the study of microscopic objects such as elementary particles or atoms, in contrast to classical mechanics, which studies the motion of macroscopic objects such us billiard balls or planets. However, recent theoretical and experimental developments have allowed to extend the domain in which quantum mechanical phenomena arise and can be probed, thus challenging our common understanding of macroscopicity. These remarkable achievements have represented a fertile ground for the discovery of new quantum mechanical effects as well as the study of the interaction between electromagnetic fields and matter in unexplored limits. On the other hand, the interaction between light and matter, which has been studied for decades, still plays a prominent role in physics and it is not completely understood. Microscopic particles such us photons can now be coupled to mesoscopic objects with dimensions ranging in the micro-nano scale, which can still be considered mascroscopic in the sense that they contain a large number of microscopic entities and need to be described by many degrees of freedom. Understanding how quantum mechanics plays a role in the dynamics of objects with such dimensions and how these systems interact with quantum light sources, not only represents a fundamental goal in many areas of physics, but it is also very relevant for the development of new technologies.

One of the novel platforms where light interacts with mesoscopic objects is optomechanics. Here, electromagnetic fields interact with micro-nano mechanical degrees of freedom and many different optomechanical systems can be experimentally realized and studied [1]. Of particular interest, both from a historic perspective and a theoretical point of view, is the archetypal Fabry-Perot cavity, which can have fixed or moving mirrors. In this last case the system has revealed to be so fundamental that now represents a subfield of quantum optics on its own that we now call cavity optomechanics [2]. In an optomechanical cavity, field and mirror can interact through the radiation pressure force (given by the photons inside the cavity) or by vacuum fluctuations. The mechanical motion of the mirror can be described with the laws of classical physics or quantum mechanics. In the first case, the movement of the mirror is governed by a prescribed equation of motion, and interesting phenomena can appear under specific physical conditions. One example is represented by the dynamical Casimir effect: a production of photon pairs from the vacuum of the electromagnetic field [3]. This, in turn, paves the way to fundamental questions related to the concept of vacuum and to the experimental challenges which need to be faced when aiming to probe this tiny radiation field. In the second case, that is when we attempt to describe the mirror as a quantum mechanical object, the mechanical degrees of freedoms need to be included in the overall system dynamics. This means that the system must follow a quantum dynamics induced by a Hamiltonian, which should describe the interaction between field and mirror [4]. In this thrilling scenario it is possible to utilize the optomechanical cavity as a tool to investigate various fundamental physical questions related to the quantum-to-classical-transition, the interface between quantum mechanics and gravity, and relevant aspects of the quantum vacuum [2].

In the context of the quantum-to-classical transition, it becomes really interesting to understand to what extent a mesoscopic object such us the moving mirror in an optomechanical cavity can behave as a quantum object. The main task in this respect is to find features, if any, that can be used as signatures of the quantum interaction of the mirror with the light and that can highlight differences between a classical and quantum description of the mechanical motion. The first Chapter of this thesis is devoted to such questions. We study the quantum-classical comparison in an optomechanical cavity by looking at the phase acquired by the electromagnetic field after its (pulsed or continuous) interaction with the mechanical mirror. We discover that many of the features, which have been previously considered quantum peculiarities in many recent proposals, can be actually reproduced within a fully classical description of the model. At the same time, we isolate peculiarities which cannot be explained classically, thus providing new ways to identify the quantum regime of an optomechanical cavity.

The ability to manipulate and control physical systems on the micro-nano scale has increased during the last years. This has attracted the attention of physicists working in different fields, since such mesoscopic systems offer not only the possibility to explore new aspects of the light-matter interaction, but also to test fundamental aspects of quantum-mechanics and its interplay with other theories. Recently, a great attention has been focused on the chance to probe possible deviations in the quantum mechanical description of the mechanical motion [5]. For example, by assuming a mirror described as a quantum harmonic oscillator, it has been suggested an optomechanical experiment which aims to probe a possible modification of the standard commutator between position and momentum operators of the mechanical oscillator [6]. In this context, it becomes very relevant to investigate the effect of other possible modifications in the system dynamics, for example intrinsic anharmonicities. In the second Chapter, we then consider an optmechanical cavity with an anharmonic mechanical oscillator, and propose a scheme to probe such anharmonicity. Our protocol offers a very general procedure which can be used to measure other possible nonlinearities in the system dynamics, for example those which might arise from a different interaction Hamiltonian.

Optomechanical cavities and, more in general, nano- and microelectromechanical systems are also an attractive platform for the research in Casimir physics [7]. In fact, Casimir and Casimir-Polder forces are electromagnetic forces (usually attractive) of purely quantum origin between metallic or dielectric macroscopic objects placed in the vacuum space (even at zero temperature), which become significant at submicrometre scales. They originate whenever a field is confined in a specific geometric configuration, which requires imposing boundary conditions on the field, and are ultimately related to a dependence of the vacuum energy from the geometric configuration [8]. The advance of the experimental achievements in the miniaturization of mechanical objects has led to a new understanding of such electromagnetic forces in complex microstructured geometries [7]. In the third Chapter of this thesis we start to study the Casimir energy (or force) in the context of the optomechanical cavity. In particular, starting from a non-equilibrium configuration of the system, we investigate dynamical corrections to the static Casimir energy between the two mirrors of the cavity, which originate because of the quantum fluctuations of the mechanical mirror. We then enlarge our study to a different scenario, where we consider the interaction between an excited atom and a fixed mirror mediated by the vacuum of the electromagnetic field. This configuration is actually a standard scenario in cavity quantum-electro-dynamics (cavity QED), where the light-matter interaction with two-level atoms coupled to radiation modes is studied. In this case, we explore dynamical corrections to the static Casimir-Polder force. We show novel features which should allow for an easier way to single-out and observe the dynamical Casimir-Polder effect.

Over the last decades, in the study of light-matter interaction, major strides have been made in increasing the strength of interaction (even at the single-photon level), leading to a perpetual exploration of new physics and applications. The most promising platform in this direction is probably represented by superconducting circuits [9]. In this field, one can study interactions between one (or many) artificial two-level atoms or qubits (represented by charge or flux circuits built according to certain specifications) with radiation fields (usually LC resonators). Because of the very strong analogy between the physics of superconducting circuits and cavity QED, the area of research studying light-matter interactions in such systems is now called circuit QED. Here, it is possible to reach the regime where these artificial atoms can be coupled ultrastrongly to microwave resonator modes and the features of the light-matter interaction drastically change [10, 11]. The last Chapter of this thesis analyzes a multi-qubit circuit QED system in the regime where the qubit-photon coupling dominates over the system's bare energy scales. We propose a feasible scheme that can be used as a probe for otherwise non-accessible correlations in strongly-coupled circuit QED systems and that clearly shows how such quantum correlations can potentially be exploited as a resource for other entanglement-based applications and quantum information-processing.

In Fig. 1 we provide a pictorial overview of this thesis and how it may be read. Central to all our investigations is indeed the study of the light-matter interaction. Chapters 2 and 3 consider an optomechanical cavity where a mechanical mirror interacts with an optical field, focusing our attention on the classical-quantum comparison of the system dynamics and on the study of mechanical nonlinearities. In Chapter 4 we move to a multimode optomechanical scenario, which naturally offers the possibility to explore modifications to the Casimir energy in a cavity. In the same Chapter we also enlarge our study to the dynamical Casimir-Polder force between an excited atom and a multimode electromagnetic field in the presence of a perfectly reflecting mirror (a typical scenario of cavity QED). Finally, Chapter 5 is dedicated to the study of a circuit QED system, where it is possible to achieve ultrastrong interactions between artificial atoms or qubits (represented by charge or flux circuits) and microwave fields.

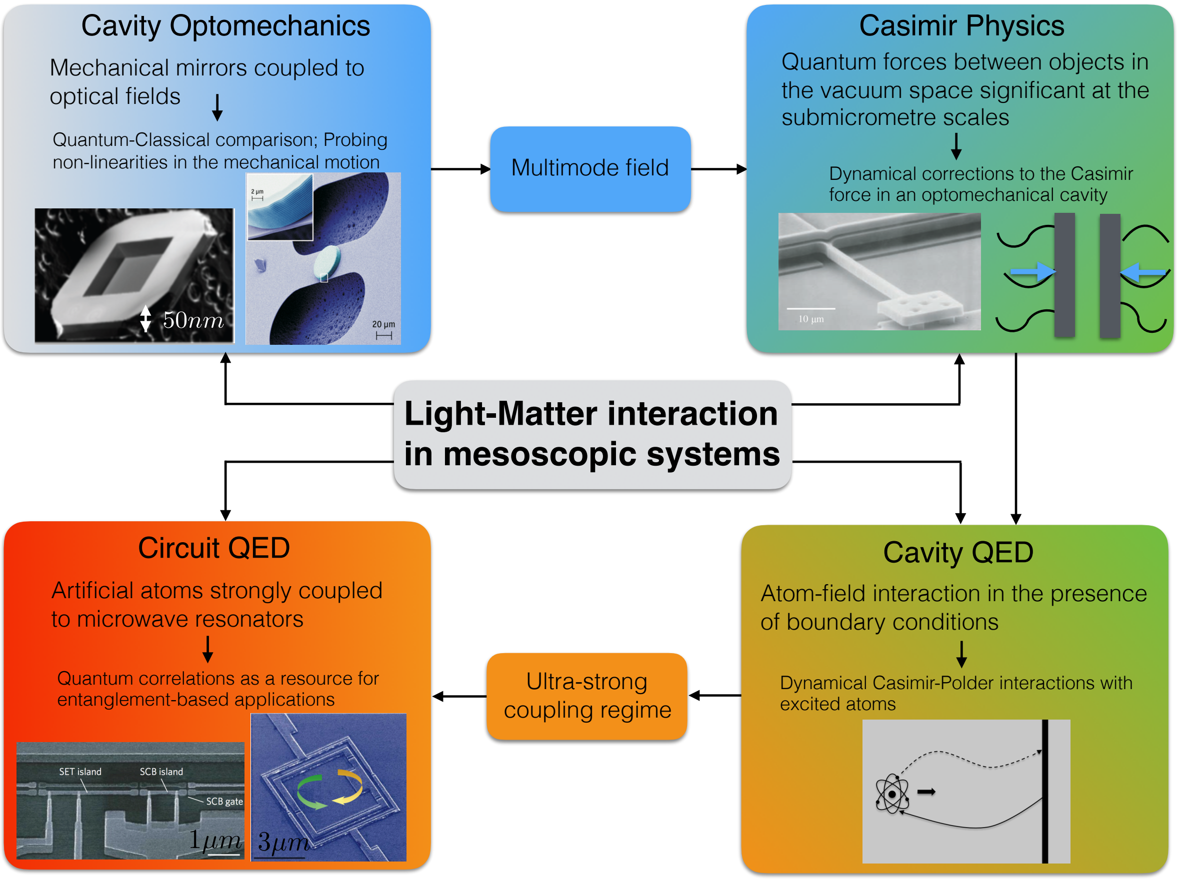

Figure 1: Pictorial overview of this thesis and how it may be read. The lines with arrows connecting the four large boxes (describing the main topics of the work) together with the scale of the colors would like to indicate a recommended route for this thesis. Of course, all these fields of research are actually connected one with the other. For example superconducting circuits have actually allowed to detect the dynamical Casimir effect [12]. The figures on the left and right, inside the "Cavity Optomechanics" box, are imported from Refs. [13] and [14]. They respectively represent a photograph of a SiN membrane (1mm × 1mm × 50nm) on a silicon chip used within an optomechanical cavity and a scanning electron micrograph of a circular (high-reflective) Bragg mirror used as the end mirror of a Fabry-Perot cavity. In the panel "Casimir Physics" the figure on the left is taken from Ref. [15] and represents a scanning electron micrograph of a micromachined torsional device with a particular close-up to the torsional rods anchored to a substrate. This device has been used to measure the static Casimir force with high-precision. While, in the box "Circuit QED" the two figures on the left and right are imported from Refs. [9, 16] and represent a micrograph of a Cooper-pair box (SCB) and of a three-junction flux qubit, respectively.

Chapter 1

Background

1.1 Overview

This Chapter provides all the background information needed for the following chapters of this thesis, and it is organized as follows. There are three main Sections, each of them describing one of the main topics treated in this work: “Cavity Optomechanics”, “Casimir Physics” and “Circuit QED”. In each of these Sections we give a brief introduction to the field mostly in relation to our interests, present the main ingredients that will constitute the starting points for our investigations, and finally provide some basic instruments that will be used in the corresponding chapters.

In the first Section, we present the general Hamiltonian formulation of the optomechanical interaction, which considers a multimode field inside a cavity with a mobile ending mirror. From this result we derive the Hamiltonian for the case of a single mode field, which is the optomechanical interaction commonly used in quantum optics applications and current experiments. For this last case, we also describe the three main interaction regimes in which an optomechanical cavity can operate. Finally, the last two paragraphs deal with the main detection schemes used to measure the optical field in the cavity and some basic tools of quantum estimation theory.

In the second Section, we start by studying the interaction between an atom and an electromagnetic field, which is at the heart of all the investigations in cavity QED and, more in particular, of many results in the field of Casimir and Casimir-Polder forces. In the next two paragraphs we then discuss two basic examples of Casimir Physics: the Casimir force between two fixed mirrors in the vacuum and the Casimir-Polder force between an atom and a fixed mirror, both mediated by the electromagnetic field. These are basic scenarios in cavity QED. To derive such forces one could calculate the net interaction between all the atoms in the specific configuration. However, this procedure is quite demanding in terms of calculation. For this reason, both the forces will be derived by using a different approach: the Casimir force is calculated through the standard renormalization procedure of a quantum field in presence of boundaries, while the atom-wall Casimir-Polder force by exploiting the interaction between the atom and the electromagnetic field with a boundary condition on the wall's position. These two paragraphs will be relevant for the first and second part of Chapter 4, respectively.

In the third Section, we describe the classical Hamiltonian formulation of the dynamics of electrical circuits and show the standard procedure of quantization. We then present the basic circuits which constitute the fundamental building-elements of every more complex circuit system. In the language of circuit QED, the quantized quantum LC resonator models an electromagnetic microwave field, while charge, transmon or flux circuits (qubits) artificial atoms. In the final Chapter of this thesis we will couple an array of flux qubits to the same LC resonator, and study the systems dynamics in the ultrastrong coupling regime. The resulting quantum Hamiltonian will be be formed by a Dicke-like term (usual interaction between a single mode electromagntic field and an atom) plus some interactions between qubits (similar to the dipole-dipole interactions between atoms).

1.2 Cavity Optomechanics

1.2.1 Introduction

The growing field of quantum optomechanics studies the coupling of optical fields with nano- or micro-mechanical degrees of freedom. It exploits the radiation pressure force, applied by the electromagnetic field on any object, to create a coupling between light and matter or a mutual interaction between mechanical objects mediated by the electromagnetic field. An optomechanical coupling can be engineered in different platforms, some examples are Fabry-Perot cavities (relevant to this work), suspended mirrors or membranes, optical microspheres, microtoroids, photonic crystals, cold atoms and even micro-fabricated superconducting resonators [1]. In Fig. 1.1 we provide scanning electron micrographs of some of these mesoscopic systems.

Thanks to advances in materials science and nano-fabrication, in particular the rise of nano- and microelectromechanical systems (MEMS), the ability to miniaturize mechanical elements has considerably increased during the last years. The mass of these mechanical objects now ranges from 10^{-6} to 10^{-22} Kg (and even 1g) [2]. This, combined to the possibility of cooling these systems to temperatures of the order of a few millidegrees Kelvin (almost to their ground state of motion), provides a new arena in which to explore the boundary between quantum and classical mechanics and fundamental questions interfacing different areas of physics and paves the way to technological applications. Also, the increasing level of control, manipulation and detection of the mechanical motion at the quantum regime by using light, the great flexibility in design and the potential to realize on-chip architectures could boost applications in quantum information processing, where optomechanical systems could be used as light-matter interfaces to transfer and convert information. As an example, it has been shown as strong optomechanical interactions in a multimode setup can be exploited to generate single photons and to perform controlled gate operations between photonic or mechanical qubits [17].

Another striking virtue of optomechanical systems is that they can be naturally hybridized to other (microscopic) quantum systems such as trapped atoms or ions, solid-state spin qubits, or superconducting devices. It has then been suggested that hybrid mechanical systems can enable new approaches to the quantum control of mechanical objects, precision sensing, and quantum information processing [18]. Also, they might provide suitable scenarios to explore the strong coupling regime of light and matter. In the next future, with more ambition, mechanical elements might be functionalized with electrodes, magnets, or mirrors and serve as universal transducers (intermediaries) between otherwise incompatible systems [19].

A part from all the technological applications, all this moves the research towards fundamental tests of the quantum theory for objects whose size and mass was previously unaccessible. In fact, optomechanical systems have been proposed as a table-top platform to also explore the boundary between quantum mechanics and gravity at low energies, in particular gravitationally induced decoherence mechanisms [20, 21] and even possible modifications to the standard quantum rules (for example modifications of the commutation relations) [5, 6].

On the other hand, optomechanical systems and more in general micro/nano -mechanical devices, have a natural potential to probe extremely small forces often with spatial resolution at atomic scales [19]. A remarkable example is given by recent high precision measurements of the Casimir force in different microstructured environments. Such quantum forces can be then used to control the motion of mechanical components of a system to prevent unwanted interactions such as 'stiction' between moving parts [7, 22].

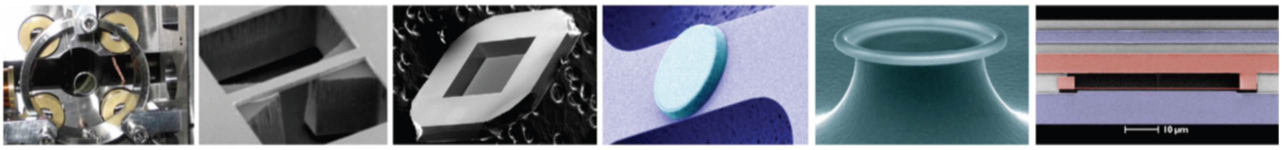

Figure 1.1: Optomechanical systems widely range in mass and size. This figure from Ref. [1] shows some of these devises. From left to right: a suspended 1g mirror which is part of a Fabry-Perot cavity [23], a suspended micro-mirror on a silicon resonator [24], a suspended 50nm thick dielectric membrane inside a cavity [13], a micro-mechanical resonator which is attached to μm-scale mirror [14], a silica micro-toroid that couples optical whispering-gallery modes to radial mechanical modes [25], and a nano-mechanical oscillator coupled to a superconducting microwave cavity [26].

In this Section we focus our attention on cavity optomechanics, whose archetypal system consists of a Fabry-Perot cavity formed by two mirrors, one fixed and and the other free to move, though subjected to an external potential. In fact, we recall that historically the first well-understood optomechanical systems were the early gravitational-wave detectors developed in the late 1970s [27, 28]. Cavity optomechanics now represents a promising and prolific field on its own [2], where the radiation pressure force, given by the photons of a single- or multi-mode field inside the cavity, has been employed for many purposes.

Among them we mention: the cooling of the mechanical oscillator, which has provided the chance to explore quantum interactions at very low temperatures [29], the investigation of standard quantum limits for position detection for quantum metrology and sensing applications, which have been essential for gravitational wave detectors such us LIGO or VIRGO [19, 28]; and, the access to strong quantum Kerr nonlinearities enhanced by the optomechanical coupling [30, 31], which realize nonclassical and entangled states of light and mechanics. At the heart of all these applications, one can find the most relevant advantage of cavity optomechanics, that is the readout of the mechanical motion through the light field transmitted through (or reflected from) the cavity, which gives the possibility to measure the displacement of a mechanical resonator via the transmitted or reflected optical phase shift [2].

1.2.2 Hamiltonian formulation of the optomechanical interaction

Here we briefly follow a very general Hamiltonian formulation of the optomechanical interaction, which holds in the non-relativistic regime [4]. Consider a scalar field $A(x,t)$ in a cavity formed by two perfectly reflecting mirrors: one fixed at the position $x = 0$, while the other of mass M free to move within a potential $V(q)$ around the equilibrium position $x = L$. The motion of the movable mirror is also influenced by the radiation pressure force of the field inside the cavity. $A(x,t)$ is defined in the region $0 \leq x \leq q(t)$, and its dynamics is described by ($c = 1$)

$$\frac{\partial^2 A(x,t)}{\partial x^2} = \frac{\partial^2 A(x,t)}{\partial t^2}, \tag{1.1}$$

where we impose Dirichlet boundary conditions: $A(0,t) = A(q(t),t) = 0$. We highlight that $A(x,t)$ can also be the potential vector of a one-dimensional electromagnetic field. On the other hand, the mirror equation of motion (in the non-relativistic regime) is

$$M\ddot{q} = -\frac{\partial V(q)}{\partial q} + \frac{1}{2}\left(\frac{\partial A(x,t)}{\partial x}\right)^2_{x=q(t)}. \tag{1.2}$$

The second term in (1.2) is the radiation pressure force which can be evaluated by computing the xx component of the energy momentum tensor of the field in the mirror comoving frame. Let us now define a set of (instantaneous) generalized coordinates $Q_k \equiv \sqrt{2/q(t)}\int_0^{q(t)} dx A(x,t)\sin[k\pi x/q(t)]$ (with k is a positive integer), which decompose the field modes in terms of basic functions (usually called *mode functions*) determined by the instantaneous position of the wall: $A(x,t) = \sum_{k=1}^{\infty} Q_k \sqrt{2/q(t)}\sin[k\pi x/q(t)]$. By using this expansion and the orthogonality of the mode functions, Eqs. (1.1) and (1.2) are equivalent to

$$\begin{aligned} \ddot{Q}_k &= -\omega_k^2 Q_k + 2\frac{\dot{q}}{q}\sum_j g_{kj}\dot{Q}_j + \frac{\ddot{q}q - \dot{q}^2}{q^2}\sum_j g_{kj}Q_j + \frac{\dot{q}^2}{q^2}\sum_{jl} g_{jk}g_{jl}Q_l, \\ M\ddot{q} &= -\frac{\partial V(q)}{\partial q} + \frac{1}{q}\sum_{kj}(-1)^{k+j}\omega_k\omega_j Q_k Q_j, \end{aligned} \tag{1.3}$$

in which $\omega_k(q) = k\pi/q$ and $g_{kj} = (-1)^{k+j}2kj/(j^2 - k^2)$ for $k \neq j$, and vanishes for $k = j$ [§] . The dynamics of system in the non-relativistic limit is completely described by the equations (1.3). We remark that following this very general approach the mechanical degrees of freedom of the mirror have been included in the overall systems dynamics. Indeed, we can construct the Lagrangian of the system

$$\begin{aligned} \mathcal{L}(q,\dot{q},Q_k,\dot{Q}_k) = \frac{1}{2}\sum_k \left[\dot{Q}_k^2 - \omega_k^2(q)Q_k^2\right] + \frac{1}{2}M\dot{q}^2 - V(q) \\ -\frac{\dot{q}}{q}\sum_{jk} g_{kj}\dot{Q}_k Q_j + \frac{\dot{q}^2}{2q^2}\sum_{jkl} g_{kj}g_{kl}Q_l Q_j, \end{aligned} \tag{1.4}$$

[§] $g_{kj} = q\int_0^q dx\, \varphi_j \frac{\partial \varphi_k}{\partial q}$ with $\varphi = \sqrt{\frac{2}{q}}\sin\frac{k\pi x}{q}$

which, in the non-relativistic limit for the motion of the wall, gives Euler-Lagrange equations equivalent to (1.3). The associated Hamiltonian is $\mathcal{H}(P_k, Q_j, p, q) \equiv p\dot{q} + \sum_k P_k \dot{Q}_k - \mathcal{L}(q, \dot{q}, Q_k, \dot{Q}_k)$, where $P_k = \dot{Q}_k - (\dot{q}/q) \sum_j g_{kj} Q_j$ and $p = M\dot{q} - (1/q) \sum_{jk} g_{kj} P_k Q_j$ are the conjugated momenta to Q_k and q, respectively. Note that the canonic momentum of the mirror p is not equal to the (mechanical) momentum related to the kinetic energy. The explicit form of the Hamiltonian is thus $\mathcal{H} = (1/2M) \left(p + (1/q) \sum_{j,k} g_{kj} P_k Q_j\right)^2 + V(q) + (1/2) \sum_k [P_k^2 + \omega_k^2 Q_k^2]$, which represents the actual total energy of the system $\mathcal{H} = \mathcal{H}_{\mathrm{f}} + M\dot{q}^2/2 + V(q)$, where $\mathcal{H}_{\mathrm{f}}$ is the total field energy defined as $\mathcal{H}_{\mathrm{f}} = (1/2) \int_0^{q(t)} dx \left[(\partial A(x,t)/\partial t)^2 + (\partial A(x,t)/\partial x)^2\right]$.

Let us now proceed to quantize the field-mirror model following the canonical procedure. We promote the dynamical variables p, q, P_k, Q_k to operators subject to the commutation rules $[q, Q_j] = [q, P_k] = [p, Q_j] = [p, P_k] = 0$, $[q, p] = i\hbar$ and $[Q_j, P_k] = i\delta_{jk}\hbar$. To specify the quantum state of the system, we define creation and annihilation operators for each mode of the cavity as $a_k(q) = \sqrt{1/2\hbar\omega_k(q)}\, [\omega_k(q) Q_k + iP_k]$, $a_k^\dagger(q) = \sqrt{1/2\hbar\omega_k(q)}\, [\omega_k(q) Q_k - iP_k]$, which depend on the cavity length. This indicates that there is a different set of Fock states for each position taken by the moving mirror. Substituting these expressions into the hamiltonian $\mathcal{H}$ and following the usual *renormalization* procedure to treat the infinite zero point energy of the field, we finally get the Hamiltonian which describes the quantum interaction between field and mirror:

$$\mathcal{H} = \frac{(p + \Gamma)^2}{2M} + \tilde{V}(q) + \hbar \sum_k \omega_k(q) a_k^\dagger(q) a_k(q), \tag{1.5}$$

where

$$\Gamma = \frac{i\hbar}{2q} \sum_{k,j} g_{kj} \left[\frac{k}{j}\right]^{1/2} \left[a_k^\dagger(q) a_j^\dagger(q) - a_k(q) a_j(q) + a_k^\dagger(q) a_j(q) - a_j^\dagger(q) a_k(q)\right], \tag{1.6}$$

and $\tilde{V}(q) = V(q) - E_{\mathrm{Cas}}(d)$ is now the new potential which includes the Casimir energy $E_{\mathrm{Cas}} = \hbar c\pi/(24q)$ for a one-dimensional cavity. This energy originates after subtracting two infinite quantities: the zero point energy fluctuations of the scalar field inside the cavity and the ones in free space (without the presence of boundary conditions). Note that, in this renormalization procedure, we have actually considered the field outside the cavity to compensate the infinite energy variation of the zero point fluctuations inside the cavity. Therefore, to have a consistent theory we should also include the dynamical degrees of freedom of the outside field. Hamiltonian (1.5) results then an approximation, since we are only taking into account the static part of the interaction between the mirror and the outside field, which is enclosed in the Casimir energy. The dynamical contribution of such interaction, which should describe the changes of the outside field, has been neglected. In the majority of physical cases, this represents a good approximation, since we commonly have a dominant field inside the cavity. A simple case is for example represented by a cavity containing (initially) a considerable number of photons, so that the dynamical effects of the outside field become negligible. We, however, remark that if the movable mirror is perfectly reflective on both sides, we could generalize the above formulation to obtain a full Hamiltonian including the outside field. We will consider this delicate aspect in Chapter 4, where we will discuss dynamical corrections to the Casimir energy in an optomechanical cavity. While, in the subsequent Section of this Chapter we will clarify the derivation of the Casimir force between the two walls in the more general case of a three-dimensional cavity.

As we can see from Eqs. (1.5) and (1.6) the resulting interaction is highly nonlinear. However, in this form, such nonlinearity is difficult to exploit. On the other hand, in the majority of cases, we can consider that the radiation pressure force acts as a very small perturbation on the mechanical motion around its equilibrium position $x = L$, such that the mirror position $x = q - L$ is much smaller than L. In this scenario (1.5) can be linearized. We can thus write $\Gamma \approx \Gamma_0 = \Gamma|_{q=L}$, $a_k(q) \approx a_k - (x/2L)a_k^\dagger$, $\omega_k(q) \approx \omega_k\,(1 - x/L)$, where now a_k and ω_k (without an explicit dependence on q) are the annihilation operator and the frequency associated with the equilibrium position of the mirror, respectively. For the sake of simplicity, we also consider the moving mirror bounded by a harmonic potential of frequency ω_0 around its equilibrium position, and introduce annihilation and creation operators $b^\dagger$ and b such that the mirror position and momentum are:

$$\begin{aligned} x =& \sqrt{\frac{\hbar}{2M\omega_0}}(b^\dagger + b), \\ p =& \sqrt{\frac{\hbar M\omega_0}{2}}i(b^\dagger - b). \end{aligned} \tag{1.7}$$

Using all these expressions and applying the unitary transformation $\mathcal{T}^\dagger\mathcal{H}\mathcal{T} \to \mathcal{H}$ with $\mathcal{T} = \exp\left(ix\Gamma_0/\hbar\right)$, we finally obtain

$$\mathcal{H} \approx \hbar\omega_0 b^\dagger b + \hbar\sum_k \omega_k a_k^\dagger a_k - x\mathcal{F} - E_{\text{Cas}}, \tag{1.8}$$

where

$$\mathcal{F} = \frac{\hbar}{2L}\sum_{kj}(-1)^{k+j}\sqrt{\omega_k\omega_j}\left(a_k a_j + a_k^\dagger a_j^\dagger + a_k^\dagger a_j + a_j^\dagger a_k\right) \tag{1.9}$$

indicates the normally ordered force due to the radiation pressure. The result of the unitary transformation $\mathcal{T}$ is to transform the canonical momentum into the kinetic one and to translate this change into an interaction between field and mirror and an interaction between different field modes due to the motion of the wall. Also, Eq. (1.9) results linearized in the form $x\mathcal{F}$, as the well-known dipole interaction between atom and field. In fact, this transformation closely recalls the Power-Zienau-Wolley transformation used in cavity QED (we will see this transformation in the subsequent Section, paragraph 1.3.2).

It is worth mentioning that the Hamiltonian (1.8) is only valid in the non-relativistic regime for the mirror dynamics and, therefore, does not describe physical phenomena that involve arbitrary high field frequencies. To be consistent with such approximation, we need to introduce a cutoff frequency ω_{cut} such that $\hbar\omega_{\mathrm{cut}}$ is much smaller than the rest energy of the wall Mc^2. Moreover, the use of a cutoff frequency is fully justified also for another reason: any real mirror is characterized by a plasma frequency and for field frequencies larger than the cutoff, the mirror becomes transparent to the radiation field. We then consider a cutoff frequency equal to the plasma frequency of the mirror.

In conclusion, Hamiltonian (1.8) describes the effective non-relativistic interaction between a field inside a one dimensional cavity and a perfect reflecting moving mechanical mirror. The linearization procedure has allowed us to accurately describe the coupling strength, thus eliminating the effects of this interaction on the geometry of the system: the volume of quantization is fixed at the equilibrium position of the wall. This fact has consequences on local properties of the field that can derive from the model. For example, the field must satisfy the particular boundary conditions at the location of the mirror, but since the mirror is free to move, these conditions should be distributed around the region swept by the mirror motion [32, 33]. This effect is not described by (1.8).

1.2.3 Single mode Hamiltonian

Let us now focus on the simplest model in cavity optomechanics, which, on the other hand, has been successfully used to describe most of current experiments [2]. We restrict our attention to one of the many optical modes within the cavity, which, from an experimental point of view, means to consider the one closest to resonance with a driving laser entering into the cavity. More specifically, we consider all physical situations where the cavity field is dominated by a single mode of frequency ω_{f} and the motion of the mirror is adiabatically slow, which implies that the frequency of the moving mirror has to be much smaller than the frequency spacing of neighboring cavity modes. Under these assumptions, we can ignore the scattering of photons between different field modes [4,34]. In fact, more generally this optomechanical setup has also been considered for discussions of the dynamical Casimir effect (DCE), where pairs of cavity photons are created by a non-adiabatic mechanical modulation of the boundaries [3]. However, by assuming an adiabatic motion for the mirror, the mechanical frequencies are too small for the DCE to play a role. As a result, the interaction term in Eq. (1.8) can be approximated as

$$x\mathcal{F} \approx x\frac{\hbar\omega_{\mathrm{f}}}{L}a^{\dagger}a, \tag{1.10}$$

such that the full single-mode Hamiltonian reads

$$H = \hbar\omega_{\mathrm{f}}a^{\dagger}a + \hbar\omega_0 b^{\dagger}b - g_0 a^{\dagger}a(b^{\dagger}+b), \tag{1.11}$$

where the coupling strength is defined as

$$g_0 = \frac{\omega_{\mathrm{f}}}{L}x_0 = \frac{\omega_{\mathrm{f}}}{L}\sqrt{\frac{\hbar}{2M\omega_0}}, \tag{1.12}$$

with x_0 the zero-point fluctuation amplitude of the mechanical vacuum state. We highlight that g_0 is a fundamental parameter in cavity-optomechanics, since it quantifies the interaction between a single phonon and a single photon [2].

It is possible to show that the time evolution operator $U = e^{-iHt/\hbar}$ associated with Hamiltonian (1.11) can be written as

$$U(t) = e^{-i\omega_{\mathrm{f}}a^{\dagger}at}e^{ik^2(a^{\dagger}a)^2(\omega_0 t-\sin(\omega_0 t))}e^{ka^{\dagger}a(\eta b^{\dagger}-\eta^* b)}e^{-ib^{\dagger}b\omega_0 t}, \tag{1.13}$$

where $k = g_0/\omega_0$ is the ratio between the single photon optomechanical coupling rate and the mechanical resonance frequency and $\eta = (1-e^{-i\omega_0 t})$. Equation (1.13) shows that the effect of the nonlinear interaction $\propto a^{\dagger}a(b^{\dagger}+b)$ is translated into a self Kerr nonlinearity [35] of the field $\propto (a^{\dagger}a)^2$ (in the second exponential). To look closer to the dynamics induced by (1.13), we consider the system initially prepared in the state $|\Psi(0)\rangle = |\alpha\rangle_{\mathrm{f}} \otimes |\gamma\rangle_{\mathrm{m}}$ where $|\alpha\rangle_{\mathrm{f}}$ and $|\gamma = \gamma_R + i\gamma_I\rangle_{\mathrm{m}}$ are coherent states for field and mirror [‡], respectively. In a frame rotating with the optical field, the resulting time evolution of the state is given by [30]

$$|\Psi(t)\rangle = e^{-\frac{|\alpha|^2}{2}}\sum_{n=0}^{\infty}\frac{\alpha^n}{\sqrt{n!}}e^{ik^2n^2(\omega_0 t-\sin\omega_0 t)}e^{ikn[\gamma_R\sin\omega_0 t+\gamma_I(1-\cos\omega_0 t)]}|n\rangle_{\mathrm{f}}\otimes|\Gamma_n(t)\rangle_{\mathrm{m}}, \tag{1.14}$$

where $|n\rangle_{\mathrm{f}}$ is a Fock state for the cavity field and $|\Gamma_n(t)\rangle_{\mathrm{m}} = |\gamma e^{-i\omega_0 t} + kn(1-e^{-i\omega_0 t})\rangle_{\mathrm{m}}$ a displaced coherent state of the mechanical oscillator. As we can see from Eq. (1.14), after $t = 0$,

---

[‡] We remind that a coherent state in the Fock basis $|n\rangle$ is written as $|\phi\rangle = e^{-\frac{|\phi|^2}{2}}\sum_{n=0}^{\infty}\frac{\phi^n}{\sqrt{n!}}|n\rangle$

field and mirror result correlated, i.e. in an entangled state. During the evolution the state accumulates a phase and the mechanical oscillator is found in a mixture of coherent states. However when the time is equal to integer multiples of the period of the mechanical motion, $t = \ell\tau_0$ with $\tau_0 = 2\pi/\omega_0$ and $\ell = 1, 2, \ldots$, field and oscillator completely decouple. Moreover, this light-matter decoupling does not depend on the initial mechanical state, as Eq. (1.13) demonstrates. In fact, at $t = \ell\tau_0$, the unitary operator reduces to $U = e^{-i2\pi\ell(\omega_\mathrm{f}/\omega_0)a^\dagger a} e^{i2\pi\ell k^2 (a^\dagger a)^2} e^{-i2\pi\ell b^\dagger b}$. This feature of the system is at the heart of many proposals and it will also be a key point for our investigations in Chapters 2 and 3.

Finally, to give a more concrete idea on the system, we provide the range of variation of the experimental parameters already achieved for the optomechanical cavity analyzed above. We have: $\omega_0/2\pi = [10^3, 10^9]$Hz, $M = [1, 10^{-22}]$Kg and $g_0/2\pi = [10^{-3}, 10^5]$Hz. Given these values the length of the cavity usually ranges in the interval $[10^{-2}, 10^{-5}]$m [2].

1.2.4 Temporal interaction regimes

We now briefly present the main temporal interaction regimes in optomechanics: the continuous, the long-pulsed and the pulsed [2,36]. Such regimes can be differentiated by comparing the interaction time τ_i with the time of the mechanical evolution τ_0. Specifically, when the interaction time is much larger than the mechanical evolution time $\tau_i \gg \tau_0$, we are in the continuous regime, where, in principle, the interaction between optical field and mirror can occur for many mechanical periods, and a steady state can be analyzed. In this case the evolution of the system is described by the unitary operator in Eq. (1.13). To realize such a scenario, we experimentally require the decay rate of the cavity $\kappa < \omega_0$, which means demanding a *good* cavity with negligible photon losses. Decreasing the interaction time we approach the long-pulsed regime $\tau_i > \tau_0$, where again the optomechanical interaction proceeds for many mechanical periods, so that the motion of the mirror is always able to modulate the field dynamics (optical sidebands are generated). Even in this case we demand the decay rate of the cavity to be lower than the mechanical frequency. In contrast, in the pulsed regime the interaction between mirror and optical field is much faster than a mechanical period $\tau_i \ll \tau_0$ and the position of the mirror is essentially fixed during the interaction time. In this regime, the optical field is not modulated by the mechanics (no optical sidebands are produced) and the evolution of the system is described by the unitary operator [36]:

$$U = e^{i\lambda a^\dagger a (b^\dagger + b)}, \text{ where } \lambda = \frac{g_0}{\kappa} \tag{1.15}$$

is the rescaled (dimensionless) coupling strength. (Note that $1/\kappa$ is the photon lifetime, i.e. the time spent by the photon inside the cavity before leaving it). Contrarily to the previous regimes, in this last case, we require the decay rate of the cavity to be much larger than the mechanical frequency $\kappa \gg \omega_0$, which means to consider a *bad* cavity, so that the light can enter and escape the cavity after the interaction time. In Chapter 2 and 3 of this thesis we will focus our attention on the continuous and the pulsed regime.

1.2.5 Detection schemes

To address many questions in cavity optomechanics, one needs to extrapolate information on the optical field after its interaction with the mechanical oscillator both in the cases of a continuous or a pulsed interaction. This will be very relevant in our investigations developed in Chapters 2 and 3. Here, we analyse the two most common detection schemes: homodyne and heterodyne.

Homodyne detection

In order to extract information about the phase of a field, one needs to rely on an interference scheme where the field can be mixed with a reference beam, which is usually called *local oscillator* (LO). When this reference has the same frequency of the field we want to measure, then the method is called *homodyne* detection [37]. Such mixing is realized by using a generalised beam-splitter BS with phase φ as shown in Fig. 1.2(a). (Note that a generalized beam-splitter is obtained by using a standard beam-splitter sandwiched between two retarding plates inducing opposite phase shifts $-\varphi$ and φ on the input mode.) The input field in mode a is described by the density operator ρ_{s}, while the LO is in the mode b and initially prepared in a coherent state $|\beta\rangle = |\beta_0 e^{i\phi}\rangle$. The intensities of the reflected LO beam and the transmitted signal are detected by counting the mean number of photons n_a in the perfect detector D_a. While, at the same time, the transmitted LO beam and the reflected signal are received by another detector D_b, which counts the mean number of photons n_b. We use the Heisenberg representation where field operators are transformed, while field states remain unchanged. Considering the following transformation for the output modes of a beam splitter

$$\begin{aligned} a' &= \cos(\theta/2)a + ie^{i\varphi}\sin(\theta/2)b, \\ b' &= ie^{-i\varphi}\sin(\theta/2)a + \cos(\theta/2)b, \end{aligned} \tag{1.16}$$

and setting $\theta = \pi/2$ (balanced homodyne detection) and $\varphi = \pi/2$, we obtain

$$\begin{aligned} n_b^a &= \frac{1}{2}\mathrm{Tr}[\rho_s \left|\beta\right\rangle \left\langle\beta\right| (a^\dagger \mp b^\dagger)(a \mp b)] \\ &= \frac{1}{2}[\left\langle\beta\right| b^\dagger b \left|\beta\right\rangle + \mathrm{Tr}(\rho_\mathrm{s} a^\dagger a)] \mp \frac{1}{2}\mathrm{Tr}[\rho_\mathrm{s} \left|\beta\right\rangle \left\langle\beta\right| (a^\dagger b + b^\dagger a)]. \end{aligned} \tag{1.17}$$

By subtracting the outputs measured in D_a and D_b, we then find

$$n_a - n_b = \beta_0 \mathrm{Tr}[\rho_\mathrm{s}(a^\dagger e^{i\phi} + a e^{-i\phi})] = \sqrt{2}\beta_0 \left\langle X_\phi \right\rangle_\mathrm{s}, \tag{1.18}$$

which provides a measure for the expectation value (in the field state described by ρ_s) of the signal field quadrature

$$X_\mathrm{f}^\phi = \frac{1}{\sqrt{2}}(a e^{-i\phi} + a^\dagger e^{i\phi}), \tag{1.19}$$

in phase with the LO. We however remark that the difference in phase between LO and input field is a consequence of our choice for φ. Indeed, $\varphi = 0$ gives a homodyne detection of the quadrature $\pi/2$-out-of-phase with LO. Importantly, by varying the phase of the LO, one can obtain a measure for the expectation value of any field quadrature.

This detection scheme has the ability to provide much more information on the input field. By considering an ensemble of identically prepared fields or a single realization where the measurement is performed many times, the distribution of the difference in the photocounts between the two output channels naturally reconstructs the probability distribution of the field quadrature around its average value. But this is true only when the LO amplitude is very large, such that our reference is essentially a classical field with a negligible amount of fluctuations [38].

Heterodyne detection

While homodyne detection is a projection over quadrature operators, heterodyne corresponds to a projection over coherent states. Here we show how we can achieve this measurement by making use of a (balance) double-homodyne scheme [39].

As depicted in Fig. 1.2(b) a quantum state ρ_s in mode a is mixed with the vacuum state of an ancillary system in mode b at a balanced beam splitter. Similarly, a' and b' indicate the bosonic operators for the modes in the transmitted and reflected arms. After the interaction of the two input modes at the beam splitter, we can jointly measure the quadrature operators

$$\begin{aligned} q_{a'} &= a' + a'^\dagger = \cos(\theta/2) q_a - \sin(\theta/2) q_b, \\ p_{b'} &= -i(b' - b'^\dagger) = \sin(\theta/2) p_a + \cos(\theta/2) p_b, \end{aligned} \tag{1.20}$$

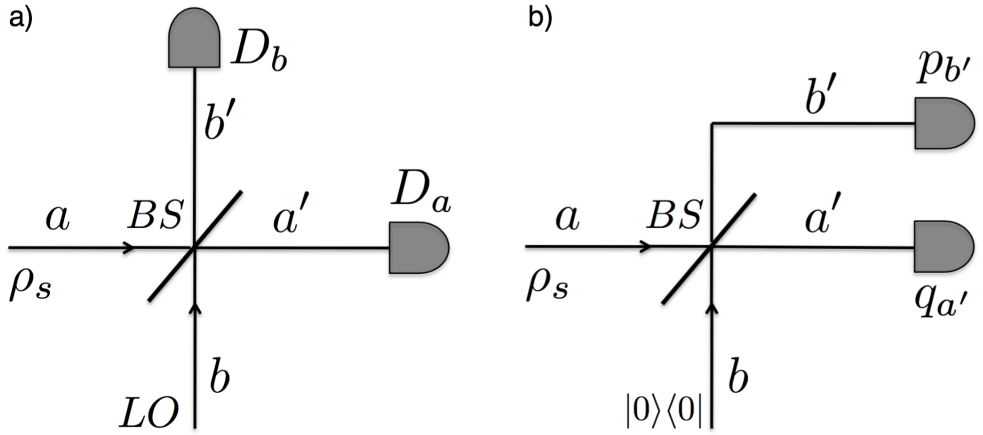

Figure 1.2: a) Scheme of the homodyne detection. An unknown field described by the density operator ρ_s (mode a) is mixed with a coherent state (the LO, given by mode b) at a beam splitter. The output modes a' and b' are measured in the two detectors D_a and D_b. b) Measurement scheme for a general-dyne detection: the quantum state ρ_s (mode a) is coupled to the vacuum (mode b) at a beam splitter. On the output modes a' and b', homodyne measurements of the quadratures $q_{a'}$ and $p_{b'}$ are performed.

since $[q_{b'}, p_{b'}] = 0$. Considering a balanced beam-splitter, i.e. $\theta = \pi/2$, the joint measurement of $q_{a'}$ and $p_{b'}$ results in the measurement of the non hermitian operator $Z = q_{a'} + ip_{b'} = a - b^\dagger$, which has eigenstates of this form

$$|z\rangle\rangle = D(z)\,|1\rangle\rangle, \tag{1.21}$$

with $D(z) = e^{za^\dagger - z^* a}$ a displacement operator and $|1\rangle\rangle = \sum_n |n\rangle\,|n\rangle$ an unnormalized maximally entangled state (superposition of correlated Fock states $|n\rangle$). It is possible to show that the probability of obtaining the result $z = z_1 + iz_2$ is

$$p(z) = \mathrm{Tr}_{ab}[\rho_s \otimes |0\rangle_b \langle 0|\,|z\rangle\rangle\langle\langle z|] = \mathrm{Tr}_a[\rho_s\,|z\rangle\,\langle z|], \tag{1.22}$$

where $|z\rangle = {}_b\langle 0|z\rangle\rangle$ is a coherent state such that $a\,|z\rangle = z\,|z\rangle$. Therefore, as previously anticipated, a balance double-homodyne detection corresponds to a projection over the coherent states $|z\rangle = D(z)\,|0\rangle$, which is exactly what we aim to obtain in a heterodyne detection scheme.

1.2.6 Estimation theory tools

We now review some basic tools of quantum estimation theory which will be useful in the following part of the thesis (Chapter 3). We are interested in providing the ultimate quantum bounds on the estimation precision of a parameter, and in comparing them with the ones that can be obtained in feasible measurement schemes such us homodyne and hetorodyne detections.

Estimation theory is a branch of statistics whose aim is to estimate the values of parameters based on measured empirical data with a random component. The solution of a general estimation problem is to find an estimator $\hat{\theta} = \hat{\theta}(x_1, x_2, ...)$ from a set $\mathcal{X}$ of measurement outcomes into the space of parameters, which attempts to approximate the unknown parameters using the measurements. The common approach in estimation theory is generally the probabilistic one, i.e. the measured data are assumed random with probability distribution dependent on the parameters of interest. In classical estimation theory we say that an estimator is optimal when it saturates the Cramer-Rao inequality [40]

$$\mathrm{V}(\theta) \geq \frac{1}{\mathcal{M} F_\theta}, \tag{1.23}$$

where $\mathrm{V}(\theta) = E_\theta[(\hat{\theta}(\{x\}) - \theta)^2]$ is the mean square error, $\mathcal{M}$ is the number of measurements and F_θ is the Fisher Information (FI), defined as

$$F_\theta = \int dx\; p(x|\theta) \left(\frac{\partial \ln p(x|\theta)}{\partial \theta} \right)^2 = \int dx \frac{1}{p(x|\theta)} \left(\frac{\partial p(x|\theta)}{\partial \theta} \right)^2, \tag{1.24}$$

with $p(x|\theta)$ the conditional probability of obtaining x given the value θ for the parameter. Equation (1.23) provides a lower bound on the mean square error $\mathrm{V}(\theta)$ for any estimator of the parameter θ. In all the common situations, we deal with unbiased estimators, i.e. estimators whose mean square error is equal to the variance $\mathrm{Var}(\theta) = E_\theta[\hat{\theta}^2] - E_\theta[\hat{\theta}]^2$.

When switching to quantum mechanics all the estimation problems can be tackled by considering a family of quantum states ρ_θ defined on a Hilbert space and labelled by a parameter θ, which, in general, does not correspond to a quantum observable. The mapping $\theta \rightarrow \rho_\theta$ gives the coordinate system. The scope is to estimate the value of θ by measuring some observable on ρ_θ. We then naturally define a quantum estimator as a selfadjoint operator O_θ for θ, which describes a quantum measurement followed by a classical data processing on the outcomes. This means that the parameter estimation is an indirect procedure involving an additional uncertainty for the measured value which, even in optimal conditions, cannot be avoided. Optimizing this procedure of inference by minimizing this additional uncertainty, represents the ultimate goal of quantum estimation theory.

More specifically, let us consider the elements of a positive measure (POVM) Π_x, such that $\int dx \Pi_x = \mathbb{I}$ and $p(x|\theta) = \mathrm{Tr}[\Pi_x \rho_\theta]$ with ρ_θ the density operator parametrized by the quantity we want to estimate. We also define the symmetric logarithmic derivative L_θ: a self-adjoint operator given by the equation $(L_\theta \rho_\theta + \rho_\theta L_\theta)/2 = \partial \rho_\theta / \partial \theta$, such that $\partial_\theta p(x|\theta) = \mathrm{Tr}[\partial_\theta \rho_\theta \Pi_x] = \Re(\mathrm{Tr}[\rho_\theta \Pi_x L_\theta])$. Using these expressions the FI becomes

$$F_\theta = \int dx \, \frac{\Re(\mathrm{Tr}[\rho_\theta \Pi_x L_\theta])^2}{\mathrm{Tr}[\rho_\theta \Pi_x]}. \tag{1.25}$$

For any given POVM (a quantum measurement), Eqs. (1.24) and (1.25) settle the classical bound on the precision reached by a proper data processing. However, the evaluation of the ultimate bounds follow only when we maximize the Fisher information over all the quantum measurements. One can show that the FI of any quantum measurement can be bounded by the Quantum Fisher Information (QFI)

$$F_\theta \leq Q_\theta = \mathrm{Tr}[\rho_\theta L_\theta^2], \tag{1.26}$$

which brings to the quantum version of the Cramér-Rao bound

$$\mathrm{V}(\theta) \geq \frac{1}{\mathcal{M} Q_\theta} \tag{1.27}$$

for the variance of any estimator. Equation (1.27) is independent of the geometry of the quantum statistical model and on the measurement, thus providing an ultimate bound for the estimation of the parameter. We then say that a POVM represents an optimal quantum measurement for the estimation of θ when its FI approaches the QFI. In other words, for measurements saturating Eq. (1.26).

In the specific case of a family of pure states $\rho_\theta = |\psi_\theta\rangle \langle\psi_\theta|$, we have $\partial_\theta \rho_\theta = (\partial_\theta \rho_\theta)\rho_\theta + \rho_\theta(\partial_\theta \rho_\theta)$ and $L_\theta = 2\partial_\theta \rho_\theta = |\psi_\theta\rangle \langle \partial_\theta \psi_\theta| + |\partial_\theta \psi_\theta\rangle \langle \psi_\theta|$, and the QFI assumes the following simple form

$$Q_\theta = 4 \left(\langle \partial_\theta \psi_\theta | \partial_\theta \psi_\theta \rangle - |\langle \partial_\theta \psi_\theta | \psi_\theta \rangle|^2 \right). \tag{1.28}$$

When assessing the performance of an estimator, which aims to measure a small parameter, and then the overall estimability of a parameter, another important figure of merit is the signal-to-noise ratio [40]. Indeed, while a large signal can be easily estimated, a quantity with a value very close to zero can be inferred only when the corresponding estimator results very precise. This means that we must demand the variance of the estimator to be small, since the relevant figure of merit is the scaling of the variance with the mean value rather than its absolute value. The signal-to-noise ratio will then compare the level of a desired signal to the level of background noise and (for a single measurement) can be defined as

$$R_\theta = \frac{\theta^2}{\mathrm{Var}(\theta)}. \tag{1.29}$$

The larger is this quantity, the better is the estimator. By using now the Cramér-Rao bound theorem in Eq. (1.27), we can find the following upper bound for the signal-to-noise ratio of any estimator

$$R_\theta \leq \bar{Q}_\theta \equiv \theta^2 \mathcal{M} Q_\theta, \tag{1.30}$$

which, on the other hand, defines the quantum signal-to-noise ratio. Quantum-mechanically, we then state that a parameter θ can be efficiently estimated if the correspondent $\bar{Q}_\theta$ is large.

1.3 Casimir Physics

1.3.1 Introduction

In classical physics, for *vacuum* we intend a region of space where we have removed all matter and radiation, thus completely empty. In quantum physics, on the other hand, the vacuum is quite far from being empty. It is full of quantum fluctuations: virtual particles which continuously appear and disappear violating the energy conservation law and that cannot be observed directly in an experiment [8]. However, once created it is natural to suppose they follow the same physical laws of real particles. One can then make predictions on the effects originated by their interaction with microscopic or mesoscopic objects. For example, virtual photons are nothing more than electromagnetic waves. We then expect that when they impinge on a perfectly conducting wall they must satisfy a boundary condition. As a result, if we put two infinite perfectly conducting walls in the vacuum, then we expect that the number of virtual particles outside the walls will be higher than inside, where, on the other hand, only photons with specific wavelengths can exist. Although the random creation of the particles both outside and inside is continuous, at any time, there is a net imbalance between the inside and outside photons, which originates an attractive force between the walls. The walls have then disturbed the quantum vacuum allowing for the observation of a quantum macroscopic effect: the Casimir force [41].

Let us now consider a different physical scenario: two atoms (or molecules) with the same amount of negative and positive charges in the quantum vacuum. Classical physics tells us that the force between the two atoms is zero. Quantum mechanics, however, gives a different answer. The Heisenberg principle says that the motion of the charges has to be random. Instantaneously, positive and negative charges in each atom are separated, and this, in turn, influences the charge distribution of the other atom. These continuous rearrangements of charge lead to a net imbalance between repulsive and attractive forces, which gives rise to an attractive force between the atoms not classically predicted. This is called van der Waals force [8, 42].

Have the aforementioned forces some connections? They actually seem very different in nature. One is originated from an imbalance of the vacuum fluctuations of the electromagnetic field because of the boundary conditions imposed on the walls, while, the other from an imbalance in the charge distribution of the atoms. In other words, the latter is a force originated by the same charges, while the former a force arising from how the walls disturb the vacuum, and not from a direct interaction between them. Looking closer into the two cases, some strong similarities can be found. First of all, charges create electromagnetic fields, which originate forces between the same charges. Secondly, the mirror is a real object, thus it is constituted by charges, which are actually responsible of the boundary conditions on the field. In fact, the charges oscillate following the fluctuating fields inside the cavity to then emit the same fluctuating fields. It is this mechanism that gives the vanishing value of the field on surfaces. We can now see that the Casimir force is not only originated by fluctuating fields but even by fluctuating charges. Viceversa, fluctuating charges in one atom create a fluctuating electromagnetic field, which then interacts with the other atom. The two atoms actually interact via the electromagnetic fields produced by the fluctuating charges.

Casimir and van der Waals forces are actually two sides of the same coin, and today we commonly refer to them as *dispersion forces*, i.e. effective electromagnetic forces acting between well-separated neutral, unpolarised and unmagnetised atoms, molecules or bodies in the complete absence of applied electromagnetic fields [†] [42]. Historically, the notion of dispersion forces has been referred to objects in the ground state. Today, we use this term also to describe situations with excited atoms (or molecules) and thermal electromagnetic fields.

We can distinguish between three kinds of dispersion forces: *van der Waals*, *Casimir-Polder*, and *Casimir*. The first is referred to interatomic forces, the second to atom-body interactions, and the third to forces between macroscopic bodies (such as two walls). Dispersion forces can be also differentiated in terms of the distance between the two objects. We have *non-retarded* forces when distances are much smaller than the atomic transition wavelength, and *retarded* in the opposite case.

[†] With well-separated we mean that the wave-functions of the electrons (of the two objects under scrutiny) do not overlap (for smaller distances Coulomb and Pauli exchange forces rule the dynamics)

Nowadays, it is recognized that dispersion forces play an important role in many different areas of physics, ranging from chemistry, atomic and surface physics, colloid science, biology and even cosmology. Competing with repulsive Coulomb and Pauli exchange interactions, van der Waals forces contribute to the creation of a stable equilibrium between two atoms or molecules, which was heuristically described by the Lennard-Jones potential [43]. Similarly, Casimir-Polder forces have an important role in the description of the adsorption of single atoms (or molecules) to surfaces: they compete with Coulomb and exchange interactions allowing the atom to find a stable equilibrium distance from the surface [44]. This role becomes even more important in macroscopic physics, especially at interfaces between different media, where atoms and molecules are very sensitive probes to these forces. From an accurate study of such interactions one can motivate many different properties of materials [44, 45]. In colloid science, a suspension of micro- or nano-particles in a medium is subjected to attractive van der Waals forces and repulsive Coulomb forces, which determine the stability of the colloidal suspension [46]. In biology, Casimir-Porder potentials allow us to understand the interaction of molecules within cells and also their transport through cell membranes [47]. More fundamentally, it has been suggested that the Casimir energy due to vacuum fluctuations might contribute to the cosmological constant [48].

Being dominant at nanoscale separations, dispersion forces have also a significant role in the interaction with nano-structured materials and in applications in micro- and nano- technologies, for example MEMS [7]. In fact, Casimir interactions give rise to unwanted 'sticking' between mechanical surfaces, and are usually exploited to design contact-less micro-mechanical devices. Most importantly, Casimir forces between a probe particle and a surface are the principle behind atomic force microscopy, which now represents the most used diagnostic instrument to probe unknown surfaces [49].

In this thesis, we will explore Casimir interactions in an optomechanical setup, which is very close to MEMS, and the Casimir-Polder force between an atom and a wall in a cavity.

1.3.2 Atom-Photon interaction in the Coulomb gauge

Consider a neutral atom, described by a non-relativistic matter field $\psi(\mathbf{r})$ modeling the electrons in a static nuclear potential, coupled to the electromagnetic field described by the transverse vector potential $\mathbf{A}$ in the Coulomb gauge. The matter field acts as a source for the electromagnetic field and viceversa. The atom of mass m is usually modelled as a positive charge

Ze concentrated in a point-like nucleus and surrounded by Z spinless electrons each of charge $q=-e$. The nucleus, which is considered fixed at the point $\mathbf{R}$ in space, is treated classically in view of its relatively large mass. The Hamiltonian built from this model takes this form [50,51]

$$\begin{aligned}\mathcal{H}=&-\frac{1}{2m}\int\psi^{\dagger}(\mathbf{r})\left[\hbar\nabla+i\frac{e}{c}\mathbf{A}(\mathbf{r})\right]^{2}\psi(\mathbf{r})d^{3}\mathbf{r}-Ze^{2}\int\psi^{\dagger}(\mathbf{r})\frac{1}{|\mathbf{R}-\mathbf{r}|}\psi(\mathbf{r})d^{3}\mathbf{r}\\&+\frac{1}{2}e^{2}\int\int\psi^{\dagger}(\mathbf{r})\psi^{\dagger}(\mathbf{r}')\frac{1}{|\mathbf{r}-\mathbf{r}'|}\psi(\mathbf{r}')\psi(\mathbf{r})d^{3}\mathbf{r}d^{3}\mathbf{r}'+\frac{1}{8\pi}\int\left\{\frac{1}{c^{2}}\dot{\mathbf{A}}^{2}(\mathbf{r})+[\nabla\times\mathbf{A}(\mathbf{r})]^{2}\right\}d^{3}\mathbf{r},\end{aligned}\tag{1.31}$$

which is commonly referred as the *minimal coupling representation.* The first term includes the kinetic energy of the atomic charges and their interaction with the electromagnetic field. The second and third terms are the electrostatic contributions to the energy: the electrostatic interaction between electrons and nucleus and the electrostatic repulsion among electrons. The last term represents the energy of the electromagnetic field. We now express the fields explicitly in terms of operators as

$$\begin{aligned}\psi(\mathbf{r})=&\sum_{n}c_{n}u_{n}(\mathbf{r}),\\\mathbf{A}(\mathbf{r},t)=&\sum_{\mathbf{k}j}\sqrt{\frac{2\pi\hbar c^{2}}{V\omega_{k}}}[\hat{e}_{\mathbf{k}j}a_{\mathbf{k}j}e^{i(\mathbf{k}\cdot\mathbf{r}-\omega_{k}t)}+\hat{e}^{*}_{\mathbf{k}j}a^{\dagger}_{\mathbf{k}j}e^{-i(\mathbf{k}\cdot\mathbf{r}-\omega_{k}t)}],\end{aligned}\tag{1.32}$$

where we assume that the electron field can be expanded in terms of the atomic eigenfunctions $u_n(\mathbf{r})$. $c_n^{\dagger}$ (c_n) is the one-electron creation (annihilation) operator of the matter field, $a^{\dagger}_{\mathbf{k}j}$ ($a_{\mathbf{k}j}$) the creation (annihilation) operator of one photon in the field mode $\mathbf{k}j$, V the volume of quantization and $\hat{e}_{\mathbf{k}j}$ an electromagnetic polarization unit vector. The quantum minimal coupling Hamiltonian in Eq. (1.31) can be thus rewritten as $\mathcal{H}=\mathcal{H}_{\mathrm{a}}^{\mathrm{min}}+\mathcal{H}_{\mathrm{f}}^{\mathrm{min}}+\mathcal{H}_{\mathrm{int}}^{\mathrm{min}}$, where

$$\begin{aligned}\mathcal{H}_{\mathrm{a}}^{\mathrm{min}}=&\sum_{n}E_{n}c_{n}^{\dagger}c_{n},\\\mathcal{H}_{\mathrm{f}}^{\mathrm{min}}=&\sum_{\mathbf{k}j}\hbar\omega_{k}\left(a^{\dagger}_{\mathbf{k}j}a_{\mathbf{k}j}+\frac{1}{2}\right),\\\mathcal{H}_{\mathrm{int}}^{\mathrm{min}}=&\frac{e}{m}\sqrt{\frac{2\pi\hbar}{V}}\sum_{nn'}\sum_{\mathbf{k}j}\frac{1}{\sqrt{\omega_{k}}}\left(\hat{e}_{\mathbf{k}j}\cdot\int e^{i\mathbf{k}\cdot\mathbf{x}}u_{n}^{*}(\mathbf{r})\frac{\hbar}{i}\nabla u_{n'}(\mathbf{r})\right)a_{\mathbf{k}j}c_{n}^{\dagger}c_{n'}\\&+\frac{e^{2}}{2m}\frac{2\pi\hbar}{V}\sum_{nn'}\sum_{\mathbf{k}\mathbf{k}'jj'}\frac{1}{\sqrt{\omega_{k}\omega_{k'}}}\left\{(\hat{e}_{\mathbf{k}j}\cdot\hat{e}_{\mathbf{k}'j'})\int d^{3}\mathbf{r}e^{i(\mathbf{k}+\mathbf{k}')\cdot\mathbf{r}}\right.\\&\times u_{n}^{*}(\mathbf{r})u_{n'}(\mathbf{r})a_{\mathbf{k}j}a_{\mathbf{k}'j'}c_{n}^{\dagger}c_{n'}+(\hat{e}_{\mathbf{k}j}\cdot\hat{e}^{*}_{\mathbf{k}'j'})\int d^{3}\mathbf{r}e^{i(\mathbf{k}-\mathbf{k}')\cdot\mathbf{r}}\\&\left.\times u_{n}^{*}(\mathbf{r})u_{n'}(\mathbf{r})a_{\mathbf{k}j}a^{\dagger}_{\mathbf{k}'j'}c_{n}^{\dagger}c_{n'}\right\}+H.c.\ .\end{aligned}\tag{1.33}$$

$\mathcal{H}_{\rm a}^{\rm min}$ is the atomic Hamiltonian where the E_n come from the eigenvalue problem $\mathcal{H}_{\rm a}^{\rm min}u_n(\mathbf{r}) = E_n u_n(\mathbf{r})$, $\mathcal{H}_{\rm f}^{\rm min}$ is the field Hamiltonian, while $\mathcal{H}_{\rm int}^{\rm min}$ the atom-field interaction. The interaction is formed by two terms. The first $\mathcal{H}_{\rm int}^{(1)}$, which originates from the double product in the first term of Eq. (1.31), is of the order e and describes processes by which one of the atomic electrons absorbs one photon $\mathbf{k}j$ and jumps from a state n' to n. This Hamiltonian term also takes into account the Hermitian conjugate process, where the electron jumps from n to n' emitting one photon $\mathbf{k}j$. The second term $\mathcal{H}_{\rm int}^{(2)}$ comes from the term $\mathbf{A}^2$ in Eq. (1.31) and is of the order e^2. It describes processes involving two photons $\mathbf{k}j$ and $\mathbf{k}'j'$: the atomic transition from state n' to n accompanied by absorption of two photons, and the opposite process: the atomic transition accompanied by the absorption of one photon and the emission of another.

If the wavelengths of the photons involved in the processes are much larger than the atomic dimension (Bohr radius), or in other terms, the vector potential does not change appreciably in a spherical region centered on the nucleus, we can perform the so called *dipole approximation*. This approximation is quite good for optical photons ($\lambda \sim 10^3$Å), which, on the other hand, are those expected to strongly interact with the atomic electrons. Equation (1.33) can then be simplified, since the integrals can be evaluated at the atomic position. Specifically, the transition amplitudes of the processes in $\mathcal{H}_{\rm int}^{(1)}$ become proportional to $\int u_n^*(\mathbf{r})\frac{\hbar}{i}\nabla u_{n'}(\mathbf{r})d^3\mathbf{r}$, which gives origin to the selection rules in spectroscopy, and the integrals in $\mathcal{H}_{\rm int}^{(2)}$ can be calculated as $\int u_n^*(\mathbf{r})u_{n'}(\mathbf{r})d^3\mathbf{r} = \delta_{nn'}$. We obtain:

$$
\begin{aligned}
\mathcal{H}_{\rm int}^{\rm min} =& i\sum_{nn'}\sum_{\mathbf{k}j}\sqrt{\frac{2\pi\hbar}{V\omega_k}}\left(\omega_{n'n}\boldsymbol{\mu}_{nn'}\cdot\hat{e}_{\mathbf{k}j}e^{i\mathbf{k}\cdot\mathbf{R}}c_n^\dagger c_{n'}a_{\mathbf{k}j} - H.c.\right)\\
&+\frac{\pi\hbar e^2}{mV}\sum_n c_n^\dagger c_n\sum_{\mathbf{k}\mathbf{k}'jj'}\frac{1}{\sqrt{\omega_k\omega_{k'}}}\Big\{(\hat{e}_{\mathbf{k}j}\cdot\hat{e}_{\mathbf{k}'j'})a_{\mathbf{k}j}a_{\mathbf{k}'j'}e^{i(\mathbf{k}+\mathbf{k}')\cdot\mathbf{R}}\\
&+(\hat{e}_{\mathbf{k}j}\cdot\hat{e}^*_{\mathbf{k}'j'})a_{\mathbf{k}j}a^\dagger_{\mathbf{k}'j'}e^{i(\mathbf{k}-\mathbf{k}')\cdot\mathbf{R}}+(\hat{e}^*_{\mathbf{k}j}\cdot\hat{e}_{\mathbf{k}'j'})a^\dagger_{\mathbf{k}j}a_{\mathbf{k}'j'}e^{-i(\mathbf{k}-\mathbf{k}')\cdot\mathbf{R}}\\
&+(\hat{e}^*_{\mathbf{k}j}\cdot\hat{e}^*_{\mathbf{k}'j'})a^\dagger_{\mathbf{k}j}a^\dagger_{\mathbf{k}'j'}e^{-i(\mathbf{k}+\mathbf{k}')\cdot\mathbf{R}}\Big\},
\end{aligned}
\tag{1.34}
$$

where $\boldsymbol{\mu}_{nn'} = \int u_n^*(\mathbf{r})\boldsymbol{\mu}(\mathbf{r})u_{n'}(\mathbf{r})d^3\mathbf{r}$ with $\boldsymbol{\mu}(\mathbf{r}) = -e(\mathbf{r}-\mathbf{R})$ is the matrix element of the electric dipole moment connecting single particle states u_n and u_n'; while, $\omega_{nn'} = (E_{n'} - E_n)/\hbar$ the corresponding transition frequency with $E_{n'(n)}$ the eigenvalue of $\mathcal{H}_{\rm a}^{\rm min}$ for the single particle state $u_{n'(n)}$. Eq. (1.34) shows that the operator for the total number of electrons commutes with the total Hamiltonian: it is a constant of motion. The term $\sum_n c_n^\dagger c_n$, which also includes a summation over the continuum of the ionized states, is thus equivalent to a constant which is Z for a neutral atom. As a result, the term proportional to $\mathbf{A}^2$ in Eq. (1.34) does not contain the electron coordinates and, for many purposes, can be included in $\mathcal{H}_\mathrm{f}^\mathrm{min}$. This gives a quadratic form in the creation and annihilation operators of the electromagnetic field, which can be diagonalized exactly yielding to a new set of operators $a'_{\mathbf{k}j}$ and $a'^{\dagger}_{\mathbf{k}j}$, and a new diagonal field Hamiltonian $\mathcal{H}_\mathrm{f}'^{\mathrm{min}} = \sum_{\mathbf{k}j} \hbar\omega'_k \left(a'^{\dagger}_{\mathbf{k}j} a'_{\mathbf{k}j} + 1/2 \right)$. By following this procedure, the interaction Hamiltonian in the minimal coupling scheme and within the dipole approximation just reads

$$\mathcal{H}_\mathrm{int}^\mathrm{min} = i \sum_{nn'} \sum_{\mathbf{k}j} \sqrt{\frac{2\pi\hbar}{V\omega'_k}} \left(\omega_{n'n} \boldsymbol{\mu}_{nn'} \cdot \hat{e}_{\mathbf{k}'j} e^{i\mathbf{k}\cdot\mathbf{R}} c_n^\dagger c_{n'} a'_{\mathbf{k}j} - H.c \right). \tag{1.35}$$

Another equivalent description of the atom-photon interaction, which is commonly referred as the *multipolar coupling* representation, can be derived by performing the so called Power-Zienau-Wolley unitary transformation $\mathcal{T}^\dagger \mathcal{H} \mathcal{T}$ on the minimal coupling Hamiltonian (1.31), with [52, 53]

$$\mathcal{T} = e^{i\int \psi^\dagger(\mathbf{r})\left(\frac{1}{\hbar c}\int \mathbf{p}(\mathbf{x},\mathbf{r})\cdot\mathbf{A}(\mathbf{x})d^3\mathbf{x}\right)\psi(\mathbf{r})d^3\mathbf{r}}, \tag{1.36}$$

and $\mathbf{p}(\mathbf{x}, \mathbf{r})$ the polarization field. The resulting interaction Hamiltonian has the useful feature that the coupling between charges and radiation is expressed in terms of the electric and magnetic fields rather than in terms of the vector potential. We highlight that, because of such transformation, one is led to define new set of fermion and field creation and annihilation operators $(c_n'^{\dagger},\ c'_{n'})$ and $(\tilde{a}^\dagger_{\mathbf{k}j},\ \tilde{a}_{\mathbf{k}j})$. While $(\tilde{a}^\dagger_{\mathbf{k}j},\ \tilde{a}_{\mathbf{k}j})$ coincide with the previous after being transformed by $\mathcal{T}$, $(c_n'^{\dagger},\ c'_{n'})$ are introduced accordingly to the definition of a new set of single-electron states $u'_n(\mathbf{r})$, which take into account all the effects coming from non-hydrogenic terms in the atom Hamiltonian.

In the electric-dipole approximation, the resulting interaction term in the multipolar scheme takes the very simple and elegant form

$$\mathcal{H}_\mathrm{int}^\mathrm{mul} = -\boldsymbol{\mu} \cdot \mathbf{D}(\mathbf{R}), \tag{1.37}$$

where

$$\mathbf{D}(\mathbf{r}, t) = \frac{1}{c}\dot{\mathbf{A}}(\mathbf{r}) + 4\pi\mathbf{p}(\mathbf{r}) = i \sum_{\mathbf{k}j} \sqrt{\frac{2\pi\hbar\omega_k}{V}} [\hat{e}_{\mathbf{k}j} \tilde{a}_{\mathbf{k}j} e^{i\mathbf{k}\cdot\mathbf{r}} - \hat{e}^*_{\mathbf{k}j} \tilde{a}^\dagger_{\mathbf{k}j} e^{-i\mathbf{k}\cdot\mathbf{r}}], \tag{1.38}$$

is the electromagnetic displacement field, while $\boldsymbol{\mu} = \int \tilde{\psi}^\dagger(\mathbf{r}) \boldsymbol{\mu}(\mathbf{r}) \tilde{\psi}(\mathbf{r}) d^3\mathbf{r}$ the overall electric dipole moment. Using Eq. (1.32) and substituting (1.38) in (1.37) we finally have

$$\mathcal{H}_\mathrm{int}^\mathrm{mul} = -i \sum_{nn'} \sum_{\mathbf{k}j} \sqrt{\frac{2\pi\hbar\omega_k}{V}} \left(\boldsymbol{\mu}'_{nn'} \cdot \hat{e}_{\mathbf{k}j} e^{i\mathbf{k}\cdot\mathbf{R}} c_n'^{\dagger} c'_{n'} \tilde{a}_{\mathbf{k}j} - H.c \right). \tag{1.39}$$

As already remarked the two formulations of the atom-photon interaction give the same physical predictions. The only difference is how the energy is partitioned: $\mathcal{H}_a^{\rm min} \neq \mathcal{H}_{\rm a}^{\rm mul}$, $\mathcal{H}_{\rm f}^{\rm min} \neq \mathcal{H}_{\rm f}^{\rm mul}$ and $\mathcal{H}_{\rm int}^{\rm min} \neq \mathcal{H}_{\rm int}^{\rm mul}$. However, in the multipolar scheme, the form of the interaction in Eq. (1.37) is much simpler than in the minimal coupling representation (1.31), and also physically clearer. In fact, it is directly connected to measurable quantities such us the electric dipole moment and the displacement field. Moreover, in the case of more atoms, the multipolar scheme naturally includes the static interaction between the atomic dipoles. We finally remark that in the following section and in Chapter 4 we will refer to the atomic and field Hamiltonians as $\mathcal{H}_{\rm a}$ and $\mathcal{H}_{\rm f}$, without making any explicit difference between the multipolar or minimal scheme; in fact, there is not ambiguity as long as we do not change from the minimal to the multipolar scheme or viceversa during the calculations.

Two level approximation

In many physical situations only two atomic levels are relevant to the atom-photon dynamics. This allows us to consider a two-level atom with two non-degenerate energy eigenvalues E_1 and E_2 (with $E_2 > E_1$) corresponding to the bare atomic eigenstates $|1\rangle$ and $|2\rangle$ of the Hamiltonian $\mathcal{H}_{\rm a}$. In a two-dimensional subspace, by using the fermion anti-commutation rules, it is possible to verify that the electron field operators satisfy the following relations: $[c_1^\dagger c_2, c_2^\dagger c_1] = c_1^\dagger c_1 - c_2^\dagger c_2$, $[c_1^\dagger c_2, c_1^\dagger c_1 - c_2^\dagger c_2] = -2c_1^\dagger c_2$, $[c_2^\dagger c_1, c_1^\dagger c_1 - c_2^\dagger c_2] = 2c_2^\dagger c_1$, $(c_1^\dagger c_2)^2 = (c_2^\dagger c_1)^2 = 0$, which coincide with the spin 1/2 angular momentum commutation relations for the following *pseudospin* operators:

$$S_+ = c_2^\dagger c_1, \quad S_- = c_1^\dagger c_2, \quad S_z = \frac{1}{2}(c_2^\dagger c_2 - c_1^\dagger c_1), \quad \text{with} \quad c_1^\dagger c_1 + c_2^\dagger c_2 = 1. \tag{1.40}$$

In fact, one can easily verify that the commutation rules for the electron field operators are equivalent to

$$[S_+, S_-] = 2S_z, \quad [S_+, S_z] = -S_+, \quad [S_-, S_z] = S_-, \quad S_+^2 = S_-^2 = 0. \tag{1.41}$$

It then follows that $c_1^\dagger c_1 = 1/2 - S_z$, $c_2^\dagger c_2 = 1/2 + S_z$, and

$$\mathcal{H}_{\rm a} = E_1 c_1^\dagger c_1 + E_2 c_2^\dagger c_2 = \frac{1}{2}(E_1 + E_2) + (E_2 - E_1) S_z \equiv \hbar\omega_{\rm a} S_z, \tag{1.42}$$

where $\omega_{\rm a} = \omega_{21}$ and a constant (and unobservable) energy shift of the atomic energy levels has been neglected in the final step. By assuming real polarization vectors, within the dipole and the two levels approximation, the two equivalent formulations of the atom-photon interaction finally read

$$\begin{aligned}\mathcal{H}^{\text{min}} &= \mathcal{H}_{\text{a}} + \mathcal{H}_{\text{f}} + \mathcal{H}_{\text{int}}^{\text{min}} \\ \mathcal{H}^{\text{mul}} &= \mathcal{H}_{\text{a}} + \mathcal{H}_{\text{f}} + \mathcal{H}_{\text{int}}^{\text{mul}},\end{aligned} \tag{1.43}$$

where

$$\begin{aligned}\mathcal{H}_{\text{a}} &= \hbar\omega_{\text{a}} S_z, \\ \mathcal{H}_{\text{f}} &= \sum_{\mathbf{k}j} \hbar\omega_k \left(a_{\mathbf{k}j}^{\dagger} a_{\mathbf{k}j} + \frac{1}{2} \right), \\ \mathcal{H}_{\text{int}}^{\text{min}} &= -i \sum_{\mathbf{k}j} \sqrt{\frac{2\pi\hbar\omega_{\text{a}}^2}{V\omega_k}} \boldsymbol{\mu}_{21} \cdot \hat{e}_{\mathbf{k}j} (S_+ - S_-)(e^{i\mathbf{k}\cdot\mathbf{R}} a_{\mathbf{k}j} + e^{-i\mathbf{k}\cdot\mathbf{R}} a_{\mathbf{k}j}^{\dagger}), \\ \mathcal{H}_{\text{int}}^{\text{mul}} &= -i \sum_{\mathbf{k}j} \sqrt{\frac{2\pi\hbar\omega_k}{V}} \boldsymbol{\mu}_{21} \cdot \hat{e}_{\mathbf{k}j} (S_+ + S_-)(e^{i\mathbf{k}\cdot\mathbf{R}} a_{\mathbf{k}j} - e^{-i\mathbf{k}\cdot\mathbf{R}} a_{\mathbf{k}j}^{\dagger}).\end{aligned} \tag{1.44}$$

We remark that the similarity between the two schemes is formal, since atom and photon refer two different objects in the two prescriptions: this is indicated by the dependence of the coupling constants on ω_k and ω_{a} [51]. It is also important to observe that the interaction in (1.44) contain four products of atomic and photon operators. The terms proportional to $S_- a^{\dagger}$ and $S_+ a$ are called *rotating* and induce transitions between atom and field conserving the energy in the single process (one excitation is created in the field and the other is annihilated in the atom, and viceversa). While, the others proportional to $S_- a$ and $S_+ a^{\dagger}$ are known as *counter-rotating* and do not conserve the energy at the level of a single process: these are responsible for the creation or annihilation of two excitations in atom or field, and for the dressing or self-dressing of the atom, which will be investigated in the fourth Chapter of this thesis. Finally, we recall that the two forms in Eqs. (1.44) are often called Dicke Hamiltonians [51, 54].

1.3.3 Casimir force

Let us now consider an *empty* rectangular cavity of dimensions $L_x = L_y = L$ and L_z, where the electromagnetic field inside the cavity is in its vacuum (ground) state. The walls of the cavity are discharged, perfectly conducting and two by two parallel. We know that the tangential component of the electromagnetic field must vanish on the surface of the walls. This means that inside the cavity only specific field modes (wavelengths) can survive. In terms of the potential vector, the mode functions satisfying these boundary conditions are [8]

$$\begin{aligned} A_x(\mathbf{r}) &= \left(\frac{8}{V}\right)^{1/2} a_x \cos(k_x x)\sin(k_y y)\sin(k_z z), \\ A_y(\mathbf{r}) &= \left(\frac{8}{V}\right)^{1/2} a_y \sin(k_x x)\cos(k_y y)\sin(k_z z), \\ A_z(\mathbf{r}) &= \left(\frac{8}{V}\right)^{1/2} a_z \sin(k_x x)\sin(k_y y)\cos(k_z z), \end{aligned} \tag{1.45}$$

where $k_x = l\pi/L$, $k_y = m\pi/L$, $k_x = n\pi/L_z$, with $l, m, n = 0, 1, 2...$, and a_x, a_y, a_z are the normalization coefficients such that $\int_0^L dx \int_0^L dy \int_0^{L_z} dz \left[A_x^2(\mathbf{r}) + A_y^2(\mathbf{r}) + A_z^2(\mathbf{r})\right] = 1$ $(a_x^2 + a_y^2 + a_z^2 = 1)$. Also, in order to satisfy $\nabla \cdot \mathbf{A} = 0$, we have $k_x A_x + k_y A_y + k_z A_z = (\pi/L)(lA_x + mA_y) + (\pi/L_z)(nA_z) = 0$. This condition implies that there are only two independent polarizations if l, m and n are not zero and only one if one of these integers is zero.

The quantity of interest is the zero point energy of the electromagnetic field inside the cavity, which is given by

$$\sum_{l,m,n}{}^{'} (2)\frac{1}{2}\hbar\omega_{lmn} = \sum_{l,m,n}{}^{'} \pi\hbar c \left[\frac{l^2}{L^2} + \frac{m^2}{L^2} + \frac{n^2}{L_z^2}\right]^{1/2}, \tag{1.46}$$

where the subscript above the sum indicates that when one of the integers l, m, n is zero, the expression should not be multiplied by (2). We can now take the continuous limit in the x, y directions ($L \gg L_z = d$), which means to consider only two walls in the vacuum. Equation (1.46) can be rewritten as

$$E_{\text{vac}}(d) = \frac{\hbar c L^2}{\pi^2} \sum_n{}^{'} \int_0^\infty dk_x \int_0^\infty dk_y \left(k_x^2 + k_y^2 + \frac{n^2\pi^2}{d^2}\right)^{1/2}. \tag{1.47}$$

As we can see, the vacuum energy of the electromagnetic field (1.47) results to be infinite for every volume V of the cavity. If we take the continuous limit also in the z direction, we get

$$E_{\text{vac}}(\infty) = \frac{\hbar c d L^2}{\pi^3} \int_0^\infty dk_x \int_0^\infty dk_y \int_0^\infty dk_z \left(k_x^2 + k_y^2 + k_z^2\right)^{1/2}, \tag{1.48}$$

which coincides with the vacuum energy of a free electromagnetic field. We can now find the potential energy of the system, that is the energy we spend to build it. This coincides with the amount of energy required to bring the two walls of the cavity from an infinite to a finite distance d:

$$\begin{aligned} U(d) &= E_{\text{vac}}(d) - E_{\text{vac}}(\infty) \\ &= \frac{\hbar c L^2}{2\pi} \left[\sum_n{}^{'} \int_0^\infty du\, u \left(u^2 + \frac{n^2\pi^2}{d^2}\right)^{1/2} \right. \\ &\qquad \left. - \frac{d}{\pi} \int_0^{\pi/2} d\vartheta \int_0^\infty dk_z \int_0^\infty du\, u \left(u^2 + k_z^2\right)^{1/2} \right], \end{aligned} \tag{1.49}$$

where we have used polar coordinates (u, ϑ) with $u^2 = k_x^2 + k_y^2$ and $\tan(\vartheta) = k_y/k_x$. Equation (1.49) is a difference between two infinite quantities, but as we are going to see it gives a finite value. To calculate it, we first introduce a cutoff function $f(k) = f([u^2 + k_z^2]^{1/2})$ such that $f(k) = 1$ for $k \ll k_{\text{cut}}$ and $f(k) = 0$ for $k \gg k_{\text{cut}}$. On the other hand, the introduction of a cutoff wavelength is physically sound, since our assumption of perfectly reflecting walls does not hold for field modes with wavelength smaller than the atomic dimension. In fact, as we have briefly discussed in the previous paragraph, the boundary condition on the field is the result of an annihilation between the field inside the cavity and the one emitting by the oscillations of the atoms in response to the the same intracavity field. Supposing then $k_{\text{cut}} \approx a_0$, with a_0 the Bohr radius, when $k \gg k_{\text{cut}}$ the atoms of the walls do not respond to the cavity field; in other words, the field does not see boundaries and we actually recover the case of a free field in the quantum vacuum. This also says that the Casimir force we are about to derive is a non-relativistic effect, essentially due to the field modes of low frequency. Equation (1.49) becomes

$$\begin{aligned}
U(d) = \frac{\pi^2 \hbar c}{4d^3} L^2 \Bigg[\sum_n{}' \int_0^\infty dx \, \left(x + n^2\right)^{1/2} f\left(\frac{\pi}{d}[x + n^2]^{1/2}\right) \\
- \int_0^\infty d\xi \int_0^\infty dx \, \left(x + \xi^2\right)^{1/2} f\left(\frac{\pi}{d}[x + \xi^2]^{1/2}\right) \Bigg] \qquad (1.50) \\
= \frac{\pi^2 \hbar c}{4d^3} L^2 \left[\frac{1}{2} F(0) + \sum\nolimits_{n=1}^{\infty} F(n) - \int_0^\infty d\xi \, F(\xi) \right],
\end{aligned}$$

where we have also performed a change of variables, $x = u^2 d^2/\pi^2$ and $\xi = k_z d/\pi$, and defined $F(\xi) \equiv \int_0^\infty dx \, (x + \xi^2)^{1/2} f\left(\frac{\pi}{d}[x + \xi^2]^{1/2}\right)$. By using the Euler-Maclaurin summation formula* we calculate $\sum_{n=1}^\infty F(n) - \int_0^\infty d\xi \, F(\xi) = -(1/2)F(0) - (4/720)$, and finally obtain the potential energy at a distance d:

$$U(d) = -\left(\frac{\pi^2 \hbar c}{720 d^3}\right) L^2, \qquad (1.51)$$

from which we can derive the expression of the force between the two walls

$$F(d) = -\frac{\partial U(d)}{\partial d} = -\frac{\pi^2 \hbar c}{240 d^4} A. \qquad (1.52)$$

Equation (1.52) is the Casimir force, which is an attractive force proportional to the area $A = L^2$ of the walls and inversely proportional to the fourth power of the distance. While the zero point

---

[*] $\sum_{n=1}^\infty F(n) - \int_0^\infty d\xi \, F(\xi) = -\frac{1}{2}F(0) - \frac{1}{12}F'(0) + \frac{1}{720}F'''(0) + \ldots$, valid when $F(\infty) \to 0$. The derivates are calculated at $\xi = 0$. By using the fact that $F(\xi) = \int_{\xi^2}^\infty dv \sqrt{v} f(\frac{\pi}{d}\sqrt{v}) = \int_0^\infty dv \sqrt{v} f(\frac{\pi}{d}\sqrt{v}) - \int_0^{\xi^2} dv \sqrt{v} f(\frac{\pi}{d}\sqrt{v})$, we obtain $F'(\xi) = \frac{d}{d\xi}\left(\int_0^\infty dv \, \sqrt{v} f(\frac{\pi}{d}\sqrt{v}) - \int_0^{\xi^2} dv \, \sqrt{v} f(\frac{\pi}{d}\sqrt{v})\right) = -\frac{d}{d\xi}\int_0^{\xi^2} dv \, \sqrt{v} f(\frac{\pi}{d}\sqrt{v}) = -2\xi^2 f(\frac{\pi}{d}\xi)$, and as a result, we have $F'(0) = 0, F'''(0) = -4$ and $F^n(0) = 0$, having assumed that all the derivates of the cutoff function vanish at $\xi = 0$.

energy inside and outside the cavity are both infinite, their variation, which is a consequence of having imposed boundary conditions on the quantum vacuum, gives a finite value. This is an example of a more general procedure in quantum field theory: the *renormalization*. In fact, we have actually renormalized the vacuum energy with respect to the vacuum energy of a free field, and the same thing can be done on the field itself or on the field Green function [34]. Also, the Casimir force between the two walls can equivalently be found as a difference between the outside and inside radiation pressure of the vacuum fluctuations on the walls [55]. For typical values of the systems: $A = 1\text{cm}^2$, $d = 1\mu\text{m}$ the force results around 10^{-7}N. Although the weak value, it has been measured with high precision [15, 56, 57].

We finally highlight that the Casimir force between two walls in (1.52), but more in general between objects, can be equivalently derived as a result of all the interactions between the many fluctuating dipoles within the bodies mediated by the electromagnetic field [15, 42]. Here, for simplicity, we have preferred to present a much simpler derivation closer in spirit to standard procedures used in quantum field theory [34, 58].

1.3.4 Casimir-Polder force between an atom and a wall

We now want to study the Casimir-Polder force between a two-level atom and a neutral perfectly conducting infinite wall in the presence of a quantum electromagnetic field in its vacuum state. This force is well-known in the literature, both for ground- and excited-state atoms [8, 59–61]. Here we follow the point of view of Refs. [62, 63], which will represent our starting point for the evaluation of dynamical (time-dependent) atom-wall interaction in the second half of Chapter 4.

We have seen that in the multipolar coupling scheme and within the dipole approximation, the atom-field interaction is described by the Hamiltonian in Eq. (1.44) (last line). However, in this case, the field must satisfy the boundary condition at the position of the wall. The interaction Hamiltonian is thus written as (where we have omitted the subscript indicating the multipolar scheme, since we will always adopt such representation) [51]

$$\mathcal{H}_{\text{int}} = -i\sum_{\mathbf{k}j}\sqrt{\frac{2\pi\hbar ck}{V}}[\boldsymbol{\mu}\cdot\mathbf{f}_{\mathbf{k}j}(\mathbf{r})],(S_+ + S_-)(a_{\mathbf{k}j} - a^\dagger_{\mathbf{k}j}). \tag{1.53}$$

where $\mathbf{f}_{\mathbf{k}j}(\mathbf{r})$ are the field mode functions evaluated at the atomic position which take into account the boundary conditions of the field. As usual in cavity QED, the quantization of the field is performed within a finite volume of space. We imagine the atom placed inside a cubic

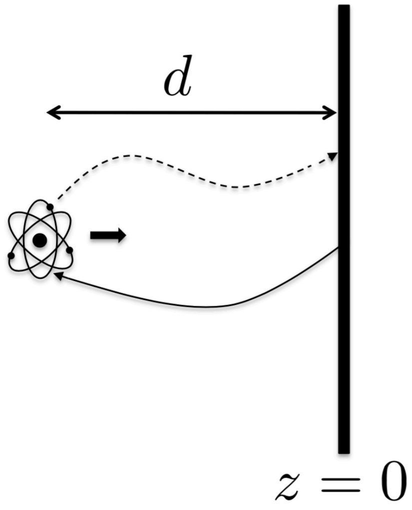

Figure 1.3: Pictorial representation of the system. An atom is placed inside a cubic cavity of side L at a distance d from a perfectly conducting wall at $z = 0$. The other walls are not represented since $d \ll L$.

cavity of side L near the wall at $z = 0$, with the other walls located at $x = \pm L/2$, $y = \pm L/2$ and $z = L$ (see Fig. 1.3). At the end of the calculation, the case of a single wall at $z = 0$ can be recovered by taking the limit $L \to \infty$. The mode functions $\mathbf{f}_{\mathbf{k}j}$, which satisfy the boundary conditions of the field on such geometry with the wall in the xy plane, take the form

$$\begin{aligned}
(\mathbf{f}_{\mathbf{k}j})_x &= \sqrt{8}(\hat{e}_{\mathbf{k}j})_x \cos\left[k_x\left(x+\frac{L}{2}\right)\right] \sin\left[k_y\left(y+\frac{L}{2}\right)\right] \sin[k_z z], \\
(\mathbf{f}_{\mathbf{k}j})_y &= \sqrt{8}(\hat{e}_{\mathbf{k}j})_y \sin\left[k_x\left(x+\frac{L}{2}\right)\right] \cos\left[k_y\left(y+\frac{L}{2}\right)\right] \sin[k_z z], \\
(\mathbf{f}_{\mathbf{k}j})_z &= \sqrt{8}(\hat{e}_{\mathbf{k}j})_z \sin\left[k_x\left(x+\frac{L}{2}\right)\right] \sin\left[k_y\left(y+\frac{L}{2}\right)\right] \cos[k_z z], \qquad (1.54)
\end{aligned}$$

where $k_x = l\pi/L$, $k_y = m\pi/L$, $k_z = n\pi/L$ (with l, m, n positive integers) are the wave-vectors, and $\hat{e}_{\mathbf{k}j}$ the polarization unit vectors.

The atom-wall potential can be calculated from the second-order energy shift of the bare ground state $|0_{\mathbf{k}j}, \downarrow(\uparrow)\rangle_B$, where $|0_{\mathbf{k}j}\rangle$ is the vacuum state of the field, while $|\downarrow(\uparrow)\rangle$ is the ground (excited) state of the atom. By using time-independent perturbation theory at the first order in the coupling constant we obtain the true ground state of the system:

$$|0_{\mathbf{k}j}, \downarrow(\uparrow)\rangle_D = |0_{\mathbf{k}j}, \downarrow(\uparrow)\rangle_B - \sum_{|\psi\rangle \neq |0_{\mathbf{k}j}, \downarrow(\uparrow)\rangle} \frac{\langle\psi| \mathcal{H}_{\text{int}} |0_{\mathbf{k}j}, \downarrow(\uparrow)\rangle_B}{E_\psi - E_B} |\psi\rangle, \qquad (1.55)$$

where E_B is the energy of the bare state. Such state is an example of a *dressed* state, i.e. a state covered by virtual particles due to the interaction Hamiltonian. We will discuss this general aspect more in detail in Chapter 4 (section 4.2). The corresponding second order energy shift (Casimir-Polder potential) thus results

$$\begin{aligned}\mathcal{E}^{(2)}_{\downarrow(\uparrow)} =& \frac{1}{2}{}_D\left\langle \{0_{\mathbf{k}j}\}, \downarrow(\uparrow)\right| \mathcal{H}_{\text{int}} \left|\{0_{\mathbf{k}j}\}, \downarrow(\uparrow)\right\rangle_D \\ =& -\frac{4\pi}{V}\sum_{\mathbf{k}j}\frac{k}{k \pm k_{\text{a}}}(\boldsymbol{\mu}_{21}\cdot\mathbf{f}(\mathbf{k}j,\mathbf{r}))^2,\end{aligned} \tag{1.56}$$

where $k_{\text{a}} = \omega_{\text{a}}/c$ and the plus (minus) sign is for a ground (excited) state atom. We underline that this result (obtained within the multipolar scheme) can be easily generalized to include a multilevel atom. We also remark that the first line of Eq. (1.56) is a general result in perturbation theory [51].

In the quasi-static approach, the Casimir-Polder force can be obtained by taking the derivative of the interaction energy (1.56) with respect to the atom-wall distance d and changing its sign as ¶

$$F_{\downarrow(\uparrow)}(d) = -\frac{\partial\mathcal{E}^{(2)}_{\downarrow(\uparrow)}}{\partial d}. \tag{1.57}$$

For isotropic atoms ($\mu_x^2 = \mu_y^2 = \mu_z^2 = \mu^2/3$) and after summation over the orientations of the atomic dipole in (1.56), the expressions for the Casimir-Polder force for a ground- and an excited-state atom are

$$\begin{aligned}F_{\downarrow}(d) =& -\frac{\mu^2}{12\pi d^4}[8k_{\text{a}}d - 6(2k_{\text{a}}^2d^2-1)g(2k_{\text{a}}d) - 4k_{\text{a}}d(2k_{\text{a}}^2d^2-3)h(2k_{\text{a}}d)], \\ F_{\uparrow}(d) =& \frac{\mu^2}{12\pi d^4}[8k_{\text{a}}d - 6(2k_{\text{a}}^2d^2-1)(g(2k_{\text{a}}d) - \pi\cos(2k_{\text{a}}d)) + \\ & - 4k_{\text{a}}d(2k_{\text{a}}^2d^2-3)(h(2k_{\text{a}}d) - \pi\sin(2k_{\text{a}}d))],\end{aligned} \tag{1.58}$$

where $g(z) = \text{Ci}(z)\sin(z) - (\text{Si}(z) - \pi/2)\cos(z)$ and $h(z) = -\text{Ci}(z)\cos(z) - (\text{Si}(z) - \pi/2)\sin(z)$ are auxiliary functions of the sine and cosine integral functions [64]. The results in Eq. (1.58) are valid for any atom-wall distance d. For a ground state atom, the force is attractive (negative) for any atom-wall distance d. In the *near zone* limit ($d \ll k_{\text{a}}^{-1}$) it decreases like d^{-4}, while in *far zone* ($d \gg k_{\text{a}}^{-1}$) like d^{-5}. This is the original result obtained by Casimir and Polder for a ground state atom in the physical situation here analyzed [59]. For an excited-state atom, Eq. (1.58) shows spatial oscillations, with regions where the force is attractive (negative) and regions where it is repulsive (positive). The oscillations have periodicity related to k_{a}.

¶Quasi-static approximation means that we calculate the force as $F = -\nabla E$ supposing that the object (the atom) is fixed. In other words, we do not include effects due to an infinitesimal movement of the object during the derivative, namely effects coming from the dynamics (for example magnetic effects). The force is derived from a potential energy and not as a variation of the momentum in time.

For completeness, we mention that the Casimir-Polder potential energy between two ground-state atoms behaves as d^{-6} for interatomic distances smaller than typical atomic transition wavelengths (near zone) and as d^{-7} for larger distances (far zone) [51, 65].

Finally, we highlight that, although its small intensity, the atom-wall Casimir-Polder force has been measured with high precision both in the near and the far zone [66–72]. On the other hand, the atom-atom van der Waals/Casimir-Polder potentials are still too weak to be detected, even though there are many indirect experimental observations of them in agreement with theoretical predictions [73]. Additionally, direct measurements of the retarded van der Waals attraction in mesoscopic systems have been obtained [74]. Recently, it has also been suggested that the presence of boundary conditions and resonance conditions can enhance such interactions [75, 76].

1.4 Circuit QED

1.4.1 Introduction

Superconducting circuits are electrical circuits macroscopic in size (being hundreds of nanometers wide) that contain trillions of electrons and can operate at milli-degrees temperatures [77]. They exhibit observable quantum features such as quantized energy levels, superposition of states, and entanglement, which are commonly associated with particles or atoms. The access to such interesting properties is made possible because they can be engineered to be almost completely isolated form the (electrical) environment. This makes superconducting circuits very robust against decoherence phenomena, which, on the other hand, is responsible of the quantum-to-classical transition. In addition, their quantum states can be manipulated with very high precision by varying electric charges or the phase difference across a Josephson junction (a device with nonlinear inductance and no energy dissipation), or even applying electromagnetic pulses to control the magnetic flux which crosses the circuit [9].

A recent direction in the research on superconducting circuits is based on the correspondence between these chip systems and cavity QED, which, on the other hand, studies the interaction between electromagnetic fields and matter (atoms or molecules) in the vacuum space or in structured environments such as photonic crystals, waveguides and cavities [78]. One of the most basic elements in circuit QED is probably the LC-resonator, which in the quantum domain (where thermal fluctuations are much smaller than the quantum energy associated to the resonance frequency of the system) is described as a mechanical oscillator. This circuit models an electromagnetic microwave field. However, this system shows trivial quantum effects and to exploit the richness of circuit QED one usually relies on a nonlinear component. An example is given by the Josephson tunnel junction, whose nonlinearity is very fundamental since it is related to the discreteness of the charge which realizes quantum tunnelling through an insulating barrier [77]. This system is then used to build very fundamental circuital elements such as the charge or the flux qubit, both modeling an artificial atom. All these elements can be assembled together to engineer very specific atom-photon interactions used to describe cavity QED systems [79].

Circuit QED now represents a novel platform, where it is possible to explore new quantum phenomena arising from the interaction between light and matter. In fact, these circuits allows us to study new domains, where light and matter are ultra-strongly coupled, which (given the current technology) cannot be experimentally tested with atoms and fields. Not only they can be designed and built to tailor specific frequencies and couplings very easily, but such frequencies and couplings can be controlled by changing external parameters and even turned on and off almost at will. Another advantage of circuit QED is that an atom (a superconducting qubit) does not move inside an actual cavity, thus giving the chance to probe at any time the light-matter interaction without losing the atom. These are the main reasons why circuit QED has been so incredibly successful. Relevant experimental results include the achievement of the strong coupling [10, 80–82], the mapping of the discrete nature of a quantized field [83], the generation of single photon sources [84], and the realization of more complex circuits which couple many qubits using intermediate buses [85].

Moreover, given that the basic components of superconducting circuits are quantum bits (qubits) of information, the interest in such devices is not only fundamental, but also important from a technological point of view. In fact, thanks to their potential for quantum computing, scalable architectures towards the creation of quantum computers based on circuit QED have already been proposed [86] and realized [87]. It is now believed that such systems can be considered as primitive building blocks for the next generation of quantum computers.

For all these reasons superconducting quantum circuits are now subjected to an intense research, which leads to flexible realizations of quantum optics on a chip and potentially opens the door to new intriguing domains of mesoscopic physics.

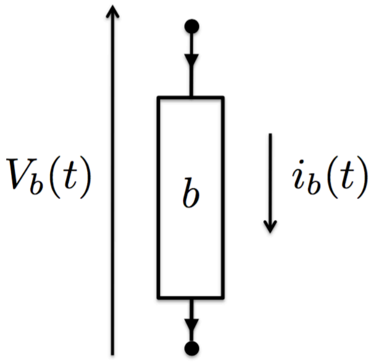

Figure 1.4: The element of each branch b is determined by two physical quantities: the voltage V_b and the current i_b, whose sign are determined by the orientation of the branch b as indicated. These quantities are defined from the underlying electromagnetic fields: $V_b = \int_{\text{beginning of b}}^{\text{end of b}} \mathbf{E} \cdot d\mathbf{s}$ and $i_b = (1/\mu_0) \oint_{\text{around b}} \mathbf{B} \cdot d\mathbf{s}$, with μ_0 the free space permeability.

1.4.2 Classical Hamiltonian formulation of the dynamics of electrical circuits

An electrical circuit can be thought as a network composed by branches which contain electrical elements, for example capacitors and inductors. At any time, each branch b is described by the voltage $V_b(t)$ and the current $i_b(t)$ (see Fig. 1.4), which are the analogue of velocities and forces in classical mechanics. The first step towards a Hamiltonian formulation of the circuit dynamics is to introduce the *branch* fluxes and charges [77]

$$\begin{aligned} \phi_b(t) &= \int_{-\infty}^{t} V_b(\tau) d\tau, \\ q_b(t) &= \int_{-\infty}^{t} i_b(\tau) d\tau, \end{aligned} \tag{1.59}$$

where we suppose that the rest configuration of the circuit is at $t = -\infty$ (this means that any external field has been turned on adiabatically from $t = -\infty$ to $t = 0$). Through the fundamental relations of any electrical element, the current and voltage variations in a branch are related to the charges and fluxes, respectively. For capacitive and inductive elements we, respectively, have

$$\begin{aligned} V_b &= f(q_b), \\ i_b &= g(\phi_b), \end{aligned} \tag{1.60}$$

where in the simple case of a linear circuit, $f(q_b) = q_b/C$ and $g(\phi_b) = \phi_b/L$. For a nonlinear inductive element such us a Josephson tunnel junction g is a sine function, in fact it is characterized by the following current-flux relation: $i(t) = I_0 \sin[\phi_J(t)/\Phi_0]$, where $\Phi_0 = (\hbar/2e)$ is the flux quantum, $I_0 = E_J/\Phi_0$ with E_J the Josephson energy [‖]. Given that the power flowing in any branch b is $V_b i_b = V_b \dot{q}_b = i_b \dot{\phi}_b$, we can also define the energy of any capacitive or inductive element as

$$\begin{aligned} E(q_b) &= \int_0^{q_b} f(q)dq, \\ E(\phi_b) &= \int_0^{\phi_b} g(\phi)d\phi, \end{aligned} \tag{1.61}$$

which give the following energies for the specific circuital element:

$$\begin{aligned} \text{Capacitor}: \quad E &= \frac{q_b^2}{2C} = \frac{C}{2}\dot{\phi}_b^2, \\ \text{Inductor}: \quad E &= \frac{\phi_b^2}{2L}, \\ \text{Junction}: \quad E &= -E_J \cos\left(\frac{\phi_b}{\Phi_0}\right). \end{aligned} \tag{1.62}$$

However, branch fluxes and charges are not suitable to describe the degrees of freedom of a circuit, since being related by the constraints imposed by Kirchhoff's laws they are not independent variables. We then define a new set of variables, called *node variables*, which only depend on the particular topology of the circuit. We first need to identify all the nodes in the circuit, which are defined as the intersections where different elements are connected. One node, called ground, is then taken as a starting point to build an open *spanning tree* running through all nodes in the circuit, without creating loops. All the other nodes are referred as *active nodes* and are connected to the ground node by only one path along the tree. The branches not included in the spanning tree are called *closure branches* and each of them is associated

---

[‖] A *Josephson tunnel junction* is formed by two superconductors separated by a thin oxide layer and can be modelled as nonlinear inductor element (called Josephson tunnel element, represented by a cross in circuit diagrams) in parallel with a capacitance. The non-linearity of the current relation is due to the discreteness of charge which tunnels the insulating barrier. For temperatures of around 10mK the electrons in the two superconductors are condensed in Cooper pairs and the junction is described by two collective degrees of freedom, the charge in the capacitance $q(t)$ and the number of Cooper pairs which have tunneled across the junction. If the junction is not connected to other electrical elements, the charge on the capacitor coincides with the one flowing through the element, i.e. $q(t) = -2eN(t)$. Equivalently, the Josephson tunnel junction can be described by the flux ϕ_J defined as in (1.59), which gives the current $i(t)$. The nonlinearity is then set by the superconducting flux quantum $\Phi_0 = \hbar/2e$ related to the Cooper pair charge $2e$. To observe tunneling typical values for I_0 and the capacitance are μA-nA and pF-fF, respectively.

to a circuital loop realized by joining the ends of the branch by using a minimal path on the spanning tree. We call C the set of closure branches and T the one of all the branches forming the spanning tree. Taking into consideration the orientation initially chosen for the branch, we associate to each circuital element (or branch) of C and T the following fluxes

$$\begin{aligned} \phi_{b\in T} &= \Phi_n - \Phi_{n'}, \\ \phi_{b\in C} &= \Phi_n - \Phi_{n'} + \tilde{\Phi}_{l(b)}, \end{aligned} \tag{1.63}$$

where $\Phi_{n(n')}$ are the (node) fluxes, defined by the time integral of the voltage measured along the path connecting the node to the ground on the spanning tree, at the end nodes n and n' of the branch, and $\tilde{\Phi}_{l(b)}$ is the magnetic flux that runs through the l loop of the branch b. We point out that the definition of node flux is intimate connected to the concept of superconducting phase φ defined at a given point of a superconducting circuit. These quantities are related as follows [77, 88]

$$\varphi = \frac{2e}{\hbar}\Phi \bmod(2\pi), \tag{1.64}$$

such that the difference between the fluxes at two different nodes can also be expressed as:

$$\Phi_n - \Phi_{n'} = \Phi_0(\varphi_n - \varphi_{n'}), \tag{1.65}$$

where $(\varphi_n - \varphi_{n'})$ is the phase difference across the branch. We however remind that the phase φ is introduced only in superconducting systems, while the concept of node flux is more general and holds for any circuit.

Once the branch fluxes have been defined, by using Eqs. (1.59) and (1.60) we can express the currents flowing through the branches in terms of the node variables for the specific circuital element:

$$\begin{aligned} \text{Capacitor}: &\quad i_b = C\dot{V}_b = C\ddot{\phi}_b = C(\ddot{\Phi}_n - \ddot{\Phi}_{n'}) \\ \text{Inductor}: &\quad i_b = \frac{\phi_b}{L} = \frac{\Phi_n - \Phi_{n'} + \tilde{\Phi}_{l(b)}}{L} \\ \text{Junction}: &\quad i_b = I_0 \sin\left[\frac{2e}{\hbar}\phi_b\right] = I_0 \sin\left[\frac{2e}{\hbar}(\Phi_n - \Phi_{n'} + \tilde{\Phi}_{l(b)})\right]; \end{aligned} \tag{1.66}$$

and obtain a set of differential equations of motion of the circuit by equating, for each active node, the sum of currents arriving from inductive elements and the sum of currents flowing into capacitive elements. These equations, which have the following form

$$\sum_{n,n'\in\text{capacitor}} C_{nn'}\delta\ddot{\Phi}_{nn'} = \sum_{n,n'\in\text{inductor}} \frac{\delta\Phi_{nn'} + \tilde{\Phi}_{l(b)}}{L_{nn'}} + \sum_{n,n'\in\text{junction}} I_0 \sin\left[\frac{2e}{\hbar}\left(\delta\Phi_{nn'} + \tilde{\Phi}_{l(b)}\right)\right], \tag{1.67}$$

with $\delta\Phi_{nn'} = \Phi_n - \Phi_{n'}$, can be derived as the Euler-Lagrange equations associated with the Lagrangian $\mathcal{L}(\Phi_n, \dot{\Phi}_n)$. The latter is obtained as a difference between the capacitive and the inductive energy of the circuit in Eq. (1.62) in terms of the node fluxes. We can then find node charges Q_n, which are the conjugate momenta of node fluxes:

$$Q_n = \frac{\partial \mathcal{L}}{\partial \dot{\Phi}_n}. \tag{1.68}$$

Each of them gives the sum of the charges on the capacitances linked to the node n. We remark that node charges are always defined, since parasitic capacitances are always present between nodes. This ensures that a Legendre transformation of the Lagrangian with respect to Q_n can be always performed. The resulting Hamiltonian of the circuit $\mathcal{H}(\Phi_n, Q_n) = \sum_n Q_n \dot{\Phi}_n - \mathcal{L}$ (where the $\dot{\Phi}_n$ are replaced in terms of charges) will be the sum of the electrostatic energy of the circuit expressed in terms of node charges and the magnetic energy in terms of node fluxes. It is also possible to verify that

$$\begin{aligned} \dot{\Phi}_n &= \frac{\partial \mathcal{H}}{\partial Q_n}, \\ \dot{Q}_n &= -\frac{\partial \mathcal{H}}{\partial \Phi_n}. \end{aligned} \tag{1.69}$$

While the Hamiltonian always gives the total energy of the circuit, its functional form can depend on the choice of the spanning tree. However, the Poisson brackets of fluxes and charges of a branch are independent of this choice:

$$\{\phi_b, q_b\} = \sum_n \frac{\partial \phi_b}{\partial \Phi_n}\frac{\partial q_b}{\partial Q_n} - \frac{\partial q_b}{\partial \Phi_n}\frac{\partial \phi_b}{\partial Q_n} = 1. \tag{1.70}$$

Finally, we highlight that in the node representation, node fluxes and charges play the same role of position and momentum coordinates in classical mechanics. Accordingly, electrostatic and magnetic energies substitute kinetic and potential energies. However, more generally, the Hamiltonian can contain additional terms which do not have a direct mechanical correspondence (for example electrostatic cross-terms).

1.4.3 Quantum description

The quantum mechanical formulation of a circuit simply follows the procedure developed in the previous paragraph. The classical variables are promoted to operators, the Hamiltonian becomes a function of operators, and the operators, which represent position coordinates and commute between them, determine a Hilbert space. We also impose that each pair of flux-charge variables satisfies the canonical commutation relation [77]

$$[\Phi_n, Q_{n'}] = i\hbar\delta_{nn'}. \tag{1.71}$$

Following the Dirac quantization procedure, which establishes that Poisson brackets are replaced by corresponding commutators, fluxes and charges of a branch verify the following commutator $[\phi_b, q_b] = i\hbar$, although they are not conjugate coordinates.

1.4.4 Quantum LC resonator

Let us consider the LC circuit in Fig. 1.5 where a capacitor C_r is coupled in parallel to an inductor L_r. This system has a trivial topology with only one active node. Following the procedure previously described, we can write down the Lagrangian of the circuit in terms of the node flux for the active node r as [77]

$$\mathcal{L}_r = \frac{C_r}{2}\dot{\Phi}_r^2 - \frac{\Phi_r^2}{2L_r}, \tag{1.72}$$

which is the difference between the capacitive (kinetic) and the inductive (potential) energy of the circuit. The node charge then is $Q_r = \partial\mathcal{L}/\partial\dot{\Phi}_r = C_r\dot{\Phi}_r$. Expressing $\dot{\Phi}_r$ in terms of the charge, the Hamiltonian results

$$\mathcal{H}_r = \frac{Q_r^2}{2C_r} + \frac{\Phi_r^2}{2L_r}, \tag{1.73}$$

which coincides with the total energy of the system as trivially expected. The commutator for flux and charge variables expressed in (1.71) establishes a correspondence between charge-flux and momentum-position which can be used to diagonalize the Hamiltonian using Fock creation and annihilation operators such that $[a, a^\dagger] = 1$. We obtain

$$\begin{aligned}
\Phi_r &= \sqrt{\frac{\hbar Z_r}{2}}(a + a^\dagger), \\
Q_r &= \sqrt{\frac{\hbar}{2Z_r}} i(a^\dagger - a), \\
\mathcal{H}_r &= \hbar\omega_r\left(a^\dagger a + \frac{1}{2}\right),
\end{aligned} \tag{1.74}$$

with $\omega_r = \sqrt{1/L_rC_r}$ the oscillator frequency and $Z_r = \sqrt{L_r/C_r}$. From the expression of ω_r it is clear that the capacitance C_r and the inductance L_r correspond to the mass and the inverse of the trapping strength of a harmonic oscillator, and combine such that the quantization of the oscillator is in terms of units of ω_r. This means that the electric energy (confined in the

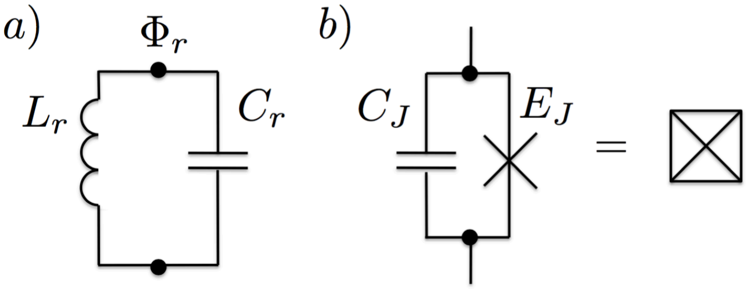

Figure 1.5: a) Circuit model for a LC resonator with inductance L_r and capacitance C_r where Φ_r is the flux corresponding to the only active node of the circuit, while the other bullet point indicates the ground. b) Schematic representation of a Josephson tunnel junction with a non-linear inductor element with energy E_J (called Josephson tunnel element and represented by a cross) in parallel with a capacitance C_J. The overall circuital element will be indicated with a box (also called Cooper-pair-box).

resonator and typically within the microwave regime) can be extracted or inserted in units, adding or subtracting a quasi-particles with energy $\hbar\omega_r$. Given their statistics, we will refer to these particles as *photons*.

1.4.5 Charge qubit

We now want to study a simple circuit formed by one superconducting *island*, that is a node whose charge can vary only by electron tunneling. We then consider the circuit in Fig. 1.6(a), where a single island is connected to a superconducting electron reservoir by a tunnel junction modelled as a non-linear inductor (a Josephson tunnel element) in parallel with the capacitor C_J (see also Fig. 1.5(b)). The Josephson element allows charges to enter and exit the island, while a voltage source V_G connected to the island through a gate capacitance C_q creates an induced charge that shifts the equilibrium state of the system. Also in this case, the topology of the circuit is trivial. Identified the node flux Φ_q, the Lagrangian of the circuit, which includes the nonlinear inductive energy of the junction, results [77, 79]

$$\mathcal{L}_q = \frac{C_\Sigma}{2}\left(\dot{\Phi}_q - V_G\right)^2 + E_J \cos\left(\frac{\Phi_q}{\Phi_0}\right), \tag{1.75}$$

where $C_\Sigma = C_J + C_q$ is the total island capacitance. The associated node charge is given by $Q_q = \partial\mathcal{L}/\partial\dot{\Phi}_q = C_\Sigma\dot{\Phi}_q - C_q V_G$, where $C_q V_G$ is the amount of charge induced by the external electrical potential in the island. This allows us to find the following Hamiltonian

$$\mathcal{H}_q = \frac{(Q_q + C_q V_G)^2}{2C_\Sigma} - E_J \cos\left(\frac{\Phi_q}{\Phi_0}\right). \tag{1.76}$$

Supposing that both island and reservoir are good superconductors, such that their energy gap for single-particle excitation is much larger than the energy $k_B T$ of the thermal fluctuations and the Coulomb energy $e^2/2C_\Sigma$ of the island, all electrons in the island will be bounded in Cooper pairs [89]. The total number of such pairs n with charge $q = -2en$ defines the degree of freedom of the island. As in cavity QED for the number of photons, the variable n is discrete, but it can take both positive and negative values ($n = 0$ corresponding to the case of a neutral island). Given that Cooper pairs can tunnel in and out the island, n can fluctuate quantum-mechanically and can be described as an operator with eigenvectors $|n\rangle$ such that $q\,|n\rangle = 2en\,|n\rangle$. The electrostatic term of the Hamiltonian in Eq. (1.76) can be then written as [89]

$$\mathcal{H}_{\text{el}} = E_C \sum_n (n - n_g)^2 \,|n\rangle\langle n|\,, \tag{1.77}$$

where $n_g = C_q V_g/(2e)$ is the dimensionless gate voltage and $E_C = (2e)^2/2C_\Sigma$ the Coulomb energy of a Cooper pair on the island. In the same number basis, the Josephson coupling Hamiltonian (the second term of (1.76)), which describes the hopping of charge pairs in and out of the superconducting island, has the following form

$$\mathcal{H}_J = -\frac{E_J}{2} \sum_n \left(|n\rangle\langle n+1| + |n+1\rangle\langle n|\right), \tag{1.78}$$

where the Josephson energy E_J is actually proportional to the area of the tunnel junction[**]. In Fig. 1.6(b) we compare the energy levels of $\mathcal{H}_{\text{el}}$ with the ones of the full Hamiltonian $\mathcal{H}_q = \mathcal{H}_{\text{el}} + \mathcal{H}_J$ for $E_J \ll E_C$ (*charge limit*), as a function of the applied gate voltage. In this limit, the effect of the Josephson Hamiltonian is to remove the degeneracy at the intersections of each parabola and create avoided crossings. For temperatures such that $k_B T \ll E_C$ [††] we can restrict our attention to the lowest energy states $|0\rangle$ and $|1\rangle$ (see Fig. 1.6(c) for the classical charge configuration corresponding to these states). Also, given the periodicity of the system with respect to the addition of a Cooper pair, the variation of the applied gate voltage can be considered in the interval $0 < n_g < 1$. Under these assumptions, the dynamics of the circuit can be mapped into the Hamiltonian of a particle with spin 1/2 interacting with an effective

---

[**] If G_T is the junction conductance, $E_J = (hG_T/8e^2)\Delta$, where Δ is the superconducting gap.

[††] For T=1K, this requires C_Σ to be much less than 1fF.

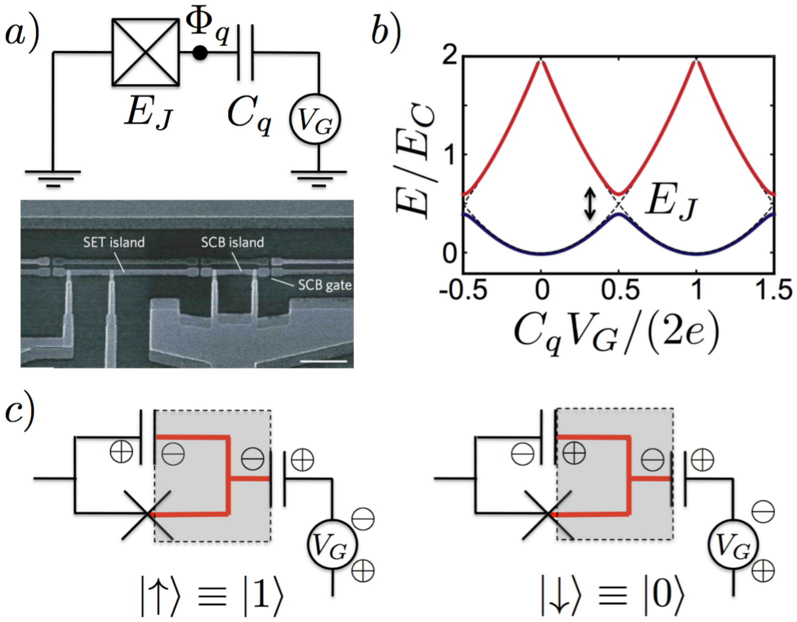

Figure 1.6: a) Circuit model of a charge qubit, where a single Josephson junction with energy E_J is coupled via a capacitance C_q with the external voltage V_G. Φ_q is the node flux corresponding to the active node of the circuit. It is also shown a scanning electron micrograph of charge qubit in an experimental realization, where a superconducting island (single-Cooper-pair box (SCB)) is coupled to a transistor (SET), scale bar 1μm (imported from Ref. [16]). b) Energy levels of the charge qubit without Josephson junction (dashed lines) and with tunnelling amplitude $E_J \ll E_C$ as a function of the displaced charge $n_g = C_q V_G/(2e)$ (continuous lines). c) Classical charge configuration in the island (box in grey) for the two states of the qubit.

magnetic field whose (x, y, z) components are $(\hbar\omega_q = E_J,\ 0,\ \hbar\epsilon = 2E_C\left(n_g - \frac{1}{2}\right))$. We thus have

$$\mathcal{H}_q = \frac{\hbar\epsilon}{2}\sigma_z + \frac{\hbar\omega_q}{2}\sigma_x, \tag{1.79}$$

where $\hbar\epsilon$ and $\hbar\omega_q$ correspond to the difference between the electrostatic energy of the two lowest states and the minimum gap, respectively; while, $\sigma_{x,z}$ are the standard Pauli spin matrices, which, in terms of the states of the basis, are defined as

$$\begin{aligned} \sigma_x &= |\downarrow\rangle\langle\uparrow| + |\uparrow\rangle\langle\downarrow|, \\ \sigma_z &= |\uparrow\rangle\langle\uparrow| - |\downarrow\rangle\langle\downarrow|, \end{aligned} \tag{1.80}$$

with $|\uparrow(\downarrow)\rangle \equiv |1(0)\rangle$. The σ_x operator describes a flip operation between the two states and replace the tunneling term in Eq. (1.78). When $\epsilon = 0$, that is $n_g = 1/2$, the true eigenstates of the system are $|\pm\rangle = (|\uparrow\rangle \pm |\downarrow\rangle)/\sqrt{2}$ separated by a frequency ω_q, where $|-\rangle$ is the ground state.

Also, in this Cooper pair box - spin $1/2$ correspondence the average value of the z-component of the spin provides the average charge in the island. In fact we have:

$$\langle n \rangle = \frac{1}{2}\left(1 + \langle \sigma_z \rangle\right), \tag{1.81}$$

where for an operator A the average is given by $\langle A \rangle = \mathrm{Tr}[e^{-\beta \mathcal{H}_q} A]$ at the equilibrium temperature $T = 1/(k_B \beta)$.

Typical parameters for a fabricated charge circuit might be $E_C/h \simeq 10\text{GHz}$ ($E_C/k_B = 0.5\text{K}$), and $E_J/E_C \simeq [0.4, 1[\text{GHz}$ [16].

1.4.6 Transmon qubit

The transmon qubit circuit actually coincides with the one for a charge qubit. The only difference is that it operates in the regime $E_J \gg E_C$. For this reason, in literature, we equivalently refer to it as a regime of the charge qubit, i.e the *transmon regime*. The Hamiltonian of the transmon qubit can be derived from Eq. (1.76) by expanding the cosine function of the Josephson element. At the second order we obtain

$$\mathcal{H}_q \simeq \frac{(Q_q + C_q V_G)^2}{2C_\Sigma} - E_J \left(1 - \frac{1}{2}\frac{\Phi_q^2}{\Phi_0^2} + \frac{1}{24}\frac{\Phi_q^4}{\Phi_0^4}\right). \tag{1.82}$$

This expansion is physically sound since, for $E_J \gg E_C$, the potential energy (Josephson energy) is more important than the kinetic energy (electrostatic energy). This means that the dynamics of the system is restricted within the minima of the parabolas in Fig. 1.6(b) and that we are considering small oscillations around these values. Introducing the following operators,

$$\begin{aligned} Q_q =& i\sqrt{\frac{\hbar\omega_q C_\Sigma}{2}}(b^\dagger - b), \\ \Phi_q =& \Phi_0\sqrt{\frac{\hbar\omega_q}{2E_J}}(b^\dagger + b), \end{aligned} \tag{1.83}$$

with $\hbar\omega_q = \sqrt{8E_J E_C}$, the Hamiltonian in (1.82) can be cast in the form of a Duffing oscillator [90]

$$\mathcal{H}_q = \hbar\omega_q\left(b^\dagger b + \frac{1}{2}\right) - \frac{E_C}{12}\left(b^\dagger + b\right)^4, \tag{1.84}$$

where b and $b^\dagger$ denote the regular annihilation and creation operators for the harmonic oscillator approximating the transmon, we have removed the constant energy $-E_J$ and set $n_g = 1/2$. More in general, one can define $\tilde{n}_q = n_q + Q_{\text{env}}/2e$, where Q_{env} represents the environment-induced offset charge. The initial experiments with charge qubits revealed to be too much sensitive to electromagnetic fluctuations and charge noises, whose effects can be encoded in $\tilde{n}_q$. And actually, it was to overcome such experimental challenge that the first transmon qubit was realized [90]. By means of the additional capacitance, which acts as an increased effective mass of the qubit, the ratio E_C/E_J can be decreased, so that the relative strength of the coupling to the environment decreases as well, without losing the anharmonicity of the system. This has allowed to achieve higher dephasing times with respect to original experiments [91]. However, decreasing the ratio E_C/E_J makes the energy levels less and less anharmonic, until the point in which the energy difference between the second and the third level $\omega_{12} = E_2 - E_1$ is too close to ω_q to experimentally resolve the qubit levels without inducing unwanted transitions to the second excited state. If we further decreased the ratio E_C/E_J, the fluctuations of n would become so large that the one would recover the standard description of the Josephson effect, where the phase on the island is a good-quantum number, without the presence of the anharmonicity in Eq. (1.84). Typical experimental values for the relevant parameters of a chip-fabricated $2D$ transmon are $E_J/E_C \simeq [50, 100]$, $\omega_q \simeq [5, 10]$GHz and $\delta\omega = \omega_q - \omega_{12} \simeq [4, 5] \times 10^2$MHz [79,90], such that it is possible to experimentally access the qubit levels without introducing unwanted processes. We finally highlight that a transmon qubit can also be used to implement quantum operations and store information in different ways with respect the charge, since one can take advantage of the extra levels in the anharmonic ladder, which are in principle manipulable and allow the circuit to operate, for example, as a qutrit [92].

1.4.7 Flux qubit

We now would like to study the circuit in Fig. 1.7(a) consisting of a superconducting loop formed by three Josephson junctions crossed by an external magnetic flux Φ_{ext} (Fig. 1.7(b) shows an experimental realization). This circuit, which is based on three (or four) junctions, is commonly called *flux qubit*. For simplicity, two Josephson junctions are identical with capacitance C_J and energy E_J, while the other has capacitance αC_J and energy αE_J with $\alpha < 1$. As depicted in Fig. 1.7(c) the circuit has two active nodes a and b and three branches whose fluxes are defined as [77,79]

$$\begin{aligned}
\phi_a =& \Phi_a, \\
\phi_b =& -\Phi_b, \qquad (1.85)\\
\phi_c =& \Phi_a - \Phi_b + \Phi_{\text{ext}} = \phi_a + \phi_b + \Phi_{\text{ext}}.
\end{aligned}$$

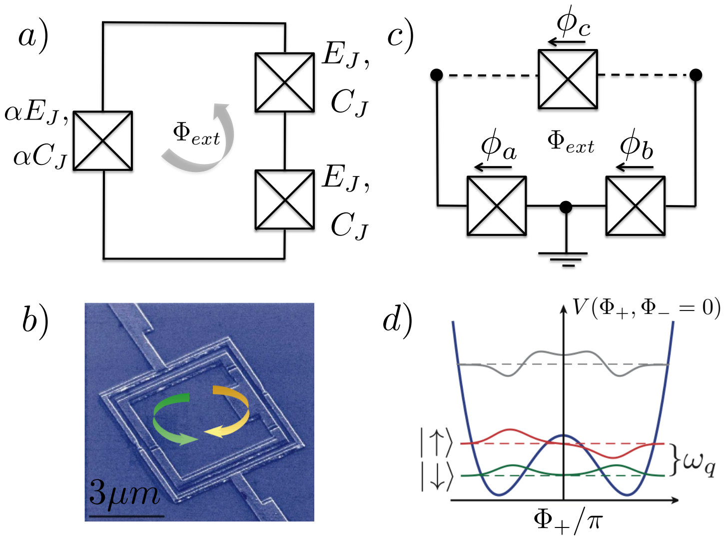

Figure 1.7: a) Circuit model for three junction flux qubit. Two junctions are characterized by the same capacitance C_J and energy E_J, while the remaining has energy αE_J and capacitance αC_J. Φ_{ext} is the external potential passing through the circuit. b) A three junction flux qubit in an experimental realization (figure imported from Ref. [9]). c) Schematic representation of the circuit in a) where the phase differences across the junctions have been indicated together with the active nodes of the circuit. d) Potential of the three junction flux qubit as a function of the variable Φ_+ having fixed the value of Φ_-. The dashed lines indicate the energies of the three lowest qubit states and the corresponding wavefunctions.

Note that $\phi_{a,b,c}$ are also referred as the phase differences across the junctions accordingly to the definition in Eqs. (1.64) and (1.65). This terminology will be convenient in the final Chapter of this thesis.

By using Eq. (1.85), the Lagrangian of the circuit results

$$\mathcal{L}_q = \frac{C_J}{2}(\dot{\phi}_a^2 + \dot{\phi}_b^2) + \frac{\alpha C_J}{2}\left(\dot{\phi}_a + \dot{\phi}_b\right)^2 + E_J\left[\cos\left(\frac{\phi_a}{\Phi_0}\right) + \cos\left(\frac{\phi_b}{\Phi_0}\right) + \alpha\cos\left(\frac{\phi_a + \phi_b + \Phi_{\text{ext}}}{\Phi_0}\right)\right], \tag{1.86}$$

which introducing the new flux variables $\Phi_\pm = (\phi_a \pm \phi_b)$, becomes

$$\mathcal{L}_q = \frac{C_J}{2}\left(\alpha + \frac{1}{2}\right)\dot{\Phi}_+^2 + \frac{C_J}{4}\dot{\Phi}_-^2 + E_J\left[2\cos\left(\frac{\Phi_+}{2\Phi_0}\right)\cos\left(\frac{\Phi_-}{2\Phi_0}\right) + \alpha\cos\left(\frac{\Phi_+ + \Phi_{\text{ext}}}{\Phi_0}\right)\right]. \tag{1.87}$$

We can now find the conjugate charges $Q_\pm$ of the fluxes $\Phi_\pm$: $Q_+ = \partial\mathcal{L}/\partial\dot{\Phi}_+ = C_J(\alpha + 1/2)\dot{\Phi}_+$ and $Q_- = \partial\mathcal{L}/\partial\dot{\Phi}_- = (C_J/2)\dot{\Phi}_-$, which, by following the standard Legendre transformation, give the Hamiltonian

$$
\begin{aligned}
\mathcal{H}_q &= \frac{Q_+^2}{2C_J(\alpha+1/2)} + \frac{Q_-^2}{C_J} + V(\Phi_+,\Phi_-), \quad \text{with} \\
V(\Phi_+,\Phi_-) &= -E_J\left[2\cos\left(\frac{\Phi_+}{2\Phi_0}\right)\cos\left(\frac{\Phi_-}{2\Phi_0}\right) + \alpha\cos\left(\frac{\Phi_+ + \Phi_{\rm ext}}{\Phi_0}\right)\right]
\end{aligned}
\tag{1.88}
$$

the resulting nonlinear potential of the circuit. For a given value of the external magnetic flux $\Phi_{\rm ext}$, the minimum of $V(\Phi_+,\Phi_-)$ occurs at $\Phi_- = 0$. This is the result of the interplay between the cosine function containing $\Phi_{\rm ext}$, which has minima at $\Phi_+ = n\pi\Phi_0 - \Phi_{\rm ext}$, and the term $\cos(\Phi_+/2\Phi_0)$ with minimum at $\Phi_+ = 0$. For an external flux $\Phi_{\rm ext}/\Phi_0 = \pi$ the total potential displays a double-well structure for the variable Φ_+, as displayed in Fig. 1.7(d). For values of the external potential around that point, we can introduce the external flux shift and the tunneling gap

$$
\begin{aligned}
\hbar\epsilon &\propto \Phi_{\rm ext} - \pi\Phi_0 \\
\hbar\omega_q &= E_1 - E_0,
\end{aligned}
\tag{1.89}
$$

with E_0 and E_1 the eigenvalues of the first two levels of the Hamiltonian, and define the basis states $|L\rangle$ and $|R\rangle$. We then recover the Hamiltonian found for the charge-qubit in Eq. (1.79):

$$
\mathcal{H}_q = \frac{\hbar\epsilon}{2}\sigma_z + \frac{\hbar\omega_q}{2}\sigma_x. \tag{1.90}
$$

By diagonalizing this Hamiltonian, one can see that for values of α within the interval $\sim [0.6, 1]$, the lowest energy states of the Hamiltonian are very close and well-separated from the rest of the spectrum. In contrast, if the Josephson energy αE_J is too small, the third energy level of the Hamiltonian becomes too much close to the first level $E_{21} = E_2 - E_1 \simeq E_1 - E_0$, which is not ideal, since in such a situation we cannot address transitions between the first two levels without having leakage to higher levels. On the other hand, having α arbitrarily high is also not desirable. In this case, not only the gap Δ approaches the zero value cancelling one of the two Hamiltonian terms, but the sensitivity of the qubit to the fluctuations of the magnetic field increases.

Typical parameters to realize the double-well potential qualitatively shown in Fig. 1.7(d) are: $C_J = 4$fF, $E_J/h = 500$GHz and $\alpha = 0.8$ [79, 93]. For such parameters the two lowest qubit states are the symmetric and antisymmetric superposition of the ground states on the left and right of the potential well, which are separated by a tunneling splitting of $\omega_q/(2\pi) \simeq 3.8$GHz. The next level is instead split by $E_{21} \simeq 46.5$GHz, such that the two level approximation is justified.

1.4.8 Single qubit operations

As we have seen, charge and flux qubits can be reduced (in the two level approximation) to the effective Hamiltonian

$$\mathcal{H}_q = \frac{\hbar\epsilon}{2}\sigma_x + \frac{\hbar\omega_q}{2}\sigma_z, \tag{1.91}$$

which has two control parameters: ϵ and ω_q. Note that here we have rotated the state of the qubit: this can be always done by applying a strong and uniform (or small time-dependent) external field. At the degeneracy point $\epsilon = 0$, the qubit gap is minimal and given by the frequency ω_q: this is the usual assumption when we start to work with these systems.

Chapter 2

Quantum-classical comparison in optomechanics

2.1 Introduction

An important goal in quantum optics is to generate nonlinearities. These are at the heart of non-Gaussian operations and, therefore, essential to deeply explore non-classicality. One way of achieving such target is to use available operations directly connected to the Hamiltonian under study, which manipulate the motion of one of the subsystems so that it undergoes a loop in its phase space. The result of the overall operation allows for the generation of a deterministic effective nonlinearity on the other subsystem. Some platforms where this technique has been employed very efficiently are trapped-ion systems [94–96], superconducting circuits [97], and photonic systems [98, 99]. In all these cases, the subsystem where the nonlinearity is generated acquires a phase which has an elegant geometric interpretation in the phase space of the other subsystem.

The interest in generating nonlinearities is now spread even in the emerging field of cavity optomechanics, where it is strongly combined to the study of non-classical properties of mechanical motion [2]. Here, the motion of the mechanical oscillator is manipulated by using the radiation pressure force and, nonlinearities can be realized by enclosing loops in the phase space of either the optical [100] or the mechanical degrees [6] of freedom. Actually, the idea of a closed loop, in which the mechanical oscillator evolves returning to its initial quantum state and the light field picks up a geometric-like nonlinear phase, was already encoded in the fundamental works of Mancini and Bose [30, 31]. In these studies, it was highlighted for the first time that, in the strong coupling regime between light and matter, a continuous quantum interaction can be used to generate nonclassical states of light and mechanics. It was also found that, at certain interaction times, the optical field decouples from the oscillator independently from the initial mechanical state. This very important feature of the system was then proposed as a key to probe the decoherence of the oscillator [101]. A very similar idea was also leveraged for the case of a micro-mechanical resonator capacitively coupled to a Cooper-pair-box [102], for an interferometric scheme built with an optomechanical cavity [20], and for an atom coupled to a mechanical oscillator [103, 104].

More specifically, it has been suggested that the creation of correlations between a single-photon path-entangled light source and a mechanical oscillator can be used to discriminate between different decoherence mechanisms, for example due to gravitational effects or wave-collapse [20, 21]. To address such a very subtle issue the interferometric visibility is invoked. In fact, this quantity is widely believed a measure of coherence (degree of correlations) between two components of the system. It actually works as a witness of mechanical coherence, which can be then affected by standard decoherence models or more exotic mechanisms. The key point is the observation of the revival of the interferometric visibility, which happens when light and matter are completely decoupled (disentangled) and the mechanical oscillator has undergone a closed loop in its phase space. The complete recovery of visibility proves the fact that light and mechanics have been entangled for previous times, while a partial recovery can happen whether the environment remembers the state of the oscillator, thus providing a way to quantify and test the decoherence of the mirror.

In all the aforementioned works, the optomechanical interaction has been described quantum mechanically. However, it is quite interesting to ask whether or not all the features, which are believed to be a consequence of quantum mechanics, are really of quantum origin. On the other hand, quantum mechanics encapsulates classical physics and, in a quite broad range of parameters, classical physics provides equal or very similar answers. In this Chapter, we want to address the non-classicality of the optomechanical interaction by comparing the quantum predictions with the ones obtained within a fully classical model. In particular, since the phase acquired by the optical field after its interaction with the mechanical oscillator is at the heart of all the fundamental previous studies, we begin our classical-quantum comparison for such phases within a quite general mathematical framework, and compare our results with the previous relevant proposals (Refs. [6, 20]). Starting from the *pulsed* interaction regime [36, 105], we then discuss the *continuous* interaction regime, where we enlarge our classical-quantum comparison to the interferometric visibility [20, 21].

The results of our analysis clearly show that many of the peculiarities, which have been considered of quantum origin in the previous setups, can be actually recovered by classical means. In particular, the two most important features of the optical quantum phase are still found in the classical scenario: the independence of the oscillator at some interactions times, which coincide with the mechanical periods, and the phase nonlinearity induced by the light-matter interaction [30, 31]. We will also see how these properties allow us to prove that the loss and revival of the visibility pattern in an interferometric scheme can have a completely classical explanation. Nevertheless, our classical-quantum comparison singles out genuine non-classical components of the system dynamics (not reproducible classically or semi-classically), which could be probed in todays cavity optomechanical experiments.

More specifically, the following Chapter is organized as follows: in Sec. 2.2 we briefly describe the model and the basic pulsed interaction. In Sec. 2.3 we explore the quantumness of the phase acquired by the optical field both in a pulsed and continuous regime. We also show how it is possible to recover the continuous regime from the pulsed one via a Trotter-Suzuki expansion on the unitary evolution operator of the system. In Sec. 2.4 we then complete our classical-quantum comparison for the interferometric visibility. To completely address the non-classicality of the optomechanical interaction, in Sec. 2.5 we compare our results with the ones found within a semiclassical picture. Finally, Sec. 2.6 summarizes our findings.

We highlight that in this Chapter we use the convention that all the quantum operators are indicated with the hat symbol as $\hat{O}$, to avoid confusion in our classical-quantum comparison.

2.2 The model

We consider the optomechanical cavity described in paragraph 1.2.3, where a single mode field and a mechanically oscillating mirror are coupled inside a cavity as depicted in Fig. 2.1(a). The effective Hamiltonian that describes this system dynamics is given by Eq. (1.11), which, in a frame rotating at the field frequency, can be rewritten as

$$\hat{H} = \hat{H}_0 + \hat{H}_{\text{int}}, \tag{2.1}$$

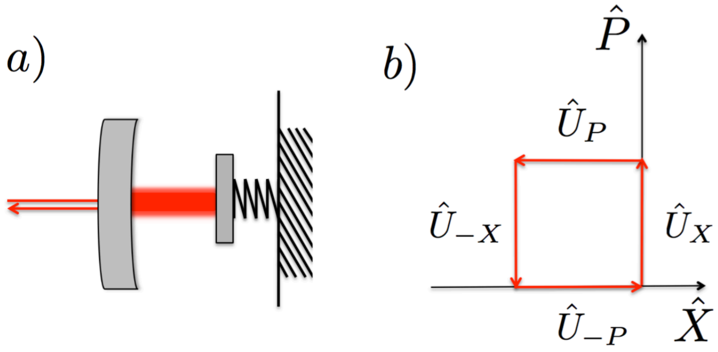

Figure 2.1: a) Optomechanical cavity with a harmonic oscillating mirror at one end. b) Representation of the four displacement operation in the phase space of the mechanical oscillator.

with

$$\begin{aligned} \hat{H}_0 &= \frac{\hbar\omega}{2}\left(\hat{X}^2+\hat{P}^2\right), \\ \hat{H}_{\text{int}} &= -\hbar\tilde{g}_0\hat{n}\hat{X}. \end{aligned} \tag{2.2}$$

$\hat{H}_0$ gives the mechanical free energy of the mechanical mirror where

$$\begin{aligned} \hat{X} =& \frac{1}{\sqrt{2}}(\hat{b}^\dagger+\hat{b}), \\ \hat{P} =& \frac{i}{\sqrt{2}}(\hat{b}^\dagger-\hat{b}) \end{aligned} \tag{2.3}$$

are the quadrature operators of the mirror, $\hat{H}_{\text{int}}$ is the interaction energy where $\hat{n}=\hat{a}^\dagger\hat{a}$ is the number operator of the optical field, while $\tilde{g}_0 = g_0\sqrt{2}$ is the new coupling constant with g_0 defined in Eq. (1.12). For the sake of simplicity, in this Chapter we have removed the subscript to the mechanical frequency, which is now indicated with ω.

As discussed in paragraph 1.2.4, in the case of a pulsed regime, the time of the interaction is much smaller than the period of the mechanical motion $\tau = 2\pi/\omega$ and the system is required to operate in the bad cavity limit, that is $\kappa \gg \omega$. To correctly neglect additional effects due to the coupling of the mechanical mirror to the environment, we also demand the characteristic mechanical decoherence time lower than the mechanical period. Under these assumptions we can then safely neglect the free evolution of the mirror during its interaction with the light. The overall dynamics can be described by the unitary operator [36]

$$\hat{U}_X = e^{i\lambda\hat{n}\hat{X}}, \text{ where } \lambda = \frac{\tilde{g}_0}{\kappa} \tag{2.4}$$

is the rescaled (dimensionless) coupling strength, which can be seen as a displacement operation by $\lambda n/\sqrt{2}$ along P in the phase space of the mechanical oscillator. We remark that the sentence is rigorous when the cavity field is prepared in a Fock state $|n\rangle$. As soon as the interaction vanishes, the oscillator is free to evolve under the Hamiltonian $\hat{H}_0$ and $\hat{X}$ and $\hat{P}$ start to interchange themselves accordingly. The pulse interaction then allows us to drive the oscillator along closed loops in phase space by selecting the appropriate time between consecutive pulsed interactions. More specifically, we imagine that the same light pulse enters the cavity, escapes after a short interaction lasting a time $1/\kappa = (2L/c)N_{rt}$, where $N_{rt} = \mathsf{F}/\pi$ is the round trip time with F the cavity finesse, and waits in an engineered loop before being injected again. This situation is commonly realized by using a cavity formed by a small ending mirror vibrating in a harmonic potential and a massive rigid mirror with lower reflectivity. This experimentally allows the light to enter and exit the cavity passing the large rigid mirror with minimal transmission through the movable mechanical mirror [2].

2.3 Quantum vs classical dynamics

2.3.1 Four pulsed interactions

We start to consider a sequence of four interactions (with the same pulse), where each interaction given by (2.4) is separated by a quarter of the mechanical period. The same scheme has been previously proposed in Ref. [6]. The full procedure corresponds to $\hat{U}_X$, followed by $\hat{U}_P$, $\hat{U}_{-X}$ and $\hat{U}_{-P}$. As represented in Fig. 2.1(b), this sequence of four pulses generates a square loop in mechanical phase space with a photon-number-dependent side-length. The effective interaction generated by the overall sequence is described by the unitary

$$\hat{\xi} = e^{-i\lambda\hat{n}\hat{P}} e^{-i\lambda\hat{n}\hat{X}} e^{i\lambda\hat{n}\hat{P}} e^{i\lambda\hat{n}\hat{X}}, \tag{2.5}$$

which, by using Baker-Campbell-Hausdorff formula[§] can be calculated as

$$\hat{\xi} = e^{\lambda^2\hat{n}^2[\hat{X},\hat{P}]} = e^{i\lambda^2\hat{n}^2}. \tag{2.6}$$

The above operation yields a highly self-Kerr nonlinear operation only acting on the optical field, as we have already found for the evolution operator in the case of a continuous interaction (Eq. (1.13)). This type of nonlinearity is very close to controlled gate operations in trapped ion qubits where the phononic mode of the harmonic oscillator is used as a mediator [94–96].

[§] The Baker-Campbell-Hausdorff formula states that when $[\hat{x},[\hat{x},\hat{y}]] = [\hat{y},[\hat{x},\hat{y}]] = 0$, the exponential of the sum of the two operators $\hat{x}$ and $\hat{y}$ can be calculated as: $e^{\hat{x}+\hat{y}} = e^{-\frac{1}{2}[\hat{x},\hat{y}]}e^{\hat{x}}e^{\hat{y}} = e^{\frac{1}{2}[\hat{x},\hat{y}]}e^{\hat{y}}e^{\hat{x}}$ [106].

To explore the effect of such nonlinearity, let us apply the four-pulse operator $\hat{\xi}$ to the initial state of the system $|\psi_0\rangle = |\alpha\rangle_{\mathrm{f}} \otimes |\phi(0)\rangle_{\mathrm{m}}$, where the field is in a coherent state $|\alpha\rangle_{\mathrm{f}}$ and the mirror in a generic initial state $|\phi(0)\rangle_{\mathrm{m}}$, and calculate the mean value of the optical field which results

$$\begin{aligned}\langle\hat{a}\rangle &= \langle\psi_0|\,\hat{\xi}^{\dagger}\;\hat{a}\;\hat{\xi}\,|\psi_0\rangle \\ &= \langle\alpha|\,e^{i\lambda^2(2\hat{n}+1)}\hat{a}\,|\alpha\rangle_{\mathrm{f}} \\ &= \alpha\; e^{-N_p(1-\cos 2\lambda^2)}e^{i(\lambda^2+N_p\sin 2\lambda^2)},\end{aligned} \tag{2.7}$$

where $N_p = |\alpha|^2$ is the mean value of the intracavity photon number. We can immediately observe that both modulus and phase of the optical field are changed by the Kerr nonlinear interaction of the Hamiltonian. More specifically, the magnitude of the mean value of $\hat{a}$ is strongly reduced because of the coherent state spreading out in phase-space [‡], while the mean phase shift results to be

$$\varphi_q = (\lambda^2 + N_p \sin 2\lambda^2), \tag{2.8}$$

and provides information on the interaction, because of the dependence from the coupling constant and photon number. Importantly, Eq. (2.8) is independent of the particular initial state of the mechanical mirror, and depends on the intensity of the optical field. These observations are going to play a crucial role in the forthcoming discussions.

In addition, Eqs. (2.5) and (2.7) show that the quantum phase derives from the commutation rules of both field and mirror operators. In particular, it is connected to the commutator between mirror quadratures operators when we calculate the effective interaction (Eq. (2.6)); and to the the bosonic commutation rule for the field annihilation and creation operators when we evaluate the mean value of the optical field (second line Eq. (2.7)). In Ref. [6] it has been proposed that the four-pulse scheme can be employed to probe possible modifications to the standard commutator between $\hat{X}$ and $\hat{P}$, which translate into an additional phase shift in the optical field in Eq. (2.7). It then becomes quite interesting to explore the deviation of the optical phase from a fully classical perspective, to determine to what extent it can be considered as a mean to infer non-classicality in the system dynamics.

From a classical point of view, to calculate the phase acquired by the optical field we need to track the path of the light during the overall dynamics. Following Refs. [107, 108], we know that the phase associated with a single reflection of a field on a movable mirror is proportional

---

[‡] For small coupling this effect scales as $O(e^{-N_p\lambda^4})$

to the product of the field wave vector k_f times the mirror position at that particular time. A radiation-pressure kick, i.e. a pulse that transfers a momentum $\mathcal{I}$ to the mechanical oscillator, can be classically depicted as the sum of N_{rt} round trips of the light inside the cavity. In the pulsed regime, the position of the movable mirror is essentially fixed during the N_{rt} reflections, and, as already discussed, the field enters the cavity, escapes after a time equal to the inverse of the decay rate $1/\kappa$, and then waits in an engineered loop before the successive injection. During the time between consecutive kicks the movable mirror is free to evolve accordingly to the equation of motion of a harmonic oscillator as $x(t) = x(t_0)\cos\omega t + p(t_0)/(M\omega)\sin\omega t$. Without losing generality, we suppose the mirror initially at the origin: at the first kick we have $x(t_0) = 0$, $p(t_0) = \mathcal{I}$, and consequently the position evolves as $x(t) = \mathcal{I}/(M\omega)\sin\omega t$ until the second kick. For every radiation-pressure kick, the field picks up an additional phase due to the movable mirror dynamics. The overall classical phase, acquired by the field escaping the cavity after the four light kicks on the mirror, results

$$\varphi_c = 2\mathrm{k_f}N_{rt}\sum_{j=0}^{3}x(t_j), \tag{2.9}$$

where $x(t_j)$ are the positions of the mirror at times $t_j = j\tau/4$. Solving the equations of motion during this dynamics (the details on this calculation will be provided in the next paragraph where we generalize the present scheme to $\mathcal{N}$ interactions), we obtain for the classical phase

$$\varphi_c = 4\mathrm{k_f}N_{rt}\frac{\mathcal{I}}{M\omega}, \tag{2.10}$$

which linearly depends on the light intensity as described by a classical nonlinear Kerr effect [109, 110]. Also, even the classical phase does not depend on the initial conditions of the mechanical oscillator. Hence, the two features which are at the heart of quantum operations also recur in the classical picture. In order to quantitatively compare Eq. (2.10) with the quantum-mechanical prediction, we firstly substitute the transferred momentum $\mathcal{I} = 2N_{rt}(E_0/c)$, where $E_0 = \hbar\omega_\mathrm{f}N_p$ is the field energy, and then rephrase the result in terms of the characteristic parameters of the optomechanical system. We obtain $\varphi_c = 2\lambda^2 N_p$: the quantum and classical predictions for the optical phase shift generally differ, but for small coupling strengths this difference is in the form of a (small) offset λ^2.

2.3.2 From the pulsed to the continuous interaction: phases and Trotter-Suzuki expansion

By reducing the waiting time between subsequent pulses, we can generalize the previous four-pulse scheme to $\mathcal{N}$ kicks (i.e. $\mathcal{N}$ field-mirror consecutive interactions), where the mechanical oscillator is driven along loops which have the shape of $\mathcal{N}$-sided polygons. For this purpose we need to define a general displacement operator $\hat{\xi}_{\mathcal{N}}$ corresponding to a loop (in the quantum phase space of the oscillator) shaping a regular polygon of $\mathcal{N}$ sides

$$\hat{\xi}_{\mathcal{N}} = \prod_{j=0}^{\mathcal{N}-1} e^{i\hat{\eta}\{\cos(\theta\cdot j)\hat{x}+\sin(\theta\cdot j)\hat{p}\}}, \tag{2.11}$$

where $\theta = 2\pi/\mathcal{N}$. After some tedious algebra, Eq. (2.11) can be calculated by using Baker-Campbell-Hausdorff formula as

$$\begin{aligned} &\hat{\xi}_{\mathcal{N}} = e^{i\hat{\Phi}(\hat{\eta},\mathcal{N})}, \text{ with} \\ &\Phi(\eta,\mathcal{N}) = \frac{1}{4}\eta^2\mathcal{N}\cot\left(\frac{\pi}{\mathcal{N}}\right), \end{aligned} \tag{2.12}$$

where $\Phi(\eta,\mathcal{N})$ (without the hat) is the area mapped out by the sequence of displacement operations of amplitude $\eta = \langle\hat{\eta}\rangle$ in the phase space of the mirror. If we now take the limit $\mathcal{N} \to \infty$ in Eq. (2.11) and, accordingly rescale $\eta \to \eta/\mathcal{N}$, we can define the *continuous displacement*

$$\hat{\xi}_{\text{cont}} = \lim_{\mathcal{N}\to\infty} \hat{\xi}_{\mathcal{N}} = e^{i\frac{\hat{\eta}^2}{4\pi}}, \tag{2.13}$$

which corresponds to a circle in the phase space with radius $\eta/2\pi$. In the case of the optomechanical interaction considered here, we have $\hat{\eta} = \lambda\hat{n}$. Applying the displacement $\hat{\xi}_{\mathcal{N}}$ to the state $|\psi_0\rangle$, we measure the mean value of the optical field as

$$\langle\hat{a}\rangle = \langle\psi_0|\hat{\xi}^{\dagger}_{\mathcal{N}}\hat{a}\,\hat{\xi}_{\mathcal{N}}|\psi_0\rangle = \alpha\, e^{-N_p(1-\cos 2c)}e^{i(c+N_p\sin 2c)}, \tag{2.14}$$

where $c = (\lambda^2/4)\mathcal{N}\cot(\pi/\mathcal{N})$. The first exponential factor represents the change of the amplitude size of the optical field, while the second gives the change of phase in the case of $\mathcal{N}$ kicks:

$$\varphi_q = \frac{\lambda^2}{4}\mathcal{N}\cot\left(\frac{\pi}{\mathcal{N}}\right) + N_p\sin\left[\frac{\lambda^2}{2}\mathcal{N}\cot\left(\frac{\pi}{\mathcal{N}}\right)\right], \tag{2.15}$$

which, when the coupling is small, is approximated as follows:

$$\varphi_q \simeq \frac{\lambda^2}{4}\mathcal{N}\cot\left(\frac{\pi}{\mathcal{N}}\right)(1+2N_p). \tag{2.16}$$

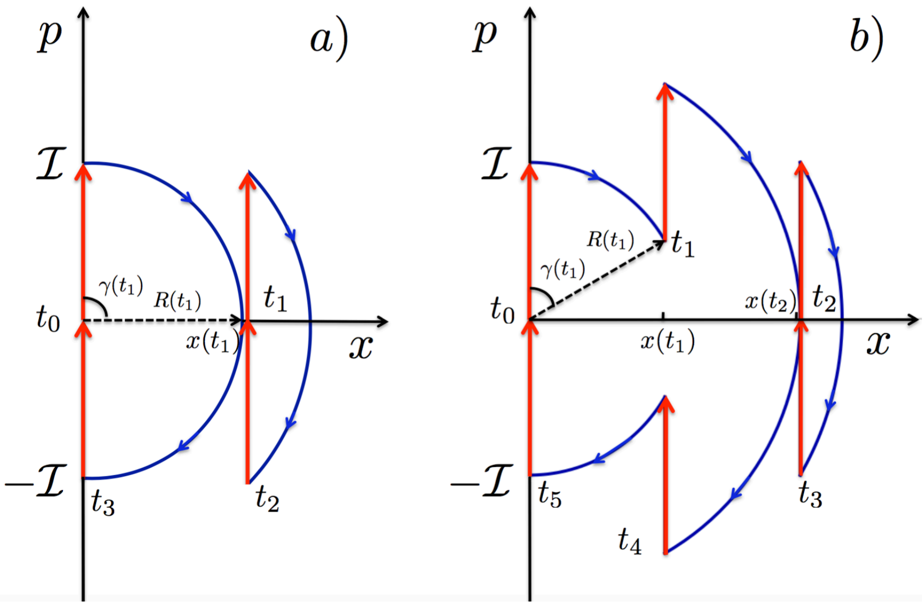

Figure 2.2: Phase space description of the dynamics of the light pulse-mechanical oscillator interaction in the classical picture. a) Four pulse interaction model: the oscillator is assumed at rest at the origin of the phase space. The oscillator gains a momentum $\mathcal{I}$ due to the interaction at $t = t_0$. Then it freely evolves to the maximum amplitude $x(t_1)$ when the second pulse happens, this causes another momentum gain of the oscillator at time t_1. At this time the oscillator evolves to $x(t_2) = x(t_1)$ where the third pulse interaction brings its momentum to zero. Now, it evolves to $x(t_3) = 0$ where its momentum becomes $-\mathcal{I}$. Finally, the oscillator is brought back to the origin of the phase space by the last pulse-oscillator interaction. b) A similar dynamics is plotted for the six pulse interaction.

As for the four-pulse case, the quantum phase does not depend on the initial mirror state. This is a consequence of having driven the mechanical oscillator along closed loops (polygons) in its phase space [30, 31].

We now generalize the pulsed scheme to $\mathcal{N}$ kicks from a classical perspective. Without loosing generality, we again start with the mirror initially at the origin (such that $x(t_0) = 0$, $p(t_0) = \mathcal{I}$ at the first kick), then the position evolves as $x(t) = \mathcal{I}/(M\omega) \sin \omega t$ until the second kick. The additional phase shift acquired by the field escaping the cavity after $\mathcal{N}$ light kicks on the mirror, occurring at times $t_j = 2j\pi/(\mathcal{N}\omega)$, results $\varphi_c = 2\mathrm{k_f} N_{rt} \sum_{i=0}^{\mathcal{N}-1} x(t_i)$, where $x(t_i)$ are the classical positions of the mirror at times t_i. Fig. 2.2 shows the loops in the classical phase space of the harmonic oscillator for four and six kicks. We remark that the generalization to a generic initial condition is straightforward by simply applying a translation in phase space. The positions appearing in φ_c can be computed through geometric considerations, and represented in the classical phase space of the mirror with polar coordinates $(R(t_i), \vartheta(t_i))$. At the first kick we have $R(t_0) = 0$ and $\vartheta(t_0) = 0$ while, for the consecutive kicks, i.e. $i = 1, ..., (\mathcal{N} - 1)$

$$\begin{aligned} R(t_i) &= \sqrt{\zeta^2 + 2R(t_{i-1})\zeta \cos\left(\vartheta(t_{i-1})\right) + R(t_{i-1})^2} \\ \vartheta(t_i) &= \frac{2\pi}{\mathcal{N}} + \arcsin\left[\frac{R(t_{i-1})}{R(t_i)} \sin\left(\vartheta(t_{i-1})\right)\right], \end{aligned} \tag{2.17}$$

where $\zeta = \mathcal{I}/(M\omega)$ quantifies the classical displacement. Since $x(t_i) = R(t_i)\sin(\vartheta(t_i))$, by numerically solving this recurrence, it can be shown that the sum of the oscillator positions gives $(\mathcal{I}/2M\omega)\, \mathcal{N} \cot\left(\pi/\mathcal{N}\right)$, and the classical phase results

$$\varphi_c = \mathrm{k_f} N_{rt} \frac{\mathcal{I}}{M\omega} \mathcal{N} \cot\left(\frac{\pi}{\mathcal{N}}\right). \tag{2.18}$$

In order to compare classical and quantum results, we substitute the expressions previously used for the transferred momentum at each kick and the field energy, and then rephrase the result in terms of the optomechanical parameters. We get

$$\begin{aligned} \varphi_c &= \frac{2\hbar N_{rt}^2 \mathrm{k_f^2} N_p}{M\omega} \mathcal{N} \cot\left(\frac{\pi}{\mathcal{N}}\right) \\ &= \frac{\lambda^2 N_p}{2} \mathcal{N} \cot\left(\frac{\pi}{\mathcal{N}}\right). \end{aligned} \tag{2.19}$$

By comparing Eqs. (2.15) and (2.19) we can see that quantum and classical optical phases generally differ. In fact, the quantum phase in Eq. (2.15) is also valid for strong coupling regimes. Besides, the +1 term in Eq. (2.16) reveals quantum peculiarities connected to the quantization of both field and mechanical oscillator, which cannot be recovered in a fully classical picture. Nevertheless, for the most common experimental conditions, i.e. small coupling ($\lambda \ll 1$) and strong laser sources ($N_p \gg 1$), the quantum and classical phases coincide.

We now want to mathematically derive the description of a continuous interaction from the pulsed one. We firstly note that the rescaled limit $\mathcal{N} \to \infty$ in Eq. (2.11) reminds the Trotter's expansion [111,112] for the total evolution operator $\hat{U} = e^{-i\hat{H}t/\hbar}$. Indeed, by algebraic manipulations we have

$$\begin{aligned} e^{-\frac{i}{\hbar}\hat{H}t} &= \lim_{\mathcal{N}\to\infty} (e^{-\frac{i}{\hbar}\hat{H}_0 t/\mathcal{N}}\, e^{-\frac{i}{\hbar}\hat{H}_{\mathrm{int}} t/\mathcal{N}})^{\mathcal{N}} \\ &= \lim_{\mathcal{N}\to\infty} \prod_{j=0}^{\mathcal{N}-1} (e^{-\frac{i}{\hbar}\hat{H}_0 tj/\mathcal{N}}\, e^{-\frac{i}{\hbar}\hat{H}_{\mathrm{int}} t/\mathcal{N}}\, e^{-\frac{i}{\hbar}\hat{H}_0 tj/\mathcal{N}}) \\ &= \lim_{\mathcal{N}\to\infty} \prod_{j=0}^{\mathcal{N}-1} e^{i\tilde{g}_0 \hat{n}(\hat{X}\cos\theta_j + \hat{P}\sin\theta_j)\frac{t}{\mathcal{N}}}, \end{aligned} \tag{2.20}$$

where $\theta_j = \omega j t/\mathcal{N}$. Considering an interaction lasting τ and bearing in mind that $\kappa = \omega/2\pi$, it follows that $\hat{n}\tilde{g}_0\tau = \hat{n}\lambda = \hat{\eta}$, therefore the displacement operation related to the unitary operator in Eq. (2.20) coincides with the circle loop in Eq. (2.13). We have thus demonstrated that the continuous dynamics can be recovered from the pulsed regime: it is sufficient to keep the light inside the cavity for an interaction time equal to the mechanical frequency in order to implement a displacement $\hat{\xi}_{\text{cont}}$. We however remark that going from the pulsed to the continuous dynamics, which corresponds to take the limit $\mathcal{N} \to \infty$, is not experimentally feasible with the same apparatus: we should be able to continuously switch from the *bad* cavity limit to the *good* one. On the other hand, given that we have established a close link between a continuous displacement operation and the unitary operator of the system, we expect that the correspondence between classical and quantum phases remains valid even in the case of a continuous interaction.

2.3.3 Continuous interaction

As we have seen, the continuous dynamics can be theoretically recovered when we mathematically take the limit $\mathcal{N} \to \infty$ in the pulsed scheme. This corresponds to a physical situation where the light escapes the cavity after a mechanical period. Considering field and mirror initially in the state $|\Psi(0)\rangle = |\alpha\rangle_{\text{f}} \otimes |\gamma\rangle_{\text{m}}$ where $|\gamma = \gamma_R + i\gamma_I\rangle_{\text{m}}$ is a coherent state of the oscillator, we solve the quantum dynamics determined by $\hat{U}$ [30, 31] obtaining the result in Eq. (1.14) where $k = \tilde{g}_0/(\sqrt{2}\omega)$ is the ratio between the single photon optomechanical coupling rate and the mechanical resonance frequency. From Eq. (1.14) we find the total density matrix of the system and then by tracing out the mechanical degrees of freedom, we get the reduced density matrix for the field

$$\begin{aligned}\hat{\rho}_{\text{f}}(t) = e^{-|\alpha|^2} \sum_{m,n} \frac{\alpha^n \alpha^{*m}}{\sqrt{n!m!}} e^{ik^2(n^2-m^2)(\omega t - \sin\omega t)} e^{-k^2(n-m)^2(1-\cos\omega t)} \\ \times e^{i2k(n-m)[\gamma_R \sin\omega t + \gamma_I(1-\cos\omega t)]} |n\rangle_{\text{f}} \langle m| ,\end{aligned} \tag{2.21}$$

from which we can calculate the mean value of the optical field

$$\begin{aligned}\langle \hat{a}(t)\rangle = \text{Tr}[\hat{a}\hat{\rho}_{\text{f}}(t)] = \alpha\, e^{-k^2(1-\cos\omega t)} e^{-N_p\left\{1-\cos\left[2k^2(\omega t-\sin\omega t)\right]\right\}} \\ \times e^{i\left\{2k[\gamma_R \sin\omega t+\gamma_I(1-\cos\omega t)]+k^2(\omega t-\sin\omega t)+N_p \sin\left[2k^2(\omega t-\sin\omega t)\right]\right\}} .\end{aligned} \tag{2.22}$$

As in the case of a pulsed interaction (Eq. (2.7) and (2.14)), both modulus and phase of the field change: the modulus is suppressed by the Kerr nonlinearity of the particular interaction

$\hat{H}_{\mathrm{int}}$, which causes the spreading of the coherent state in phase-space, while the acquired phase

$$\varphi_q(\gamma,t) = 2k\left[\gamma_R \sin\omega t + \gamma_I(1-\cos\omega t)\right] + k^2\left(\omega t - \sin\omega t\right) + N_p \sin\left[2k^2(\omega t - \sin\omega t)\right], \quad (2.23)$$

encodes all the information on the overall dynamics: the initial condition of the mechanical oscillator and the values of coupling constant and number of photons [†].

On the other hand, from a classical perspective, the dynamics might be well-described by the Hamiltonian

$$H_c = \frac{1}{2}M\omega^2 x^2 + \frac{p^2}{2M} - \frac{E_0}{L}x, \quad (2.24)$$

where the continuous interaction is depicted as constant force during the whole evolution whose intensity is given by the field energy. As a result, the classical phase can be accordingly generalized to the integral over the positions of the mirror as $\varphi_c(t) = 2(\mathrm{k_f}/d\tilde{t})\int_0^t x(t')dt'$ with $d\tilde{\tau} = 2L/c$ the single round trip time of the light. By working out the classical continuous dynamics, we obtain the equation of motion

$$x(t) = x(0)\cos\omega t + \frac{p(0)}{M\omega}\sin\omega t + \frac{E_0}{M\omega^2 L}(1-\cos\omega t). \quad (2.25)$$

Therefore, the classical phase at time t in the case of a continuous interaction results to be

$$\varphi_c(x(0),p(0),t) = \frac{\omega_{\mathrm{f}}}{L\omega}\left[x(0)\sin\omega t + \frac{p(0)}{M\omega}(1-\cos\omega t)\right] + \frac{\omega_{\mathrm{f}}}{\omega^3 M L^2}E_0(\omega t - \sin\omega t). \quad (2.26)$$

By using the optomechanical parameters (and $E_0 = \hbar\omega_{\mathrm{f}}N_p$) Eq. (2.26) can be rephrased as

$$\varphi_c(x(0),p(0),t) = k\sqrt{\frac{2M\omega}{\hbar}}\left[x(0)\sin\omega t + \frac{p(0)}{M\omega}(1-\cos\omega t)\right] + 2N_p k^2(\omega t - \sin\omega t), \quad (2.27)$$

which, in the case of a closed loop, gives $\varphi_c = 4\pi k^2 N_p$. Remembering that an initial displaced gaussian quantum state $|\gamma\rangle_{\mathrm{m}}$ corresponds to the classical boundary conditions $x(0) = \sqrt{2}\gamma_R\sqrt{\hbar/(M\omega)}$ and $p(0) = \sqrt{2}\gamma_I\sqrt{\hbar M\omega}$, we observe that the classical and quantum phases in Eq. (2.23) and (2.27) coincide at every time t (for every initial condition) in the limit $\lambda \ll 1$ and $N_p \gg 1$. In the next paragraph we will see that it is because of this equality at every time that we will find the same loss and revival for the classical and quantum visibilities.

In the specific case of a closed loop, the main difference between the classical and quantum predictions for the phase is an offset, which is equal to λ^2 for the four pulse case and depends

---

[†] Note that in the case of a single photon source, the optical phase is actually related to the modulus of the off diagonal terms of the reduced density matrix of the field, which is indeed a measure of coherence [113].

on k^2 for the continuous case. We anticipate that this offset is not predicted within a semi-classical description of the model where either the light or mechanics are quantized and the other is treated classically. Experimentally observing this phase offset would therefore certify the quantum nature of the interaction between light and mirror. This witness could be found by measuring the phase as a function of the photon number per pulse and fitting the obtained data to get an estimate for the offset. Against our intuition, a large optomechanical coupling is not strictly necessary to achieve our goal, as long as the phase can be measured with a high precision. Indeed, uncertainty is mainly amenable to the quantum noise of the coherent state probe, which scales approximately as $\delta\varphi_q \sim 1/\sqrt{N_p N_r}$, where N_r is the number of averages. We thus require $\delta\varphi_q < \lambda^2$ to provide a good estimate for the quantum offset, which can be easily achieved with current experiments ($10^{-5} \lesssim \lambda \lesssim 10^{-1}$ and $N_p \sim 10^8$) [114, 115].

Aside from this small phase shift that demostrates the quantum nature of the interaction, we pinpoint that, in the context of pulsed interactions, the nonlinear phase of the optical field is mainly due to the classical contribution. If the quantum nature of the system is relevant for the interpretation of an experiment, it might be necessary, in order to also verify the non-classical nature of the interaction, to rely on quantum state preparation of the mechanics, to study the non-classical photon statistics after the interaction or to observe the quantum offset discussed above. For example, this is the case for Ref. [6], where the phase acquired by the optical field after four pulsed interactions with the mirror is used to extract quantum information from the system.

2.4 Interferometric visibilities

We have observed that for closed loops in both classical and quantum pictures the phase does not depend on the initial conditions of the mechanical oscillator. Here we are going to see how this property has a non-trivial implication on the quantum-classical comparison.

Let us consider the Michelson interferometer depicted in Fig. 2.3 where the ending mirror of the cavity in arm 1 interacts with an incoming coherent state via the Hamiltonian (2.1). We start with calculating the quantum dynamics in the case of a movable mirror initially prepared in a thermal state $\hat{\rho}_{\text{th}} = (\pi\bar{n})^{-1}\int d^2\gamma\ e^{-|\gamma|^2/\bar{n}}\,|\gamma\rangle_{\text{m}}\langle\gamma|$, where $\bar{n} = 1/(e^{\beta\hbar\omega} - 1)$ is the average thermal occupation number and $\beta = (k_B T)^{-1}$ with k_B the Boltzmann constant and T the initial mirror temperature. We now solve the Liouville equation $\dot{\hat{\rho}} = -(i/\hbar)[\hat{\rho}, \hat{H}]$. The time

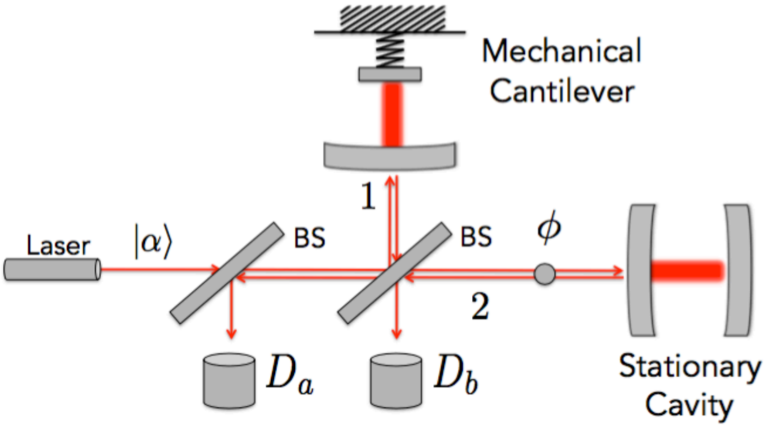

Figure 2.3: Michelson interferometer: a coherent field $|\alpha\rangle_{\rm f}$ is split by a beam splitter (BS) in the two arms of the interferometer. Arm 1 ends with an optomechanical cavity with an end movable oscillator, while arm 2 is composed by a phase shifter and a stationary cavity.

dependent density matrix of the system results

$$\hat{\rho}(t) = e^{-|\alpha|^2}\sum_{m,n}\frac{\alpha^n\alpha^{*m}}{\sqrt{n!m!}}e^{ik^2(n^2-m^2)(\omega t-\sin\omega t)}e^{kn(\gamma\hat{b}^\dagger-\gamma^*\hat{b})}\hat{\rho}_{\rm th}e^{km(\gamma^*\hat{b}-\gamma\hat{b}^\dagger)}\,|n\rangle_{\rm f}\,\langle m|\,, \tag{2.28}$$

from which, by tracing out the mechanical degrees of freedom, we get the reduced density matrix of the field

$$\hat{\rho}_{\rm f}(t) = e^{-|\alpha|^2}\sum_{m,n}\frac{\alpha^n\alpha^{*m}}{\sqrt{n!m!}}e^{ik^2(n^2-m^2)(\omega t-\sin\omega t)}e^{-k^2(n-m)^2(1-\cos\omega t)(2\bar{n}+1)}\,|n\rangle_{\rm f}\,\langle m|\,, \tag{2.29}$$

and, in turn, the mean value of the optical field in the case of an initial thermal mechanical state

$$\begin{aligned}\langle\hat{a}(t)\rangle = \mathrm{Tr}[\hat{a}\hat{\rho}_{\rm f}(t)] &= \alpha\; e^{-k^2(1-\cos\omega t)(2\bar{n}+1)}e^{-N_p\left\{1-\cos\left[2k^2(\omega t-\sin\omega t)\right]\right\}}\\ &\quad\times e^{i\left\{k^2(\omega t-\sin\omega t)+N_p\sin\left[2k^2(\omega t-\sin\omega t)\right]\right\}}.\end{aligned} \tag{2.30}$$

We can note that Eq. (2.30) is exactly the average over all the possible initial configuration given by the thermal distribution of the mean value of the optical field in Eq. (2.22) for an initial coherent state. As we have seen for the Homodyne detection in paragraph 1.2.5, it can be easily shown that the Michelson interferometer represented in Fig. 2.3 corresponds to a measure of the expectation value $\langle\hat{X}_{\rm f}^\phi\rangle = \mathrm{Tr}[\hat{X}_{\rm f}^\phi(t=0)\hat{\rho}_{\rm f}(t)] = \mathrm{Tr}[\hat{X}_{\rm f}^\phi(t)\hat{\rho}_{\rm f}(t=0)]$ for the field quadrature operator in Eq. (1.19), which now reads $\hat{X}_{\rm f}^\phi(t) = (1/\sqrt{2})[\hat{a}(t)e^{-i\phi}+\hat{a}^\dagger(t)e^{i\phi}]$ with $\hat{a}(t)$ in Eq. (2.30) is the time evolution of the field operator entering the cavity at time $t=0$ and escaping it at time t. Therefore, by using Eqs. (1.17) and (1.18), together with (2.30), the

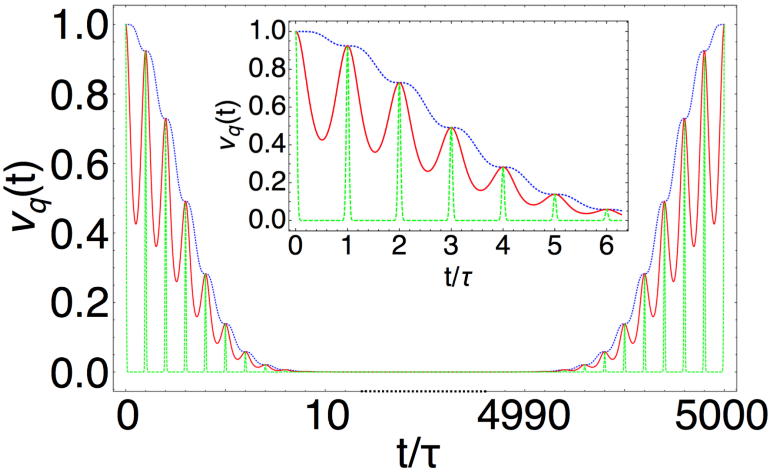

Figure 2.4: Quantum visibility $\nu_q(t)$ in Eq. (2.33) for $T = 10^{-5}$K (blue dotted line), $T = 10^{-2}$K (red continuous line) and $T = 1$ K (green dashed line); optomechanical coupling $k = 10^{-2}$, number of photons $N_p = 10^5$ and period $\tau = 10^{-5}s$. For relatively high temperature the visibility is strongly suppressed within every single oscillating period. Instead, in the low temperature limit, the visibility is slightly lowered and the main effect is due to the Kerr nonlinearity experienced by the field.

two intensities on detectors a and b result

$$\begin{aligned} I^a_b(t) &= \frac{I_0}{2}\left(1 \pm \frac{\langle \hat{X}^\phi_{\rm f} \rangle}{\sqrt{2}}\right) \\ &= \frac{I_0}{2}\{1 \mp e^{-\left\{k^2(1-\cos\omega t)(2\bar{n}+1)+N_p[1-\cos(2k^2(\omega t-\sin\omega t))]\right\}} \\ &\qquad \times \cos[k^2(\omega t-\sin\omega t) - N_p\sin(2k^2(\omega t-\sin\omega t)) - \phi]\}. \end{aligned} \tag{2.31}$$

We are now interested in evaluating the interference visibility, which is defined as the ratio

$$\nu = \frac{I_{\rm max} - I_{\rm min}}{I_{\rm max} + I_{\rm min}}, \tag{2.32}$$

where $I_{\rm max}$ and $I_{\rm min}$ are the maximum and minimum intensities on the detectors. By using Eq. (2.31), the quantum prediction for the visibility can be written conveniently as $\nu_q(t) = \nu_q^{\rm cor}(t)\nu_q^{\rm Kerr}(t)$, where

$$\begin{aligned} \nu_q^{\rm cor}(t) &= e^{-k^2(1-\cos\omega t)(2\bar{n}+1)}, \\ \nu_q^{\rm Kerr}(t) &= e^{-N_p[1-\cos(2k^2(\omega t-\sin\omega t))]}. \end{aligned} \tag{2.33}$$

In Fig. 2.4 we plot the time-dependent dynamics of the quantum visibility $\nu_q(t)$. We can see that it results the composition of two periodic functions (with distinct frequencies), which cause two different set of revivals: the short ones of period τ due to the term $\nu_q^{\mathrm{cor}}(t)$, while the long ones of period $\tau' = \tau/(2k^2)$ related to $\nu_q^{\mathrm{Kerr}}(t)$. The former revivals of the visibility occur because of the decoupling between field and mirror at integer multiples of the mechanical period, that is when we drive the oscillator along closed loops in its phase space. In fact, they are considered as a proof of correlations at intermediate times, that is when field and mirror are in an entangled state, as it can be seen from the expression for the state of the system in Eq. (1.14). These revivals are clearly manifested in Fig. 2.4. On the other hand, the term $\nu_q^{\mathrm{Kerr}}(t)$ coincides with the second exponential term in Eq. (2.30), which is responsible of the suppression of the modulus of the mean optical field, and it is then originated by the nonlinear Kerr interaction experienced by the field when entering into the cavity because of Hamiltonian (2.1). This contribution to the quantum visibility is responsible for a reduction of the interferometric pattern. In other words, this reduction of visibility stems from the squeezing of the coherent optical state due to the Kerr nonlinearity. As a result, even if mirror and field are completely uncorrelated after an interaction that lasts a mechanical period, we still cannot fully recover visibility.

Now that we have explored the quantum prediction for the interferometric visibility, we would like to explore its classical counterpart. We already anticipate that even within a fully classical treatment we can explain a recovery of the visibility at some specific times. Let us then consider a classical mirror that at time $t = 0$ is subjected to classical thermal fluctuations around the origin described by a Maxwell-Boltzmann distribution. This is the analogue of the initial thermal state considered quantum-mechanically. The initial position and momentum of the oscillator can be parameterized by using polar coordinates (θ, ϱ) as follows

$$\begin{aligned} x(t=0,\ \theta,T) &= \sqrt{2/(M\omega^2)}\varrho(T)\cos\theta, \\ p(t=0,\ \theta,T) &= \sqrt{2M}\varrho(T)\sin\theta, \\ \varrho^2(T) &= \frac{M\omega^2}{2}x^2(0,\theta,T) + \frac{p^2(0,\theta,T)}{2M}, \end{aligned} \tag{2.34}$$

where $\varrho^2(T)$ is the initial thermal energy of the oscillator at temperature T. Consequently, the classical phase acquired by the field after an interaction time t in Eq. (2.26) will depend on these initial conditions:

$$\varphi_c(\varrho,\theta,t) = \sqrt{2}\chi\varrho\left[\cos\theta\sin\omega t + \sin\theta(1-\cos\omega t)\right] + \frac{\omega}{\omega_{\mathrm{f}}}\chi^2 E_0\left(\omega t - \sin\omega t\right), \tag{2.35}$$

where $\chi = \omega_{\mathrm{f}}/(\omega^2 L\sqrt{M})$. Indicating with I_0 the intensity of the incoming field, the classical intensities on the detectors D_a and D_b depend on the phase difference between the two arms as

$$I_b^a(\varrho,\theta,t)=\frac{I_0}{2}[1\pm\cos(\varphi_c(\varrho,\theta,t)-\phi)]. \tag{2.36}$$

If we now average over all the initial mechanical states given by the thermal distribution, we obtain the final result for the intensities

$$\begin{aligned}\langle I_b^a(t)\rangle&=\frac{\beta}{\pi}\iint\varrho\,d\varrho\,d\theta\,I_b^a(\varrho,\theta,t)\,e^{-\beta\varrho^2}\\&=\frac{I_0}{2}\left[1\pm e^{-\frac{\chi^2}{\beta}(1-\cos\omega t)}\cos\left(\frac{\omega}{\omega_{\mathrm{f}}}E_0\chi^2(\omega t-\sin\omega t)-\phi\right)\right],\end{aligned} \tag{2.37}$$

which gives the classical visibility

$$\nu_c(t)=e^{-\frac{\chi^2}{\beta}(1-\cos\omega t)}. \tag{2.38}$$

Equation (2.38) reveals fully classical revivals at times equal to integer multiples of the mechanical oscillator, i.e. $t=j\tau$ with $j=1,2\ldots$. The reason why we have these revivals even in a classical picture can be traced back to the particular property of the phase acquired by the field, which still holds in the classical scenario: its independence from the initial mirror conditions after periods of the mechanical oscillator. Indeed, the loss of classical visibility has to be attributed to the uncertainty on the initial conditions due to the initial thermal fluctuations of the mirror, which appear in the same form both classically and quantum-mechanically. For times equal to integer multiples of the mechanical period, even the classical phase does not depend on the initial conditions of the oscillator, and the maximum value of visibility is recovered. We however highlight that, in the case of zero temperature, the classical visibility will result equal to one at all times.

We now want to compare the quantum result $\nu_q(t)$ with the fully classical one in Eq. (2.38). By manipulating the optomechanical parameters we find $k=\chi\sqrt{\hbar\omega/2}$, and, as a result, the classical visibility can be rewritten as

$$\nu_c(t)=e^{-\frac{2k^2}{\beta\hbar\omega}(1-\cos\omega t)}. \tag{2.39}$$

The first observation we can make is that, in the limit $k_BT\gg\hbar\omega$, the quantum thermal part of the visibility $\nu_q^{\mathrm{cor}}(t)$ approaches the classical expression. However, the difference between ν_q^{cor}, which comes from mirror-field correlations, and the classical visibility is insignificant even when the temperature is very low. For example, when $T=10^{-6}$K and $\omega=2\pi\times10^5$Hz we have $|\nu_q^{\mathrm{cor}}-\nu_c|\leq|e^{-2k^2}-1|\sim0.01$, even pushing the coupling to $k=0.1$. Differences appear when further increasing the coupling strength: the parameter k is thus crucial to get access to the

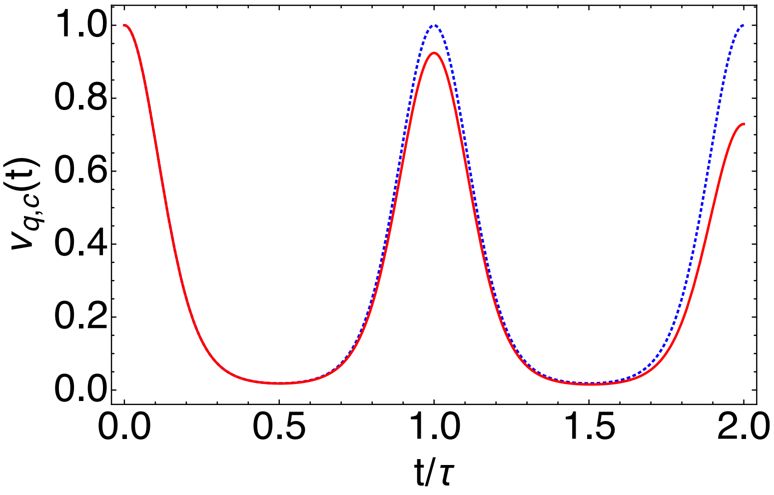

Figure 2.5: Comparison between quantum (red continuous line) and classical (blue dotted line) visibilities in Eqs. (2.33) and (2.38) for $T = 5 \times 10^{-2}$K. All the other parameters are as in Fig. 2.4.

quantum behavior in these setups, as also stressed in Refs. [20, 116]. We also note that within a hybrid framework where light is treated quantum-mechanically and the mechanics classically and in case of a single photon source, a similar result was found in Ref. [117].

Apart from identifying parallelisms between the classical and quantum results, our analysis naturally identifies quantum peculiarities, specifically in ν_q^{Kerr}. This additional term in the quantum result is due to the quantum-mechanical description of the Kerr nonlinear interaction. In fact, as Fig. 2.5 clearly shows, unlike the classic result, where a complete revival occurs after every mechanical period τ, the quantum Kerr nonlinearity lowers the visibility giving rise to a partial revival.

Since coherent states are minimum uncertainty states having the same uncertainty associated with each quadrature, the noise in a coherent state has an intrinsic quantum origin [106]. Nevertheless, we can bring our classical model closer to the quantum scenario. To this scope, we assume that our classical coherent field is affected by a Gaussian noise [110] such that the field energy in the (classical) Hamiltonian H_c can be written as $E(\epsilon) = E_0(1-\epsilon)$ where the dimensionless parameter ϵ is described by the normal distribution

$$\mathcal{P}(\epsilon) = \frac{1}{\sqrt{2\pi}\Delta} e^{-\frac{\epsilon^2}{2\Delta^2}}, \tag{2.40}$$

with Δ^2 the variance. The classical phase in Eq. (2.35) and, in turn, the intensities in Eq. (2.37) will now depend on the noise parameter ϵ. Equation (2.37) can be then averaged over the gaussian distribution (2.40), obtaining

$$
\begin{aligned}
\langle I_b^a(t)\rangle = \frac{I_0}{2}\Bigg\{ 1 \pm e^{-\frac{\chi^2}{\beta}(1-\cos\omega t)} e^{-\frac{\omega^2}{\omega_{\mathrm{f}}^2}\chi^4 E_0^2 \Delta^2 (\omega t - \sin\omega t)^2} \\
\times \Bigg[\cos\left(\frac{\omega}{\omega_{\mathrm{f}}} E_0 \chi^2 (\omega t - \sin\omega t) - \phi\right) \\
- \frac{\omega}{\omega_{\mathrm{f}}}\chi^2 E_0 \Delta^2 (\omega t - \sin\omega t) \sin\left(\frac{\omega}{\omega_{\mathrm{f}}} E_0 \chi^2 (\omega t - \sin\omega t) - \phi\right) \Bigg] \Bigg\}.
\end{aligned}
\tag{2.41}
$$

By selecting $\phi = \frac{\omega}{\omega_{\mathrm{f}}} E_0 \chi^2 (\omega t - \sin\omega t)$ through the phase shifter of the interferometer (see Fig. 2.3), the expression of intensity can be simplified, and the new classical visibility results

$$
\tilde{\nu}_c(t) = e^{-\frac{\chi^2}{\beta}(1-\cos\omega t)} e^{-\frac{\omega^2}{\omega_{\mathrm{f}}^2}\chi^4 E_0^2 \Delta^2 (\omega t - \sin\omega t)^2}. \tag{2.42}
$$

Contrarily to the classical result obtained in Eq. (2.39), the classical visibility in Eq. (2.42) now shows a loss due to the second exponential, which is due to the the (classical) Kerr-nonlinearity experienced by the noisy field. By rephrasing Eq. (2.42) in terms of the optomechanical parameters, and using $\chi = \sqrt{2/\hbar\omega}k$ and $E_0 = \hbar\omega_{\mathrm{f}} N_p$,

$$
\tilde{\nu}_c(t) = e^{-\frac{2k^2}{\beta\hbar\omega}(1-\cos\omega t)} e^{-2N_p^2 k^4 \Delta^2 (\omega t - \sin\omega t)^2}. \tag{2.43}
$$

We can now note that the field energy distribution $E(\epsilon) = E_0(1-\epsilon)$ is equivalent to the photon distribution $N(\epsilon) = N_p(1-\epsilon)$ which has variance $N_p^2\Delta^2$. Therefore, to make our classical result even closer to the quantum prediction, we consider a Poissonian distribution of the noise and set $\Delta^2 = 1/N_p$, obtaining

$$
\begin{aligned}
\tilde{\nu}_c(t) &= e^{-\frac{2k^2}{\beta\hbar\omega}(1-\cos\omega t)} e^{-2N_p k^4 (\omega t - \sin\omega t)^2} \\
&= \nu_c(t) e^{-2k^4 N_p (\omega t - \sin\omega t)^2}.
\end{aligned}
\tag{2.44}
$$

This result clearly shows that the introduction of a classical noise permits to exploit the classical Kerr-nonlinearity of the phase (encoded in Eq. (2.10) as previously discussed) to recover a reduction in the classical visibility, which exactly coincides with the quantum result ν_q^{Kerr} in Eq. (2.33) in the limit $k^2\omega t \ll 1$ and of large intensities. However, while ν_q^{Kerr} is periodic so to cause revivals, the classical Kerr nonlinearity in Eq. (2.44) only lowers the visibility. This comparison further highlights the great importance of the parameter k to regulate the quantum behavior in optomechanical systems. It is worth mentioning that having taken the mirror initially at its rest position does not affect the generality of our result in Eq. (2.43): the interference in Eq. (2.41) can always be obtained by adapting the phase shifter ϕ to cancel out the extra initial contribution coming from Eq. (2.26).

Quantum and classical visibilities show qualitatively the same behavior and to observe significant deviations in current optomechanical experiments, i.e $|\nu_q - \nu_c| \gtrsim 10^{-4}$ within a mechanical period, we should increase the coupling constant or the number of intracavity photons to $k \gtrsim 10^{-3}$ and $N_p \gtrsim 10^6$, respectively (keeping fixed all the other parameters as in Fig. 2.5). This is valid independently of the initial temperature of the mechanical oscillator. Moreover, we should note that, while ν_q tends to ν_c in the limit $k^2 N_p \ll \bar{n}$ and $k_B T \gg \hbar\omega$, in the same limit, the classical visibility and its quantum counterpart (for an initial coherent state for the field) coincide with the quantum visibility for a single photon as input, as obtained in Refs. [20, 116]. Importantly, this makes clear that just looking at the visibility patter is not sufficient to extrapolate non-classicality in the system dynamics. To truly interpret the results within a quantum framework it becomes essential to rely on additional assumptions. For example, in Refs. [20, 116], where the cause of the collapse of visibility is referred to the entanglement between oscillator and field, one has to rely on the initial state preparation of the field (single photon source) and the mechanical oscillator (ground state). On the other hand, form a classical perspective, in the case of zero effective temperature, the visibility is always one without a collapse. However, we have seen that any small initial thermal noise in the mechanics causes a reduction of the visibility. Therefore, an unequivocal proof of quantumness might require additional measurements, for example the verification of the entanglement between field and mechanics.

2.5 Semiclassical approach

Here we want to explore what happens when we use a semiclassical approach to describe the interaction between light and mechanical oscillator. We anticipate that a semiclassical description of such interaction will produce the results obtained within the full classical framework, therefore, even a semiclassical description is insufficient to describe all features of the full interaction.

Firstly, let us consider the case of a quantum field and a classical mechanical oscillator. In a frame rotating with the field frequency, the interaction Hamiltonian can be written as $\hat{H}_{\mathrm{f}} = \epsilon \hat{a}^\dagger \hat{a} x(t)$ where $x(t)$ indicated the classical equation of motion of the oscillator, while ϵ the resulting coupling constant. Taking the field initially prepared in a coherent state, the field density matrix results

$$\hat{\rho}_{\mathrm{f}}(t) = e^{-|\alpha|^2} \sum_{n,m} \frac{\alpha^n \alpha^{*m}}{\sqrt{n!m!}} e^{-\frac{i}{\hbar}\epsilon(n-m)\int_0^t x(\tau)d\tau} |n\rangle_{\mathrm{f}}\langle m| \tag{2.45}$$

and, as a result, the mean value of the optical field, which provides the acquired optical phase, is

$$\langle \hat{a} \rangle = \alpha e^{-\frac{i}{\hbar}\epsilon \int_0^t x(\tau)d\tau}. \tag{2.46}$$

If we now describe the classical oscillating mirror as a harmonic oscillator subjected to a constant force E_0/L as in Eq. (2.24), we can safely substitute the dynamics in Eq. (2.25) into Eq. (2.46) obtaining

$$\langle \hat{a} \rangle = \alpha e^{-i\varphi(t)}, \tag{2.47}$$

where the phase $\varphi(t)$ coincides with the classical phase given in Eq. (2.26). Equation (2.47) thus shows that when we consider a quantum field and a classical oscillator, the full classical result for the phase is recovered.

Secondly, we consider the inverse situation where the field is described classically and the mirror quantum-mechanically. In this case, the phase acquired by the optical field can be written as

$$\varphi(t) = 2\frac{\mathrm{k_f}}{d\tilde{\tau}} \int_0^t \langle \hat{x}(\tau) \rangle d\tau, \tag{2.48}$$

that is the integral over the interaction time of the mean value of the mechanical position. If we assume the mirror initially prepared in a coherent state $|\tilde{\Psi}(0)\rangle = |\gamma_R + i\gamma_I\rangle$, its evolution under the quantum hamiltonian $\hat{H}_{\mathrm{m}} = \hbar\omega\hat{b}^\dagger\hat{b} - (E_0/L)\sqrt{\hbar/(2M\omega)}(\hat{b}^\dagger + \hat{b})$ reads

$$|\tilde{\Psi}(t)\rangle = e^{ik^2N_p^2(\omega t - \sin\omega t)} e^{i2kN_p[\gamma_I(1-\cos\omega t)+\gamma_R \sin\omega t]} |\gamma e^{-i\omega t} + kN_p(1-e^{-i\omega t})\rangle, \tag{2.49}$$

where we have used $kN_p = E_0/(L\omega\sqrt{2\hbar M\omega})$ to express the result in terms of the characteristic optomechanical parameters. Easily, one can verify that the mean value of the position operator over the state (2.49) gives the results we obtain within a fully quantum and/or classical description of the interaction. As a consequence, the phase acquired by the optical field given in Eq. (2.48) coincides with the classical result showed in Eq. (2.27). Once again, a semiclassical description of optomechanical interaction for the optical phase shift returns the same result obtained in the case of a fully classical picture. We can thus conclude that a semiclassical approach (as the classical one) is not able to capture all the feature given by a full quantum interaction. Similar considerations can be extended to the visibility, since the visibility is strictly connected to the phase.

2.6 Conclusions

Central to a variety of optomechanical schemes is the ability to change and read-out the phase of a system by exploiting the particular nonlinear light-matter interaction. This natural advantage of the system has also been used to investigate fundamental questions of quantum mechanics. In this Chapter, we have explored the non-classicality of such phases by comparing the quantum predictions to the ones obtained within a fully classical description of the system dynamics. This has allowed us to transparently analyze the classical and quantum nature of the phase acquired by an optical field during the nonlinear light-matter interaction. We have found that some of the key features, which have been assumed to have a quantum origin in recent proposals, also occur in classical physics; in particular: the Kerr nonlinearity of the interaction induced by the mechanical oscillator and the complete decoupling of light and mechanics at specific interactions times. Moreover, the results on the classical phase have further allowed us to extend the classical-quantum comparison to the interferometric visibility, which, on the other hand, has been always used as a witness to probe the quantum signature of the system dynamics. Our approach to tackle the classical-quantum comparison has revealed that in the common (and also current) optomechanical experimental regimes, i.e. large photon numbers and small coupling constants, classical and quantum descriptions essentially coincide. However, we have also been able to isolate genuine quantum signatures of the optomechanical interaction, which appear in the dynamics of both phase and visibility. We have argued how these quantum trademarks could be probed in future optomechanical setups, without necessarily requiring a strong coupling regime.

Chapter 3

Probing anharmonicity of a mechanical oscillator

3.1 Introduction

As we have discussed in Chapter 1, the ability to control and probe the motion of a massive mechanical object, which can be a moving mirror [24,118], a cavity membrane [13], or a levitated nanosphere [119–121], has increased in the last years. This combined to the possibility to access very low temperatures has allowed to exploit the quantum features of these systems in a variety of contexts [2]. On this route, optomechanical systems seem to be a natural test bench to address many fundamental questions. For example, it has been proposed that they might be used to probe collapse models of quantum mechanics [122, 123], and even to explore the interface between quantum mechanics and gravity at low energies [6, 124]. In particular, by pushing our ability to build more sensitive experiments, it has been suggested that a table-top quantum optics experiment with a standard optomechanical cavity might be able to test deformations induced by gravity to the standard quantum commutators [6]. At the heart of these challenging proposals, one can find the widely used and probably principal advantage of cavity optomechanics: the high-precision readout of the mechanical motion via the light field reflected from the cavity [2].

In all the above mentioned cases, the motion of the mechanical oscillator has been considered harmonic. However, when one is interested in studying how to probe possible modifications in the dynamics of the mechanical mirror due to exotic effects (one example might be represented by different commutation rules), it becomes very important to verify whether there could be other kinds of modifications due to intrinsic properties of the oscillator. In fact, both the two kinds of modifications (intrinsic and exotic) are often translated into mechanical nonlinearities. Therefore, even though these nonlinearities might be very different in nature, they could, in principle, give rise to similar effects, and it could be experimentally hard to understand their origin.

On the other hand, anharmonicity gives rise to new interesting features on its own. Milburn and Holmes by studying the properties of the quantum and classical dynamics for an anharmonic oscillator have been able to demonstrate a decoherence reduction in the quantum-to-classical-transition [125]. Also, it is a common believe that, in general, anharmonicities might provide an important resource to generate non-classical quantum states [126–128]. In the same spirit, the problem of how to quantify the nonlinearity of a quantum oscillator has been recently addressed [129]. Moreover, nonlinearities in the mechanical motion have been recently accessed in many different physical platforms, which range from standard mechanical resonators [130] and cantilivers based on graphene and carbon nanotubes (see [131, 132] and references therein) to levitated nanospheres [133, 134], where the thermal energy has been proven to be sufficient to reach such regime.

All this suggests that it would be very useful to design an experimentally feasible protocol able to provide a measure for the mechanical anharmonicity. In this Chapter, we study how we can probe the anharmonicity of the mechanical oscillator in an optomechanical cavity. We show that by measuring the phase shift acquired by the field after its multiple interactions with the anharmonic oscillator, one gets access to all the fundamental parameters of the system and, in particular, to the anharmonic constant. Only requiring an easily achievable initial mechanical cooling, we find the protocol robust versus possible losses, and we provide the ultimate quantum bounds on the achievable precision. We then compare such ultimate bounds with the ones obtained via feasible experimental phase-measurements like homodyne and heterodyne detections.

The Chapter is organized as follows: in Sec. 3.2 we analyse the model of the optomechanical cavity and recall the useful and more specific principles of pulsed-optomechanics underlined in Chapter 1 (paragraph 1.2.4). In Sec. 3.3 we calculate the unitary operator which describes an effective anharmonic interaction between field and oscillator. This net nonlinear operation, which under some assumptions acts only on the field mode, naively corresponds to a sequence of displacement operations on the mechanical state. Indeed, the oscillator results to be driven along a closed path in its phase space. We thus explore the effect of such a nonlinear dynamics on the phase acquired by the optical field. Moreover, in Sec. 3.4, by using the basic tools of quantum estimation theory described in 1.2.6, we explore the performance of our protocol. In Sec. 3.5 following the same procedure we reproduce all the previous results for a cubic mechanical anharmonicity, and argue how we can in principle discriminate it from the quartic one. To address the robustness of our protocol we then study the effect of possible losses in the system in Sec. 3.6. Finally, Sec. 3.7 summarizes our findings and conclusive remarks.

3.2 The model

Let us now consider again the optomechanical cavity described in paragraph 1.2.3, which is now formed by a quantum anharmonic oscillator coupled to the single mode optical field. The effective Hamiltonian obtained in Eq. (1.11) can thus be rewritten as $H = H_0 + H_{\mathrm{int}}$, where, in a frame rotating with the optical field, H_{int} is the interaction Hamiltonian given in Eq. (2.2), while the free Hamiltonian of the mechanical oscillator is now

$$H_0 = \frac{1}{2}\hbar\omega_0 \left(X^2 + P^2\right) + \frac{\gamma}{4}\hbar\omega_0 X^4, \tag{3.1}$$

with X and P defined as in Eq. (2.3), and $\gamma \ll 1$ the quartic anharmonic parameter.
We again investigate the system dynamics in the pulsed regime, where, as we have previously discussed in paragraph 1.2.4, the interaction time between field and oscillator is much faster than the mechanical motion: the mirror position is practically fixed during each interaction. Within this regime, it is possible to neglect the free evolution of the mechanics and the evolution operator of the system is given by Eq. (2.4). When the light is out of the cavity, the oscillator can evolve accordingly to H_0, conversely, it can be driven along closed paths in phase space by engineering the times between subsequent light-pulse interactions. We indeed imagine that a light pulse can enter the cavity, leave it after a certain time and then wait in a fiber-loop before its next injection into the cavity, as depicted in Fig. 3.1.

3.3 The estimation scheme

Now we utilise the scheme with four pulsed interactions as described in paragraph (2.3.1) to drive the mechanical oscillator along a loop in its phase space, where each pulse represents a

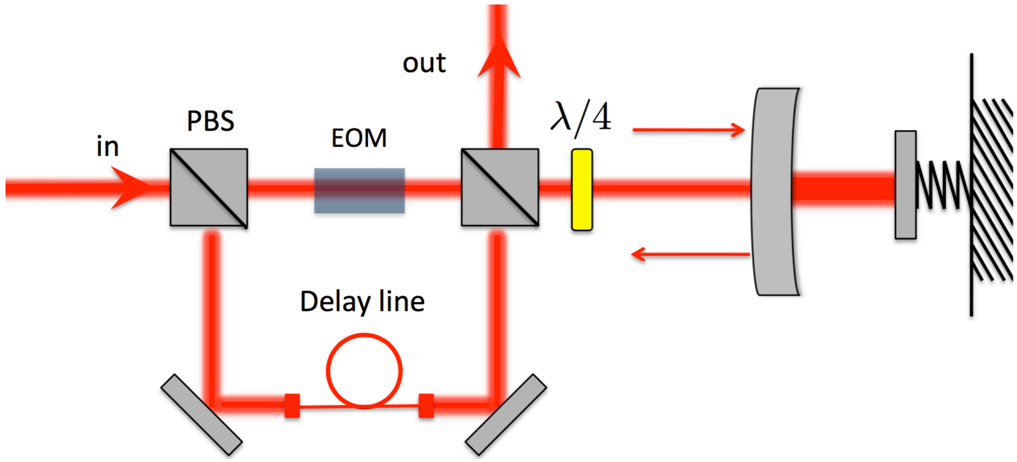

Figure 3.1: Representation of the model. A laser pulse enters an optomechanical cavity and then escapes going into a delay loop for an engineered time. In order to rotate the polarization of the light before and after a pulse, we require polarizing beam splitters (PBSs), a $\lambda/4$ wave plate and an Electro-optic Modulator (EOM). Immediately after the last interaction the EOM does not rotate the polarization anymore and the light pulses are free to leave the optomechanical cavity.

field-oscillator interaction described by U. The resulting operation is modelled as

$$U_{\text{anh}} = e^{i\lambda n X(\frac{3\tau}{4})} e^{i\lambda n X(\frac{\tau}{2})} e^{i\lambda n X(\frac{\tau}{4})} e^{i\lambda n X}, \tag{3.2}$$

where $\tau = 2\pi/\omega$ is now the mechanical period of the quantum anharmonic oscillator and $X(t) = (1/\sqrt{2})(b^{\dagger}(t) + b(t))$. In order to calculate the operation in Eq. (3.2), we need to obtain the evolution for the mechanical operators. By using the method of successive approximation where the frequency shift due to the anharmonic potential is taken into account in accordance with similar standard procedures in classical mechanics [135, 136], we get at the first order in γ

$$b(t) \simeq b e^{-i\omega t} + \frac{\gamma}{4}\left[\left(e^{-i\omega t} - e^{+3i\omega t}\right)\frac{b^{\dagger 3}}{4} + \left(e^{-3i\omega t} - e^{-i\omega t}\right)\frac{b^{3}}{2} + \left(e^{-i\omega t} - e^{i\omega t}\right)\frac{3}{2} b^{\dagger}\left(1 + b^{\dagger} b\right)\right], \tag{3.3}$$

where the operators without an explicit time-dependence must be considered at $t = 0$, and

$$\omega = \omega_0 + \frac{3}{8}\gamma\omega_0\,(2 + |A|^2), \tag{3.4}$$

is the new frequency of the anharmonic oscillator, with $|A|$ the initial amplitude of the unperturbed harmonic oscillator. It is worth mentioning that to be consistent with our perturbation approach, the condition $\gamma|A|^2 \ll 1$ must be satisfied. Now, from Eq. (3.3) it is easy to calculate the quadrature operators at times the $t = 0, \tau/4, \tau/2, 3\tau/4, \tau$:

$$
\begin{aligned}
X(0) &= X, \\
X\left(\frac{\tau}{4}\right) &\simeq P + i\frac{\gamma}{4\sqrt{2}}(b^3 - b^{\dagger 3} - 3b^\dagger + 3b - 3b^{\dagger 2}b + 3b^\dagger b^2), \\
X\left(\frac{\tau}{2}\right) &\simeq -X, \\
X\left(\frac{3\tau}{4}\right) &\simeq -P - i\frac{\gamma}{4\sqrt{2}}(b^3 - b^{\dagger 3} - 3b^\dagger + 3b - 3b^{\dagger 2}b + 3b^\dagger b^2), \\
X(\tau) &\simeq X.
\end{aligned}
\tag{3.5}
$$

As can been noted from Eq. (3.5), after a period the oscillator is again at its initial position at the first order in γ. This will be a crucial point in our scheme since only at this time (or integer multiples) field and mirror become disentangled. We can also note that to close the loop, we should know the mechanical frequency and, therefore, the anharmonic constant, which is actually the parameter that we would like to estimate with our protocol. However, this fact does not represent an important issue, besides a very common situation in estimation theory easily bypassed by using subsequent adaptive measurements [137–139]. Nevertheless, our final goal is to find the anharmonic constant by measuring the phase of the field after multiple light-mirror interactions in an interferometric scheme (via homodyne or heterodyne detection), and one can thus verify the closure of the path by checking the revival of the visibility dynamics explored in the previous Chapter. We already anticipate that, in the case of a cubic anharmonicity, the mechanical frequency is not modified, and we do not need to require subsequent measurements. This fact might be also used to distinguish the two different anharmonicities.

By tracing over the mechanical degrees of freedom, we would like to compute the dynamics of the cavity field given by the completely-positive map

$$
\mathcal{E}(\varrho_{\mathrm{f}}) = \mathrm{Tr}_{\mathrm{m}}[U_{\mathrm{anh}}\varrho_{\mathrm{f}} \otimes \varsigma\, U^\dagger_{\mathrm{anh}}],
\tag{3.6}
$$

where ϱ_f (ς) is the initial density matrix of the field (oscillator). We consider the case in which the state of the mechanics is diagonal in the Fock basis: $\varsigma = \sum_n \varsigma_n |n\rangle\langle n|$, this includes thermal states. By substituting the quadratures operators in Eq. (3.5) into the operator in Eq. (3.2), after lengthy algebra, we have

$$
U_{\mathrm{anh}} \simeq e^{i\lambda n(-P - i\frac{\gamma}{4\sqrt{2}}\Delta)} e^{-i\lambda n X} e^{i\lambda n(P + i\frac{\gamma}{4\sqrt{2}}\Delta)} e^{i\lambda n X},
\tag{3.7}
$$

where for convenience we have defined

$$
\Delta = b^3 - b^{\dagger 3} - 3b^\dagger + 3b - 3b^{\dagger 2}b + 3b^\dagger b^2
\tag{3.8}
$$

the correction induced by the anharmonic dynamics. As a starting point, the operator in Eq. (3.7) can be analytically computed by using Zassenhaus formula [§] on the first and third exponential. More specifically, at the first order in γ, we get

$$
\begin{aligned}
e^{i\lambda n(-P-i\frac{\gamma}{4\sqrt{2}}\Delta)} &= e^{-i\lambda nP}e^{\frac{1}{4\sqrt{2}}\lambda n\Delta}e^{-\frac{3}{8}\gamma\lambda^2n^2(b^{\dagger 2}-b^2)}e^{i\frac{\gamma}{4}\lambda^3n^3P} \\
&\simeq e^{-i\lambda nP}e^{\frac{\gamma}{4\sqrt{2}}f_1(b,b^\dagger)}, \\
e^{i\lambda n(P+i\frac{\gamma}{4\sqrt{2}}\Delta)} &= e^{i\lambda nP}e^{-\frac{1}{4\sqrt{2}}\lambda n\Delta}e^{-\frac{3}{8}\gamma\lambda^2n^2(b^{\dagger 2}-b^2)}e^{-i\frac{\gamma}{4}\lambda^3n^3P} \\
&\simeq e^{i\lambda nP}e^{\frac{\gamma}{4\sqrt{2}}f_2(b,b^\dagger)},
\end{aligned}
\tag{3.9}
$$

where we have defined

$$
\begin{aligned}
f_1(b,b^\dagger) &= \lambda n\Delta - \frac{3}{\sqrt{2}}\lambda^2n^2(b^{\dagger 2}-b^2) + \sqrt{2}i\lambda^3n^3P, \\
f_2(b,b^\dagger) &= -\lambda n\Delta - \frac{3}{\sqrt{2}}\lambda^2n^2(b^{\dagger 2}-b^2) - \sqrt{2}i\lambda^3n^3P.
\end{aligned}
\tag{3.10}
$$

Then we can switch the last factors in Eq. (3.9) respectively to the left and right by using again the Zassenhaus expansion obtaining

$$
U_{\text{anh}} \simeq \left(1+\frac{\gamma}{4\sqrt{2}}F_1(b,b^\dagger)\right)e^{i\lambda^2n^2}\left(1+\frac{\gamma}{4\sqrt{2}}F_2(b,b^\dagger)\right), \tag{3.11}
$$

where

$$
\begin{aligned}
F_1(b,b^\dagger) &= -2\sqrt{2}i\lambda^4n^4 + \sqrt{2}i\lambda^3n^3(3X-4P) + 3\sqrt{2}\lambda^2n^2\left[\frac{b^2-b^{\dagger 2}}{2} - i(1-2b^\dagger b)\right] \\
&\quad + \lambda n[b^{\dagger 3} - b^3 + 3(b^{\dagger 2}b - b^\dagger b^2) - 3\sqrt{2}iP], \\
F_2(b,b^\dagger) &= -4\sqrt{2}i\lambda^3n^3P + \frac{3\sqrt{2}}{2}\lambda^2n^2\left(b^{\dagger 2}-b^2\right) + \lambda n[b^3 - b^{\dagger 3} - 3(b^{\dagger 2}b - b^\dagger b^2) + 3\sqrt{2}iP]
\end{aligned}
\tag{3.12}
$$

are the two resulting functions which correspond to $f_{1(2)}$ after having performed the above operation. Since we are interested in a correction at the first order in γ, the two functions F_1 and F_2 can be summed up so that

$$
\begin{aligned}
U_{\text{anh}} &\simeq \xi_h\left[1+\frac{\gamma}{4\sqrt{2}}\left(F_1(b,b^\dagger)+F_2(b,b^\dagger)\right)\right] \\
&= \xi_h\left[1+\frac{\gamma}{4}\left(-2i\lambda^4n^4 + 3i\lambda^3n^3X - 3i\lambda^2n^2(1-2b^\dagger b)\right)\right],
\end{aligned}
\tag{3.13}
$$

where $\xi_h = e^{i\lambda^2n^2}$ is the unitary operator which can be found from (3.2) in the case of a harmonic dynamics, and that indeed we have already obtained in the previous Chapter (Eqs.(2.5)

[§] Zassenhaus formula: $e^{\hat{x}+\hat{y}} = e^{\hat{x}}e^{\hat{y}}\prod_{i=1}^{\infty}e^{\hat{z}_i}$, with $\hat{z}_1 = -\frac{1}{2}[\hat{x},\hat{y}]$, $\hat{z}_2 = \frac{1}{6}[\hat{x},[\hat{x},\hat{y}]] + \frac{1}{3}[\hat{y},[\hat{x},\hat{y}]]$, $\hat{z}_3 = -\frac{1}{8}\left([\hat{y},[\hat{x},[\hat{x},\hat{y}]]] + [\hat{y},[\hat{y},[\hat{x},\hat{y}]]]\right) - \frac{1}{24}[\hat{x},[\hat{x},[\hat{x},\hat{y}]]], \ldots$ [140].

and (2.6)) for the same four-pulse scheme. Now, we can perform the partial trace over the mechanical degrees of freedom with the oscillator initially prepared in a thermal state. We find the effective unitary operator

$$\xi_{\text{eff}} \simeq \exp\left\{ i(\lambda^2 n^2 - \frac{\gamma}{2}(\lambda^4 n^4 + 3\lambda^2 n^2 \bar{n}) \right\}, \tag{3.14}$$

where $\bar{n}$ represents the initial population of the mechanical state. As a result, at the first order in γ, and in the limit $\lambda^2 \langle n \rangle^2 \gg \bar{n}$, the evolution of the field, after enclosing a closed loop in the oscillator phase space, reads like

$$\mathcal{E}(\varrho_{\text{f}}) \simeq \xi_{\text{eff}}\, \varrho_{\text{f}} \xi_{\text{eff}}^{\dagger}. \tag{3.15}$$

This represents an effective unitary operator which only acts on the field and depends on the anharmonic parameter we aim to estimate. Equation (3.15) also tells us that the field experiences a Kerr nonlinearity when entering into the cavity due to the particular interaction Hamiltonian [35]. Very importantly, the estimation of γ does not require a demanding cooling of the mechanical motion, since the condition $\lambda^2 \langle n \rangle^2 \gg \bar{n}$, which allows us to have field and mirror uncorrelated at a mechanical period, can be easily satisfied in todays experiments [2].

Given the result for the effective map, we are now ready to evaluate the mean value of the optical field after the four pulsed interactions. Considering a field initially in a coherent state $\varrho_{\text{f}} = |\alpha\rangle_{\text{f}} \langle\alpha|$, we have

$$\begin{aligned}
\langle a \rangle &= {}_{\text{f}}\langle \alpha | \xi_{\text{eff}}^{\dagger} a \xi_{\text{eff}} | \alpha \rangle_{\text{f}} \\
&= \alpha e^{-(|\alpha|^2 - i\lambda^2)} \sum_{n=0}^{\infty} \frac{|\alpha|^{2n}}{n!} e^{2i\lambda^2 n} e^{-i\frac{\gamma}{2}\lambda^4(4n^3+6n^2+4n+1)} \\
&\simeq \alpha e^{-(|\alpha|^2 - i\lambda^2)} \sum_{n=0}^{\infty} \frac{|\alpha|^{2n}}{n!} e^{2i\lambda^2 n} \left[1 - i\frac{\gamma}{2}\lambda^4(4n^3 + 6n^2 + 4n + 1) \right] \\
&= \alpha e^{-(|\alpha|^2 - i\lambda^2)} \left[e^{N_p e^{2i\lambda^2}} - i\frac{\gamma}{2}\lambda^4(4N_p^3 + 18N_p^2 + 14N_p + 1) e^{N_p e^{-2i\lambda^2}} \right] \\
&= \alpha \langle a \rangle_h e^{-i\frac{\gamma}{2}\lambda^4(4N_p^3+18N_p^2+14N_p+1)},
\end{aligned} \tag{3.16}$$

where $\langle a \rangle_h = \langle \alpha | \xi_h^{\dagger} a \xi_h | \alpha \rangle = e^{i\lambda^2 - N_p(1-e^{i2\lambda^2})}$ is the mean value of the optical field in the case of a harmonic evolution of the mechanical oscillator as already found in Eq. (2.7). Note that we have assumed $\lambda^2 N_p^2 \gg \bar{n}$ to safely consider the effective map ξ_{eff} and $\gamma\lambda^4 N_p^3 \ll 1$ in the third line. Also, we remind that $N_p = \langle n \rangle = |\alpha|^2$. Additionally, we must satisfy the condition after Eq. (3.4), which, given the choice of the initial optical state, reads $\gamma|A|^2 = \gamma(\lambda N_p)^2 \ll 1$.

By looking at Eq. (3.16) we see that the phase acquired by the field after the interaction with the oscillator does not depend on the mechanical initial conditions, but it provides all the information on the interaction.

As already mentioned in the previous Chapter, in the case of a harmonic oscillator, the same four-pulse scheme has been suggested to probe possible modifications (due to gravity) to the standard commutation rule between X and P. The protocol relies on the fact that the operation in Eq. (2.5) can be reduced to an effective operator, which acts only on the field and encodes information on the mechanical commutator. Equation (2.6) illustrates this result within the framework of standard quantum mechanics. Interestingly, our anharmonic optical phase shift in Eq. (3.16) (derived for a quartic anharmonicity) has the same form (same dependence from the optomechanical parameters) of the one obtained in Ref. [6] for a particular deformation of the commutator between X and P. This tells us that, in a possible experimental realization of the protocol in Ref. [6], one should be able to rely on the assumption of a harmonic mechanical motion, otherwise it might be difficult to understand the origin of an additional phase shift.

3.4 Estimation properties of the anharmonic parameter

Here we are going to make use of the quantum estimation techniques presented in the first Chapter of this thesis (see paragraph 1.2.6 for more details) to find out how precisely we can estimate the anharmonic parameter γ. In particular, we are going to calculate the ultimate quantum bounds on the estimation precision of γ, and to compare them with the ones that can be achieved in feasible measurement schemes such us homodyne and heterodyne detection [40] (see paragraph 1.2.5 for more details).

The first quantity we want to calculate is the QFI with respect to the parameter γ for a specific output state given by the map in Eq. (3.15). Since the effective dynamics described by the operator ξ_{eff} is unitary, if we consider an input pure state for the field, the output state will still be pure, and we can use the expression of the QFI for pure states in Eq. (1.28). Specifically, taking the field initially in the coherent state $|\alpha\rangle_{\text{f}}$, the final (pure) state will be $|\psi_\gamma\rangle = \xi_{\text{eff}}|\alpha\rangle_{\text{f}}$, and the QFI results

$$\begin{aligned} Q_\gamma &= 4\left(\langle\partial_\gamma\psi_\gamma|\partial_\gamma\psi_\gamma\rangle - |\langle\partial_\gamma\psi_\gamma|\psi_\gamma\rangle|^2\right) \\ &= \lambda^8\left(\langle\psi_\gamma|n^8|\psi_\gamma\rangle - \langle\psi_\gamma|n^4|\psi_\gamma\rangle^2\right) \\ &= 16\lambda^8 N_p^7 + O(N_p^6), \end{aligned} \tag{3.17}$$

where $|\partial_\gamma \psi_\gamma\rangle$ indicates the derivative of the state with respect to γ. As we know, the QFI provides the lower bound on the estimation precision for the variance of parameter we are interested in, as stated in the quantum Cramér-Rao theorem (Eq. (1.27)). In our specific case, we have

$$\mathrm{Var}(\gamma) \geq \frac{1}{\mathcal{M} Q_\gamma} \gtrsim \frac{1}{16 \mathcal{M} \lambda^8 N_p^7}\,, \tag{3.18}$$

where we remind that $\mathcal{M}$ is the number of measurements. A careful reading of Eq. (3.18) tells us that our estimation of the parameter is well-enhanced by the self optical Kerr nonlinearity ($\propto n^4$) induced by the interaction Hamiltonian and encoded in the displacement operator given in Eq. (3.14). From a theoretical point of view the ultimate bound given by Eq. (3.18) is always achievable in the framework of single-parameter estimation [40]. This means that, in principle, there should be a POVM whose classical FI reaches the value of the QFI. Therefore, it becomes important to explore which kind of feasible measurements have a FI close to the QFI. The FI is given by Eq. (1.24), which now is written as

$$F_\gamma = \int d\bullet\, \frac{(\partial_\gamma p(\bullet|\gamma))^2}{p(\bullet|\gamma)}\,, \tag{3.19}$$

with $p(\bullet|\gamma)$ a generic conditional probability of obtaining the outcome $\bullet$ assuming to know the value of the parameter γ. Among all the possible measurement schemes we restrict our attention on homodyne and heterodyne detection discussed in paragraph 1.2.5. Defined the quadrature operator of the field X_f^ϕ as in Eq. (1.19) homodyne detection corresponds to a projection on the quadrature eigenstates defined by $X_\mathrm{f}^\phi |X_\mathrm{f}\rangle_\phi = X_\mathrm{f} |X_\mathrm{f}\rangle_\phi$. In the Fock basis, these are given by [141]

$$|X_\mathrm{f}\rangle_\phi = e^{-X_\mathrm{f}^2/2} \left(\frac{1}{\pi}\right)^{1/4} \sum_{m=0}^{\infty} \frac{\mathsf{H}_m(X_\mathrm{f})}{2^{m/2}\sqrt{m!}} e^{-im\phi} |m\rangle, \tag{3.20}$$

where $\mathsf{H}_m(x)$ are the Hermite polynomials. Given the value of γ, the conditional probability results equal to the following series

$$\begin{aligned} p(X_\mathrm{f}|\gamma) &= |{}_\phi\langle X_\mathrm{f}|\psi_\gamma\rangle|^2 \\ &= \frac{e^{-(|\alpha|^2 + X_\mathrm{f})}}{\sqrt{\pi}} \left| \sum_{m=0}^{\infty} \frac{\alpha^m \mathsf{H}_m(X_\mathrm{f})}{2^{\frac{m}{2}} m!} e^{im\left[\phi - \lambda^2 m (1 + \frac{\gamma}{2}\lambda^2 m^2)\right]} \right|^2, \end{aligned} \tag{3.21}$$

which cannot be calculated analytically. However, by fixing the parameters $\{\alpha,\ \phi,\ \lambda,\ \gamma\}$, Eq. (3.21) can be numerically evaluated as a function of the measurement outcome X_f. We can

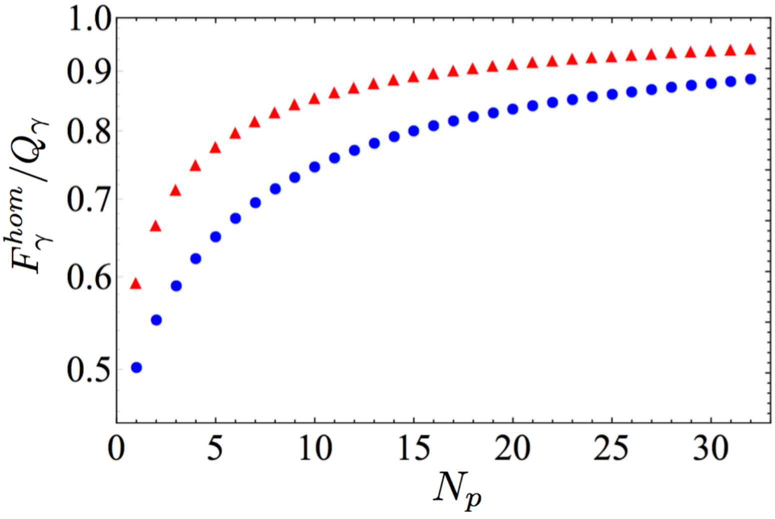

Figure 3.2: Plot of $F_\gamma^{\mathrm{hom}}/Q_\gamma$ for the cubic (red triangles) and the quartic (blue dots) anharmonicities by varying the number of photons inside the cavity. The parameters are: $\lambda \sim 1.5 \times 10^{-5}$, $\gamma = 10^{-25}$ and $\phi = \pi/2$.

then calculate the FI in Eq. (3.19). Figure 3.2 shows the ratio between the FI and QFI in the case of the homodyne measurement, where the phase ϕ has been optimised to $\pi/2$. We can immediately see that by increasing the number of photons, the ratio between FI and QFI progressively grows, reaching already a high value ($F_\gamma^{\mathrm{hom}}/Q_\gamma \sim 0.9$) when $N_p \sim 30$. Given that for such a weak photon source we already achieve a good agreement, we can infer that if we could further increase the number of photons, this ratio would become optimal, eventually approaching one. And, this is actually the case in todays experiments, where optical laser sources usually used are quite strong to enhance the optomechanical coupling strength. We then conclude that homodyne detection results an optimal scheme in a feasible experimental condition.

Now we can study another feasible measurement scheme: heterodyne detection. It results in a projection on a coherent state $|z\rangle$ that, as we have seen, can be easily realized via a double homodyne (paragraph 1.2.5) [39]. In this case, the conditional probability is

$$\begin{aligned} p(\eta|\gamma) &= |\langle z|\psi_\gamma\rangle|^2 \\ &= e^{-(|\alpha|^2+|z|^2)} \left| \sum_{m=0}^{\infty} \frac{\alpha^m z^{*m}}{m!^2} e^{-i\lambda^2 m^2 (1+\frac{\gamma}{2}\lambda^2 m^2)} \right|^2, \end{aligned} \tag{3.22}$$

while the FI is obtained integrating Eq. (3.22) as

$$F_\gamma^{\mathrm{het}} = \frac{1}{\pi} \int d^2 z \, \frac{(\partial_\gamma p(z|\gamma))^2}{p(z|\gamma)}, \tag{3.23}$$

where we do not have a dependence on the phase parameter. Following the same procedure as before, the FI can be now numerically evaluated. For numerical reasons we select a field initially prepared in a coherent state with a maximum value of photons of about 35. We find that the ratio between FI and QFI results $F_\gamma^{\rm het}/Q_\gamma = 0.5$, which is not affected by any parameter, including the number of photons. It is therefore possible to conclude that homodyne measurement is experimentally more efficient to probe the anharmonicity of the mechanical oscillator. Indeed, by using homodyne detection, we can perform an optimal estimate of the parameter we are interested in, and, eventually, achieve the limit given by quantum mechanics.

Another important figure of merit of any estimation protocol aiming to measure small parameters is the signal-to-noise ratio. As already discussed in paragraph 1.2.6, this quantity compares the level of a desired signal to the level of background noise, being defined as the ratio between the signal and the noise power. By using the upper bound for the signal-to-noise ratio in Eq. (1.30) and the expression for the QFI obtained in (3.17), in the limit of large number of photons, we find that

$$R_\gamma \leq \gamma^2 \mathcal{M} Q_\gamma = 16\gamma^2\lambda^8 N_p^7 \mathcal{M}. \tag{3.24}$$

To have an efficient protocol it is required a significant value of the signal-to-noise ratio after a feasible number of measurements $\mathcal{M}$, i.e. $R_\gamma > 1$. By using realistic experimental parameters such as $N_p \sim 10^9$, $\lambda \sim 10^{-4}$, and fixing the number of measurements $\mathcal{M} \sim 10^4$, our analysis shows that we can aim to probe quartic anharmonicities of about $\gamma \sim 10^{-20}$. We remark that the selected number of experimental runs allows us to still adopt optimal asymptotic estimators like the Bayesian or the MaxLik. Also, for an initial temperature of a few degrees Kelvin, which is experimentally achieved using dilution refrigeration [2], all the values used for the parameters satisfy the assumptions that we have made to derive our results ($\gamma\lambda^4 N_p^3 \ll 1$, $\lambda^2 N_p^2 \gg \bar{n}$, $\epsilon\bar{n} \ll N_p$).

3.5 Cubic anharmonicity

Here, we briefly reproduce all the previous results for the case of a cubic mechanical anharmonicity. Specifically, we consider the following Hamiltonian for the mechanical mirror

$$H_0 = \frac{1}{2}\hbar\omega_0 \left(X^2 + P^2\right) + \frac{\delta}{3}\hbar\omega_0 X^3, \tag{3.25}$$

with δ the cubic anharmonic parameter. By following the procedures in Ref. [135, 136], at the first order in δ and for an initial displacement satisfying $\delta\lambda N_p \ll 1$, the annihilation operator at time t is

$$b(t) \simeq be^{-i\omega t} + \frac{\delta}{2^{3/2}}\left[\left(e^{-i\omega t}-1\right)\left(2b^{\dagger}b+1\right)+\left(e^{-2i\omega t}-e^{-i\omega t}\right)b^2+\left(e^{-i\omega t}-e^{2i\omega t}\right)\frac{b^{\dagger 2}}{3}\right], \tag{3.26}$$

where again the operators without an explicit time-dependence must be considered at $t = 0$ and, importantly, now the frequency of the anharmonic oscillator coincides with the bare mechanical frequency ω_0. We highlight that this discrepancy between the two kinds of anharmonicity might be used to distinguish them, for example by looking at the first revival of the visibility pattern in the interferometric scheme analysed in the previous Chapter. By using Eq. (3.26) the mechanical position operators at the times $t = 0, \tau/4, \tau/2, 3\tau/4, \tau$ result

$$\begin{aligned} X(0) &= X, \\ X\left(\frac{\tau}{4}\right) &\simeq P + \delta(\Delta + b^{\dagger 2}\nu + b^2\nu^*), \\ X\left(\frac{\tau}{2}\right) &\simeq -X + \delta(2\Delta + \frac{1}{3}(b^{\dagger 2} + b^2)), \\ X\left(\frac{3\tau}{4}\right) &\simeq -P + \delta(\Delta + b^{\dagger 2}\nu^* + b^2\nu), \end{aligned} \tag{3.27}$$

with $\Delta = -(b_0^{\dagger}b_0 + 1/2)$ and $\nu = -(1/6)(2i+1)$. By substituting Eq. (3.27) into the overall evolution operator in Eq. (3.2), and following the same procedure as for the quartic anharmonicity, we find the final effective evolution operator only describing the evolution of the cavity field in the limit $\lambda^2 N_p^2 \gg \bar{n}$:

$$\xi_{\text{eff}} \simeq \exp\{i(\lambda^2 n^2 - \frac{2\delta}{9}\lambda^3 n^3)\}, \tag{3.28}$$

which gives the following mean value for the optical field (in the limit $\delta\lambda^3 N_p^2 \ll 1$)

$$\langle a \rangle \simeq \alpha \langle a \rangle_h e^{-i\frac{2}{9}\delta\lambda^3(3N_p^2+3N_p+1)}. \tag{3.29}$$

Equation (3.28) shows again that the optical field experiences a Kerr nonlinearity ($\propto n^3$) when it enters into the cavity in (3.29). This results in an additional optical phase proportional to the number of photons. In turn, by using the effective operator ξ_{eff} and taking the field in the initial coherent state $|\alpha\rangle_{\text{f}}$, we can calculate the QFI for the cubic anharmonicity, which reads

$$Q_\delta \simeq \frac{16}{81}\lambda^6(9N_p^5 + 54N_p^4 + 84N_p^3 + 30N_p^2 + N_p). \tag{3.30}$$

This brings us to the following results for the Cramér-Rao bound and the signal-to-noise ratio

$$\begin{aligned} \text{Var}(\delta) &\geq \frac{1}{\mathcal{M}Q_\delta} \gtrsim \frac{9}{16\mathcal{M}\lambda^6 N_p^5}, \\ R_\delta &\lesssim \frac{16}{9}\delta^2\lambda^6 N_p^5 \mathcal{M}. \end{aligned} \tag{3.31}$$

By using the parameter values of the previous paragraph, and always requiring an initial mechanical temperature of a few degrees Kelvin, we find that we can in principle probe cubic anharmonicities as low as $\delta \sim 10^{-15}$.

3.6 Effect of losses

We now would like to investigate how possible losses in the optical fiber when the light is out of the cavity can affect our previous results (see Fig. 3.1). A measure of the loss between two consecutive light pulses is provided by the ratio of the two rescaled coupling constants $\lambda_{i+1}/\lambda_i = 1 - \epsilon$ with $i = 1, ..., 4$ the number of consecutive light-mirror interactions. This means that for every pulse the optomechanical interaction is weaker, and, in turn, we expect the overall full operation (3.2) and the effective operator acting on the field (3.14) to be affected. We can also predict that field and mirror will result correlated even after a mechanical period, when the oscillator encloses a loop in its phase space.

More specifically, the evolution operator is now

$$\begin{aligned}\tilde{U}_{\text{anh}} &\simeq e^{-i\lambda_4 nP} e^{\frac{\gamma}{4} f_1(b,b^\dagger)} e^{i\lambda_3 nX} e^{-i\lambda_2 nP} e^{\frac{\gamma}{4} f_2(b,b^\dagger)} e^{i\lambda_1 nX} \\ &= e^{-i\lambda_4 nP} e^{\frac{\gamma}{4} f_1(b,b^\dagger)} e^{i\lambda_4 nP} \tilde{\xi}_h e^{-i\lambda_1 nX} e^{\frac{\gamma}{4} f_2(b,b^\dagger)} e^{i\lambda_1 nX},\end{aligned} \tag{3.32}$$

where

$$\tilde{\xi}_h = D(n\mu) e^{in^2[\lambda_3\lambda_2 + \frac{1}{2}(\lambda_2 - \lambda_4)(\lambda_1 - \lambda_3)]}, \tag{3.33}$$

with $D(n\mu) = e^{n(\mu b^\dagger - \mu^* b)}$ and $\mu = (1/\sqrt{2})[(\lambda_4 - \lambda_2) + i(\lambda_1 - \lambda_3)]$. We can note that the displacement operator $D(n\mu)$ in Eq. (3.33) entangles light and mirror even in the case of closed loops, as expected. To calculate Eq. (3.32) we follow the same procedure as before. We firstly note that the two functions $f_1(b, b^\dagger)$ and $f_2(b, b^\dagger)$ have the same formal definition given in Eq. (3.10) with $\lambda \to \lambda_4$ and $\lambda \to \lambda_1$, respectively. We then switch the exponential depending on the functions $f_{1,2}$ on the left and on the right. At the first order in γ the operator in Eq. (3.32) can thus be written as

$$\tilde{U}_{\text{anh}} \simeq \xi_h + \frac{\gamma}{4}[F_1(b, b^\dagger)\tilde{\xi}_h + \tilde{\xi}_h F_2(b, b^\dagger)], \tag{3.34}$$

where $F_{1,2}$ follow the same convention as $f_{1,2}$. At this point, to quantify the impact of losses on the effective map, we trace over the degrees of freedom of the mirror, obtaining

$$\begin{aligned}\tilde{\xi}_{\text{eff}} \simeq &\exp\left\{-\frac{|\mu|^2}{2} n^2 (1 + 2\bar{n})\right\} \\ &\times \exp\left\{i\left[n^2\left(\lambda_3\lambda_2 + \frac{1}{2}(\lambda_2 - \lambda_4)(\lambda_1 - \lambda_3)\right) - \frac{\gamma}{2}\left(\lambda^4 n^4 + O(\epsilon\lambda^4 n^3 \bar{n})\right)\right]\right\},\end{aligned} \tag{3.35}$$

By looking at Eq. (3.35) we see that in the limit $\epsilon\bar{n} \ll N_p$ losses in the fibers can be safely neglected. We can further say that losses also affect the amplitude of the harmonic operator. This is usually translated in a lowering of the visibility in the interferometric scheme built as in Fig. 2.3. However, this deleterious outcome can be easily evaluated before running the experiment.

3.7 Conclusions

In this Chapter, we have studied a protocol able to estimate the anharmonic constant of a mechanical oscillator in an optomechanical cavity. To achieve this goal we have used four pulsed interactions between field and mechanical oscillator. Demanding a reasonable initial mechanical cooling, we have found that mechanical oscillator and field are disentangled at specific times, which coincide with multiples of the period of the oscillator. Between these specific times the field undergoes an effective unitary operation, which encodes the relevant information about the dynamics and, more specifically, on the anharmonicity. We have also seen that we can in principle distinguish between different kinds of anharmonicity, since the mechanical frequency is modified only in the case of a quartic anharmonicity. The efficiency of our protocol has been tested by using the tools of quantum estimation theory: we have calculated the ultimate bounds on the estimation precision and found how we can achieve such limits via feasible measurements, i.e. homodyne and heterodyne detections. Comparing these two possible ways of measuring the optical phase, we have proved that homodyne detection is more convenient, providing an optimal result when we approach the large photon number limit in the cavity. Finally, by studying the signal-to-noise-ratio, we have verified the performance of our protocol with respect to the background noise.

Our protocol shows a general procedure which might be used to probe other kinds of non-linearities, for example, the ones arising from an optomechanical interaction behind the linear approximation. Furthermore, it might be employed for similar problems in other platforms with similar Hamiltonians.

Chapter 4

Dynamical dressing process in Casimir scenarios

4.1 Introduction

As we have seen in Sec. 1.3, Casimir and Casimir-Polder forces are originated whenever the vacuum fluctuations of the electromagnetic field are disturbed by the presence of boundaries given for example by neutral macroscopic bodies and/or atoms [8].

New interesting effects arise when boundary conditions on a field are set in motion with a nonuniform acceleration, or a relevant parameter of the system changes non-adiabatically in time. In this case, quantum mechanics predicts an emission of photon pairs from the vacuum [3, 142]. This effect is known as dynamical Casimir effect (DCE) and has been observed in superconducting circuits [12] and Bose-Einstein condensates [143]. However, the observation of the DCE originated by the non-adiabatic motion of an oscillating macroscopic boundary is still an experimental challenge, since to detect a measurable number of photon pairs high mechanical oscillation frequencies are required. To overcome such difficulties, the control of the optical properties of the mechanical boundary seems to be essential [144].

A very related physical situation is when the mechanical degrees of freedom of the boundaries, which are allowed to move, are treated quantum-mechanically. In the context of an optomechanical cavity, as discussed in paragraph 1.2.2, an effective interaction between the field and the mechanical degrees of the wall (phonons), and between field modes mediated by the movable wall, is generated [4]. It has been proven that such new interactions influence the vacuum energy density of the electromagnetic field inside the cavity [34, 145–148]. More specifically in Refs. [34, 145] it has been discovered an effect very similar to the DCE, though different in nature.These works can also be of broader interest if one thinks of the exciting recent developments of the growing field of cavity optomechanics. Nowadays, building optomechanical cavities with movable mirror of masses of the order of 10^{-11}Kg or even less [2] and reaching temperatures of the order of a few millidegrees Kelvin [149] is within current technology. The exploration of vacuum effects arising from a quantum description of the boundaries acting on fields seems now to be experimentally accessible.

It is now well-recognised in QED that having a dynamical (time-dependent) component in the system opens the door to new physical effects, which, not directly involving the creation of real photons from the vacuum, can actually be very different with respect the DCE. In the context of Casimir-Polder forces, a dynamical component of the force may appear as a consequence of a population-induced dynamics related to atomic spontaneous decay, the motion of atoms or macroscopic bodies, a time-dependent change of the matter-radiation coupling, or even self-dressing processes of the system. In the latter case, the system undergoes an evolution from an initial non-equilibrium quantum state such us a bare or partially dressed state and the Casimir-Polder force has a temporal evolution with new peculiarities with respect to the static case, such as temporal oscillations, including the possibility of transient repulsive forces [63]. This scenario also occurs when some physical parameters of the Hamiltonian change instantaneously, for example the atomic transition frequency induced by Stark shift through an external electric field suddenly switched on or off. Again, the state of the system is no longer an eigenstate of the new Hamiltonian and a time-dependent Casimir-Polder force appears [150]. This kind of studies have also been extended to more complex configurations where, for example, real surfaces [151], dielectric media [152] or chiral molecules [153] are considered. In all these investigations two main features have been highlighted: the Casimir-Polder force can be much stronger with respect to the stationary case at the round trip time, which coincides with the time spent by the radiation emitted by the atom to go back to the atom after a reflection on the plate; and, the dynamical force can display a new transient repulsive character, contrarily to static electric atom-surface Casimir-Polder forces which are always attractive. In a nutshell, all these studies, which have considered atoms or molecules in their bare or partially dressed ground states, have clearly demonstrated that time-dependent aspects allow for the observation of new features in Casimir-Polder interactions. In parallel, conceptually related problems have been recently addressed in various physical systems and have enlarged the interest in investigating the time-dependent dressing. For example, we recall the experimental and theoretical study of the response of a quasi-particle to a fast external force [154, 155], the observation of the time-dependent dressing of a quasiparticle in condensed matter physics [156], and the study of the onset of an effective mass in Bose-Einstein condensates [157].

In this Chapter, we study the non-equilibrium dynamical (time-dependent) dressing process for the interaction between a one-dimensional scalar (or electromagnetic) field with a quantum mechanical boundary and for the Casimir-Polder force between an atom and perfectly conducting wall. In Sec. 4.2 we provide a general framework to describe the non-equilibrium dressing process in a general physical system, which has been previously used for the interaction between atoms [158] or between an atom and a conducting mirror [63, 150]. In Sec. 4.3 we start our investigation in a multimode optomechanical scenario. By using the multimode Hamiltonian described in paragraph 1.2.2 of Chapter 1, we consider the mechanical degrees of freedom of the moving boundary in the system dynamics. In the equilibrium configuration, due to the quantum description of the field-mirror interaction, both field and mirror contain virtual excitations, i.e. the ground state of the system becomes dressed. This situation has been recently studied in [145] for a one-dimensional massless scalar field, and successively extended to a one-dimensional electromagnetic field and a three-dimensional massless scalar field in [34]. By using the framework developed in Sec. 4.2, we investigate the dynamical dressing process bringing the field-mirror system, initially out of equilibrium, to a dressed configuration. By calculating the local dynamical energy shift of the system, we explore the transient dynamical dressing process of the wall and the features emerging when approaching the equilibrium configuration of the coupled system. We also extend our conclusions to the case of a single wall interacting with two different cavity fields through a generalization of our effective Hamiltonian, which allows to include the effect of vacuum radiation pressure on both sides of the movable wall. In Sec. 4.4 we instead study the non-equilibrium dressing process for the dynamical Casimir-Polder force between an initially excited atom and a perfectly conducting plate (a typical cavity QED scenario). The choice of the initial non-equilibrium atomic configuration shows new relevant peculiarities compared to the case of a ground-state atom, due to the presence of an atom-field resonance. The time-dependent Casimir-Polder force exhibits oscillations in time changing from attractive to repulsive depending on the atom-wall distance. Our results for the atomic excited state provide a much more convenient way to detect the dynamical Casimir-Polder effect. In fact, contrarily to the ground-state case, the static atom-wall Casimir-Polder force on an excited atom oscillates in space, vanishing at well defined atom-wall distances whose position is related to the atomic transition wavelength. This means that we can single-out more efficiently the dynamical contribution to the force, by choosing specific atom-wall distances where the static force is zero. Also, we find the dynamical force for the excited atom much stronger (some orders of magnitude) than the dynamical force for a ground-state atom. Finally, Sec. 4.5 is devoted to our conclusive remarks.

4.2 Non-equilibrium dressing

Let us consider a system of two interacting objects described by the Hamiltonian $\mathcal{H} = \mathcal{H}_0 + \mathcal{H}_{\text{int}}$, where $\mathcal{H}_0$ is the bare Hamiltonian and $\mathcal{H}_{\text{int}}$ the interaction.

In the context of Casimir physics, one is usually interested in the equilibrium ground state of the overall interacting system $|\Psi_D\rangle$, which is then used to calculate the Casimir or Casimir-Polder potential (force) between the two objects (as we have seen in paragraph 1.3.4). $|\Psi_D\rangle$ is often referred to as the *dressed* vacuum state of the overall system, since both objects, due to their mutual interaction, continuously exchange particles and result covered of excitations. Since we are in the overall ground state, such excitations cannot be probed and are usually called *virtual*. To calculate the dressed state of the system one can rely on non-perturbative or perturbative methods. However, given that commonly $\mathcal{H}_{\text{int}}$ is quite complex and that the coupling constant between the two objects is much smaller than the bare frequencies, the dressed state is usually computed by using stationary perturbation theory at the lowest significant order in the coupling constant on the initial state bare ground state $|\Psi_B\rangle$, where both subsystems are in their ground states. Supposing that the second order is the lowest significant, it is possible to show that the stationary second-order energy shift of the overall system can be obtained as

$$\mathcal{E}^{(2)}_{\text{stat}} = \langle\Psi_D|\,\mathcal{H}\,|\Psi_D\rangle = \frac{1}{2}\,\langle\Psi_D|\,\mathcal{H}_{\text{int}}\,|\Psi_D\rangle\,, \tag{4.1}$$

where $|\Psi_D\rangle$ is the dressed (i.e. perturbed) state of the system obtained by second-order perturbation theory. In the context of Casimir-like configurations, where, for example, we have a scalar or electromagnetic field inside a cavity with one wall free to move within a potential, Eq. (4.1) provides a change of the Casimir energy of the system with respect to the configuration in which the boundaries are fixed. Whereas, in the context of Casimir-Polder interactions between an atom and a wall mediated by an electromagnetic field, Eq. (4.1) relates the energy shift to the local electromagnetic field felt by the atom at its position. In all the cases, Eq.

(4.1) connects the second order energy shift of the overall system to the *local* interaction between the two objects. We remind that Eq. (4.1) has already been used to calculate the static Casimir-Polder force between an atom and a wall in paragraph 1.3.4, where we have also seen that, in the quasi-static approach, the static Casimir-Polder force can be obtained by taking the derivative of the stationary interaction energy (4.1) with respect to the atom-wall distance d and changing its sign.

The results in Eq. (4.1) is valid when the system described by the Hamiltonian $\mathcal{H}$ is at equilibrium in the state $|\Psi_D\rangle$. The initial state $|\Psi_B\rangle$ is just the initial point around which we perform the perturbation theory. This means that the interaction is always on, and we directly calculate the relevant quantities at the equilibrium configuration. However, we can suppose that the system is initially (at $t = 0$) prepared in a state $|\Psi_B\rangle$ which is not an eigenstate of $\mathcal{H}$. Then, for $t > 0$, we turn on the the interaction Hamiltonian and let the system evolve freely. Once the interaction is on, the interacting objects start to exchange virtual particles. This process, eventually bringing the system to an equilibrium configuration, is the *dynamical dressing process* we wish to investigate in this Chapter. The final configuration will be a dressed state, which will not necessarily coincide with the *dressed* state $|\Psi_D\rangle$ that one can find by performing the stationary perturbation theory on $|\Psi_B\rangle$. Note that the above discussion can be generalized to any non-equilibrium initial state for the total system.

To investigate the *dynamical dressing process* one needs to find a quantity which takes into account the local dynamical interaction of the two objects. The most natural way is to generalize Eq. (4.1) as

$$\mathcal{E}^{(2)}_{\text{loc,dyn}}(t) = \frac{\langle\Psi_B|\, \mathcal{H}^{(2)}_{\text{int}}(t)\, |\Psi_B\rangle}{2}, \tag{4.2}$$

where $\mathcal{H}^{(2)}_{\text{int}}(t)$ is the interaction Hamiltonian in the Heisenberg representation at the second order in the coupling constant. The procedure in Eq. (4.2) is analogous to the one used in [63, 150] for the atom-plate Casimir-Polder force. Contrarily to the stationary case, the energy shift in Eq. (4.2) is the *local* interaction energy between the two objects, and in general does not coincide (in particular at very large times) to the overall energy shift of the system in Eq. (4.1) (we will clarify this subtle point in the following part of the Chapter), which, on the other hand, is time-independent due to the unitary time evolution. Nevertheless, as we will discuss, in the limit of large times Eq. (4.2) provides the correct expression for the static Casimir or Casimir-Polder energy, since

$$\lim_{t\to\infty} \mathcal{E}^{(2)}_{\text{loc,dyn}}(t) = \mathcal{E}^{(2)}_{\text{stat}}. \tag{4.3}$$

However, we will see that a similar relation does not hold for all the relevant physical quantities. In a quasi-static approach, the dynamical Casimir-Polder force can be thus obtained by taking the derivative of the dynamical local interaction energy (4.3) as

$$F(d,t) = -\frac{\partial}{\partial d}\,\mathcal{E}^{(2)}_{\text{loc,dyn}}(d,t). \tag{4.4}$$

Also for this case, we will see that, in the limit of large times, Eq. (4.4) returns the correct expression for the static Casimir-Polder energy in Eq. (1.57).

4.3 Dynamical dressing in multi-mode optomechanics

4.3.1 The model

Let us consider a massless scalar field inside the one-dimensional cavity with a mobile wall, as described in paragraph 1.2.2. The system is sketched in Fig. 4.1, where for the moment we do not consider the fixed wall on the right side. By including the mechanical degrees of freedom of the moving mirror in the overall system dynamics, and treating them quantum-mechanically, the effective non-relativistic Hamiltonian describing our one-dimensional coupled mirror-field system is given by Eq. (1.8). It can be rewritten as $\mathcal{H} = \mathcal{H}_0 + \mathcal{H}_{\text{int}}$, where

$$\begin{aligned}\mathcal{H}_0 &= \mathcal{H}_{\text{f}} + \mathcal{H}_{\text{m}}\\ &= \hbar\sum_k \omega_k a^\dagger_k a_k + \hbar\omega_0 b^\dagger b\end{aligned} \tag{4.5}$$

is the unperturbed Hamiltonian with $\mathcal{H}_{\text{f}}$ and $\mathcal{H}_{\text{m}}$ field and mirror Hamiltonians. We remember that we have imposed Dirichlet boundary conditions on the field operator at the positions of the walls: the field modes are then referred to the equilibrium position L of the moving mirror, and, as a result, the possible wave-numbers are $k_j = j\pi/L$, with j an integer number. While, the effective interaction between mirror and field and between different field modes (due to the motion of the wall), is rewritten as [4]

$$\mathcal{H}_{\text{int}} = -\sum_{kj}\mathcal{C}_{kj}(b+b^\dagger)\left[a_k a_j + a^\dagger_j a_k + a^\dagger_k a_j + a^\dagger_k a^\dagger_j\right], \tag{4.6}$$

where we have defined the coupling constant

$$\mathcal{C}_{kj} = (-1)^{k+j}\left(\frac{\hbar}{2}\right)^{\frac{3}{2}}\frac{1}{L\sqrt{M}}\sqrt{\frac{\omega_k\omega_j}{\omega_0}}, \tag{4.7}$$

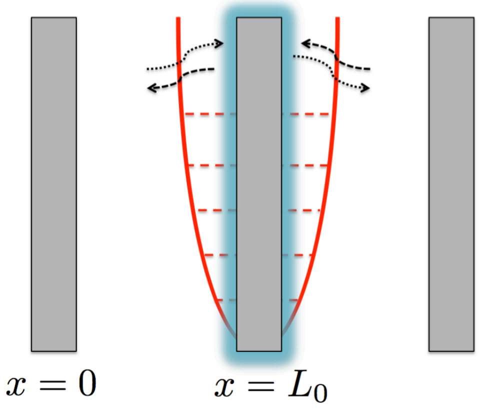

Figure 4.1: Pictorial description of the system. A movable wall, described quantum-mechanically, is bounded by a harmonic potential of frequency ω_0 (represented by the red well) around its equilibrium position L. The wall can interact with two different set of cavity modes, at its left and right sides. In the first part of this work we only consider the coupling with one cavity field. Due to the interaction with the field vacuum fluctuations, the state of the wall starts its time-dependent self-dressing process: the two objects interchange virtual particles (black-dotted arrows). This process ends when the dressed equilibrium configuration is reached. As a result, the mirror results covered by a cloud of virtual quanta, mainly concentrated at the proximity of its equilibrium position.

with k and j integer numbers specifying the field modes relative to the equilibrium position L of the wall. We remark that in our Hamiltonian $\mathcal{H}$ we have taken the zero of the energy such that it includes the static Casimir energy between the two walls E_{Cas}, and that all energy corrections we are going to discuss are meant as corrections to this value of the energy.

4.3.2 Stationary configuration: dressed state

We now want to consider the ground state of our system. The unperturbed ground state is the bare state $|\Psi_B\rangle = |\{0_p\}, 0\rangle$, where both field and mirror are in their ground state with $|\{0_p\}\rangle$ the vacuum state for all cavity modes and $|0\rangle$ the vacuum state of the mirror. This state is not an eigenstate of the total Hamiltonian due to the mirror-field interaction. By using stationary perturbation theory on $\mathcal{H}_{\text{int}}$, we can find the true ground state of the system, which corresponds to the equilibrium configuration of the system where both field and mirror contain virtual excitations. At the lowest significant order in the coupling constant, it reads [145]

$$|\Psi_D\rangle = |\Psi_B\rangle + \sum_{jk} \mathcal{D}_{jk} |\{1_j, 1_k\}, 1\rangle, \tag{4.8}$$

where

$$\mathcal{D}_{jk} = (-1)^{j+k}\frac{1}{L}\sqrt{\frac{\hbar\omega_j\omega_k}{8M\omega_0}}\frac{1}{(\omega_0+\omega_k+\omega_j)} \tag{4.9}$$

quantifies the correction which is given by a pair of virtual excitations of the field (indicated inside the curly brackets) and one excitation (phonon) of the wall. The dressing effect is thus more relevant for low mechanical masses and/or low binding frequencies. The fact that the dressed state is covered with pairs of field particles is very similar to what happens in the DCE, where indeed photons are produced in pairs from the vacuum [3,142]. However, in the DCE the emitted photons are actually real particles which are produced in an energy-conserving process after a non-adiabatic change of the mirror position. Their frequency is indeed related to specific resonance conditions with the mechanical frequency.

From the dressed state, the second-order energy shift of the system due to the interaction can be calculated by using Eq. (4.1) as [145]

$$\begin{aligned}\mathcal{E}^{(2)}_{\text{stat}} &= \frac{1}{2}\langle\Psi_D|\,\mathcal{H}_{\text{int}}\,|\Psi_D\rangle\\ &= -\sum_{kj}\frac{\hbar^2}{4L^2M}\frac{\omega_k\omega_j}{\omega_0}\frac{1}{(\omega_0+\omega_k+\omega_j)},\end{aligned} \tag{4.10}$$

which gives a change of the Casimir energy E_{Cas} of the system with respect to the configuration where the walls are fixed. Due to the sum over all the field modes, Eq. (4.10) diverges. This is a typical ultraviolet divergence due to high-frequency modes. To regularize this singular behavior, we use an upper cutoff frequency in the sum over the field modes. On the other hand, the introduction of an upper cutoff is physically motivated by the fact that a real mirror becomes transparent at frequencies larger than its plasma frequency, and thus its interaction with the field is strongly suppressed above such frequency.

The analogous Casimir force for fixed mirrors is of the order of 10^{-15}N for $L = 1\mu$m, and numerical evaluation of Eq. (4.10) gives a correction to the force, which scales as M^{-1}, of around a few percent of this value for $M = 10^{-21}$Kg, $\omega_0 = 10^5 s^{-1}$ and a cutoff frequency $\omega_{\text{cut}} = 10^{16}s^{-1}$. Considering the actual precision of Casimir force measurements of around a few percent [159,160], and the strong achievements towards the miniaturization of mechanical oscillators in optomechanics [2], the possibility to detect the tiny effect due to the wall's quantum movement (position fluctuations) will be within the range of future technology.

As already discussed in Ref. [145], the second order energy shift in (4.10) can be elegantly connected to the oscillation energy of the mirror, the emitted photons and the interaction energy. In fact, given the stationary energy shifts for each term of the Hamiltonian

$$\begin{aligned}
\mathcal{E}^{(2)}_{\mathrm{f,stat}} &= \langle\Psi_D|\, \mathcal{H}_{\mathrm{f}}\, |\Psi_D\rangle \\
&= \sum_{kj} \frac{\hbar^2}{2L^2M} \frac{\omega_k^2\omega_j}{\omega_0(\omega_0+\omega_k+\omega_j)^2}, \\
\mathcal{E}^{(2)}_{\mathrm{m,stat}} &= \langle\Psi_D|\, \mathcal{H}_{\mathrm{m}}\, |\Psi_D\rangle \\
&= \sum_{j} \frac{\hbar^2}{2L^2M} \frac{\omega_k\omega_j}{(\omega_0+\omega_k+\omega_j)^2}, \\
\mathcal{E}^{(2)}_{\mathrm{int,stat}} &= \langle\Psi_D|\, \mathcal{H}_{\mathrm{int}}\, |\Psi_D\rangle = 2\mathcal{E}^{(2)}_{\mathrm{stat}},
\end{aligned} \tag{4.11}$$

and keeping in mind that the total energy shift is $\mathcal{E}^{(2)}_{\mathrm{stat}} = \mathcal{E}^{(2)}_{\mathrm{f,stat}} + \mathcal{E}^{(2)}_{\mathrm{m,stat}} + \mathcal{E}^{(2)}_{\mathrm{int,stat}}$, the following equation holds

$$\mathcal{E}^{(2)}_{\mathrm{f,stat}} + \mathcal{E}^{(2)}_{\mathrm{m,stat}} = -\frac{1}{2}\mathcal{E}^{(2)}_{\mathrm{int,stat}} = -\mathcal{E}^{(2)}_{\mathrm{stat}}. \tag{4.12}$$

Namely, the sum of the field and mirror energy shifts is actually related to the interaction energy shift, which, in turn, as already seen in Eq. (4.10) is linked to the total stationary energy shift of the system. This means that the total energy shift is coming from a positive energy contribution stored in both field and mirror, and a negative one originated by the mirror-field interaction, which is twice the stationary energy shift of the system. For the dynamical situation we are going to study, these considerations will be very important. We are indeed going to generalize the relation between the energy shift and the average value of the interaction Hamiltonian on the dressed ground state in Eqs. (4.10) and (4.12) to the time-dependent case.

4.3.3 Dynamical dressing of the movable mirror: bare initial state

We now want to investigate the time-dependent dressing process of our system as described in paragraph 4.2, starting from a non-equilibrium configuration. Let us suppose to prepare at $t = 0$ the system in the bare state $|\Psi_B\rangle$, and that the interaction Hamiltonian is "switched on" at this time. For subsequent times, the bare state $|\Psi_B\rangle$ is not an overall eigenstate anymore, and the system evolves to find a new equilibrium configuration: field and mirror immediately start interchanging virtual excitations and the dynamical dressing process begins. The expected final configuration for the system will be a dressed state, which, however, does not necessarily coincide with the state $|\Psi_D\rangle$ previously found.

In order to describe this situation, we want to evaluate the local time-dependent interaction energy by using Eq. (4.2). To this scope, we firstly solve the Heisenberg equations for field and mirror operators by using a perturbative approach at the lowest significant order, where the time-dependent field and mirror annihilation and creation operators are obtained as a series expansion in the coupling constant, i.e. $a_k(t) = a_k^{(0)}(t) + a_k^{(1)}(t) + ... + a_k^{(i)}(t)$ and $b(t) = b^{(0)}(t) + b^{(1)}(t) + ... + b^{(i)}(t)$, with $a_k^{(i)}(t)$ and $b^{(i)}(t)$ proportional to the i-th power of $\mathcal{C}_{kj}$. Trivially, the zero orders are

$$b^{(0)}(t) = b e^{-i\omega_0 t}, \quad a_k^{(0)}(t) = a_k e^{-i\omega_k t}, \tag{4.13}$$

while, the first order corrections result

$$\begin{aligned} b^{(1)}(t) = \frac{i}{\hbar}\sum_{kj}\mathcal{C}_{kj}e^{-i\omega_0 t}[&a_k a_j\ f(\omega_0-\omega_k-\omega_j) + a_j^\dagger a_k\ f(\omega_0-\omega_k+\omega_j) \\ &+ a_k^\dagger a_j\ f(\omega_0+\omega_k-\omega_j) + a_k^\dagger a_j^\dagger\ f(\omega_k+\omega_j+\omega_0)], \\ a_k^{(1)}(t) = \frac{2i}{\hbar}\sum_{j}\mathcal{C}_{kj}e^{-i\omega_k t}[&a_j b; f(\omega_k-\omega_j-\omega_0) + a_j b^\dagger\ f(\omega_k-\omega_j+\omega_0) \\ &+ a_j^\dagger b\ f(\omega_k+\omega_j-\omega_0) + a_j^\dagger b^\dagger\ f(\omega_k+\omega_j+\omega_0)], \end{aligned} \tag{4.14}$$

where we have defined

$$f(\omega, t) = \int_0^t e^{i\omega\tau}d\tau = \frac{e^{i\omega t}-1}{i\omega}, \tag{4.15}$$

and all operators without an explicit time dependence are considered at time $t = 0$. By using the series expansion of the annihilation and creation operators and considering only terms up to the second order in the coupling constant, the time-dependent interaction energy can be written as a sum of two different contributions, $\mathcal{H}_{\text{int}}^{(2)}(t) = \mathcal{H}_{\text{int,a}}^{(2)}(t) + \mathcal{H}_{\text{int,b}}^{(2)}(t)$, where

$$\begin{aligned} \mathcal{H}_{\text{int,a}}^{(2)}(t) = -\sum_{kj}\mathcal{C}_{kj}\left[b^{(0)}(t) + b^{\dagger^{(0)}}(t)\right]\Big[&a_k^{(1)}(t)a_j^{(0)}(t) + a_k^{\dagger^{(1)}}(t)a_j^{\dagger^{(0)}}(t) + a_k^{\dagger^{(1)}}(t)a_j^{(0)}(t) \\ &+ a_j^{\dagger^{(1)}}(t)a_k^{(0)}(t) + \{(1)\leftrightarrow(0)\}\Big], \end{aligned} \tag{4.16}$$

is obtained by substituting the zero-th order mirror operator $b^{(0)}(t)$ and the first-order field operator $a_k^{(1)}(t)$, while

$$\begin{aligned} \mathcal{H}_{\text{int,b}}^{(2)}(t) = -\sum_{kj}\mathcal{C}_{kj}\left[b^{(1)}(t) + b^{\dagger^{(1)}}(t)\right]\Big[&a_k^{(0)}(t)a_j^{(0)}(t) + a_k^{\dagger^{(0)}}(t)a_j^{\dagger^{(0)}}(t) \\ &+ a_k^{\dagger^{(0)}}(t)a_j^{(0)}(t) + a_j^{\dagger^{(0)}}(t)a_k^{(0)}(t)\Big], \end{aligned} \tag{4.17}$$

the first-order correction $b^{(1)}(t)$ for the mirror operator and the zero-th order $a_k^{(0)}(t)$ for the field operator. We remark that in the the last term of (4.16) the two indices (0) and (1) within curly brackets have been swapped. Now, by inserting Eqs. (4.13) and (4.14) into (4.16) and (4.17), we obtain

$$\begin{aligned}
\mathcal{H}^{(2)}_{\text{int,a}}(t) = &-\frac{2i}{\hbar}\mathcal{C}_{kj}\left(be^{-i\omega_0 t} + b^\dagger e^{i\omega_0 t}\right) \\
&\times \Bigg\{ e^{-i(\omega_j+\omega_k)t}\Bigg[\sum_{j'}\mathcal{C}_{jj'}a_k\big[a_{j'}b\ f(\omega_j-\omega_{j'}-\omega_0) + a_{j'}b^\dagger\ f(\omega_j-\omega_{j'}+\omega_0) \\
&\qquad + a^\dagger_{j'}b\ f(\omega_j+\omega_{j'}-\omega_0) + a^\dagger_{j'}b^\dagger\ f(\omega_j+\omega_{j'}+\omega_0)\big] \\
&\qquad + \mathcal{C}_{kj'}\big[a_{j'}b\ f(\omega_k-\omega_{j'}-\omega_0) + a_{j'}b^\dagger\ f(\omega_k-\omega_{j'}+\omega_0) \\
&\qquad + a^\dagger_{j'}b\ f(\omega_k+\omega_{j'}-\omega_0) + a^\dagger_{j'}b^\dagger\ f(\omega_k+\omega_{j'}+\omega_0)\big]a_j\Bigg] \\
&\quad + e^{i(\omega_k-\omega_j)t}\Bigg[\sum_{j'}\mathcal{C}_{jj'}a^\dagger_k\big[a_{j'}b\ f(\omega_j-\omega_{j'}-\omega_0) + a_{j'}b^\dagger\ f(\omega_j-\omega_{j'}+\omega_0) \\
&\qquad + a^\dagger_{j'}b\ f(\omega_j+\omega_{j'}-\omega_0) + a^\dagger_{j'}b^\dagger\ f(\omega_j+\omega_{j'}+\omega_0)\big] \\
&\qquad + \mathcal{C}_{kj'}\big[a^\dagger_{j'}b^\dagger\ f^*(\omega_k-\omega_{j'}-\omega_0) + a^\dagger_{j'}b^\dagger\ f^*(\omega_k-\omega_{j'}+\omega_0) \\
&\qquad + a_{j'}b^\dagger\ f^*(\omega_k+\omega_{j'}-\omega_0) + a_{j'}b\ f^*(\omega_k+\omega_{j'}+\omega_0)\big]a_j\Bigg] + H.c.\Bigg\},
\end{aligned} \tag{4.18}$$

$$\begin{aligned}
\mathcal{H}^{(2)}_{\text{int,b}}(t) = &-\frac{i}{\hbar}\sum_{kj}\sum_{k'j'}\mathcal{C}_{kj}\mathcal{C}_{k'j'} \\
&\times \Big\{ a_{k'}a_{j'}\left[e^{-i\omega_0 t}\ f(\omega_0-\omega_{k'}-\omega_{j'}) - e^{i\omega_0 t}\ f^*(\omega_0+\omega_{k'}+\omega_{j'})\right] \\
&\qquad + a^\dagger_{k'}a_{j'}\left[e^{-i\omega_0 t}\ f(\omega_0+\omega_{k'}-\omega_{j'}) - e^{i\omega_0 t}\ f^*(\omega_0-\omega_{k'}+\omega_{j'})\right] - H.c.\Big\} \\
&\times \left[a_k a_j e^{-i(\omega_k+\omega_j)t} + a^\dagger_k a^\dagger_j e^{i(\omega_k+\omega_j)t} + a^\dagger_k a_j e^{i(\omega_k-\omega_j)t} + a^\dagger_j a_k e^{i(\omega_k-\omega_k)t}\right],
\end{aligned} \tag{4.19}$$

which averaged over the the initial bare state $|\Psi_B\rangle$ yield

$$\begin{aligned}
\langle\Psi_B|\,\mathcal{H}^{(2)}_{\text{int,a}}(t)\,|\Psi_B\rangle &= -\frac{2i}{\hbar}\sum_{kj}\mathcal{C}^2_{kj}e^{-i\omega_0 t}[e^{i(\omega_k+\omega_j)t}\ f^*(\omega_k+\omega_j-\omega_0) \\
&\qquad - e^{-i(\omega_j+\omega_k)}\ f(\omega_j+\omega_k+\omega_0)], \\
\langle\Psi_B|\,\mathcal{H}^{(2)}_{\text{int,b}}(t)\,|\Psi_B\rangle &= -\frac{2i}{\hbar}\sum_{kj}\mathcal{C}^2_{kj}e^{i(\omega_k+\omega_j)t}\left[e^{-i\omega_0 t}\ f(\omega_0-\omega_j-\omega_k)\right. \\
&\qquad \left. -e^{i\omega_0 t}\ f^*(\omega_j+\omega_k+\omega_0)\right].
\end{aligned} \tag{4.20}$$

Summing up the results in (4.20), and using the expression (4.7), we can finally obtain the second-order local dynamical energy shift

$$\mathcal{E}^{(2)}_{\text{loc,dyn}}(t) = -\frac{\hbar^2}{4L_0^2 M}\sum_{kj}\frac{\omega_k\omega_j}{\omega_0}\frac{1}{\omega_0+\omega_k+\omega_j}\left\{1-\cos\left[(\omega_0+\omega_k+\omega_j)\,t\right]\right\}, \tag{4.21}$$

which, describes the *local* interaction between field and mobile wall. Some comments on Eq. (4.21) are now in order. As we can immediately see at $t = 0$ it vanishes, since at this time the interaction has not taken place yet. On the other hand, we want to know what happens in the opposite situation, that is when we consider large times. This scenario should correspond to the stationary regime for the system. Firstly, let us then discuss such interesting limit in the case where we have a continuous of modes in the cavity, which means to bring the cavity length to infinity ($L \to \infty$). We then substitute the sum over the two indices i, j with two integrals over the frequencies: $\sum_{kj} \to L^2/(2\pi)^2 \int_0^\infty \int_0^\infty dk dk'$. Equation (4.21) can be rewritten as

$$\mathcal{E}^{(2)}_{\text{loc,dyn}}(t) = -\frac{\hbar^2\omega_0^2}{16\pi^2 Mc^2}\int_0^\infty dx \int_0^\infty dx' \frac{xx'}{1+x+x'}\left\{1-\cos\left[a\left(1+x+x'\right)t\right]\right\}, \tag{4.22}$$

where $a = \omega_0 t$ and $x = ck/\omega_0$. In the limit $t \to \infty$ the cosine function appearing in Eq. (4.22) rapidly oscillates and eventually vanishes, giving the following limit for the energy shift:

$$\mathcal{E}^{(2)}_{\text{loc,dyn}}(t) \longrightarrow \mathcal{E}^{(2)}_{\text{stat}}. \tag{4.23}$$

The local dynamical energy shift coincides with the static result for the overall energy shift of the system in Eq. (4.10), where the state of the system is in the fully dressed configuration. This confirms that the generalization of the static second-order energy shift to the dynamical case in Eq. (4.2) is physically sound. The same procedure has also provided consistent results for the dynamical Casimir-Polder interaction energy between an initially bare or partially dressed atom and a perfectly conducting wall [63, 150, 161].

As can be clearly seen from Eq. (4.22) to calculate the dynamical energy shift (as in the case of the static one), we need to introduce an ultraviolet cutoff frequency. We again emphasize that this is not just a pure mathematical regularization for allowing a finite result. Indeed, the introduction of a cutoff is well-motivated from a physical point of view, since a real conducting wall is always characterized by a plasma frequency, and cavity modes with frequencies higher than the plasma frequency do not see the boundary, thus not contributing to the effective wall-field interaction. Therefore, by using a sharp cutoff frequency, the integrals appearing in Eq. (4.22) can be numerically evaluated: the result is plotted in Fig. 4.2. This shows that

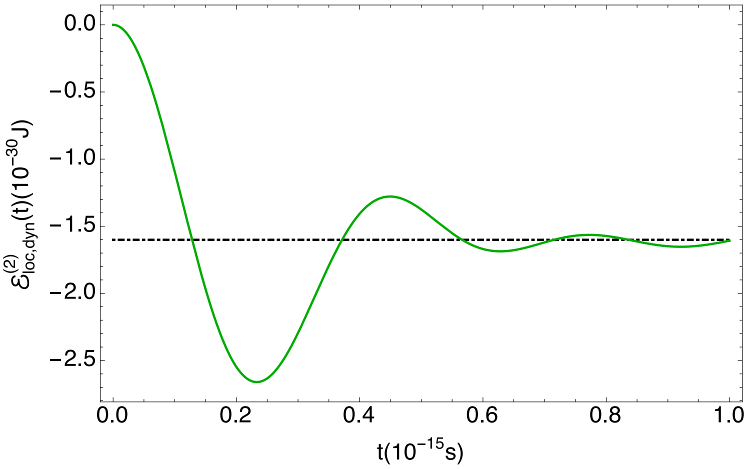

Figure 4.2: The plot (green continuous line) shows the time evolution of the local dynamical interaction energy shift of the system in the continuous limit (Eq.(4.22)), i.e. when the length of the cavity goes to infinity. It shows oscillations around its stationary value ($t \to \infty$) represented by the black dot-dashed line, which coincides with the overall energy shift in the fully dressed configuration (Eq. (4.10)). There are time intervals where the dynamical interaction energy is larger than its stationary value. The numerical values used for the mass and frequency of the movable mirror are respectively $\omega_0 = 10^4 s^{-1}$ and $M = 10^{-14}$Kg, while the cutoff frequency has been set to $\omega_{\text{cut}} = 10^{16} s^{-1}$.

the interaction energy vanishes at $t = 0$ and, at successive times, shows oscillations around its stationary limit $\mathcal{E}^{(2)}_{\text{stat}}$. Moreover, at specific time intervals, the absolute value of the dynamical interaction energy can be larger than in the static case, thus leading to an increase of the Casimir energy of the system. This could be a relevant feature to use for observing the dynamical effect.

To deeply understand the dynamical dressing process it is necessary to compare the local dynamical energy shift in Eq. (4.21) with the dynamical shifts related to the unperturbed Hamiltonians of field and mirror, thus separating the single contributions from the overall energy shift. We follow the same procedure substituting the perturbative solutions (4.14) for mirror and field operators into the expressions of field and mirror Hamiltonians. After the average over the the initial bare state of the system $|\Psi_B\rangle$, we get

$$\begin{aligned}\mathcal{E}^{(2)}_{\text{f,dyn}}(t) &= \langle\Psi_B|\,\mathcal{H}^{(2)}_{\text{f}}(t)\,|\Psi_B\rangle \\ &= \frac{\hbar^2}{L_0^2 M}\sum_{kj}\frac{\omega_k^2\omega_j}{\omega_0}\frac{1}{(\omega_0+\omega_k+\omega_j)^2}\left\{1-\cos[(\omega_0+\omega_k+\omega_j)t]\right\},\end{aligned} \tag{4.24}$$

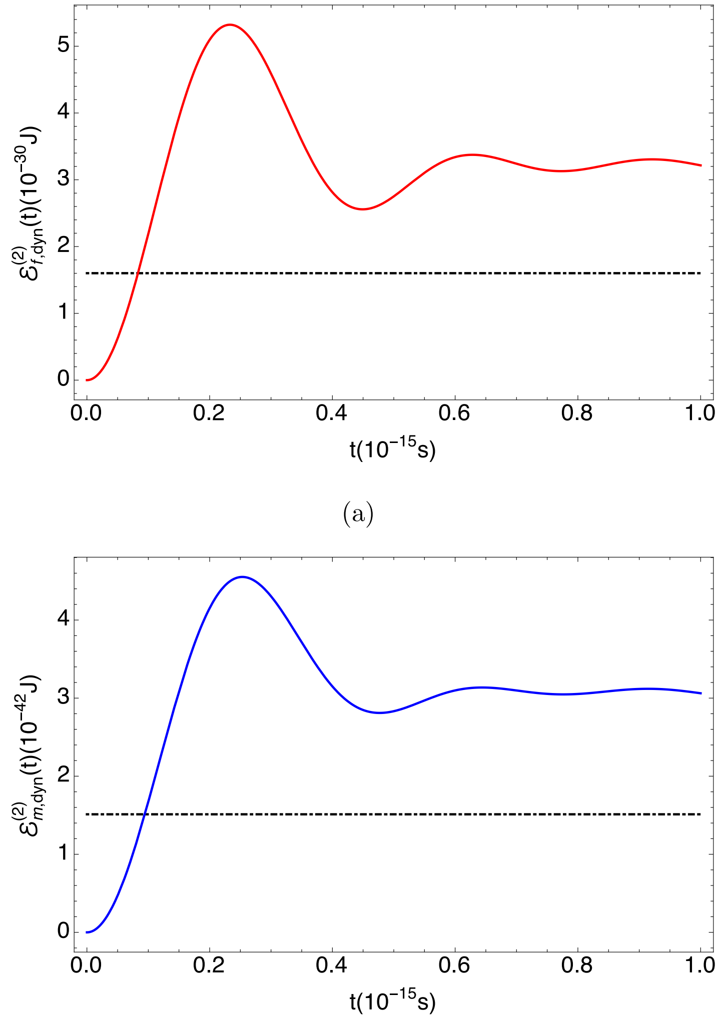

(a)

(b)

Figure 4.3: Time evolution of dynamical energy shifts in the continuous limit $L \to \infty$ (Eq. (4.27)): (a) field energy (red continuous line); (b) mirror energy (blue continuous line). Their dynamics shows oscillations which tend to twice the corresponding stationary value, represented by the black dot-dashed line. The numerical values of the parameters are the same as in the plot in Fig. 4.2.

$$
\begin{aligned}
\mathcal{E}^{(2)}_{\rm m,dyn}(t) &= \langle \Psi_B | \, \mathcal{H}^{(2)}_{\rm m}(t) \, | \Psi_B \rangle \\
&= \frac{\hbar^2}{2L_0^2 M} \sum_{kj} \frac{\omega_k \omega_j}{(\omega_0 + \omega_k + \omega_j)^2} \left\{ 1 - \cos[(\omega_0 + \omega_k + \omega_j) t] \right\} .
\end{aligned} \tag{4.25}
$$

This immediately tells us that overall dynamical energy shift is zero

$$
\langle \Psi_B | \, \mathcal{H}^{(2)}(t) \, | \Psi_B \rangle = 0, \tag{4.26}
$$

as expected given that the system undergoes a unitary evolution from the non-equilibrium initial state $|\Psi_B\rangle$, i.e. the total energy of the system is conserved. In the continuous limit for the cavity modes Eqs. (4.24) and (4.25) become

$$\begin{aligned}\mathcal{E}^{(2)}_{\mathrm{f,dyn}}(t) &= \frac{\hbar^2\omega_0^2}{4\pi^2 Mc^2}\int_0^\infty dx\int_0^\infty dx'\frac{x^2x'}{(1+x+x')^2}\left\{1-\cos\left[a\left(1+x+x'\right)t\right]\right\}\\ \mathcal{E}^{(2)}_{\mathrm{m,dyn}}(t) &= \frac{\hbar^2\omega_0^2}{8\pi^2 Mc^2}\int_0^\infty dx\int_0^\infty dx'\frac{xx'}{(1+x+x')^2}\left\{1-\cos\left[a\left(1+x+x'\right)t\right]\right\},\end{aligned} \tag{4.27}$$

which provide the following limits for large times ($t\to\infty$):

$$\begin{aligned}\mathcal{E}^{(2)}_{\mathrm{f,dyn}}(t) &\longrightarrow 2\mathcal{E}^{(2)}_{\mathrm{f,stat}},\\ \mathcal{E}^{(2)}_{\mathrm{m,dyn}}(t) &\longrightarrow 2\mathcal{E}^{(2)}_{\mathrm{m,stat}}.\end{aligned} \tag{4.28}$$

Both the dynamical energies stored in the field and in the mirror tend to twice their stationary values, as shown in Fig. 4.3. On the contrary, using Eqs. (4.2) and (4.22), we find that at large times the energy stored in the interaction Hamiltonian approaches its stationary value, which is equal to twice the total energy shift of the system in the equilibrium (fully dressed) configuration:

$$\mathcal{E}^{(2)}_{\mathrm{int,dyn}} \longrightarrow \mathcal{E}^{(2)}_{\mathrm{int,stat}} = 2\mathcal{E}^{(2)}_{\mathrm{stat}}. \tag{4.29}$$

Therefore, during the dressing process, since the energy stored in the interaction will approach its stationary value, field and mirror have to raise their energy to preserve the energy conservation. Furthermore, the additional energy stored in field and oscillator takes into account the energy difference between the two initial configurations for the stationary and the dynamical regimes (dressed and bare, respectively). A subtle and very general aspect of the approach to equilibrium of our system is then revealed: a *local* quantity such as the mirror-field interaction energy (localized at the mirror's position) approaches its stationary value, contrarily to *global* quantities such as the field energy, which include contributions from the field emitted during the self-dressing [162, 163] and propagating at very large distances. Indeed, the same happens for the dynamical dressing and related Casimir-Polder energies of an atom close to a conducting wall, which will be investigated in the next Section.

So far the large time limit has been discussed in the case of $L\to\infty$, that is for the dynamical dressing of a single wall interacting with the field vacuum fluctuations. We now want to address such limit for Eqs. (4.21), (4.24), (4.25), thus considering a discrete number of cavity modes (a finite distance between the walls). Actually, the result of the limits in (4.23), (4.28), and (4.29) can be extended to the case of a finite cavity length as long as we consider times shorter than the round trip time of a photon inside the cavity $\bar{t} = 2L/c$. Whereas, for $t = n\bar{t}$ (with

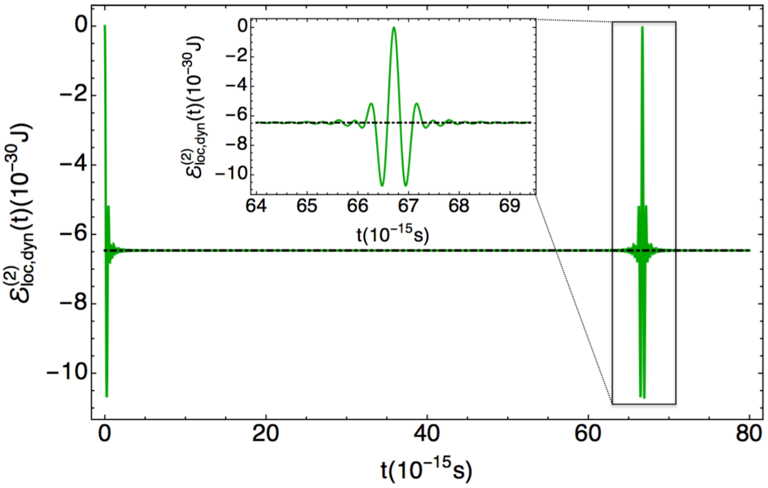

Figure 4.4: The plot (green continuous line) shows the time evolution of the dynamical interaction energy shift of the system in the case of a finite value for the distance between the walls. After the oscillations around its stationary value (represented by the black dot-dashed line) the energy shift approaches its stationary value to then reappear again. The revivals occur for integer multiples of the round trip time $\bar{t} = 2L/c$. We have used $L = 10^{-5}$, the other numerical values are as in Fig. 4.2.

n a non-negative integer) Eq. (4.21) shows a revival, as Fig. 4.4 shows (of course, the same happens for (4.24) and (4.25)). This feature is a distinctive trait of our system, which does not find a correspondence in the study of the dynamical Casimir-Polder force between atom and wall that we will face in the next section. In fact, we will see that in this latter case the radiation emitted by the atom, which is in part reflected by the wall, propagates to infinity, no longer participating to the dynamical dressing of the wall. On the other hand, in the present case, the radiation emitted at the proximity of the movable wall propagates along the cavity and then is reflected by the fixed mirror, thus revealing these revivals. However, when we take the continuous limit ($L \to \infty$), we let this energy propagate to infinity, thereby ensuring that it does not contribute to the dressing process.

4.3.4 Two cavities scenario

The Hamiltonian in Eq. (4.6) neglects the effect of the electromagnetic field in the regions external to the plates. This is usually a good approximation in quantum optics, for example, where strong single or multimode fields are coupled to the mobile mirror [2, 4]. However, when studying effects arising from the presence of vacuum fluctuations the inclusion of the external field to the cavity might become relevant. We then want to generalize our model to include the effect of the vacuum field fluctuations on the right side of the movable mirror on the dynamical dressing process of the system. In other words, we consider two distinct cavities sharing the same movable mirror (see Fig. 4.1). Since we assume to have a perfectly reflective movable mirror for both cavities, the effective Hamiltonian (4.6) can be easily generalized to this new case. The unperturbed and interaction Hamiltonians can be rewritten as

$$\begin{aligned} \tilde{\mathcal{H}}_0 &= \hbar\omega_0 b^\dagger b + \hbar \sum_k \sum_{l=1}^{2} [\omega_{k,l} a^\dagger_{k,l} a_{k,l}], \\ \tilde{\mathcal{H}}_{\text{int}} &= -(b+b^\dagger) \sum_{kj} \sum_{l=1}^{2} \mathcal{C}^l_{kj} [a_{k,l} a_{j,l} + a^\dagger_{j,l} a_k + a^\dagger_{k,l} a_{j,l} + a^\dagger_{k,l} a^\dagger_{j,l}], \end{aligned} \tag{4.30}$$

where $a_{k,1}$ ($a_{k,2}$) are the field operators for the two cavities, while L_i and $\omega_{k,i} = ck\pi/L_i$ with $i = 1,2$ the generic equilibrium frequencies and lengths of the two cavities. The new coupling constants $\mathcal{C}^1_{kj}$ and $\mathcal{C}^2_{kj}$ are accordingly modified, though preserving the same form as in Eq. (4.7). We however highlight that if we take the value of $\mathcal{C}^1_{kj}$ as that given by (4.7), the value of $\mathcal{C}^2_{kj}$ must be taken with the opposite sign. In fact, in the expansion in the mirror's displacement around its equilibrium position performed in paragraph 1.2.2, the linear term has a different sign depending on the direction of the wall's displacement [4]. We also want to stress that the generalization in Eq. (4.30) is possible since (4.6) is an *effective* Hamiltonian, which means that the interaction between cavity modes and mechanical degrees of freedom is encoded in its operational form and not in the physical parameters such as the cavity length or frequency (indeed related to the equilibrium position of the moving wall).

Similarly to the single-cavity case, the equations of motion for mirror and field operators at the zeroth and first order in the coupling constant result

$$b^{(0)}(t) = b e^{-i\omega_0 t},\ a^{(0)}_{k,l}(t) = a_{k,l} e^{-i\omega_{k,l} t}, \tag{4.31}$$

$$\begin{aligned} b^{(1)}(t) = \frac{i}{\hbar} e^{-i\omega_0 t} \sum_{kj} \sum_{l=1}^{2} \mathcal{C}^l_{kj} \big[& a_{k,l} a_{j,l}\, f(\omega_0 - \omega_{k,l} - \omega_{j,l}) + a^\dagger_{j,l} a_{k,l}\, f(\omega_0 - \omega_{k,l} + \omega_{j,l}) \\ & + a^\dagger_{k,l} a_{j,l}\, f(\omega_0 + \omega_{k,l} - \omega_{j,l}) + a^\dagger_{k,l} a^\dagger_{j,l}\, f(\omega_{k,l} + \omega_{j,l} + \omega_0) \big], \\ a^{(1)}_{k,l}(t) = \frac{2i}{\hbar} \sum_j \mathcal{C}^l_{jk} e^{-i\omega_{k,l} t} \big[& a_{j,l} b\, f(\omega_{k,l} - \omega_{j,l} - \omega_0) + a_{j,l} b^\dagger\, f(\omega_{k,l} - \omega_{j,l} + \omega_0) \\ & + a^\dagger_{j,l} b\, f(\omega_{k,l} + \omega_{j,l} - \omega_0) + a^\dagger_{j,l} b^\dagger\, f(\omega_{k,l} + \omega_{j,l} + \omega_0) \big], \end{aligned} \tag{4.32}$$

where again the operators without an explicit time-dependence must be considered at $t = 0$. These equations show that, at the second order in the coupling constants, fields operators are independent, contrarily to the mirror operator which instead depends on both field operators. The fields inside the two cavities can then interact one with the other only through the mirror displacement operator.

Let us now study how the mirror's dressing process is modified by the interaction with the two different cavity fields. We again take as initial state ($t = 0$) a bare state where both mirror and cavity fields are in the vacuum state, and insert Eqs. (4.31) and (4.32) into the interaction Hamiltonian (4.30) and then in (4.2). After calculating the expectation value on the initial bare state, we find the local dynamical energy shift of the system

$$\begin{aligned}\tilde{\mathcal{E}}^{(2)}_{\text{loc,dyn}}(t) &= \frac{\langle\Psi_B|\,\tilde{\mathcal{H}}^{(2)}_{\text{int}}(t)\,|\Psi_B\rangle}{2} \\ &= -\frac{\hbar^2}{4M}\sum_{kj}\sum_{l=1}^{2}\frac{1}{(L_l)^2}\frac{\omega_{k,l}\omega_{j,l}}{\omega_0}\frac{1}{\omega_0+\omega_{k,l}+\omega_{j,l}}\left\{1-\cos\left[(\omega_0+\omega_{k,l}+\omega_{j,l})t\right]\right\}\end{aligned} \tag{4.33}$$

In the particular case of two cavities with the same equilibrium length L, we get

$$\tilde{\mathcal{E}}^{(2)}_{\text{loc,dyn}}(t) = 2\mathcal{E}^{(2)}_{\text{loc,dyn}}(t), \tag{4.34}$$

which says that the local energy shift is twice the local energy shift obtained in the case of a movable mirror interacting with a single cavity field. This result completes our study of the dressing process of a single wall in the presence of the electromagnetic vacuum, since one can easily consider the limit $L \to \infty$ for both cavities. In addition, Eq. (4.34) shows that the dressing process of the wall with the two semi-spaces occurs independently, although the two semi-spaces can interact one with the other through the mirror operators. However, we expect that this behavior holds up to the second order in the coupling constant. At the fourth order, which is the next not-vanishing, the independence of tho cavity fields should be lost, and, as a consequence, the dressing process of the wall with the two semi-spaces should result correlated, possibly revealing new interesting modifications of the Casimir force between two (fixed) walls when a perfectly conducting mobile wall is inserted between them.

4.4 Dynamical Casimir-Polder force between an excited atom and a conducting wall

4.4.1 Dynamical energy shift

We now consider a two-level atom placed near a perfectly conducting wall at $z = 0$ in the presence of a quantum electromagnetic field in its vacuum state, as described in paragraph 1.3.4. In the multipolar coupling scheme and within the dipole approximation, the atom-field interaction $\mathcal{H}_{\text{int}}$ is given by Eq. (1.53), while the bare Hamiltonian of atom and field are given by the first two lines of Eq. (1.43), respectively. To obtain the time-dependent atom-plate Casimir-Polder force, we again follow the procedure outlined in Eqs. (4.2) and (4.4), which follow the one used in [63, 150]. Firstly, we solve iteratively the Heisenberg equations for the field and atomic operators at the lowest significant order [164], obtaining

$$\begin{aligned} a_{\mathbf{k}j}(t) &= e^{-i\omega_k t} a_{\mathbf{k}j}(0) + e^{-i\omega_k t}\sqrt{\frac{2\pi\omega_k}{\hbar V}}[\boldsymbol{\mu}\cdot\mathbf{f}_{\mathbf{k}j}(\mathbf{r})] \\ &\qquad \times [S_+(0)\, f(\omega_{\mathrm{a}}+\omega_k, t) + S_-(0)\, f(\omega_k-\omega_{\mathrm{a}}, t)], \\ S_\pm(t) &= e^{\pm i\omega_{\mathrm{a}} t} S_\pm(0) \mp 2S_z(0) e^{\pm i\omega_{\mathrm{a}} t}\sum_{kj}\sqrt{\frac{2\pi\omega_k}{\hbar V}}[\boldsymbol{\mu}\cdot\mathbf{f}_{\mathbf{k}j}(\mathbf{r})] \\ &\qquad \times [a_{\mathbf{k}j}(0)\, f^*(\omega_k \pm \omega_{\mathrm{a}}, t) - a^\dagger_{\mathbf{k}j}(0)\, f(\omega_k \mp \omega_{\mathrm{a}}, t)], \end{aligned} \tag{4.35}$$

where the function $f(\omega, t)$ is defined as in Eq. (4.15). Secondly, we need to calculate the dynamical atom-plate Casimir-Polder interaction during the dynamical self-dressing process of the excited atom. By using stationary second-order perturbation theory, we have already shown in Eq. (4.1) that the second-order energy shift of the overall system can be obtained by averaging the time-independent interaction Hamiltonian $\mathcal{H}_{\text{int}}$ over the dressed (i.e. perturbed) state of the system $|\Psi_D\rangle$ obtained by second-order perturbation theory. In this context, Eq. (4.1) establishes an important connection between the overall energy shift of the system and the local electromagnetic field felt by the atom at its position. The time-dependent Casimir-Polder energy shift can be then calculated by using the appropriate generalization of Eq. (4.1) given in (4.2), which has been already used in Refs. [63, 150]. We thus proceed calculating the interaction Hamiltonian in the Heisenberg representation at the second-order in the coupling $\mathcal{H}^{(2)}_{\text{int}}(t)$ by substituting Eqs. (4.35) into the interaction energy (1.53). After some algebra, we obtain

$$
\begin{aligned}
\mathcal{H}^{(2)}_{\text{int}}(t) = &-\frac{2\pi i c}{V}\sum_{kj} k[\boldsymbol{\mu}\cdot\mathbf{f}_{\mathbf{k}j}(\mathbf{r})]^2[S_+(0)e^{i\omega_{\mathrm{a}}t}+h.c] \\
&\qquad\times\left\{S_+(0)\left[e^{-i\omega_k t}\, f(\omega_{\mathrm{a}}+\omega_k,t)-e^{i\omega_k t}\, f^*(\omega_k-\omega_{\mathrm{a}},t)\right]-H.c\right\} \\
&+\frac{4\pi i c}{V}S_z(0)\sum_{\mathbf{kk'}jj'}\sqrt{kk'}[\boldsymbol{\mu}\cdot\mathbf{f}_{\mathbf{k}j}(\mathbf{r})][\boldsymbol{\mu}\cdot\mathbf{f}_{\mathbf{k'}j'}(\mathbf{r})] \\
&\qquad\times\left\{a_{\mathbf{k'}j'}(0)[e^{i\omega_{\mathrm{a}}t}\, f^*(\omega_{\mathrm{a}}+\omega_{k'},t)-e^{-i\omega_{\mathrm{a}}t}\, f^*(\omega_{k'}-\omega_{\mathrm{a}},t)]+H.c\right\}[a_{\mathbf{k}j}(0)e^{-i\omega_k t}-H.c]
\end{aligned}
\tag{4.36}
$$

Taking the atom in its excited state and the field in the vacuum state as initial configuration at $t=0$, the dynamical energy shift can be thus evaluated by averaging Eq. (4.36) on the initial bare state of the system $|\Psi_B\rangle = |\{0_{\mathbf{k}j}\},\uparrow\rangle$ as

$$
\begin{aligned}
\mathcal{E}^{(2)}_{\uparrow\text{loc,dyn}}(t) &= \frac{\langle\{0_{\mathbf{k}j}\},\uparrow|\,\mathcal{H}_{\text{int}}(t)\,|\{0_{\mathbf{k}j}\},\uparrow\rangle}{2} \\
&= -i\frac{\pi c}{V}\sum_{kj} k[\boldsymbol{\mu}\cdot\mathbf{f}_{\mathbf{k}j}(\mathbf{r})]^2[e^{-i(\omega_k-\omega_{\mathrm{a}})t}\, f(\omega_k-\omega_{\mathrm{a}},t)-e^{i(\omega_k-\omega_{\mathrm{a}})t}\, f^*(\omega_k-\omega_{\mathrm{a}},t)].
\end{aligned}
\tag{4.37}
$$

We remark that (4.37) assumes that the time-dependent interaction energy, in analogy to the static case, can be obtained by the local interaction energy between atom and field at the specific atomic position. We however note that the overall energy shift of the system is time-independent due to the unitary time evolution. Nevertheless, as we shall discuss below in more detail, in the limit of large times (4.37) will give back the correct expression of the static atom-plate Casimir-Polder force.

In the continuum limit, after a sum over polarizations and angular integrations, we finally get

$$
\begin{aligned}
\mathcal{E}^{(2)}_{\uparrow\text{loc,dyn}}(d,t) &= -\frac{\mu^2}{4\pi d^3}\int_0^\infty \frac{-2x\cos[x]+(2-x^2)\sin[x]}{x-x_0}\left\{1-\cos[a(x-x_0)]\right\}\,dx \\
&= -\frac{\mu^2}{4\pi d^3}\lim_{m\to 1}\left[\mathcal{D}_m\left(\int_0^\infty \frac{\sin(mx)}{x-x_0}\,dx-\int_0^\infty\frac{\sin(mx)}{x-x_0}\cos[a(x-x_0)]\,dx\right)\right], \\
\text{where}\qquad \mathcal{D}_m &= 2-2\frac{\partial}{\partial m}+\frac{\partial^2}{\partial m^2}
\end{aligned}
\tag{4.38}
$$

is a differential operator, $z=d$ is the atom-wall distance, $x=2kd$, $x_0=2k_a d$, and $a=ct/2d$. For the sake of simplicity, we have assumed an isotropic atom, i.e $\mu_x^2=\mu_y^2=\mu_z^2=\mu^2/3$. From the second line of Eq. (4.38) we can see that two terms (integrals) contribute to the dynamical energy shift. The first is time-independent and gives the Casimir-Polder energy shift for an excited atom as obtained with a time-independent approach in Eq. (1.56). The second term is

time-dependent and it is related to the dynamical dressing of the excited atom. The presence of a pole for $k = k_{\mathrm{a}}$ in the static part takes into account the possibility of emission of a real photon by the excited atom, and it is responsible of the well-known oscillatory behavior of the static atom-wall Casimir-Polder force [60, 62]. However, our overall dynamical result does not display poles in the integration over the field frequency, as the first line of (4.38) clearly shows. By explicitly calculating the time-dependent term in (4.38) one can verify that, after a transient time yielding a time-dependent Casimir-Polder interaction, it vanishes asymptotically in time bringing the interaction energy to its stationary value. The stationary result found in Eq. (1.56) is thus correctly recovered for $t \to \infty$.
We also find that at the round-trip time, that is when $a = 2d/ct = 1$, the energy shift diverges similarly to what happens for a system initially in the ground state [63]. Such behavior is a manifestation of well-known divergences of the radiation reaction and source fields on the light cone in case of point-like sources [165]. Their complete removal is still an open problem in QED [8, 166]. Similar singularities are also found for the field energy densities near a reflecting surface [167–169]. This is the reason why, in the subsequent calculation of the dynamical atom-wall Casimir-Polder force, we are going to consider two separate temporal regions: before and after the *back-reaction* (or round-trip) time, i.e. $t < 2d/c$ and $t > 2d/c$.

We now want to discuss a conceptually subtle issue about the asymptotic limit $t \to \infty$ (or large-time limit), which, on the other hand, can only consider times shorter than the decay time of the excited state because of our perturbative approach. Our result in (4.38) shows that

$$\lim_{t\to\infty} \mathcal{E}^{(2)}_{\uparrow\mathrm{loc,dyn}}(d,t) = \mathcal{E}^{(2)}_{\uparrow\mathrm{stat}}(d), \tag{4.39}$$

where $\mathcal{E}^{(2)}_{\uparrow\mathrm{stat}}(d)$ is the correspondent stationary value as obtained by the usual time-independent approach. However, a similar relation does not hold for all physical quantities: the asymptotic approach to the corresponding stationary values for the expectation values of quantities only related to the field or the atom should not be taken for granted. In fact, if we calculate the time-dependent expectation values of the atomic, field, and interaction energy ($\langle \mathcal{H}^{(2)}_{\mathrm{a}}(t)\rangle$, $\langle \mathcal{H}^{(2)}_{\mathrm{f}}(t)\rangle$ and $\langle \mathcal{H}^{(2)}_{\mathrm{int}}(t)\rangle$), we can verify that their sum is constant because the total energy is conserved, and differ from the static one (bare and dressed excited states have a different energy). Therefore, the average total energy of the interacting system does not settle to its static value for large times. As a result, this must also happen for the atomic and field energies. However, these results do not question the capability of the system to find some *local* equilibrium configuration, as Eq. (4.39) shows. Indeed, during the self-dressing process, the atom emits some radiation [170] that for $t \to \infty$ moves to very large distances. While this amount of energy does not affect the interaction energy with the atom, it still contributes to the total field energy. Ultimately, global quantities such as the total field energy do not approach their stationary values, while local field quantities such us the interaction energy reach their stationary values at any finite distance. In our specific case, this happens because the total field energy takes also into account the field energy density at a very large distance. This interplay between these physical quantities has also been suggested for the dynamical Casimir-Polder interaction between two atoms [171]. Consequently, we expect that quantities related to the local field energy-density distribution as the atom-field interaction, tend to their relative stationary value for $t \to \infty$, as proved by our result (4.39).

4.4.2 Dynamical Casimir-Polder force

As shown in Eq. (4.4), within the quasi-static approach, the dynamical Casimir-Polder force can be found by taking the derivative of the interaction energy (4.38) with respect to the atom-wall distance d:

$$F_{\uparrow}(d,t) = -\frac{\partial}{\partial d}\,\mathcal{E}^{(2)}_{\uparrow\mathrm{loc,dyn}}(d,t). \tag{4.40}$$

After tedious algebraic manipulations, the expression of the force can be written as

$$F_{\uparrow}(d,t) = F_{\mathrm{stat}}(d) + F_{\mathrm{dyn}}(d,t). \tag{4.41}$$

$F_{\mathrm{stat}}(d)$ is a time-independent term which corresponds to the limit $t \to \infty$ of the force. It actually coincides with the static force between an excited atom and a conducting wall that we obtained within a time-independent approach in Eq. (1.58) (second line). The time-dependent part of the force is instead given by

$$\begin{aligned}
F_{\mathrm{dyn}}(d,t) = \mu^2\Bigg\{ &\frac{1}{3\pi d^3}\,\frac{ct\,(16d^4(9-2d^2k_{\mathrm{a}}^2)+16c^2t^2d^2(-2+d^2k_{\mathrm{a}}^2)+c^4t^4(3-2d^2k_{\mathrm{a}}^2))\sin(ck_{\mathrm{a}}t)}{(4d^2+c^2t^2)^3} \\
&+\frac{4}{3\pi d}\,\frac{k_{\mathrm{a}}(-8d^2+c^2t^2)\cos(ck_{\mathrm{a}}t)}{(4d^2-c^2t^2)^2} \\
&+\frac{1}{12\pi d^4}\,\Big[(\mathrm{Ci}(2dk_{\mathrm{a}}-ck_{\mathrm{a}}t)+\mathrm{Ci}(2dk_{\mathrm{a}}+ck_{\mathrm{a}}t)) \\
&\qquad\qquad\times\big(2dk_{\mathrm{a}}(3-2d^2k_{\mathrm{a}}^2)\cos(2dk_{\mathrm{a}})+3(-1+2d^2k_{\mathrm{a}}^2)\sin(2dk_{\mathrm{a}})\big) \\
&\qquad+(\pi+\mathrm{Si}(ck_{\mathrm{a}}t+2dk_{\mathrm{a}})+\mathrm{Si}(2dk_{\mathrm{a}}-ck_{\mathrm{a}}t)) \\
&\qquad\qquad\times\big(3(1-2d^2k_{\mathrm{a}}^2)\cos(2dk_{\mathrm{a}})+2dk_{\mathrm{a}}(3-2d^2k_{\mathrm{a}}^2)\sin(2dk_{\mathrm{a}})\big)\Big]\Bigg\},
\end{aligned} \tag{4.42}$$

before the round-trip time ($t < 2d/c$), and by

$$
\begin{aligned}
F_{\mathrm{dyn}}(d,t) = \mu^2 \Bigg\{ & \frac{-4k_{\mathrm{a}}d^2\cos(ck_{\mathrm{a}}t) + ct(1-2d^2k_{\mathrm{a}}^2)\sin(ck_0t)}{3\pi d^3(4d^2-c^2t^2)} - \frac{16dk_a\cos(ck_at)}{3\pi(4d^2-c^2t^2)^2} \\
& + \frac{ct(64d^4-12c^2d^2t^2+c^4t^4)\sin(ck_{\mathrm{a}}t)}{3\pi d^3(4d^2-c^2t^2)^3} \\
& + \frac{1}{2\pi d^4}\big[(\mathrm{Ci}(ck_{\mathrm{a}}t+2dk_{\mathrm{a}}) + \mathrm{Ci}(ck_{\mathrm{a}}t-2dk_{\mathrm{a}})) \\
& \qquad\qquad \times \big(2dk_{\mathrm{a}}(3-2d^2k_{\mathrm{a}}^2)\cos(2dk_{\mathrm{a}}) + 3(-1+2d^2k_{\mathrm{a}}^2)\sin(2dk_{\mathrm{a}})\big) \\
& \qquad + (\mathrm{Si}(ck_{\mathrm{a}}t+2dk_{\mathrm{a}}) - \mathrm{Si}(ck_{\mathrm{a}}t-2dk_{\mathrm{a}})) \\
& \qquad\qquad \times \big(3(1-2d^2k_{\mathrm{a}}^2)\cos(2dk_{\mathrm{a}}) + 2dk_{\mathrm{a}}(3-d^2k_{\mathrm{a}}^2)\sin(2dk_{\mathrm{a}})\big)\big] \Bigg\},
\end{aligned}
\tag{4.43}
$$

after the round-trip time ($t > 2d/c$), where $\mathrm{Si}(x)$ and $\mathrm{Ci}(x)$ are the sine and cosine integral functions, respectively [64].

As expected from our previous discussion on the dynamical energy shift, the dynamical Casimir-Polder force in Eq. (4.41) has a singularity on the light-cone $t = 2d/c$. This might be reduced or smeared out by relaxing the assumptions of a point-like atom (dipole approximation) and of a perfectly reflecting mirror, which, on the other hand, fail at frequencies larger than c/a_0, with a_0 the Bohr's radius, and the mirror's plasma frequency ω_P, respectively. Since such high-frequency photons largely contribute around the round-trip time $t = 2d/c$, we expect our results not to be reliable within a time interval around the round-trip time of the order of the largest of a_0/c or ω_P^{-1} (to satisfy both assumptions). For example, using the numerical value of the plasma frequency of gold $\omega_P \simeq 1.4 \times 10^{16}\, s^{-1}$ and considering a hydrogen atom, times closer than about $7 \times 10^{-17}\,\mathrm{s}$ to the singularity at $t = 2d/c$ are outside our treatment.

The singular behavior of the force around the round-trip time can be seen in Figs. 4.5 (for $t < 2d/c$) and 4.6 (for $t > 2d/c$). From these plots we immediately notice that the dynamical force oscillates continuously switching sign from positive (repulsive) to negative (attractive) and viceversa. This also happens in the case of an atom initially prepared in a bare or partially dressed ground state near a perfectly conducting wall [63, 150] or a real surface [151], and for a chiral molecule [153]. Figure 4.5 also shows that the force vanishes at $t = 0$. This is because, in the case of a system initially prepared in the bare state, the atom-field interaction is suddenly "switched-on" at $t = 0$, which is also the time when the atomic dynamical dressing starts to take place. If we considered an initial partially dressed state, the force at $t = 0$ would not be zero, as discussed in [150]. Whereas, the non-vanishing value of the force before the round-trip

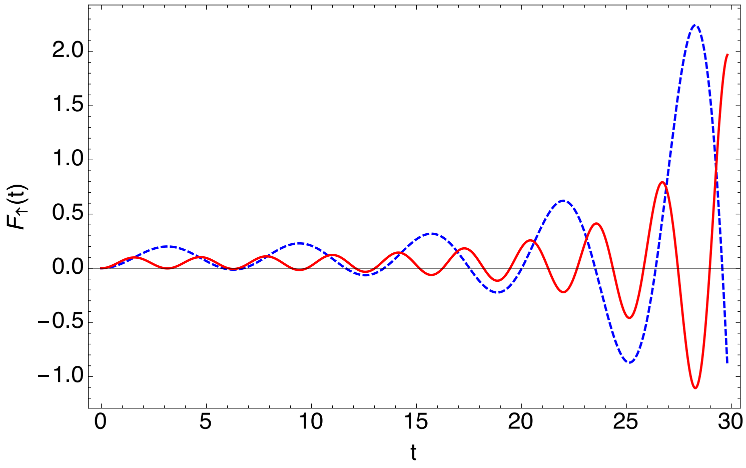

Figure 4.5: Time evolution of the dynamical Casimir-Polder force on the atom for times smaller than the round-trip time, that is for $t < 2d/c$ (force and time are both in arbitrary units). The atom-wall distance is $d = 20$, $c = 1$, so that the round-trip time is $t = 40$. The dashed (blue) and continuous (red) lines represent the force for $k_{\rm a} = 1$ and $k_{\rm a} = 2$, respectively. The plot shows time oscillations of the force and a strong increase of the force around the round-trip time (where it diverges).

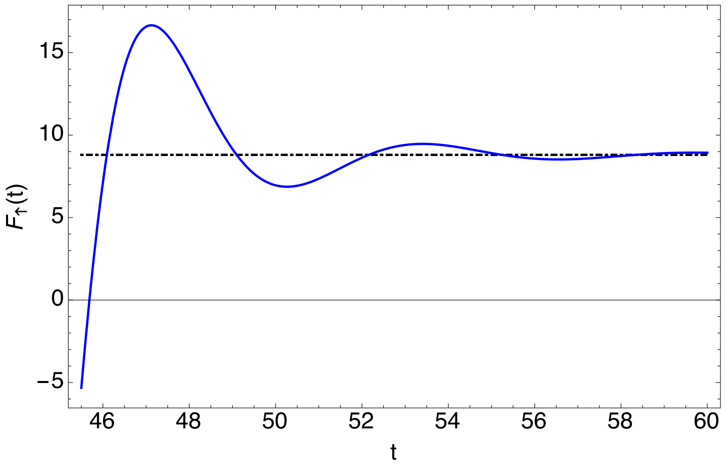

Figure 4.6: Time evolution of the dynamical force for time $t > 2d/c$, that is after the round-trip time (force and time are both in arbitrary units). The atom-wall distance is $d = 20$ and $c = 1$, as in Fig. 4.5, and $k_{\rm a} = 1$. The time-dependent force shows oscillations around the stationary value represented by the (black) dot-dashed lines. The absolute value of the force strongly increases in the proximity of the round-trip time $t = 40$.

time (see Fig. 4.5) is fully consistent with relativistic causality, since the atom interacts with the vacuum field fluctuations modified by the presence of the reflecting wall from the outset. Figure 4.6 also shows that in the limit $t \to \infty$ (large times), we recover the known static value

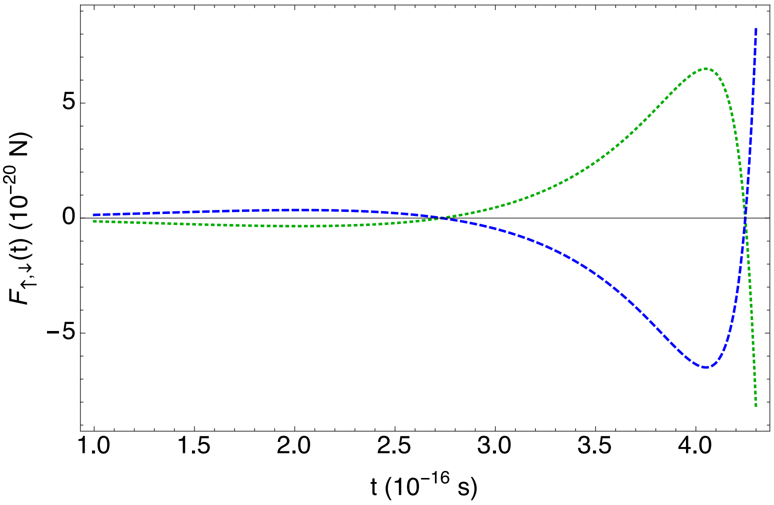

Figure 4.7: Comparison of the dynamical Casimir-Polder force between an initially excited atom (green dotted line) and an ground-state atom (blue dashed line) before the round-trip time ($t < 2d/c$). The following typical numerical values for atomic parameters and atom-wall distance have been used: $\mu = 6.31 \times 10^{-30}$Cm, $\lambda = 2\pi/k_{\mathrm{a}} = 1.215 \times 10^{-7}$m, $d = 7.03 \times 10^{-8}$m. The atom-wall distance has been chosen at a value where the (spatially oscillating) static force for the excited atom reaches its first maximum. The round-trip time is 4.69×10^{-16}s.

of the force for the excited atom as found within a time-independent approach in Eq. (1.58) (second line) [60, 62]. This confirms that the dynamical Casimir-Polder force and the related local field quantities at a finite distance between atom and wall, asymptotically (in time) reach the equilibrium configuration. However, we should keep in mind that when we refer to the large time limit, we are always considering times shorter than the decay time of the excited state, which is typically of the order of 10^{-8}s. On the other hand, the main effects of the dynamical dressing process discussed here, i.e. the strong increase of the force around the round-trip time and the space-time oscillations, involve much shorter times, normally of the order of 10^{-16}s and 10^{-15}s, respectively. Thus, the results are fully compatible with our approximations.

We now want to compare our results to the ones found in [63, 172] where the atom is initially prepared in a bare ground-state. Figures 4.7 and 4.8 provide such comparison for the time evolution of the force before and after the round-trip time, in the case of a hydrogen atom, and for an atom-wall distance $d \simeq 7 \times 10^{-8}$m, that is when the excited-atom static force has its first maximum. For $t < 2d/c$, that is before the round-trip time (Fig. 4.7), the force changes from attractive to repulsive, with oscillation-amplitudes comparable in size for the two cases. While, for $t > 2d/c$, i.e. after the round-trip time (Fig. 4.8), the intensity of the dynamical

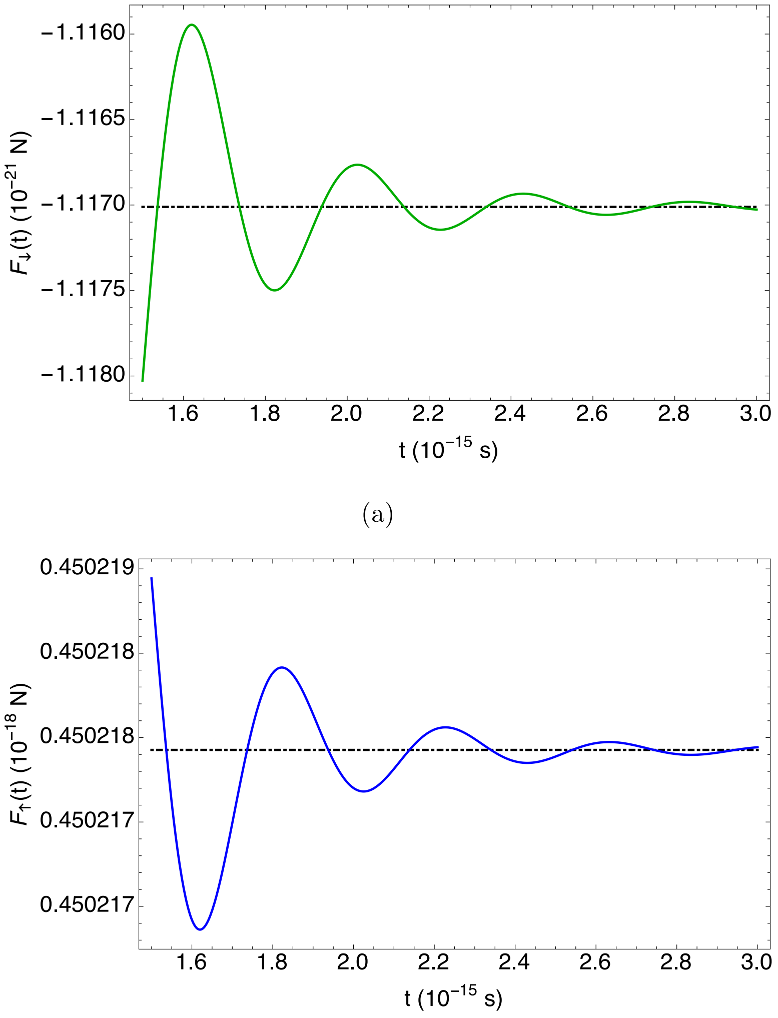

(a)

(b)

Figure 4.8: Comparison of the dynamical Casimir-Polder force between an initially excited atom (b) and a ground-state atom (a) after the round-trip time ($t > 2d/c$). In both cases the force approaches a (non-vanishing) stationary values for $t \to \infty$. The dynamical force for an excited atom can be much stronger (three orders of magnitude) than that the one for a ground-state atom. The following typical numerical values for atomic parameters and atom-wall distance have been used: $\mu = 6.31 \times 10^{-30}$Cm, $\lambda = 2\pi/k_{\rm a} = 1.215 \times 10^{-7}$m, $d = 7.03 \times 10^{-8}$m. The atom-wall distance has been chosen at a value where the (spatially oscillating) static force for the excited atom reaches its first maximum. The round-trip time is $2d/c = 4.69 \times 10^{-16}$s.

force (Fig. 4.8(b)) for the excited atom exceeds that for the initially bare ground state (Fig. 4.8(a)) by about three orders of magnitude. This is because in the case of an excited atom, a much stronger contribution comes from field modes near resonance with the atomic transition frequency.

Another important aspect is that, the static force for the excited atom is vanishing at specific atom-wall distances, thus the dynamical term gives the main contribution to the overall atom-wall force around such distances. We remark that this does not occur in the case of a ground state atom, where, in fact, the static force is attractive at all distances (see first line of Eq. (1.58)). The case of an excited atom considered here thus results more suitable to single out and then experimentally detect the time-dependent dynamical Casimir-Polder effect arising from a non-equilibrium initial state. On the other hand, the static Casimir-Polder force between a mirror and an excited barium ion has already been observed, and its oscillating behavior has been confirmed [68, 70].

Experimental considerations

Suitable experimental schemes for the observation of the dynamical component of the force could then be similar to those already used to probe static vacuum (van der Waals and Casimir-Polder) level shifts, or changes of the spontaneous decay, for a single trapped atom or ion placed near a metallic or dielectric wall [68, 70, 173, 174]. The trapped atom, for instance an alkali atom such as Cs or Rb, is initially laser-excited using an optical dipole transition, for example the D_2 line of Rubidium 87, $5^2D_{1/2} \rightarrow 5^2P_{1/2}$ at 780 nm [174]: the subsequent dynamical Casimir-Polder interaction of the atom with the plate perturbs the harmonic trapping potential, thus modifying the motion of the atom in the trap. As a result, a modification of the atomic oscillation frequency in the trap is a signature of atom-wall interaction. A very similar setup has also been used to test the dependence of the static Casimir-Polder potential from the temperature [72]. Furthermore, by using Rydberg atoms the intensity of the dynamical Casimir-Polder force could be increased even by several orders of magnitude, since this kind of atoms displays high dipole moments scaling as n^2 with n the principal quantum number [175]. Lastly, given that the time scale of the space and time oscillations of the dynamical force is regulated by k_{a}, Rydberg atoms could also help to slow down the dynamical dressing process because of their lower transition frequency, thus allowing for an easier detection of the transient (repulsive) force.

4.5 Conclusions

In this Chapter we have studied the dynamical dressing process for the Casimir energy in a cavity with a mobile boundary treated quantum-mechanically and for the Casimir-Polder force between an excited atom and a classical perfectly conducting wall. In both cases, we have explored the time-dependent process which progressively leads the system to its equilibrium dressed configuration, finding that local quantities such as field-mirror or atom-wall interaction energies converge to their stationary value, while global quantities such as the field energy do not. This process involves a timescale given by the particular round-trip time of the system. We have seen how the evolution of the dynamical dressing essentially depends on the boundary conditions of the system. In particular, contrarily to the atom-wall system, where the radiation emitted by the atom propagates to infinity (no longer participating to the dynamical dressing of the wall), for the the field-mirror system the radiation emitted during the dynamical dressing is reflected by the fixed mirror, thus yielding peculiar revivals of the interaction energy. However, in both scenarios, we have shown how the time-dependent interaction oscillates with time, and that, at specific time intervals, it is larger than the corresponding stationary case. This should be relevant for the detection of the Casimir corrections due to the quantum nature of the boundary in the optomechanical cavity, or of the dynamical Casimir-Polder forces. On the other hand, for the atom-wall system, we have also verified that having considered an initial excited atom represents a much more suitable choice for detecting the dynamical Casimir-Polder effect. Firstly, the static Casimir-Polder force for excited atoms vanishes for specific atom-wall distances, where the force changes its character from attractive to repulsive and viceversa, therefore our dynamical contribution is essentially the main one around such points (this does not occur for a ground-state atom, where the force is attractive at any distance). Secondly, around and after the round-trip time, the dynamical contribution to the Casimir-Polder force is much greater for the excited atom compared with the known case of a ground-state atom.

Chapter 5

Harvesting entanglement from ultrastrong interactions in circuit QED

5.1 Introduction

Strictly speaking, cavity QED concerns the study of quantum light-matter interactions between real atoms and single (or multi-) mode radiation fields confined within a specific geometry. In this scenario, one is usually interested in exploring the regime where the interaction strengths between such objects are so strong to become comparable or larger than appreciable fractions of the bare photon energy of the system. This regime, which has been explored for many years theoretically, has recently been accessed by a few experiments in cavity QED systems [176–180].

On the other hand, ultrastrong coupling (USC) regimes, where the coupling strength becomes comparable or even larger than the bare photonic frequencies [181, 182], are experimentally hard to achieve [§]. Instead, in the field of circuit QED, single artificial atoms (charge or flux qubits) have already been coupled ultra-strongly to microwave fields (LC-resonators) [80–82, 183–186]. In this novel regime our common understanding of the physics behind light-matter interactions is drastically challenged. In fact, even in the ground state, non-trivial effects such as spontaneous vacuum polarization [187–189], light-matter decoupling [190, 191] and different degrees of entanglement [191–194] can in principle appear.

However, compared to the vast literature on cavity QED systems in the weak coupling

---

[§] Note that here we do not distinguish between USC [181], usually referred to situations where the coupling strength is comparable or larger than appreciable fractions of the mode frequency, and the deep strong coupling (DSC) regime, where the coupling strength is comparable or even larger than the bare photonic frequencies [182] regime, the limit of extremely strong interactions in QED is to a large extent still unknown both theoretically and experimentally. Even though we are at an early stage, one interesting question concerns the possibility of using the USC effect for practical applications. In QED USC interactions have been proposed to realize high-fidelity quantum operations [195], ultrafast quantum gates [196], quantum memory devices [197, 198] and quantum computation [199, 200]. But, ideas on how USC effects can be controlled, manipulated and exploited for practical applications and new technologies remain still very restricted.

In this Chapter we consider a circuit QED system where multiple flux qubits (artificial atoms) are coupled to a single LC-resonator (a microwave field). This system has recently been investigated in the USC regime [191]. In particular, it has been found that the full Hamiltonian of the system is formed by a Dicke-like term plus direct qubit-qubit interactions. In the limit where the coupling between resonator and qubits is small compared to the fundamental frequencies, the system dynamics can be well-described by the Dicke Hamiltonian. Whereas, in the USC, such additional qubit-qubit interactions cannot be ignored and the circuit exhibits a manifold of non-superradiant ground- and low-energy states with a high degree of multi-qubit entanglement. However, since any attempt to locally manipulate or measure the individual qubits would necessarily introduce a severe perturbation to the strongly-coupled system, such entanglement cannot be accessed and used for further applications.

Our goal is then to find a simple entanglement-harvesting protocol [201–206] which is able to access the USC correlations between light and matter, extract such quantum correlations and convert them into equivalent multi-partite entangled states of qubits completely decoupled from the resonator. To achieve such goal, we design a scheme that combines adiabatic and non-adiabatic parameter variations and exploit the counter-intuitive decoupling of qubits and photons for ultrastrong interactions [191]. The entanglement extraction reveals to be intrinsically robust and, remarkably, fully consistent with the available experimental tuning capabilities in circuit QED. We can in principle extract symmetric and anti-symmetric Dicke states belonging to a vast family of robust multi-partite entangled states [207, 208], which have been demonstrated a resource for Heisenberg-limited metrology applications [209]. Last but not least, our study generally demonstrates that the USC regime can actually be exploited to realize non-trivial tasks which could have a high technological potential.

5.2 The model

In Chapter 1 we have studied the basic circuits which model an artificial atom (flux or charge circuit) and a microwave field (LC-resonator). Now, we consider a more complicated circuit where we couple these basic elements to actually build up a light-matter interaction in a circuit scenario. We consider the circuit QED system in Fig. 5.1(a), where a single LC-resonator with inductance L and capacitance C is collectively coupled to a an even number N of flux qubits. Following the quantization procedure discussed in paragraphs 1.4.2 and 1.4.3, the Lagrangian of the circuit results [210]

$$\mathcal{L} = \frac{C\dot{\Phi}_r^2}{2} - \frac{(\Phi_r - \Phi_N)^2}{2L} + \sum_{i=1}^{N} \mathcal{L}_q^{(i)}, \tag{5.1}$$

where Φ_r is the node flux corresponding to the resonator, $\Phi_N = \sum_{i=1}^{N} \Delta\Phi_i = \sum_{i=1}^{N} \Phi_i - \Phi_{i-1}$ is the flux difference between the active node N and the ground expressed in terms of the flux differences $\Delta\Phi_i = \Phi_i - \Phi_{i-1}$ across each qubit (note that here for $i = 0$ $\Phi_0 \equiv \Phi_G$ is the value of the flux for the ground of the circuit); and, $\mathcal{L}_q^{(i)}$ is the free Lagrangian for each flux qubit as in Eq. (1.86). By using Eq. (1.64) and (1.65), the node flux Φ_N can be written as

$$\Phi_N = \Phi_0 \sum_{i=1}^{N} \varphi_i, \tag{5.2}$$

where φ_i is the difference of the superconducting phase across the i-th qubit's subcircuit. Since no capacitive coupling between resonator and qubits is present, the Hamiltonian of the circuit can be easily found. We obtain

$$\mathcal{H} = \frac{Q_r^2}{2C} + \frac{(\Phi_r - \Phi_0 \sum_{i=1}^{N} \varphi_i)^2}{2L} + \sum_{i=1}^{N} \mathcal{H}_q^{(i)}, \tag{5.3}$$

where Q_r is the charge operator for the resonator such that $[\Phi_r, Q_r] = i\hbar$ and $\mathcal{H}_q^{(i)}$ denotes the free Hamiltonian for each qubit. As discussed in paragraph in 1.4.7, the dynamics of the flux circuit can be restricted to the lowest states $|{\downarrow}\rangle$ and $|{\uparrow}\rangle$ of a symmetric double-well potential as depicted in Fig. 1.7(c). Under this assumption we can write $\Delta\Phi_i = \Phi_0 \langle{\downarrow_i}|\, \varphi_i \,|{\uparrow_i}\rangle\, \sigma_x^i$. Also, expressing the resonator flux and charge in terms of annihilation and creation operators a and $a^\dagger$ as in Eq. (1.74), we find [191]

$$\mathcal{H} = \hbar\omega_r a^\dagger a + \hbar \sum_{i=1}^{N} \frac{g_i}{2}(a^\dagger + a)\sigma_x^i + \hbar \sum_{i=1}^{N} \frac{\omega_q^i}{2}\sigma_z^i + \hbar \sum_{i,j=1}^{N} \frac{g_i g_j}{4\omega_r}\sigma_x^i \sigma_x^j, \tag{5.4}$$

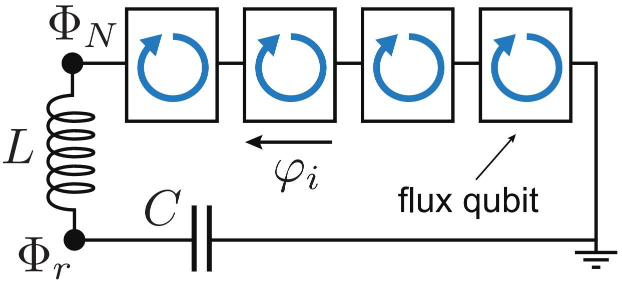

Figure 5.1: (a) Sketch of the multi-qubit circuit QED setup considered. Each flux qubit is represented by the two lowest states $|\downarrow\rangle$ and $|\uparrow\rangle$ of an effective double-well potential for the phase variable (see Fig. 1.7(c)).

where σ_k^i are the Pauli operators, ω_q^i the qubit level splittings, while $g_i = \Phi_0\sqrt{|\varphi_0^i|^2\omega_r/(2\hbar L)}$ with $\varphi_0^i = 2\langle\downarrow_i|\,\varphi_i\,|\uparrow_i\rangle$ is the coupling of the i-th qubit with the resonator. The three terms of Eq. (5.4) give a Dicke-like Hamiltonian, where the second term accounts for the collective interaction between qubits and resonator. In fact, without the last term, the Hamiltonian coincides with the one describing the interaction between a single-mode electromagnetic field and one or more atoms, as found in Eq. (1.44). However, in the context of circuit QED, we highlight that not only the condition $g_i > \omega_r, \omega_q^i$ can be reached with a suitable flux-qubit design [81, 82, 187, 196, 211, 212], but also that $g_i(t)$ and $\omega_q^i(t)$ can be individually tuned by manipulating, for example, the matrix element φ_0^i and the height of the tunnel barrier through local magnetic fluxes [196, 204]. In paragraph 5.7 we will propose a specific flux-qubit design, which combines strong interactions with a high degree of tunability and that reveals to be optimal for our goals. Last but not least, the term proportional to $\sigma_x^i\sigma_x^j$ in Eq. (5.4) describes an additional qubit-qubit interaction between qubits. This term recalls the usual magnetic dipole-dipole interactions between atoms in cavity QED [213]. This is usually neglected in cavity or circuit QED problems in the weak or moderately strong coupling regime. However, in the USC regime such interaction rules the dynamics and it is responsible for the generation of non-trivial ground-state correlations which are at the focus of the Chapter.

Finally, we want to mention that Hamiltonian (5.4) can also be realized with N charge qubits coupled via a capacitance to the resonator. In this case, the coupling constant would then depend on all the capacitances involved and on both resonator and qubit charges [191].

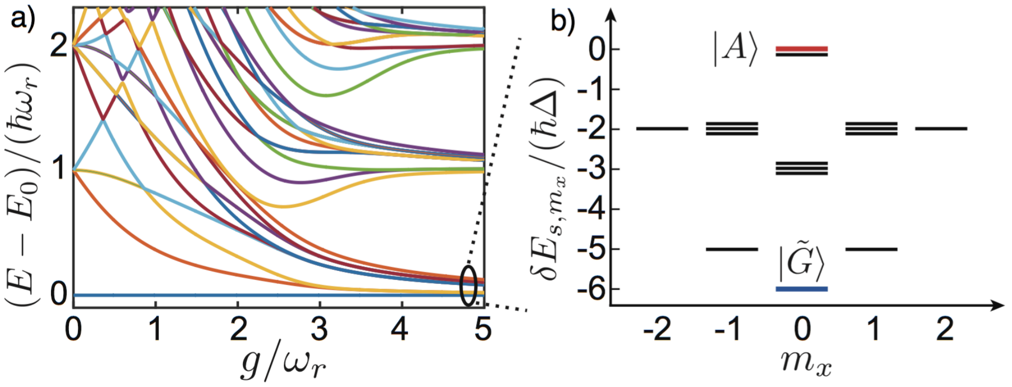

Figure 5.2: a) Energy spectrum (with respect to the ground state energy E_0) of the extended Dicke model (5.5) as a function of the coupling strength g for $N = 4$ and $\omega_q = \omega_r$. b) Ordering of the lowest energy states in the USC regime as determined by Eq. (5.9) for the case $N = 4$. The multiple lines indicate the two- and three-fold degeneracy of states with total angular momentum $s = 0$ and $s = 1$, respectively.

5.3 USC spectrum and eigenstates

Let us start considering a complete symmetric configuration where $g_i = g$ and $\omega_q^i = \omega_q$. In this scenario one can introduce collective spin operators $S_k = \sum_i \sigma_k^i/2$ such that Eq. (5.4) becomes the extended Dicke-like Hamiltonian [191]

$$\mathcal{H} = \hbar\omega_r a^\dagger a + \hbar g(a^\dagger + a)S_x + \hbar\omega_q S_z + \hbar\frac{g^2}{\omega_r}S_x^2. \tag{5.5}$$

When the coupling constant is much smaller than the bare frequencies, that is $g \ll \omega_r, \omega_q$, the rotating wave approximation can be performed and, Hamiltonian (5.5) reduces to the common Tavis-Cummings model of cavity QED [37] with the trivial ground state $|G\rangle = |n=0\rangle \otimes |\downarrow\rangle^{\otimes N}$. Adding the condition $|\omega_q - \omega_r| \gg g$, we can also consider all the excited states practically decoupled and, by using additional control fields, the qubit subsystem can appropriately be prepared, controlled, manipulated and measured. On the other hand, when $g \gg \omega_r, \omega_q$, both the coupling terms proportional to S_x and S_x^2 dominate the dynamics and, as described in Fig. 5.2(a), the structure of the eigenvalues is drastically modified. For $g/\omega_r \gtrsim 3$ the spectrum is formed by manifolds of 2^N nearly-degenerate eigenstates. In this regime, the full Hamiltonian can be conveniently written as $\mathcal{H} = \mathcal{H}_0 + \mathcal{H}_1$. $\mathcal{H}_1 = \hbar\omega_q S_z$ is treated as a perturbation, while $\mathcal{H}_0 = \hbar\omega_r a^\dagger a + \hbar g(a^\dagger + a)S_x + \hbar\frac{g^2}{\omega_r}S_x^2$ commutes with S_x and can be diagonalized exactly by the transformation $\mathcal{H}_0' = \mathcal{U}^\dagger \mathcal{H}_0 \mathcal{U}$, with $\mathcal{U} = e^{-\frac{g}{\omega_r}(a^\dagger - a)S_x}$. By using

$$\begin{aligned} \mathcal{U}^\dagger \hbar g(a^\dagger - a)S_x \mathcal{U} &= \hbar g(a^\dagger + a)S_x - 2\hbar \frac{g^2}{\omega_r} S_x^2 \\ \mathcal{U}^\dagger \hbar \omega_r a^\dagger a \mathcal{U} &= \hbar \omega_r a^\dagger a - \hbar g(a^\dagger + a)S_x + \hbar \frac{g^2}{\omega_r} S_x^2, \end{aligned} \tag{5.6}$$

we obtain

$$\mathcal{H}_0' = \hbar \omega_r a^\dagger a + \hbar \left(D - \frac{g^2}{\omega_r} \right) S_x^2 = \hbar \omega_r a^\dagger a, \tag{5.7}$$

whose eigenstates and energies are $|n\rangle \otimes |s, m_x\rangle$ and $E_n = \hbar \omega_r n$, with $|n\rangle$ the number state of the resonator mode and s and m_x the total spin and the spin projection quantum number, respectively. Going back to the original frame and performing perturbation theory on $\mathcal{H}_1$, we find that the eigenstates of $\mathcal{H}$ can be approximated by the displaced photon number states [191]:

$$|\Psi_{s,m_x,n}\rangle \simeq e^{-\frac{g}{\omega_r}(a^\dagger - a)S_x} |n\rangle \otimes |s, m_x\rangle, \tag{5.8}$$

with corresponding energies $E_{s,m_x,n} \simeq \hbar \omega_r n + \delta E_{s,m_x}^{(n)}$. In the lowest manifold, the remaining level splittings are given by

$$\delta E_{s,m_x}^{(0)} = \hbar \Delta \left[m_x^2 - s(s+1) \right], \qquad \Delta = \frac{\omega_q^2 \omega_r}{2g^2}, \tag{5.9}$$

and the resulting ordering of the states is shown in Fig. 5.2(b) for $N = 4$ qubits. Very remarkably, when the circuit is formed by an even number of qubits N, Eqs. (5.8) and (5.9) say that in the USC regime light and matter decouples. In fact, in this case, the true ground state of the circuit QED system results $|\tilde{G}\rangle \simeq |n = 0\rangle \otimes |S_0\rangle$, where $|S_0\rangle = |s = N/2, m_x = 0\rangle$ is the fully symmetric Dicke state with vanishing projection along x. This USC state, where resonator and qubits are almost completely decoupled, shows a high degree of qubit-qubit entanglement [191]. In the subsequent paragraphs our goal will consist in identifying a convenient and experimentally feasible protocol to realize such state and convert it into an equivalent decoupled state for the overall system, which can then be used as an entanglement resource.

Before going to the description of the protocol to achieve this non-trivial task, we provide more details about the USC eigenstates of the Dicke Hamiltonian in Eq. (5.5) for $N = 2$ and $N = 4$. For an even number of qubits, these states are labelled by $s = 0, 1, \ldots, N/2$ and $m_x = -s, \ldots, s$, such that $\vec{S}^2 |s, m_x\rangle = s(s+1)|s, m_x\rangle$ and $S_x |s, m_x\rangle = m_x |s, m_x\rangle$, with $\vec{S}^2$ the total angular momentum. In addition, because of the permutation symmetry of the Hamiltonian, for $N > 2$ the states $|s \neq N/2, m_x \neq \pm N/2\rangle$ appear as multiplets [214]. By using the rotated basis

$$|\downarrow\rangle_x = \frac{1}{\sqrt{2}} \left(|\downarrow\rangle - |\uparrow\rangle \right), \qquad |\uparrow\rangle_x = \frac{1}{\sqrt{2}} \left(|\downarrow\rangle + |\uparrow\rangle \right), \tag{5.10}$$

for two qubits we have the states of the triplet

$$\begin{aligned} |s=1, m_x=1\rangle &= |\uparrow\uparrow\rangle_x\,, \\ |s=1, m_x=0\rangle &= \frac{1}{\sqrt{2}}(|\uparrow\downarrow\rangle_x + |\downarrow\uparrow\rangle_x), \\ |s=1, m_x=-1\rangle &= |\downarrow\downarrow\rangle_x\,, \end{aligned} \tag{5.11}$$

and the (completely antisymmetric) singlet state

$$|s=0, m_x=0\rangle = \frac{1}{\sqrt{2}}(|\uparrow\downarrow\rangle_x - |\downarrow\uparrow\rangle_x). \tag{5.12}$$

For our purposes, we will be interested in the two states with $m_x = 0$, which, in terms of the original qubit basis, read

$$|s=1, m_x=0\rangle = \frac{1}{\sqrt{2}}(|\downarrow\downarrow\rangle - |\uparrow\uparrow\rangle), \qquad |s=0, m_x=0\rangle = \frac{1}{\sqrt{2}}(|\uparrow\downarrow\rangle - |\downarrow\uparrow\rangle). \tag{5.13}$$

On the other hand, for $N = 4$ qubits, the structure of the levels is already more complex. We have a quintuplet of states corresponding to $s = 2$, three triplets for $s = 1$ and a doublet (two singlets states) for $s = 0$. The maximally symmetric states with $s = 2$ are:

$$\begin{aligned} |s=2, m_x=2\rangle &= |\uparrow\uparrow\uparrow\uparrow\rangle_x\,, \\ |s=2, m_x=1\rangle &= \frac{1}{2}(|\downarrow\uparrow\uparrow\uparrow\rangle_x + |\uparrow\downarrow\uparrow\uparrow\rangle_x + |\uparrow\uparrow\downarrow\uparrow\rangle_x + |\uparrow\uparrow\uparrow\downarrow\rangle_x), \\ |s=2, m_x=0\rangle &= \frac{1}{\sqrt{6}}(|\downarrow\downarrow\uparrow\uparrow\rangle_x + |\uparrow\uparrow\downarrow\downarrow\rangle_x + |\downarrow\uparrow\uparrow\downarrow\rangle_x + |\uparrow\downarrow\downarrow\uparrow\rangle_x + |\downarrow\uparrow\downarrow\uparrow\rangle_x + |\uparrow\downarrow\uparrow\downarrow\rangle_x), \\ |s=2, m_x=-1\rangle &= \frac{1}{2}(|\downarrow\uparrow\downarrow\downarrow\rangle_x + |\downarrow\downarrow\downarrow\uparrow\rangle_x + |\downarrow\downarrow\uparrow\downarrow\rangle_x + |\uparrow\downarrow\downarrow\downarrow\rangle_x), \\ |s=2, m_x=-2\rangle &= |\downarrow\downarrow\downarrow\downarrow\rangle_x\,, \end{aligned} \tag{5.14}$$

which coincide with the usual Dicke states in the x-basis. While, the corresponding 3-fold degenerate states for each value of $s = 1$ are

$$
\begin{aligned}
|s=1, m_x=1\rangle &= \begin{cases} \frac{1}{2}(|\uparrow\uparrow\uparrow\downarrow\rangle_x + |\uparrow\uparrow\downarrow\uparrow\rangle_x - |\uparrow\downarrow\uparrow\uparrow\rangle_x - |\downarrow\uparrow\uparrow\uparrow\rangle_x), \\ \frac{1}{2}(|\uparrow\uparrow\uparrow\downarrow\rangle_x - |\uparrow\uparrow\downarrow\uparrow\rangle_x + |\uparrow\downarrow\uparrow\uparrow\rangle_x - |\downarrow\uparrow\uparrow\uparrow\rangle_x), \\ \frac{1}{2}(|\uparrow\uparrow\uparrow\downarrow\rangle_x - |\uparrow\uparrow\downarrow\uparrow\rangle_x - |\uparrow\downarrow\uparrow\uparrow\rangle_x + |\downarrow\uparrow\uparrow\uparrow\rangle_x), \end{cases} \\
|s=1, m_x=0\rangle &= \begin{cases} \frac{1}{\sqrt{2}}(|\uparrow\uparrow\downarrow\downarrow\rangle_x - |\downarrow\downarrow\uparrow\uparrow\rangle_x), \\ \frac{1}{\sqrt{2}}(|\uparrow\downarrow\uparrow\downarrow\rangle_x - |\downarrow\uparrow\downarrow\uparrow\rangle_x), \\ \frac{1}{\sqrt{2}}(|\uparrow\downarrow\downarrow\uparrow\rangle_x - |\downarrow\uparrow\uparrow\downarrow\rangle_x), \end{cases} \\
|s=1, m_x=-1\rangle &= \begin{cases} \frac{1}{2}(|\uparrow\downarrow\downarrow\downarrow\rangle_x + |\downarrow\uparrow\downarrow\downarrow\rangle_x - |\downarrow\downarrow\uparrow\downarrow\rangle_x - |\downarrow\downarrow\downarrow\uparrow\rangle_x), \\ \frac{1}{2}(|\uparrow\downarrow\downarrow\downarrow\rangle_x - |\downarrow\uparrow\downarrow\downarrow\rangle_x + |\downarrow\downarrow\uparrow\downarrow\rangle_x - |\downarrow\downarrow\downarrow\uparrow\rangle_x), \\ \frac{1}{2}(|\uparrow\downarrow\downarrow\downarrow\rangle_x - |\downarrow\uparrow\downarrow\downarrow\rangle_x - |\downarrow\downarrow\uparrow\downarrow\rangle_x + |\downarrow\downarrow\downarrow\uparrow\rangle_x). \end{cases}
\end{aligned}
\tag{5.15}
$$

Finally, for $N = 4$ and within the antisymmetric subspace for $s = 0$, we get a doublet of states given by

$$
|s=0, m_x=0\rangle = \begin{cases} \frac{1}{2}(|\uparrow\downarrow\uparrow\downarrow\rangle_x - |\uparrow\downarrow\downarrow\uparrow\rangle_x - |\downarrow\uparrow\uparrow\downarrow\rangle_x + |\downarrow\uparrow\downarrow\uparrow\rangle_x), \\ \frac{1}{\sqrt{3}}(|\uparrow\uparrow\downarrow\downarrow\rangle_x + |\downarrow\downarrow\uparrow\uparrow\rangle_x) - \frac{1}{\sqrt{12}}(|\uparrow\downarrow\uparrow\downarrow\rangle_x + |\uparrow\downarrow\downarrow\uparrow\rangle_x + |\downarrow\uparrow\uparrow\downarrow\rangle + |\downarrow\uparrow\downarrow\uparrow\rangle_x). \end{cases}
\tag{5.16}
$$

For the subsequent entanglement harvesting protocol, we will be interested in the state $|s = 2, m_x = 0\rangle$, which in the original qubit basis is written as

$$
|s=2, m_x=0\rangle = \frac{3}{\sqrt{24}}(|\uparrow\uparrow\uparrow\uparrow\rangle + |\downarrow\downarrow\downarrow\downarrow\rangle) - \frac{1}{\sqrt{24}}(|\uparrow\uparrow\downarrow\downarrow\rangle + |\uparrow\downarrow\uparrow\downarrow\rangle + |\uparrow\downarrow\downarrow\uparrow\rangle + |\downarrow\uparrow\uparrow\downarrow\rangle + |\downarrow\uparrow\downarrow\uparrow\rangle + |\downarrow\downarrow\uparrow\uparrow\rangle),
\tag{5.17}
$$

and in the states of the doublet $s = 0$, which are invariant under rotations, and have the same form in the original qubit basis:

$$
|s=0, m_x=0\rangle = \begin{cases} \frac{1}{2}(|\uparrow\downarrow\uparrow\downarrow\rangle - |\uparrow\downarrow\downarrow\uparrow\rangle - |\downarrow\uparrow\uparrow\downarrow\rangle + |\downarrow\uparrow\downarrow\uparrow\rangle), \\ \frac{1}{\sqrt{3}}(|\uparrow\uparrow\downarrow\downarrow\rangle + |\downarrow\downarrow\uparrow\uparrow\rangle) - \frac{1}{\sqrt{12}}(|\uparrow\downarrow\uparrow\downarrow\rangle + |\uparrow\downarrow\downarrow\uparrow\rangle + |\downarrow\uparrow\uparrow\downarrow\rangle + |\downarrow\uparrow\downarrow\uparrow\rangle). \end{cases}
\tag{5.18}
$$

We highlight that to obtain the states above, the 4-spins have been coupled in a particular pairwise way (which will be connected to a forthcoming protocol). In particular, we have firstly combined the states of the first spin (qubit) with the second, and the states of the third spin with the fourth, and finally combined these resulting states. While the completely symmetric states for $s = 2$ are not affected by this particular way of breaking the total symmetry, the states for $s = 1, 0$ ($N = 4$) are instead dependent on this choice, which, in fact, singles out a particular basis within the subspace $(s,\, m_x)$ of interest. However, combining the states of such basis, one can then find all the other states of the subspace, which, in principle, might have different symmetry properties under exchange of a particular pair of spins.

5.4 Entanglement harvesting

5.4.1 From the ground state

We are now ready to describe our entanglement-harvesting protocol. The basic idea is showed in Fig. 5.3(a) together with the general pulse sequence achieved by using a time-dependent variation of the parameters $\omega_q(t)$ and $g(t)$. We start with the system initially prepared in the ground state $|G\rangle$ of the weakly-coupled system, where the qubit subsystem is far-detuned from the resonator, that is $\omega_q = \omega_{\max} \gg \omega_r$, and the coupling is at a minimal value $g = g_{\min} < \omega_r$. During the first two steps, which last T_1 and T_2 respectively, we adiabatically tune the system into the USC regime by firstly increasing the coupling strength up to $g_{\max} > \omega_r$ and, secondly, decreasing the qubit frequency to the low value $\omega_{\min} \lesssim \omega_r$. As a result, the system is prepared in the USC ground state $|\tilde{G}\rangle$. For the subsequent time steps, lasting T_3 and T_4 respectively, we separate again qubits and resonator by performing a non-adiabatic parameter variation in the reverse order: we tune the coupling and then the qubit frequency to their initial values $g_{\min}$ and $\omega_{\max}$. In the ideal case, during this last part of the protocol, the system remains in the state $|\tilde{G}\rangle$, which at the end of the protocol at $T_{\mathrm{f}} = \sum_{n=1}^{4} T_n$ becomes the desired excited state for the system in the weak coupling regime.

A few remarks are in order. Firstly, we highlight that the adiabatic state-preparation can be performed very fast. This is because we only need to demand the overall time $T_1 + T_2$ slower than the fast timescales given by $\omega_{\max}^{-1}$ and $g_{\max}^{-1}$. Secondly, the overall time $T_3 + T_4$ of the non-adiabatic decoupling process must only be fast compared to the slow timescales set by ω_r^{-1}, $\omega_{\min}^{-1}$ and $g_{\min}^{-1}$. As we will see in the next paragraph, this means that the switching times achieve two main goals: they avoid unwanted excitations out of the two-level qubit subspace and make our scheme completely compatible with the experimental capability for a time-dependent control of USC systems.

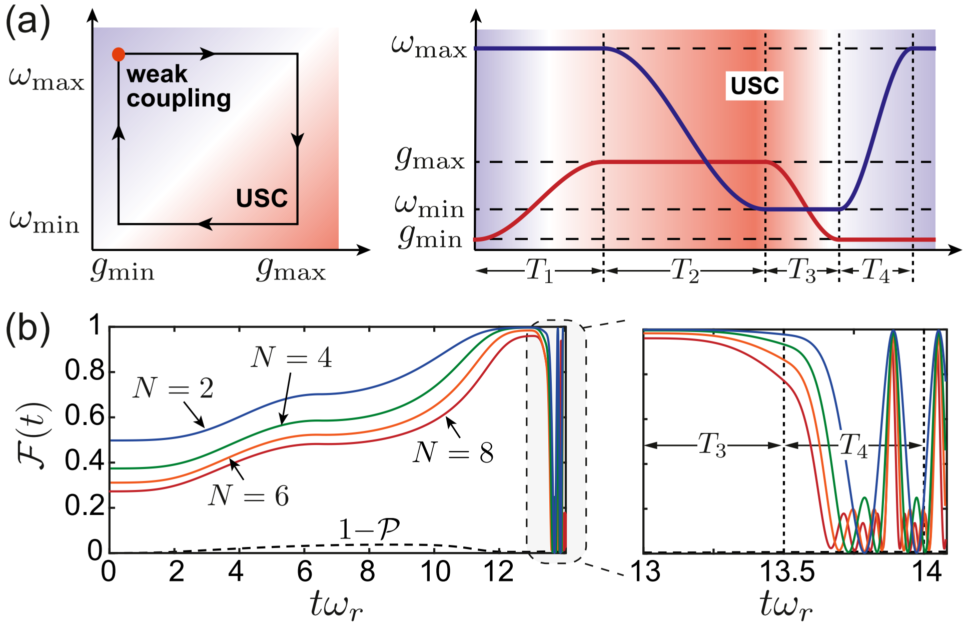

Figure 5.3: (a) General pulse sequence for the qubit parameters $\omega_q(t)$ and $g(t)$ considered for the implementation of the entanglement harvesting protocol. (b) The fidelity $\mathcal{F}(t)$ is plotted as a function of time and for different qubit numbers. The dashed line indicates the quantity $1-\mathcal{P}(t)$ for the case $N = 4$. For all values of N the same parameters $\omega_{\max}/\omega_r = 20$, $\omega_{\min}/\omega_r = 0.5$, $g_{\max}/\omega_r = 4.5$, $g_{\min}/\omega_r = 0.1$ and times intervals $T_1 = T_2 = 6.5\omega_r^{-1}$ and $T_3 = T_4 = 0.5\omega_r^{-1}$ have been assumed.

For a specific set of pulse parameters, Fig. 5.3(b) shows the fidelity

$$\mathcal{F}(t) = \mathrm{Tr}\{\rho(t)|S_0\rangle\langle S_0|\}, \tag{5.19}$$

with $\rho(t)$ the density operator of the overall system. Loosely speaking, this physical quantity compute the overlap between the two "states" $\rho(t)$ and $|S_0\rangle\langle S_0|$, giving a measure of the "closeness" between them [‡]. We can then see that the value of the relevant entanglement extraction fidelity (EEF) $\mathcal{F}_{\mathrm{E}} = \max\{\mathcal{F}(t)|t \geq T_{\mathrm{f}}\}$, that is the maximal fidelity after the final decoupling step of the protocol, achieves an optimal value of $\mathcal{F}_{\mathrm{E}} \simeq 0.95 - 0.99$, depending on the (even) number of qubits considered in the circuit. Remarkably, after the final time T_{f} we do not need to require any additional fine-tuning over the control pulses. We also note that the fidelity shows some oscillations after the final time T_{f}. However, such oscillations are trivial since they occur only because our target state (in this case $|S_0\rangle$) is not an eigenstate of the bare

---

[‡] More rigorously, given two quantum states described by the density matrices ρ and σ, if σ is pure, i.e. $\sigma = |\psi\rangle\langle\psi|$, the Fidelity is defined as $\mathcal{F}(\rho,\sigma) = \langle\psi|\rho|\psi\rangle = \mathrm{Tr}\{\rho\,\sigma\}$. When also ρ is pure, that is $\rho = |\varphi\rangle\langle\varphi|$, the Fidelity reduces to the standard probability: $\mathcal{F}(\rho,\sigma) = |\langle\psi|\varphi\rangle|^2$ [215].

qubit Hamiltonian $\mathcal{H}_q = \omega_q S_z$ anymore (it was an eigenstate for the qubit subsystem in the USC regime as we have seen). Furthermore, the triviality of these oscillations can be verified by calculating the purity $\mathcal{P}(t) = \mathrm{Tr}\{\rho_q^2(t)\}$ (or equivalently $1 - \mathcal{P}$), where $\rho_q(t) = \mathrm{Tr}_r\{\rho(t)\}$ is the reduced qubit state [†]. When $\mathcal{P} = 1$ (or $1 - \mathcal{P}(t) = 0$) the state of the qubits is pure, therefore completely decoupled from the resonator; otherwise, the state is mixed, thus revealing that qubits and resonator are entangled. As we can see from Fig. 5.3(b) the purity is initially one (qubits and resonator are initially decoupled), then increases and when we approach the USC settles to one, thus saying that we have achieved a completely decoupling of light and matter. The oscillations are then trivial since they do not affect the purity or the degree of entanglement of the final qubit state and can be undone by local qubit rotations.

Experimental considerations

Although operating in the USC regime, the protocol is fully compatible with the typical values in circuit QED experiments. Indeed, for an experimental realization, we consider a characteristic qubit frequency of $\omega_{\max}/(2\pi) \approx 10$ GHz and a resonator of frequency $\omega_r/(2\pi) = 500$ MHz. As a result, for the maximum value of the coupling strength we get $g_{\max} \simeq 4.5\omega_r \approx 2\pi \times 2.25$GHz: perfectly consistent with the achieved values [81, 82]. Given this choice of parameters, the times for the non-adiabatic switching result $T_{3,4} \simeq 0.16$ ns, which are within the range of the experimentally achievable tuning capabilities for flux qubits [12]. Moreover, the overall time to complete the protocol $T_{\mathrm{f}} = 15/\omega_r \approx 5$ ns is much faster than usual coherence times (1-100 μs) for a flux qubit [216], or the lifetime of a photon $T_{\mathrm{ph}} = Q/\omega_r$ in a microwave resonator of quality factor $Q = 10^4 - 10^6$. In a nutshell, while several experimental techniques for the manipulation of a circuit QED in the USC need to be developed, these estimates show the feasibility of the protocol to realize a high-fidelity control operation with the current technology, and, more generally, the great potential of such devices to undertake very non-trivial tasks.

On the other hand, deleterious effects for the protocol might come from the lack of complete tunability for $g(t)$ or $\omega_q(t)$. In Fig. 5.4(a) we plot the evolution of the lowest eigenvalues of the system during the whole protocol for the specific case of $N = 2$ and a finite value of $g_{\min}$. During the final ramp-up step of the scheme, several avoided crossing might in principle prevent the

---

[†] Note that the quantity $1 - \mathcal{P}$ is also called *linear entropy* or *impurity*, and actually coincides with a lower approximation of the (quantum) von Neumann entropy defined in Eq. (5.20), obtained expanding the logarithm as $\log_2 = \log_2(1 - (1 - \rho))$ around a pure state $\rho^2 = \rho$ [37, 215].

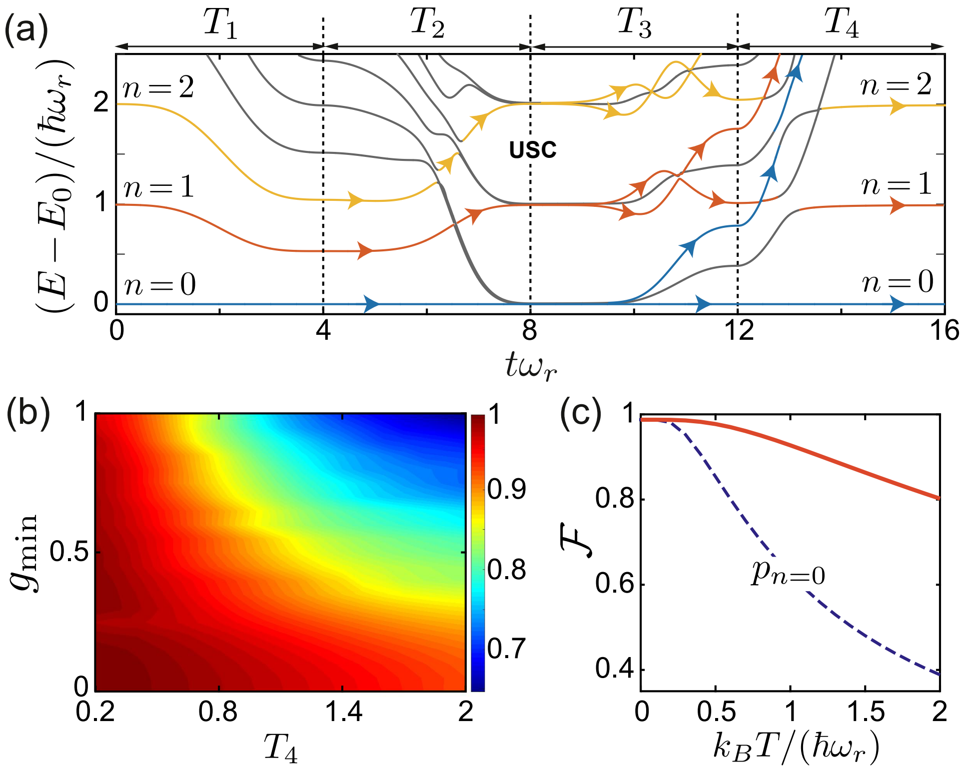

Figure 5.4: (a) Evolution of the lowest eigenvalues during different stages of the protocol for the case $N = 2$. Here $g_{\min}/\omega_r = 0.2$, $\omega_{\min}/\omega_r = 0.4$, and in the final step of the protocol $\omega_{\max}/\omega_r = 5$. For clarity only the $s = 1$ states are shown. For different initial photon number states $|n\rangle$, the colored segments and arrows indicate the ideal evolution of the systems, which maximizes the probability to end up in the qubit state $|S_0\rangle = (|\uparrow\uparrow\rangle - |\downarrow\downarrow\rangle)/\sqrt{2}$. (b) Plot of the EEF for varying $T_4(= T_3)$ and $g_{\min}$ and for the case $N = 4$. (c) EEF (solid line) for a resonator mode, which is initially in a thermal state at temperature T, for $N = 4$. The dashed line indicates the corresponding population of the ground state manifold. All the other pulse parameters in (a), (b) and (c) are the same as in Fig. 5.3(b).

fully non-adiabatic decoupling, which is a fundamental ingredient in our proposal. To address this specific problem, Fig. 5.4(b) displays the EEF as a function of $g_{\min}$ and T_4. This plot not only shows the expected trade-off between the residual coupling and the minimal switching time, but, notably, quantifies the robustness of the protocol. Extraction fidelities quite above $\mathcal{F}_{\mathrm{E}} > 0.9$ are achieved for couplings of a few hundred MHz or switching times approaching $\sim$ 1ns. Quite similar conclusions will be found in the case of couplings or qubit frequencies affected by fabrication uncertainties. We will address this more specific issue in paragraph 5.6.

5.4.2 From a thermal state

So far we have considered a quite low frequency for the resonator, which has been essential to increase the ratio g/ω_r and the switching times in the non-adiabatic final steps. However, this means that, even considering a very low equilibrium temperature of $T = 20$ mK, the populations in higher resonator states with $n \geq 1$ participate to the dynamics and, in turn, must be taken into account. To understand the impact of such states, we consider a resonator initially prepared in a thermal state $\rho_{\text{th}} = \sum_n \bar{n}^n/(1+\bar{n})^{n+1} |n\rangle \langle n|$ with $\bar{n} = 1/(e^{\hbar\omega_r/k_BT} - 1)$ the Bose-Einstein distribution for the mean photon number. In Fig. 5.4(c) we plot the EEF against initial equilibrium temperature T. As we can see, fidelities $\mathcal{F}_E > 0.8$ can be reached until a thermal occupation of $\bar{n} \sim 1.55$ (for $k_BT/\hbar\omega_r = 2$), which, for characteristic resonator frequencies within the interval $\omega_r \sim [1, 2\pi] \times 500$ MHz, corresponds to typical circuit QED temperatures $T \sim [8, 50]$ mK [82]. Surprisingly, this happens even though the remaining population in the ground state $|G\rangle$ drastically decreases as we increase the temperature to such value. The physical reason behind this behavior can be explained with the help of the eigenvalue plot in Fig. 5.4(a). If for example we start the protocol with the initial decoupled eigenstate $|n = 1\rangle \otimes |{\downarrow}\rangle^{\otimes N}$ in the weak coupling regime, the protocol maps such state into the corresponding USC eigenstate $|n = 1\rangle \otimes |s = N/2, m_x = 0\rangle$, even though during the dynamics higher-order avoided crossing are present. As a result, the intermediate achieved state as well as the final (target) state conserve the photonic excitation $|1\rangle$. Noticeably, this is also true for initial states with higher photonic excitations, although they pass through even more relevant avoided crossings. The protocol approximately implements the mapping $|n\rangle \otimes |{\downarrow}\rangle^{\otimes N} \rightarrow |n\rangle \otimes |s = N/2, m_x = 0\rangle$, almost independently from the resonator state $|n\rangle$. And, this is the physical reason why it is so insensitive to the initial thermal occupation of the resonator. We thus do not need to require additional unfeasible active cooling techniques to consider the system prepared in the ground state $|G\rangle$.

5.5 Entanglement protection

The maximally symmetric state $|\tilde{G}\rangle$ is not the only one of interest. Many other entangled states are generated in the lowest manifold of the USC regime, as shown in Fig. 5.2(d). Among them, there are the energetically highest states $|\tilde{E}\rangle = |n = 0\rangle \otimes |A\rangle$, where $|A\rangle$ is one of the qubit entangled states within the antisymmetric subspace with total spin number $s = 0$, such that

$S_z|A\rangle = S_x|A\rangle = 0$*.

However, to address a generic qubit state $|A\rangle$ we need to break the symmetry of the system, so that we can allow for a transfer between two states with different total angular momenta. In Fig. 5.5(a) we show the optimal protocol for the case of $N = 4$ qubits. We start with the system initialized in the excited state $|\Psi_0\rangle = |0\rangle \otimes |\uparrow\uparrow\downarrow\downarrow\rangle$ (with total spin $s = 2$), where the first two qubits have the same frequency $\omega_q^{1,2}$, and the others $\omega_q^{3,4}$. While adiabatically increasing the coupling strength during the whole scheme, at the first stage (lasting T_1) both the frequencies ($\omega_q^{1,2}$ and $\omega_q^{3,4}$) are lowered below the resonator frequency, such that level crossings with higher photon number states can be avoided. At the second stage (lasting T_2), we then bring the qubits at the same frequencies and, without demanding a very strong coupling, at $g/\omega_r \approx 1.8$ we already achieve the antisymmetric manifold with total angular momentum $s = 0$. At the final step (lasting T_3) we simply bring again qubits and resonator far-detuned to allow for an easier manipulation of the qubit state. It is important to realize that, the selection of a particular state within the spin subspace $s = 0$ both depends on the way we break the symmetry at the beginning of the protocol and on the particular choice of the pulse. For $N = 4$, the protocol can then generate both the two states of the doublet in Eq. 5.18, which indeed are the states of four particles (with spin 1/2) where the spins are pairwise indistinguishable (in particular the first and the second, and the third and the fourth). In particular, one of them is the maximal antisymmetric qubit state (see Eqs. 5.12 and 5.18). More generally, for $N \geq 4$ there are actually multiple degenerate USC states with $s = 0$ [214, 217] (see Fig. 5.2(d)) out of which the protocol selects a specific superposition.

Although the harvesting protocol for the states within the antisymmetric spin manifold can generally appear less robust than the one discussed for the ground state $|\tilde{G}\rangle$, it shows a new interesting effect. Specifically, the extracted state $|A\rangle$, which is energetically separated by all the other states with $s \neq 0$, can be protected against small frequency fluctuations by keeping a finite coupling $g_{\mathrm{f}} = g(t = T_{\mathrm{f}}) \sim \omega_r$ at the end of the protocol. This is illustrated in Fig. 5.5(c), where, in the presence of small random shifts of the individual qubit frequencies, we plot the evolution of the total spin number of the extracted state against different values of the final coupling strength. In particular, by retaining the coupling to a finite value we can substantially suppress the dephasing of the qubits and the rapid transition out of the $s = 0$

---

*Note that the states within the subspace $s = 0$ (given in Eqs. 5.12 and 5.18, for $N = 2, 4$) are exact dark states of the Hamiltonian in (5.5), and therefore, once prepared they remain completely decoupled from the resonator for all the coupling regimes.

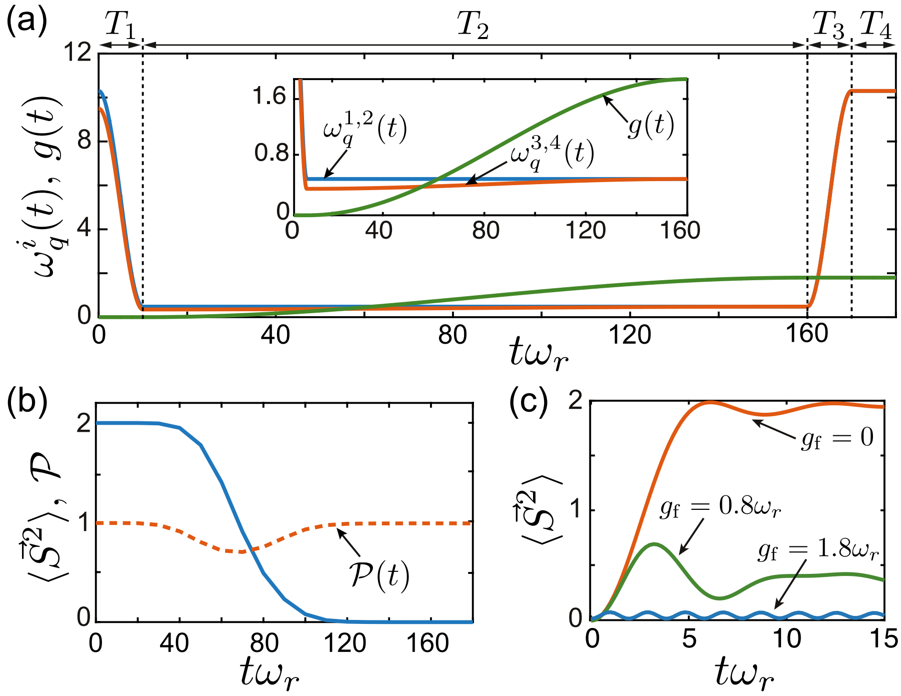

Figure 5.5: (a) Pulse sequence for harvesting the 4-qubit entangled state $|A\rangle$ in Eq. (5.18) (second line) with total angular momentum $s = 0$. As shown in the inset, during the first part of the protocol a finite difference between the qubit frequencies $\omega_q^{1,2}$ and $\omega_q^{3,4}$ is used to break the symmetry and couple different angular momentum states. (b) The expectation value of the total spin, $\langle \vec{S}^2(t) \rangle$, (solid line) and the purity of the reduced qubit state, $\mathcal{P}(t)$, (dashed line) are plotted for the pulse sequence shown in (a) and for an initial state $|\Psi_0\rangle = |0\rangle \otimes |\uparrow\uparrow\downarrow\downarrow\rangle$. (c) Evolution of the extracted state $|0\rangle \otimes |A\rangle$ (characterized by the expectation value of the total spin) after the protocol for different final values of the couplings g_f. For this plot an average over random distributions of the qubit frequencies, $\omega_q^i = \omega_q(1 + \epsilon_i)$, has been assumed, where $\omega_q/\omega_r = 10$ and the ϵ_i are chosen randomly from the interval $[-0.05, 0.05]$.

subspace obtained for $g_\mathrm{f} = 0$. The USC regime can thus be used not only to generate complex multi-qubit entangled states, but also to protect them from unwanted experimental fluctuations.

5.6 Disorder

Until now we have assumed that our qubits are perfectly identical: all with the same frequency and all coupled to the resonator via the same coupling constant. However, as we have already anticipated, another experimental limitation for our protocol might be represented by non-uniform couplings $g_i(t)$ and/or qubit frequencies $\omega_q^i(t)$ due to fabrication uncertainties. This is especially true for experiments involving many qubits.

We start considering frequency disorder. Specifically, we suppose that the qubit frequencies evolve as $\omega_q^i(t) = \omega_q(t)(1+\epsilon_i)$, where $\omega_q(t)$ is the noiseless evolution considered in Fig. 5.3, while ϵ_i is a random fluctuation uniformly distributed within the interval $[-0.1, 0.1]$. In Fig. 5.6(a) we thus plot the average fidelity assuming that for each run of the protocol the individual qubit frequencies follow $\omega_q^i(t)$. Essentially, because in the USC regime the system dynamics is dominated by the interaction terms, frequency disorder does not affect the realization of the desired state. It only becomes more relevant at the final stage of the protocol, where it dephases the symmetric state $|S_0\rangle$. However, such dephasing can be undone, since it does not degrade the purity or the degree of entanglement of the quit state. To verify this point we calculate the von Neumann entropy [37]

$$S_E(t) = -\mathrm{Tr}\{\rho(t)\log_2(\rho(t))\} \tag{5.20}$$

for the qubit state $\rho_q(t)$ and the single qubit state $\rho_1(t) = \mathrm{Tr}_{N-1}\{\rho_q(t)\}$. As we know from standard quantum mechanics, this quantity can certify if the qubit subsystem is decoupled from the resonator and also if the qubit state is a maximally entangled state (for a specific bipartition) [¶]. Fig. 5.6(b), thus shows that having introduced frequency noise leads to almost no degradation of the purity or the degree of entanglement of the qubit state. At the final step of the protocol the qubit subsystem is still completely decoupled from the resonator and the qubit state is found in a maximally entangled state (where a single bipartition is given by two qubits).

In Fig. 5.6 (c) and (d) we instead provide the same results for the case of coupling disorder $g_i(t) = g(t)(1+\epsilon_i)$. As we can see, while this new kind of noise does not affect in any sense the trend of the time-dependent fidelity, it affects the entanglement entropy of the qubit subsystem, which does not approach the value of zero, thus showing that qubits and resonator are not perfectly decoupled at the end of the protocol. However, this measure of entanglement is very sensitive in our case, since the qubit state that we realize at the end of the protocol coincides

---

[¶] The Von Neumann entropy is defined as in Eq. (5.20). For a bipartite system $C = A\otimes B$, described by the density matrix ρ_C, the Von Neumann entropy of a bipartition is $S = S_A = S_B = -\mathrm{Tr}\{\rho_A\log_2(\rho_A)\} = -\mathrm{Tr}\{\rho_B\log_2(\rho_B)\}$, where $\rho_A = \mathrm{Tr}_B\{\rho_C\}$ and $\rho_B = \mathrm{Tr}_A\{\rho_C\}$. If the system C is separable then the entropy of a bipartition assumes its lowest value $S = 0$, which means that we have maximum information on the states of both parts, i.e A and B are in pure states. On the other hand, if the entropy of a bipartition reaches the highest value $S = 1$, we lose all the information of the state of both parts, i.e A and B are described by mixed states. In turn, this means that the system C is in a maximally entangled state [37].

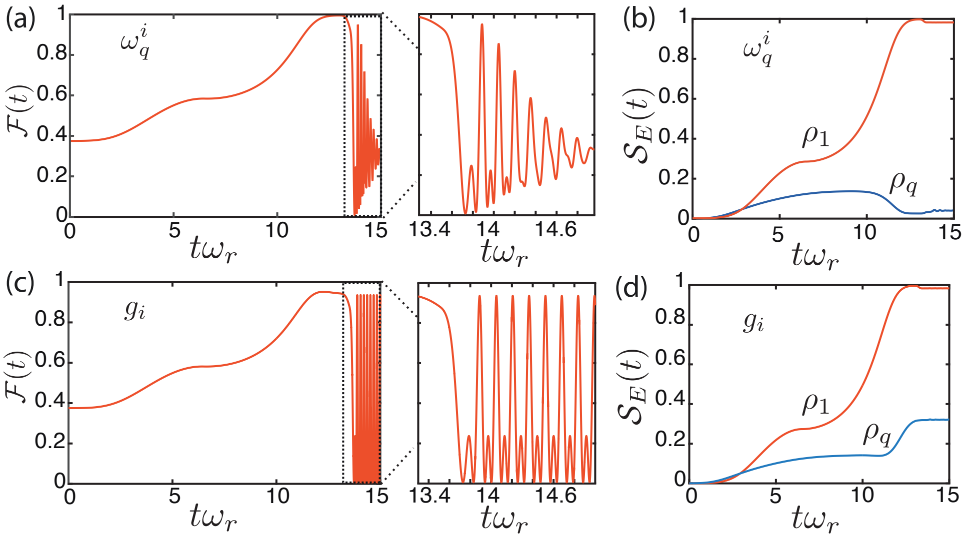

Figure 5.6: (a)-(d) Fidelities and time-dependent entanglement entropies as function of time in the presence of disorder obtained averaging over 10 simulation runs for $N = 4$. In particular we show the entanglement entropy $S_E(t)$ for the reduced density matrix of the qubit subsystem $(\rho_q(t))$ (blue line) and of a single qubit $(\rho_1(t))$ (red line). In (a)-(b) the qubit frequency disorder is $\omega_q^i(t) = \omega_q(t)(1+\epsilon_i)$, while in (c)-(d) we have considered the coupling strength disorder $g^i(t) = g(t)(1+\epsilon_i)$, where ϵ_i are chosen randomly from a uniform distribution $[-0.1, 0.1]$. All the other parameters for the protocol are as in Fig. 5.3(b).

with our target state with EEF $\mathcal{F}_{\text{E}} \gtrsim 0.9$, which, on the other hand, does not display any loss of the qubit-qubit entanglement.

In conclusion, these numerical simulations under such realistic experimental conditions, demonstrate that our protocol can easily tolerate 10% of fabrication uncertainties, and this proves once again that no precise fine-tuning of the system parameters is required.

5.7 Implementation of the protocol

In this final Section we describe an example of a specific circuit QED system which is suitable to implement our protocol. In fact, it can operate in the USC regime and allows for a high tunability of the parameters of interest. The circuit is depicted in Fig. 5.7: fours flux qubits are coupled together, and two of them (indicated with 2 and 4) have junctions with a flux-tunable Josephson energy (commonly called SQUID-loops [210]). The two tunable junctions have Josephson energies αE_J and βE_J, respectively, where E_J is the Josephson energy of

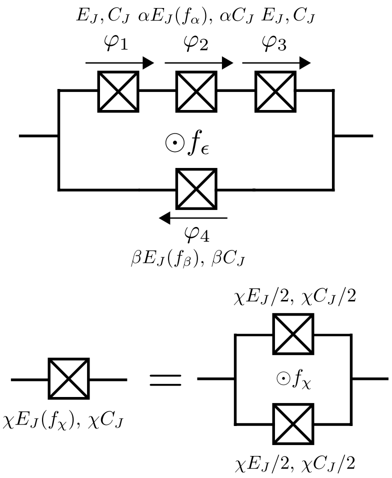

Figure 5.7: Flux-qubit circuits considered for the implementation of tunable qubit frequencies and qubit-resonator couplings. The SQUID-loops behave as an effective junction with a flux-tunable Josephson energy.

junctions 1 and 3. Following the quantization procedure discussed in paragraphs 1.4.2 and 1.4.3, we indicate with $\varphi_i = \Phi_i/\Phi_0$ the jump of the superconducting phase across the junction i with Φ_i the jump of the node flux, and with n_i the conjugate charge to φ_i. As we have already seen for the basic flux qubit in paragraph 1.4.7 (Eq. (1.85)), the phases φ_i are not independent. For the three loops, which are the big one and the two SQUID-loops characterized by α and β, we have

$$\begin{aligned} \sum_{i\in\{1,2,3,4\}} \varphi_i + f_\epsilon = 0, \\ \sum_{i\in\{2,6\}} \varphi_i + f_\alpha = 0, \\ \sum_{i\in\{4,5\}} \varphi_i + f_\beta = 0, \end{aligned} \tag{5.21}$$

where $f_\eta = \Phi_\eta/\Phi_0$ with Φ_η the external magnetic fluxes through the loop $\eta = \alpha$, β, ϵ. We can the get rid of phase jumps φ_2, φ_5 and φ_6 to obtain the following Hamiltonian

$$\begin{aligned} \mathcal{H}_q = {} & \frac{4E_C}{\alpha+\beta+2\alpha\beta}\left[(\alpha+\beta+\alpha\beta)(n_1^2+n_3^2)+(1+2\alpha)n_4^2-2\alpha\beta n_1 n_3-2\alpha(n_1+n_3)n_4\right] \\ & - E_J\left[\cos(\varphi_1)+\alpha\cos\left(\frac{f_\alpha}{2}\right)\cos(\varphi_1+\varphi_3+\tilde{\varphi}_4+\tilde{f}_\epsilon)+\cos(\varphi_3)+\beta\cos\left(\frac{f_\beta}{2}\right)\cos(\tilde{\varphi}_4)\right], \end{aligned} \tag{5.22}$$

where we have: $\tilde{\varphi}_4 = \varphi_4 - f_\beta/2$ and $\tilde{f}_\epsilon = f_\epsilon + (f_\beta - f_\alpha)/2$. We can observe that, by changing the parameters f_α, f_β and f_ϵ such that $f_\epsilon = (2\pi + f_\alpha - f_\beta)/2$ is verified, the Hamiltonian does

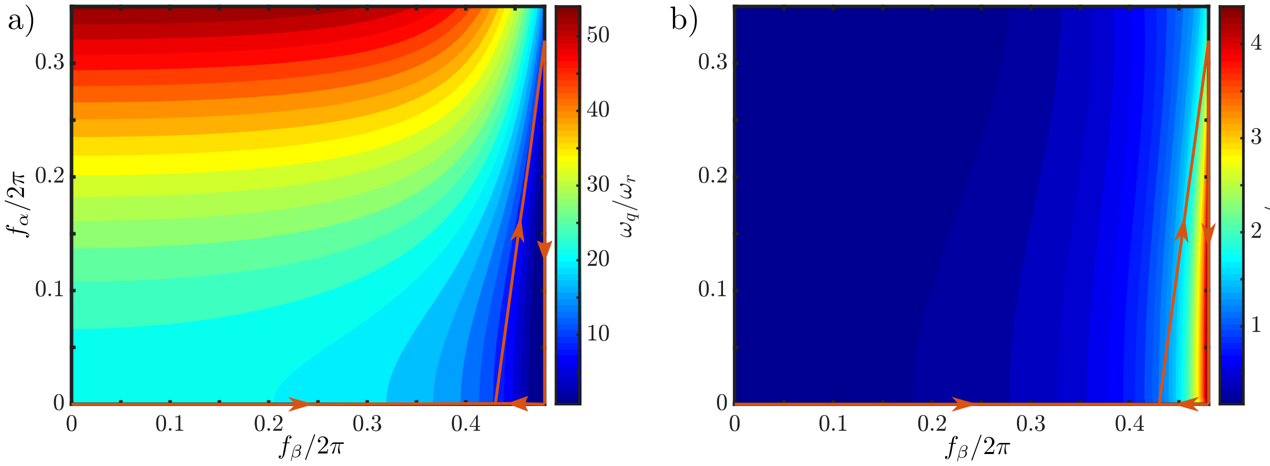

Figure 5.8: Tunability of the qubit. a) Transition frequency of the qubit, ω_q, as a function of the external fluxes in the SQUID-loops in units of the resonator frequency. b) Normalized coupling constant g/ω_r of the qubit to the LC-resonator. Parameters used to produce this plot are given in the text.

not change its form. This means that we can then fix $\tilde{f}_\epsilon = \pi$ and, at the same time, change the potential shape.

As we have seen in Eq. (5.4), the qubits are coupled to the resonator via the phase jump over the entire qubit sub-circuit. For this implementation, such phase jump is given by $\Delta\varphi = \tilde{\varphi}_4$. The coupling strength g is then related to the matrix element of $\Delta\varphi$ between the first two lowest qubit states, that is $\Delta\varphi_{eg} = \langle e|\Delta\varphi|g\rangle$. It is worthwhile to mention that, because of the coupling between resonator and qubits, the qubit Hamiltonian is renormalized by the additional term $E_L\Delta\varphi^2/2$, with $E_L = \Phi_0^2/L$ the inductive energy related to the resonator inductance L.

We can now show that this Hamiltonian (5.4) allows for the tunability of the qubit frequency and qubit-resonator coupling as we described in paragraph 5.4. Firstly, we numerically diagonalize $\mathcal{H}_q$, including the additional term from the coupling and find the lowest eigenvalues. Secondly, we evaluate the transition matrix element $\Delta\varphi_{eg}$. For such simulation the following parameters are selected: $\alpha = 0.6$, $\beta = 6$, $E_L/h = 2.57\,\mathrm{GHz}$ (which gives $L = 63.7\,\mathrm{nH}$), $E_C/h = 4.99\,\mathrm{GHz}$ and $E_J/h = 99.7\,\mathrm{GHz}$. Additionally, we take $C = 1.59\,\mathrm{pF}$, which, in turn, fixes the resonator frequency and impedance to $\omega_r = (LC)^{-1/2} = 2\pi \times 500\,\mathrm{MHz}$ and $Z_r = \sqrt{L/C} = 200\,\Omega$, respectively. Lastly, we change f_α in the interval from 0 to 0.70π and f_β from 0 to 0.96π (f_ϵ changes accordingly to keep the qubit at $\tilde{f}_\epsilon = \pi$). Figures 5.8(a)-(b) show the transition frequency of the qubit ω_q/ω_r and the the coupling constant g/ω_r versus the external fluxes in the two SQUID-loops. Remarkably, both of them result highly tunable spanning

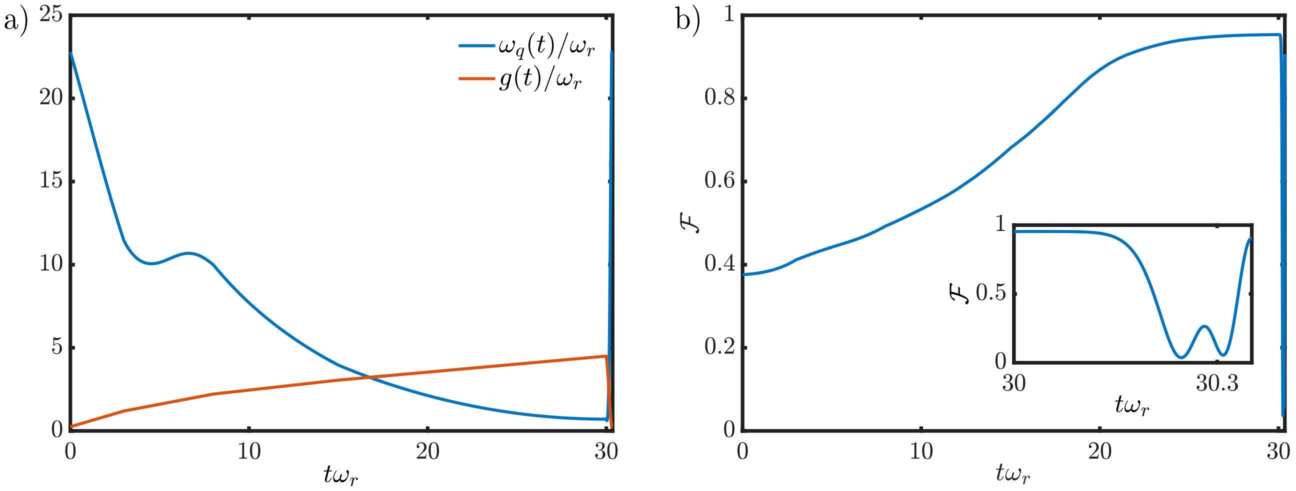

Figure 5.9: a) Pulse shapes for the parameters g and ω_q obtained from following the path outlined in Fig. 5.8 (red lines) for the external control parameters. b) Fidelity of the protocol for $N = 4$.

from $\sim 50\omega_r$ all the way to $\sim 0.5\omega_r$ and from $\sim 0.17\omega_r$ up to $\sim 4.5\omega_r$, respectively. The only real limitation might arise because qubit transition frequency and coupling strength cannot be tuned entirely separately. We find that an optimal path in the parameter space (f_α, f_β) is described by the red curves in the plots of Fig. 5.8. From the starting point (0, 0) we follow a clockwise loop. This determines the two time-dependent pulses $g(t)$ and $\omega_q(t)$ given in Fig. 5.9(a). Given the dependence of the two pulses, we have initially determined the shape for the g-pulse, and then from this, the resulting one for ω_q. Similarly to the pulse described in the ideal case, we firstly increase g/ω_r from 0.25 to 4.5 adiabatically, and then, non-adiabatically, we decrease it to its initial value. In the opposite way, the qubit frequency is decreased from $22.8\omega_r$ to $0.7\omega_r$, and then increased to its initial value as well. For this pulse, in Fig. 5.9(b) we plot the result for the time-dependent fidelity in the case of $N = 4$ qubits coupled collectively to the same resonator mode. Although we have exploited a limited tunability for both coupling and qubit frequency, we are able to achieve EEFs of $\mathcal{F}_\mathrm{E} > 0.9$. In particular, using the same pulse for $N = 2$, we instead obtain $\mathcal{F}_\mathrm{E} \approx 0.96$.

5.8 Conclusions

In summary, in this Chapter we have analyzed a multi-qubit circuit QED system in the extreme regime where the interaction between light and matter dominates over the system's bare energy scales. In such a regime the system shows new phenomena such as the light matter decoupling and the generation of a manifold of low-energy states with a high degree of entanglement. Our main goal has been to design a protocol able to extract such correlations, which otherwise would be hidden in the ground state of the system, and to convert them into well-defined multi-partite entangled states of non-interacting qubits. These states could be then manipulated and used for any quantum information task. More specifically, to achieve such goal, we have used a time-dependent protocol based on a variation of the system parameters: the coupling strength and the qubit frequency. We have showed that the scheme works in a fast and robust manner, and it is also fully compatible with experimental constraints on switching times and typical energy scales encountered in circuit QED systems. On this regard, we have actually prosed a particular circuital design for a possible experimental realization. The detailed analysis of this protocol has illustrated how various and so far unexplored USC effects can contribute not only to the generation of complex multi-qubit states, but also to the protection of them. Of course, these principles, which are behind the study of the light-matter interaction in the USC regime, can be also explored in different platforms. Moreover, our results represent a starting point for all the future investigations aiming to realize more complex operations (of preparation, storage and control) in circuit QED experiments operating in the USC and involving more than two artificial atoms.

Conclusions

Central to all the investigations of this thesis has been the study of the light-matter interaction in mesoscopic systems, where single- or multi-mode electromagnetic fields can interact with objects whose dimensions range in the micro-nano scale domain. In particular, among the platforms which offer the possibility to investigate such scenario, we have considered: optomechanics, cavity QED and circuit QED, which, on the other hand, have been very successful both from a theoretical and an experimental point of view.

In the context of the optomechanical cavity we have studied the interaction of both a single- and multi-mode field with a moving mirror. For a single mode field inside the cavity (typical scenario in quantum optics), our efforts have been focused on two main research lines: the individuation of clear signatures of the quantum interaction between the optical field and the mechanical oscillator and the exploration of possible deviations in the mechanical dynamics. Along the first line, we have studied the quantum-classical comparison of the phases acquired by the radiation field after its pulsed or continuous interaction with the mechanical mirror. Our approach to tackle such comparison has revealed that many of the features, which in literature have been considered of quantum origin, can be actually explained by classical means. In particular, we have demonstrated that the interferometric visibility cannot be completely used as a witness of the quantum interaction between light and oscillator. In addition, we have been able to identify new peculiarities that might prove the quantum behaviour of a mesoscopic object such us the movable mirror in future optomechanical experiments.

On the other hand, following the second line of research, we have proposed a protocol to probe possible anharmonicities of the mechanical mirror in the optomechanical pulsed regime. This investigation has been motivated by the recent attention gained by optomechanical cavities for the exploration of possible deviations of quantum mechanics (induced by gravity). In fact, such deviations might be translated in mechanical anharmonicities. Therefore, designing a feasible scheme, which can be able to probe nonlinearities of the mechanical motion, becomes essential.

Our proposal can be a starting point for further implementations in systems displaying similar Hamiltonians and can be easily generalized to probe different kinds of anharmonicities.

In the multimode scenario, an optomechanical cavity can be easily connected to the field of Casimir physics. In fact, Casimir and Casimir-Polder forces are zero-temperature electromagnetic forces of purely quantum origin, which appear every time a quantum multimode field is confined within a specific geometric configuration (in this specific case a cavity), and become prominent at the micro-nano scale. Today Casimir forces have intensively been studied in micro-nano mechanical devices to prevent friction and design contact-less surfaces. In this scenario, starting from a non-equilibrium configuration of the optomechanical system, we have investigated possible dynamical modifications to the static Casimir force between the two walls of the optomechanical cavity, induced by a quantum description of the mechanical mirror. The procedure behind this study has revealed to be very general. We have thus applied it to also explore non-equilibrium dynamical corrections of the Casimir-Polder force between an excited atom and a wall, mediated by the electromagnetic field inside a cavity. This, on the other hand, represents the typical and most fundamental system in cavity QED. In both cases, we have analyzed the time-dependent process which leads the overall system to its equilibrium configuration, where local quantities such as field-mirror or atom-wall interaction energies converge to their stationary value, contrarily to global quantities such as the field energy. Furthermore, we have seen how a dynamical component can increase the absolute value of Casimir or Casimir-Polder forces. This should be relevant for the detection of the Casimir corrections due to the quantum nature of the boundary in an optomechanical cavity, or of the dynamical Casimir-Polder forces. Also, for the dynamical Casimir-Polder force, we have found that using an atom initially in its excited state is very convenient to single out the elusive dynamical Casimir-Polder effect.

Novel phenomena appear when the coupling between light and matter is pushed to the regime where it overcomes the bare energies of the system. However, both in optomechanics and cavity QED it is experimentally quite hard to enter into this regime. One usually deals with systems in the weakly-coupled regime, and the opposite limit of strong or extremely strong interactions is to a very large extent still unexplored. On the other hand, in the arising field of circuit QED, where artificial atoms (charge or flux qubits) are coupled to microwave fields (resonators), single superconducting two-level systems have been already coupled ultrastrongly to resonator modes. For this reason, we have then moved our attention from cavity QED to circuit QED. In this context, we have analyzed a circuit where several qubits are coupled to a single resonator in the USC regime. Very counter-intuitively, in the extreme domain of very USC interactions, light and matter completely decoupled and the system displays a high degree of entanglement. We have then described a time-dependent protocol to extract and convert such correlations into defined multi-partite entangled states of non-interacting qubits. We have also seen that the USC regime can be exploited to protect such correlations once extracted. We have finally discussed in detail the feasibility of our scheme, which has illustrated how we can actually use the USC regime of circuit QED to complete very non-trivial operations.

Our results clearly show that studying the interaction between light and matter in mesoscopic systems (in the micro- or nano-scale) allows to address problems very different in nature and that, historically, belong to different fields of Physics. They also demonstrate how such devices represent a very promising platform to probe and test fundamental aspects of quantum mechanics, as well as to perform control operations, which might have potential for the development of practical applications.

Bibliography

[1] F. Marquardt and S. M. Girvin, "Trend: Optomechanics," *Physics*, vol. 2, p. 40, 2009.

[2] M. Aspelmeyer, T. J. Kippenberg, and F. Marquardt, "Cavity optomechanics," *Rev. Mod. Phys.*, vol. 86, p. 1391, 2014.

[3] V. Dodonov, "Current status of the dynamical Casimir effect," *Phys. Scr.*, vol. 82, p. 038105, 2010.

[4] C. K. Law, "Interaction between a moving mirror and radiation pressure: a Hamiltonian formulation," *Phys. Rev. A*, vol. 51, p. 2537, 1995.

[5] A. D. K. Plato, C. N. Hughes, and M. S. Kim, "Gravitational effects in quantum mechanics," *Contemp. Phys.*, vol. 57, p. 477, 2016.

[6] I. Pikovski, M. R. Vanner, M. Aspelmeyer, M. S. Kim, and Č. Brukner, "Probing Planck-scale physics with quantum optics," *Nature Phys.*, vol. 8, p. 393, 2012.

[7] A. W. Rodriguez, F. Capasso, and S. G. Johnson, "The Casimir effect in microstructured geometries," *Nature Photon.*, vol. 5, p. 211, 2011.

[8] P. W. Milonni, *The Quantum Vacuum: An Introduction To Quantum Electrodynamics.* Academic Press, San Diego, CA, 1994.

[9] J. Clarke and F. K. Wilhelm, "Superconducting quantum bits," *Nature (London)*, vol. 453, p. 1031, 2008.

[10] A. Wallraff, D. I. Schuster, A. Blais, L. Frunzio, R. S. Huang, J. Majer, S. Kumar, S. M. Girvin, and R. J. Schoelkopf, "Strong coupling of a single photon to a superconducting qubit using circuit quantum electrodynamics," *Nature (London)*, vol. 431, p. 162, 2004.

[11] A. Blais, R.-S. Huang, A. Wallraff, S. M. Girvin, and R. J. Schoelkopf, "Cavity quantum electrodynamics for superconducting electrical circuits: An architecture for quantum computation," *Phys. Rev. A*, vol. 69, p. 062320, 2004.

[12] C. Wilson, G. Johansson, A. Pourkabirian, J. Johansson, T. Duty, F. Nori, and P. Delsing, "Observation of the dynamical Casimir effect in a superconducting circuit," *Nature (London)*, vol. 479, p. 376, 2011.

[13] J. D. Thompson, B. M. Zwickl, A. M. Jayich, F. Marquardt, S. M. Girvin, and J. G. E. Harris, "Strong dispersive coupling of a high-finesse cavity to a micromechanical membrane," *Nature (London)*, vol. 452, p. 72, 2008.

[14] S. Groeblacher, J. B. Hertzberg, M. R. Vanner, G. D. Cole, S. Gigan, K. C. Schwab, and M. Aspelmeyer, "Demonstration of an ultracold micro- optomechanical oscillator in a cryogenic cavity," *Nature Phys.*, vol. 5, p. 485, 2009.

[15] H. Chan, V. Aksyuk, R. Kleinman, D. Bishop, and F. Capasso, "Quantum mechanical actuation of microelectromechanical systems by the Casimir force," *Science*, vol. 291, p. 1941, 2001.

[16] T. Duty, D. Gunnarsson, K. Bladh, and P. Delsing, "Coherent dynamics of a Josephson charge qubit," *Phys. Rev. B*, vol. 69, p. 140503(R), 2004.

[17] K. Stannigel, P. Komar, S. J. M. Habraken, S. D. Bennett, M. D. Lukin, P. Zoller, and P. Rabl, "Optomechanical quantum information processing with photons and phonons," *Phys. Rev. Lett.*, vol. 109, p. 013603, 2012.

[18] P. Treutlein, C. Genes, K. Hammerer, M. Poggio, and P. Rabl, "Hybrid mechanical systems," in *Cavity Optomechanics* (M. Aspelmeyer, T. Kippenberg, and F. Marquardt, eds.), Springer, 2012.

[19] M. Aspelmeyer, P. Meystre, and K. Schwab, "Quantum optomechanics," *Phys. Today*, vol. 65, p. 29, 2012.

[20] W. Marshall, C. Simon, R. Penrose, and D. Bouwmeester, "Towards quantum superpositions of a mirror," *Phys. Rev. Lett.*, vol. 91, p. 130401, 2003.

[21] R. Penrose, "Quantum computation, entanglement and state reduction," *Phil. Trans. R. Soc. Lond. A*, vol. 356, p. 0256, 1998.

[22] S. Lamoreaux, "Casimir forces: Still surprising after 60 years," *Phys. Today*, vol. 60, p. 40, 2007.

[23] T. Corbitt, Y. Chen, E. Innerhofer, H. Müller-Ebhardt, D. Ottaway, H. Rehbein, D. Sigg, S. Whitcomb, C. Wipf, and N. Mavalvala, "An all-optical trap for a gram-scale mirror," *Phys. Rev. Lett.*, vol. 98, p. 150802, 2007.

[24] O. Arcizet, P. F. Cohadon, T. Briant, M. Pinard, and A. Heidmann, "Radiation-pressure cooling and optomechanical instability of a micromirror," *Nature (London)*, vol. 444, 2006.

[25] A. Schliesser, O. Arcizet, R. Riviere, G. Anetsberger, and T. J. Kippenberg, "Resolved-sideband cooling and position measurement of a micromechanical oscillator close to the heisenberg uncertainty limit," *Nature Phys.*, vol. 5, p. 509, 2009.

[26] J. D. Teufel, J. W. Harlow, C. A. Regal, and K. W. Lehnert, "Dynamical backaction of microwave fields on a nanomechanical oscillator," *Phys. Rev. Lett.*, vol. 101, p. 197203, 2008.

[27] V. B. Braginsky, Y. I. Vorontsov, and K. S. Thorne, "Quantum nondemolition measurements.," *Science*, vol. 209, p. 547, 1980.

[28] C. M. Caves, K. S. Thorne, R. W. P. Drever, V. D. Sandberg, and M. Zimmermann, "On the measurement of a weak classical force coupled to a quantum-mechanical oscillator. I. issues of principle," *Rev. Mod. Phys.*, vol. 52, p. 341, 1980.

[29] P. F. Cohadon, A. Heidmann, and M. Pinard, "Cooling of a mirror by radiation pressure," *Phys. Rev. Lett.*, vol. 83, p. 3174, 1999.

[30] S. Bose, K. Jacobs, and P. L. Knight, "Preparation of nonclassical states in cavities with a moving mirror," *Phys. Rev. A*, vol. 56, p. 4175, 1997.

[31] S. Mancini, V. I. Man'ko, and P. Tombesi, "Ponderomotive control of quantum macroscopic coherence," *Phys. Rev. A*, vol. 55, p. 3042, 1997.

[32] L. H. Ford and N. F. Svaiter, "Vacuum energy density near fluctuating boundaries," *Phys. Rev. D*, vol. 58, p. 065007, 1998.

[33] N. Bartolo, S. Butera, M. Lattuca, R. Passante, L. Rizzuto, and S. Spagnolo, "Vacuum Casimir energy densities and field divergences at boundaries," *J. Phys.: Condens. Matter*, vol. 27, p. 214015, 2015.

[34] F. Armata and R. Passante, "Vacuum energy densities of a field in a cavity with a mobile boundary," *Phys. Rev. D*, vol. 91, p. 025012, 2015.

[35] S. Aldana, C. Bruder, and A. Nunnenkamp, "Equivalence between an optomechanical system and a Kerr medium," *Phys. Rev. A*, vol. 88, p. 043826, 2013.

[36] M. R. Vanner, I. Pikovski, G. D. Cole, M. S. Kim, Č. Brukner, K. Hammerer, G. J. Milburn, and M. Aspelmeyer, "Pulsed quantum optomechanics," *PNAS*, vol. 108, p. 16182, 2011.

[37] S. Haroche and J. M. Raimond, *Exploring the Quantum.* Oxford University Press, Oxford, 2006.

[38] D. T. Smithey, M. Beck, M. G. Raymer, and A. Faridani, "Measurement of the Wigner distribution and the density matrix of a light mode using optical homodyne tomography: Application to squeezed states and the vacuum," *Phys. Rev. Lett.*, vol. 70, p. 1244, 1993.

[39] S. M. M. G. Genoni and A. Serafini, "General-dyne unravelling of a thermal master equation," *Russian Journal of Mathematical Physics*, vol. 21, p. 329, 2014.

[40] M. G. A. Paris, "Quantum estimation for quantum technology," *Int. J. Quantum Information*, vol. 7, p. 125, 2009.

[41] H. B. G. Casimir, "On the attraction between two perfectly conducting plates," *Proc. K. Ned. Akad. Wet.*, vol. 51, p. 793, 1948.

[42] S. Buhmann, *Dispersion Forces I and II.* Springer, Heidelberg, 2012.

[43] J. E. Lennard-Jones, "On the determination of molecular fields," *Proc. R. Soc. Lond. A*, vol. 106, p. 441, 1924.

[44] L. W. Bruch, M. W. Cole, and E. Zaremba, *Physical Adsorption: Forces and Phenomena.* Oxford Science Pubblications, 1997.

[45] D. Bonn and D. Ross, “Wetting transitions,” *Rep. Prog. Phys.*, vol. 64, p. 1085, 2001.

[46] T. F. Tadros, “Industrial applications of dispersions,” *Adv. Colloid Interface Sci.*, vol. 46, p. 1, 1993.

[47] J. N. Israelachvili, *Intermolecular ans Surface Forces.* Academic Press, London, 1991.

[48] K. A. Milton, “The Casimir effect: recent controversies and progress,” *J. Phys. A*, vol. 37, p. R209, 2004.

[49] G. Binnig, C. F. Quate, and C. Gerber, “Atomic force microscope,” *Phys. Rev. Lett.*, vol. 56, p. 930, 1986.

[50] R. Loudon, *The Quantum Theory of Light.* Oxford University Press, 2000.

[51] G. Compagno, R. Passante, and F. Persico, *Atom-Field Interactions and Dressed Atoms.* Cambridge University Press, Cambridge, 1995.

[52] E. A. Power and S. Zienau, “Coulomb gauge in no-relativistic quantum electrodynamics and the shape of the spectral lines,” *Phil. Trans. R. Soc. Lond. A*, vol. 251, p. 557, 1959.

[53] R. G. Wolley, “Molecular quantum electrodynamics,” *Proc. R. Soc. Lond. A*, vol. 321, p. 557, 1971.

[54] J. S. Peng and G. X. Li, *Introduction to Modern Quantum Optics.* World Scientific, Singapore, 1998.

[55] P. W. Milonni, R. J. Cook, and M. E. Goggin, “Radiation pressure from the vacuum: Physical interpretation of the Casimir force,” *Phys. Rev. A*, vol. 38, p. 1621, 1988.

[56] U. Mohideen and A. Roy, “Precision measurement of the Casimir force from 0.1 to 0.9μm,” *Phys. Rev. Lett.*, vol. 81, p. 4549, 1998.

[57] G. Bressi, G. Carugno, R. Onofrio, and G. Ruoso, “Measurement of the Casimir force between parallel metallic surfaces,” *Phys. Rev. Lett.*, vol. 88, p. 041804, 2002.

[58] L. S. Brown and G. J. Maclay, “Vacuum stress between conducting plates: An image solution,” *Phys. Rev.*, vol. 184, p. 1272, 1969.

[59] H. B. G. Casimir and D. Polder, "The influence of retardation on London-van der Waals forces," *Phys. Rev.*, vol. 73, p. 360, 1948.

[60] G. Barton, "Quantum-electrodynamic level shifts between parallel mirrors: Analysis," *Proc. R. Soc. Lon. A*, vol. 410, p. 141, 1987.

[61] E. A. Power and T. Thirunamachandran, "Quantum electrodynamics in a cavity," *Phys. Rev. A*, vol. 25, p. 2473, 1982.

[62] R. Messina, R. Passante, L. Rizzuto, S. Spagnolo, and R. Vasile, "Casimir-Polder forces, boundary conditions and fluctuations," *J. Phys. A: Math. Theor.*, vol. 41, p. 164031, 2008.

[63] R. Vasile and R. Passante, "Dynamical Casimir-Polder force between an atom and a conducting wall," *Phys. Rev. A*, vol. 78, p. 032108, 2008.

[64] M. Abramowitz and I. Stegun, *Handbook of Mathematical Functions.* Dover Publ., New York, 1965.

[65] D. P. Craig and T. Thirunamachandran, *Molecular Quantum Electrodynamics.* Dover, Mineola, 1998.

[66] V. Sandoghdar, C. I. Sukenik, E. A. Hinds, and S. Haroche, "Direct measurement of the van der Waals interaction between an atom and its images in a micron-sized cavity," *Phys. Rev. Lett.*, vol. 68, p. 3432, 1992.

[67] C. I. Sukenik, M. G. Boshier, D. Cho, V. Sandoghdar, and E. A. Hinds, "Measurement of the Casimir-Polder force," *Phys. Rev. Lett.*, vol. 70, p. 560, 1992.

[68] M. Wilson, P. Bushev, J. Eschner, F. Schmidt-Kaler, C. Becher, R. Blatt, and U. Dorner, "Vacuum-field level shifts in a single trapped ion mediated by a single distant mirror," *Phys. Rev. Lett.*, vol. 91, p. 213602, 2003.

[69] V. Druzhinina and M. DeKieviet, "Experimental observation of quantum reflection far from threshold," *Phys. Rev. Lett.*, vol. 91, p. 193202, 2003.

[70] P. Bushev, A. Wilson, J. Eschner, C. Raab, F. Schmidt-Kaler, C. Becher, and R. Blatt, "Forces between a single atom and its distant mirror image," *Phys. Rev. Lett.*, vol. 92, p. 223602, 2004.

[71] D. M. Harber, J. M. Obrecht, J. M. McGuirk, and E. A. Cornell, “Measurement of the Casimir-Polder force through center-of-mass oscillations of a Bose-Einstein condensate,” *Phys. Rev. A*, vol. 72, p. 033610, 2005.

[72] J. M. Obrecht, R. J. Wild, M. Antezza, L. P. Pitaevskii, S. Stringari, and E. A. Cornell, “Measurement of the temperature dependence of the Casimir-Polder force,” *Phys. Rev. Lett.*, vol. 98, p. 063201, 2007.

[73] E. J. W. Verwey and J. T. G. Overbeek, *Theory of the Stability of Lyophobic Colloids.* Dover Publications, Mineola, 2003.

[74] M. A. Bevan and D. C. Prieve, “Direct measurement of retarded van der Waals attraction,” *Langmuir*, vol. 15, p. 7925, 1999.

[75] M. Marcovitch and H. Diamant, “Enhanced dispersion interaction in confined geometry,” *Phys. Rev. Lett.*, vol. 95, p. 223203, 2005.

[76] M. S. Tomas, “Enhanced van der Waals interaction at interfaces,” *J. Phys. A: Math. Theor.*, vol. 41, p. 164020, 2008.

[77] U. Vool and M. Devoret, “Introduction to quantum electromagnetic circuits,” *Int. J. Circ. Theor. Appl.*, vol. 45, pp. 897–934, 2017.

[78] N. K. Langford, “Circuit QED - lecture notes,” *arXiv:1310.1897*, 2013.

[79] J. J. Garcia-Ripoll, “Lectures notes on superconducting quantum circuits,” *http://juanjose.garciaripoll.com/lectures-quantum-circuits*, 2014.

[80] T. Niemczyk, F. Deppe, H. Huebl, E. P. Menzel, F. Hocke, M. J. Schwarz, J. J. Garcia-Ripoll, D. Zueco, T. Hümmer, E. Solano, A. Marx, and R. Gross, “Circuit quantum electrodynamics in the ultrastrong-coupling regime,” *Nature Phys.*, vol. 6, p. 772, 2010.

[81] P. Forn-Diaz, J. J. G. ia Ripoll, B. Peropadre, M. A. Yurtalan, J.-L. Orgiazzi, R. Belyansky, C. M. Wilson, and A. Lupascu, “Ultrastrong coupling of a single artificial atom to an electromagnetic continuum,” *Nature Phys.*, vol. 13, p. 39, 2017.

[82] F. Yoshihara, T. Fuse, S. Ashhab, K. Kakuyanagi, S. Saito, and K. Semba, “Superconducting qubit-oscillator circuit beyond the ultrastrong-coupling regime,” *Nature Phys.*, vol. 13, p. 44, 2017.

[83] D. I. Schuster, A. A. Houck, J. A. Schreier, A. Wallraff, J. M. Gambetta, A. Blais, L. Frunzio, J. Majer, B. Johnson, M. H. Devoret, S. M. Girvin, and R. J. Schoelkopf, "Resolving photon number states in a superconducting circuit," *Nature (London)*, vol. 445, p. 515, 2007.

[84] A. A. Houck, D. I. Schuster, J. M. Gambetta, J. A. Schreier, B. R. Johnson, J. M. Chow, L. Frunzio, J. Majer, M. H. Devoret, S. M. Girvin, and R. J. Schoelkopf, "Generating single microwave photons in a circuit," *Nature (London)*, vol. 449, p. 443, 2007.

[85] J. Majer, J. M. Chow, J. M. Gambetta, J. Koch, B. R. Johnson, J. A. Schreier, L. Frunzio, D. I. Schuster, A. A. Houck, A. Wallraff, A. Blais, M. H. Devoret, S. M. Girvin, and R. J. Schoelkopf, "Coupling superconducting qubits via a cavity bus," *Nature (London)*, vol. 449, p. 443, 2007.

[86] A. A. Houck, H. E. Tureci, and J. Koch, "On-chip quantum simulation with superconducting circuits," *Nature Phys.*, vol. 8, p. 292, 2012.

[87] A. Corcoles, E. Magesan, S. J. Srinivasan, A. W. Cross, M. Steffen, J. M. Gambetta, and J. M. Chow, "Demonstration of a quantum error detection code using a square lattice of four superconducting qubits," *Nature Commun.*, vol. 6, p. 6979, 2015.

[88] R. Feynman, R. Leighton, and M. Sands, *The Feynman Lectures on Physics, Vol. III.* Addison Wesley, 1971.

[89] V. Bouchiat, D. Vion, P. Joyez, D. Esteve, and M. H. Devoret, "Quantum coherence with a single Cooper pair," *Phys. Scr.*, vol. T76, p. 165, 1998.

[90] J. Koch, T. M. Yu, J. Gambetta, A. A. Houck, D. I. Schuster, J. Majer, A. Blais, M. H. Devoret, S. M. Girvin, and R. J. Schoelkopf, "Charge-insensitive qubit design derived from the Cooper pair box," *Phys. Rev. A*, vol. 76, p. 042319, 2007.

[91] J. A. Schreier, A. A. Houck, J. Koch, D. I. Schuster, B. R. Johnson, J. M. Chow, J. M. Gambetta, J. Majer, L. Frunzio, M. H. Devoret, S. M. Girvin, and R. J. Schoelkopf, "Suppressing charge noise decoherence in superconducting charge qubits," *Phys. Rev. B*, vol. 77, p. 180502(R), 2008.

[92] I. C. Hoi, A. F. Kockum, T. Palomaki, T. M. Stace, B. Fan, L. Tornberg, S. R. Sathyamoorthy, G. Johansson, P. Delsing, and C. M. Wilson, "Giant cross–Kerr effect

for propagating microwaves induced by an artificial atom," *Phys. Rev. Lett.*, vol. 111, p. 053601, 2013.

[93] T. P. Orlando, J. E. Mooij, L. Tian, C. H. van der Wal, L. S. Levitov, S. Lloyd, and J. J. Mazo, "Superconducting persistent-current qubit," *Phys. Rev. B*, vol. 60, p. 15398, 1999.

[94] G. J. Milburn, S. Schneider, and D. F. V. James, "Ion trap quantum computing with warm ions," *Fortschr. Phys.*, vol. 48, p. 801, 2000.

[95] A. Sørensen and K. Mølmer, "Entanglement and quantum computation with ions in thermal motion," *Phys. Rev. A*, vol. 62, p. 022311, 2000.

[96] D. Leibfried, B. DeMarco, V. Meyer, D. Lucas, M. Barrett, J. Britton, W. M. Itano, B. Jelenković, C. Langer, T. Rosenband, and D. J. Wineland, "Experimental demonstration of a robust, high-fidelity geometric two ion-qubit phase gate," *Nature (London)*, vol. 422, p. 412, 2003.

[97] P. J. Leek and et al., "Observation of Berry's phase in a solid-state qubit," *Science*, vol. 318, p. 1889, 2007.

[98] M. Ericsson, D. Achilles, J. T. Barreiro, D. Branning, N. A. Peters, and P. G. Kwiat, "Measurement of geometric phase for mixed states using single photon interferometry.," *Phys. Rev. Lett.*, vol. 94, p. 050401, 2005.

[99] N. K. Langforda, S. Ramelow, R. Prevedel, W. J. Munro, G. J. Milburn, and A. Zeilinger, "Efficient quantum computing using coherent photon conversion," *Nature (London)*, vol. 478, p. 360, 2011.

[100] K. E. Khosla, M. R. Vanner, W. P. Bowen, and G. J. Milburn, "Quantum state preparation of a mechanical resonator using an optomechanical geometric phase," *New J. Phys.*, vol. 15, p. 043025, 2013.

[101] S. Bose, K. Jacobs, and P. L. Knight, "Scheme to probe the decoherence of a macroscopic object," *Phys. Rev. A*, vol. 59, p. 3204, 1999.

[102] A. D. Armour, M. P. Blencowe, and K. C. Schwab, "Entanglement and decoherence of a micromechanical resonator via coupling to a Cooper-pair box," *Phys. Rev. Lett.*, vol. 88, p. 148301, 2002.

[103] G. Vacanti, R. Fazio, M. S. Kim, G. M. Palma, M. Paternostro, and V. Vedral, "Geometric-phase backaction in a mesoscopic qubit-oscillator system," *Phys. Rev. A*, vol. 85, p. 022129, 2012.

[104] M. Scala, M. S. Kim, G. W. Morley, P. F. Barker, and S. Bose, "Matter-wave interferometry of a levitated thermal nano-oscillator induced and probed by a spin," *Phys. Rev. Lett.*, vol. 111, p. 180403, 2013.

[105] V. Braginsky and F. Khalili, *Quantum measurement.* Cambridge University Press, Cambridge, 1995.

[106] S. M. Barnett and P. M. Radmore, *Methods in theoretical quantum optics.* Oxford Science Pubblications, Oxford, 1997.

[107] M. Rakhmanov, "Doppler-induced dynamics of fields in Fabry-Perot cavities with suspended mirrors," *Applied Optics*, vol. 40, no. 12, p. 1942, 2001.

[108] M. Rakhmanov, R. Savage, D. Reitze, and D. Tanner, "Dynamic resonance of light in Fabry–Perot cavities," *Phys. Lett. A*, vol. 305, p. 239, 2002.

[109] M. Fox, *Quantum Optics.* Oxford University Press, Oxford, 2005.

[110] B. Sanders and G. Milburn, "Quantum limits to all-optical phase shifts in a Kerr nonlinear medium," *Phys. Rev. A*, vol. 45, p. 1919, 1992.

[111] H. F. Trotter, "On the product of semi-groups of operators," *Proc. Amer. Math. Soc.*, vol. 10, p. 545, 1959.

[112] M. Suzuki, "Generalized Trotter's formula and systematic approximants of exponential operators and inner derivations with applications to many-body problems," *Comm. Math. Phys.*, vol. 51, p. 183, 1976.

[113] T. Baumgratz, M. Cramer, and M. Plenio, "Quantifying coherence," *Phys. Rev. Lett.*, vol. 113, p. 140401, 2014.

[114] F. Brennecke, S. Ritter, T. Donner, and T. Esslinger, "Cavity optomechanics with a Bose-Einstein condensate," *Science*, vol. 322, p. 235, 2008.

[115] R. Leijssen and E. Verhagen, "Strong optomechanical interactions in a sliced photonic crystal nanobeam," *Sci. Rep.*, vol. 5, p. 15974, 2015.

[116] D. Kleckner, I. Pikovski, E. Jeffrey, L. Ament, E. Eliel, J. van den Brink, and D. Bouwmeester, "Creating and verifying a quantum superposition in a micro-optomechanical system," *New J. Phys*, vol. 10, p. 095020, 2008.

[117] A. Lampo, L. Fratino, and H. T. Elze, "Mirror-induced decoherence in hybrid quantum-classical theory," *Phys. Rev. A*, vol. 90, p. 042120, 2014.

[118] S. Gigan, H. R. Böhm, M. Paternostro, F. Blaser, G. Langer, J. B. Hertzberg, K. C. Schwab, D. Bäuerle, M. Aspelmeyer, and A. Zeilinger, "Self-cooling of a micromirror by radiation pressure," *Nature (London)*, vol. 444, p. 67, 2006.

[119] P. F. Barker and M. N. Shneider, "Cavity cooling of an optically trapped nanoparticle," *Phys. Rev. A*, vol. 81, p. 023826, 2010.

[120] D. E. Chang, C. A. Regal, S. B. Papp, D. J. Wilson, J. Yeb, O. Painter, H. J. Kimble, and P. Zoller, "Cavity opto-mechanics using an optically levitated nanosphere," *Proc. Natl Acad. Sci. USA*, vol. 107, p. 1005, 2010.

[121] A. C. Pflanzer, O. Romero-Isart, and J. I. Cirac, "Master-equation approach to optomechanics with arbitrary dielectrics," *Phys. Rev. A*, vol. 86, p. 013802, 2012.

[122] O. Romero-Isart, "Quantum superposition of massive objects and collapse models," *Phys. Rev. A*, vol. 84, p. 052121, 2011.

[123] M. Bahrami, M. Paternostro, A. Bassi, and H. Ulbricht, "Proposal for a noninterferometric test of collapse models in optomechanical systems," *Phys. Rev. Lett.*, vol. 112, p. 210404, 2014.

[124] M. Bawaj, C. Biancofiore, M. Bonaldi, F. Bonfigli, A. Borrielli, G. D. Giuseppe, L. Marconi, F. Marino, R. Natali, A. Pontin, G. Prodi, E. Serra, D. Vitali, and F. Marin, "Probing deformed commutators with macroscopic harmonic oscillators," *Nature Commun.*, vol. 6, p. 7503, 2015.

[125] G. J. Milburn and C. A. Holmes, "Dissipative quantum and classical liouville mechanics of the anharmonic oscillator," *Phys. Rev. Lett.*, vol. 56, p. 2237, 1986.

[126] C. Joshi, M. Jonson, E. Andersson, and P. Ohberg, “Quantum entanglement of anharmonic oscillators,” *J. Phys. B*, vol. 44, p. 245503, 2011.

[127] X.-Y. Lü, J.-Q. Liao, L. Tian, and F. Nori, “Steady-state mechanical squeezing in an optomechanical system via Duffing nonlinearity,” *Phys. Rev. A*, vol. 91, p. 013834, 2015.

[128] B. Teklu, A. Ferraro, M. Paternostro and M. A. Paris, “Nonlinearity and nonclassicality in a nanomechanical resonator,” *EPJ Quantum Technology*, vol. 2, p. 15, 2015.

[129] M. Paris, M. G. Genoni, N. Shammah, and B. Teklu, “Quantifying the nonlinearity of a quantum oscillator,” *Phys. Rev. A*, vol. 90, p. 012104, 2014.

[130] S. Rips, I. Wilson-Rae, and M. J. Hartmann, “Nonlinear nanomechanical resonators for quantum optoelectromechanics,” *Phys. Rev. A*, vol. 89, p. 013854, 2014.

[131] M. Dykman, *Fluctuating nonlinear oscillators: from nanomechanics to quantum superconducting circuits.* Oxford University Press, Oxford, 2012.

[132] A. Eichler, J. Moser, J. Chaste, M. Zdrojek, I. Wilson-Rae, and A. Bachtold, “Nonlinear damping in mechanical resonators made from carbon nanotubes and graphene,” *Nature Nanotech.*, vol. 6, p. 339, 2011.

[133] J. Gieseler, L. Novotny, and R. Quidant, “Thermal nonlinearities in a nanomechanical oscillator,” *Nature Phys.*, vol. 9, p. 806, 2013.

[134] P. Z. G. Fonseca, E. B. Aranas, J. Millen, T. S. Monteiro, and P. F. Barker, “Nonlinear dynamics and millikelvin cavity-cooling of levitated nanoparticles,” *Phys. Rev. Lett. 117*, vol. 117, p. 173602, 2016.

[135] L. D. Landau and E. M. Lifshitz, *Mechanics.* Butterworth-Heinemann, 1976.

[136] S. G. Krivoshlykov, V. I. Man’ko, and I. N. Sissakian, “Coherent state evolution for the quantum anharmonic oscillator,” *Phys. Lett. A*, vol. 90, p. 165, 1982.

[137] B. L. Higgins, D. W. Berry, S. D. Bartlett, H. M. Wiseman, and G. J. Pryde, “Entanglement-free Heisenberg-limited phase estimation,” *Nature (London)*, vol. 450, p. 393, 2007.

[138] D. Brivio, S. Cialdi, S. Vezzoli, B. T. Gebrehiwot, M. G. Genoni, S. Olivares, and M. G. A. Paris, “Experimental estimation of one-parameter qubit gates in the presence of phase diffusion,” *Phys. Rev. A*, vol. 81, p. 012305, 2010.

[139] A. A. Berni, T. Gehring, B. M. Nielsen, V. H́andchen, M. G. A. Paris, and U. L. Andersen, “Ab initio quantum-enhanced optical phase estimation using real-time feedback control,” *Nature Photon.*, vol. 9, p. 577, 2015.

[140] M. Suzuki, “On the convergence of exponential operators - the Zassenhaus formula, BCH formula and systematic approximants,” *Comm. Math. Phys.*, vol. 57, p. 193, 1977.

[141] A. Ferraro, S. Olivares and M. G. A. Paris, *Gaussian States in Quantum Information.* Bibliopolis, 2005.

[142] G. Moore, “Quantum theory of the electromagnetic field in a variable-length one-dimensional cavity,” *J. Math. Phys.*, vol. 11, p. 2679, 1970.

[143] J.-C. Jaskula, G. B. Partridge, M. Bonneau, R. Lopes, J. Ruaudel, D. Boiron, and C. I. Westbrook, “Acoustic analog to the dynamical Casimir effect in a Bose-Einstein condensate,” *Phys. Rev. Lett.*, vol. 109, p. 220401, 2012.

[144] A. Agnesi, C. Braggio, G. Bressi, G. Carugno, F. D. Valle, G. Gaelazzi, G. Messineo, F. Pirzio, G. Reali, G. Ruoso, D. Scarpa, and D. Zanello, “Mir: An experiment for the measurement of the dynamical Casimir effect,” *J. Phys. Conf. Series*, vol. 161, p. 012028, 2009.

[145] S. Butera and R. Passante, “Field fluctuations in a one-dimensional cavity with a mobile wall,” *Phys. Rev. Lett.*, vol. 111, p. 060403, 2013.

[146] Q. Wang and W. Unruh, “Motion of a mirror under infinitely fluctuating quantum vacuum stress,” *Phys. Rev. D*, vol. 89, p. 085009, 2014.

[147] Q. Wang and W. Unruh, “Mirror moving in quantum vacuum of a massive scalar field,” *Phys. Rev. D*, vol. 92, p. 063520, 2015.

[148] G. Volovik and M. Zubkov, “Mirror as polaron with internal degrees of freedom,” *Phys. Rev. D*, vol. 90, p. 087702, 2014.

[149] T. J. Kippenberg and K. J. Vahala, "Cavity optomechanics: Back-action at the mesoscale," *Science*, vol. 321, p. 1172, 2008.

[150] R. Messina, R. Vasile, and R. Passante, "Dynamical Casimir-Polder force on a partially dressed atom near a conducting wall," *Phys. Rev. A*, vol. 82, p. 062501, 2010.

[151] H. Haakh, C. Henkel, S. Spagnolo, L. Rizzuto, and R. Passante, "Dynamical Casimir-Polder interaction between an atom and surface plasmons," *Phys. Rev. A*, vol. 89, p. 022509, 2014.

[152] H. Yang, T. Y. Zheng, X. Zhang, X. Q. Shao, and S. M. Pan, "Dynamical Casimir-Polder force on a partially dressed atom in a cavity comprising a dielectric," *Ann. Phys.*, vol. 344, p. 69, 2014.

[153] P. Barcellona, R. Passante, L. Rizzuto, and S. Buhmann, "Dynamical Casimir-Polder interaction between a chiral molecule and a surface," *Phys. Rev. A*, vol. 93, p. 032508, 2016.

[154] F. Duque-Gomez and J. Sipe, "Response of a particle in a one-dimensional lattice to an applied force: Dynamics of the effective force," *Phys. Rev. A*, vol. 85, p. 053412, 2012.

[155] P. Gaal, W. Kuhen, K. Reimann, M. Woerner, T. Elsaesser, and R. Hey, "Internal motion of a quasiparticle governing its ultrafast nonlinear response," *Nature (London)*, vol. 450, p. 1210, 2007.

[156] M. Hase, M. Kitajima, A. Constantinescu, and H. Petek, "The birth of a quasiparticle in silicon observed in time-frequency space," *Nature (London)*, vol. 426, p. 51, 2003.

[157] R. Chang, S. Potnis, R. Ramos, C. Zhuanga, M. Hallaji, A. Hayat, F. Duque-Gomez, J. Sipe, and A. Steinberg, "Observing the onset of effective mass," *Phys. Rev. Lett.*, p. 170404, 2014.

[158] R. Passante and F. Persico, "Time-dependent Casimir-Polder forces and partially dressed states," *Phys. Lett. A*, vol. 312, p. 319, 2003.

[159] S. K. Lamoreaux, "The Casimir force: background, experiments, and applications," *Rep. Prog. Phys.*, vol. 68, p. 201, 2005.

[160] L. Woods, D. Dalvit, A. Tkatchenko, P. Rodriguez-Lopez, A. Rodriguez, and R. Podgornik, “A materials perspective on Casimir and van der Waals interactions,” *Rev. Mod. Phys.*, vol. 88, p. 045003, 2016.

[161] F. Armata, R. Vasile, P. Barcellona, S. Buhmann, L. Rizzuto, and R. Passante, “Dynamical Casimir-Polder force between an excited atom and a conducting wall,” *Phys. Rev. A*, vol. 94, p. 042511, 2016.

[162] R. Passante, T. Petrosky, and I. Prigogine, “Long-time behaviour of self-dressing and indirect spectroscopy,” *Physica A*, vol. 218, p. 437, 1995.

[163] G. Compagno and D. Valenti, “Long-time dynamics of self-dressing,” *J. Phys. B*, vol. 32, p. 4705, 1999.

[164] E. Power and T. Thirunamachandran, “Quantum electrodynamics with nonrelativistic sources. II. Maxwell fields in the vicinity of a molecule,” *Phys. Rev. A*, vol. 28, p. 2663, 1983.

[165] P. Milonni, “Semiclassical and quantum-electrodynamical approaches in nonrelativistic radiation theory,” *Phys. Rep.*, vol. 25, p. 1, 1976.

[166] E. Moniz and D. Sharp, “Radiation reaction in nonrelativistic quantum electrodynamics,” *Phys. Rev. D*, vol. 15, p. 2850, 1977.

[167] N. Bartolo and R. Passante, “Electromagnetic-field fluctuations near a dielectric-vacuum boundary and surface divergences in the ideal conductor limit,” *Phys. Rev. A*, vol. 86, p. 012122, 2012.

[168] R. Passante, L. Rizzuto, and S. Spagnolo, “Vacuum local and global electromagnetic self-energies for a point-like and an extended field source,” *Eur. Phys. J. C*, vol. 73, p. 2419, 2013.

[169] S. Murray, C. Whisler, S. Fulling, J. Wagner, H. Carter, D. Lujan, F. Mera, and T. Settlemyre, “Vacuum energy density and pressure near a soft wall,” *Phys. Rev. D*, vol. 93, p. 105010, 2016.

[170] R. Passante, T. Petrosky, and I. Prigogine, “Virtual transitions, self-dressing and indirect spectroscopy,” *Opt. Comm.*, vol. 99, p. 55, 1993.

[171] L. Rizzuto, R. Passante, and F. Persico, “Dynamical Casimir-Polder energy between an excited- and a ground-state atom,” *Phys. Rev. A*, vol. 70, p. 012107, 2004.

[172] R. Messina, R. Passante, L. Rizzuto, S. Spagnolo, and R. Vasile, “Dynamical Casimir-Polder potentials in non-adiabatic conditions,” *Phys. Scr.*, vol. T160, p. 014032, 2014.

[173] J. Eschner, C. Raab, F. Schmidt-Kaler, and R. Blatt, “Light interference from single atoms and their mirror images,” *Nature (London)*, vol. 413, p. 495, 2001.

[174] H. Failache, S. Saltiel, M. Fichet, D. Bloch, and M. Ducloy, “Resonant coupling in the van der Waals interaction between an excited alkali atom and a dielectric surface: an experimental study via stepwise selective reflection spectroscopy,” *Eur. Phys. J.*, vol. 73, p. 237, 2003.

[175] T. Gallagher, “Rydberg atoms,” *Rep. Prog. Phys.*, vol. 143, p. 143, 1988.

[176] Y. Todorov, A. M. Andrews, R. Colombelli, S. D. Liberato, C. Ciuti, P. Klang, G. Strasser, and C. Ciuti, “Ultrastrong light-matter coupling regime with polariton dots,” *Phys. Rev. Lett.*, vol. 105, p. 196402, 2010.

[177] T. Schwartz, J. A. Hutchison, C. Genet, and T. W. Ebbesen, “Reversible switching of ultrastrong light-molecule coupling,” *Phys. Rev. Lett.*, vol. 106, p. 196405, 2011.

[178] M. Geiser, F. Castellano, G. Scalari, M. Beck, L. Nevou, and J. Faist, “Ultrastrong coupling regime and plasmon polaritons in parabolic semiconductor quantum wells,” *Phys. Rev. Lett.*, vol. 108, p. 106402, 2012.

[179] G. Scalari, C. Maissen, S. Cibella, R. Leoni, C. Reichl, W. Wegscheider, M. Beck, and J. Faist, “THz ultrastrong light-matter coupling,” *Il Nuovo Saggiatore*, vol. 31, p. 4, 2015.

[180] Q. Zhang, M. Lou, X. Li, J. L. Reno, W. Pan, J. D. Watson, M. J. Manfra, and J. Kono, “Collective non-perturbative coupling of 2d electrons with high-quality-factor terahertz cavity photons,” *Nature Phys.*, vol. 12, p. 1005, 2016.

[181] C. Ciuti, G. Bastard, and I. Carusotto, “Quantum vacuum properties of the intersubband cavity polariton field,” *Phys. Rev. B*, vol. 72, p. 115303, 2005.

[182] J. Casanova, G. Romero, I. Lizuain, J. J. Garcia-Ripoll, and E. Solano, "Deep strong coupling regime of the Jaynes-Cummings model," *Phys. Rev. Lett.*, vol. 105, p. 263603, 2010.

[183] P. Forn-Diaz, J. Lisenfeld, D. Marcos, J. J. Garcia-Ripoll, E. Solano, C. J. P. M. Harmans, and J. E. Mooij, "Observation of the Bloch-Siegert shift in a qubit-oscillator system in the ultrastrong coupling regime," *Phys. Rev. Lett.*, vol. 105, p. 237001, 2010.

[184] A. Baust, E. Hoffmann, M. Haeberlein, M. J. Schwarz, P. Eder, J. Goetz, F. Wulschner, E. Xie, L. Zhong, F. Quijandria, D. Zueco, J.-J. Garcia-Ripoll, L. Garcia-Alvarez, G. Romero, E. Solano, K. G. Fedorov, E. P. Menzel, F. Deppe, A. Marx, and R. Gross, "Ultrastrong coupling in two-resonator circuit QED," *Phys. Rev. B*, vol. 93, p. 214501, 2016.

[185] Z. Chen, Y. Wang, T. Li, L. Tian, Y. Qiu, K. Inomata, F. Yoshihara, S. Han, F. Nori, J. S. Tsai, and J. Q. You, "Multi-photon sideband transitions in an ultrastrongly-coupled circuit quantum electrodynamics system," *Phys. Rev. A*, vol. 96, p. 012325, 2017.

[186] S. J. Bosman, M. F. Gely, V. Singh, A. Bruno, D. Bothner, and G. A. Steele, "Multi-mode ultra-strong coupling in circuit quantum electrodynamics," *arXiv:1704.06208*, 2017.

[187] P. Nataf and C. Ciuti, "Vacuum degeneracy of a circuit QED system in the ultrastrong coupling regime," *Phys. Rev. Lett.*, vol. 104, p. 023601, 2010.

[188] P. Nataff and C. Ciuti, "No-go theorem for superradiant quantum phase transitions in cavity QED and counter-example in circuit QED," *Nature Commun.*, vol. 1, p. 72, 2010.

[189] M. Bamba, K. Inomata, and Y. Nakamura, "Superradiant phase transition in a superconducting circuit in thermal equilibrium," *Phys. Rev. Lett.*, vol. 117, p. 173601, 2016.

[190] S. D. Liberato, "Light-matter decoupling in the deep strong coupling regime: The breakdown of the Purcell effect," *Phys. Rev. Lett.*, vol. 112, p. 016401, 2014.

[191] T. Jaako, Z.-L. Xiang, J. Garcia-Ripoll, and P. Rabl, "Ultrastrong coupling phenomena beyond the Dicke model," *Phys. Rev. A*, vol. 94, p. 033850, 2016.

[192] G. Levine and V. N. Muthukumar, "Entanglement of a qubit with a single oscillator mode," *Phys. Rev. B*, vol. 69, p. 113203, 2004.

[193] A. P. Hines, C. M. Dawson, R. H. McKenzie, and G. J. Milburn, “Entanglement and bifurcations in Jahn-Teller models,” *Phys. Rev. A*, vol. 70, p. 022303, 2004.

[194] S. Ashhab and F. Nori, “Qubit-oscillator systems in the ultrastrong-coupling regime and their potential for preparing nonclassical states,” *Phys. Rev. A*, vol. 81, p. 042311, 2010.

[195] P. Nataf and C. Ciuti, “Protected quantum computation with multiple resonators in ultrastrong coupling circuit QED,” *Phys. Rev. Lett.*, vol. 107, p. 190402, 2011.

[196] G. Romero, D. Ballester, Y. M. Wang, V. Scarani, and E. Solano, “Ultrafast quantum gates in circuit QED,” *Phys. Rev. Lett.*, vol. 108, p. 120501, 2012.

[197] T. H. Kyaw, S. Felicetti, G. Romero, E. Solano, and L.-C. Kwek, “Scalable quantum memory in the ultrastrong coupling regime,” *Sci. Rep.*, vol. 5, p. 8621, 2015.

[198] R. Stassi and F. Nori, “Quantum memory in the ultrastrong-coupling regime via parity symmetry breaking,” *arXiv:1703.08951*, 2017.

[199] Y. Wang, J. Zhang, C. Wu, J. Q. You, and G. Romero, “Holonomic quantum computation in the ultrastrong-coupling regime of circuit QED,” *Phys. Rev. A*, vol. 94, p. 012328, 2016.

[200] Y. Wang, C. Guo, G.-Q. Zhang, G. Wang, and C. Wu, “Ultrafast quantum computation in ultrastrongly coupled circuit QED systems,” *Sci. Rep.*, vol. 7, p. 44251, 2017.

[201] B. Reznik, A. Retzker, and J. Silman, “Violating Bell’s inequalities in vacuum,” *Phys. Rev. A*, vol. 71, p. 042104, 2005.

[202] M. Han, S. J. Olson, and J. P. Dowling, “Generating entangled photons from the vacuum by accelerated measurements: Quantum-information theory and the Unruh-Davies effect,” *Phys. Rev. A*, vol. 78, p. 022302, 2008.

[203] S. J. Olson and T. C. Ralph, “Extraction of timelike entanglement from the quantum vacuum,” *Phys. Rev. A*, vol. 85, p. 012306, 2012.

[204] C. Sabin, B. Peropadre, M. del Rey, and E. Martin-Martinez, “Extracting past-future vacuum correlations using circuit QED,” *Phys. Rev. Lett.*, vol. 109, p. 033602, 2012.

[205] G. Salton, R. B. Mann, and N. C. Menicucci, “Acceleration-assisted entanglement harvesting and rangefinding,” *New J. Phys.*, vol. 17, p. 035001, 2015.

[206] L. Dai, W. Kuo, and M. C. Chung, "Extracting entangled qubits from majorana fermions in quantum dot chains through the measurement of parity," *Sci. Rep.*, vol. 5, p. 11188, 2015.

[207] O. Gühne, F. Bodoky, and M. Blaauboer, "Multiparticle entanglement under the influence of decoherence," *Phys. Rev. A*, vol. 78, p. 060301 (R), 2008.

[208] M. Bergmann and O. Gühne, "Entanglement criteria for Dicke states," *J. Phys. A: Math. Theor.*, vol. 46, p. 385304, 2013.

[209] G. Toth and I. Apellaniz, "Quantum metrology from a quantum information science perspective," *J. Phys. A: Math. Theor.*, vol. 47, p. 424006, 2014.

[210] U. Vool and M. Devoret, "Introduction to quantum electromagnetic circuits," *arXiv:1610.03438*, 2016.

[211] J. Bourassa, J. M. Gambetta, A. A. Abdumalikov, O. Astafiev, Y. Nakamura, and A. Blais, "Ultrastrong coupling regime of cavity qed with phase-biased flux qubits," *Phys. Rev. A*, vol. 80, p. 032109, 2009.

[212] B. Peropadre, D. Zueco, D. Porras, and J. J. Garcia-Ripoll, "Nonequilibrium and nonperturbative dynamics of ultrastrong coupling in open lines," *Phys. Rev. Lett.*, vol. 111, p. 243602, 2013.

[213] C. C. Tannoudji, J. Dupont-Roc, and G. Grynberg, *Atom-Photon Interactions: Basic processes and Applications.* Wiley-VCH, Weinheim, 1998.

[214] F. T. Arecchi, E. Courtens, R. Gilmore, and H. Thomas, "Atomic coherent states in quantum optics," *Phys. Rev. A*, vol. 6, p. 2211, 1972.

[215] M. Nielsen and I. Chuang, *Quantum Computation and Quantum Information.* Cambridge University Press, 2000.

[216] F. Yan, S. Gustavsson, A. Kamal, J. Birenbaum, A. Sears, D. Hover, D. Rosenberg, G. Samach, T. J. Gudmundsen, J. L. Yoder, T. P. Orlando, J. Clarke, A. J. Kerman, and W. D. Oliver, "The flux qubit revisited to enhance coherence and reproducibility," *Nature Commun.*, vol. 7, p. 12964, 2016.

[217] R. H. Dicke, “Coherence in spontaneous radiation processes,” *Phys. Rev.*, vol. 93, p. 99, 1954.